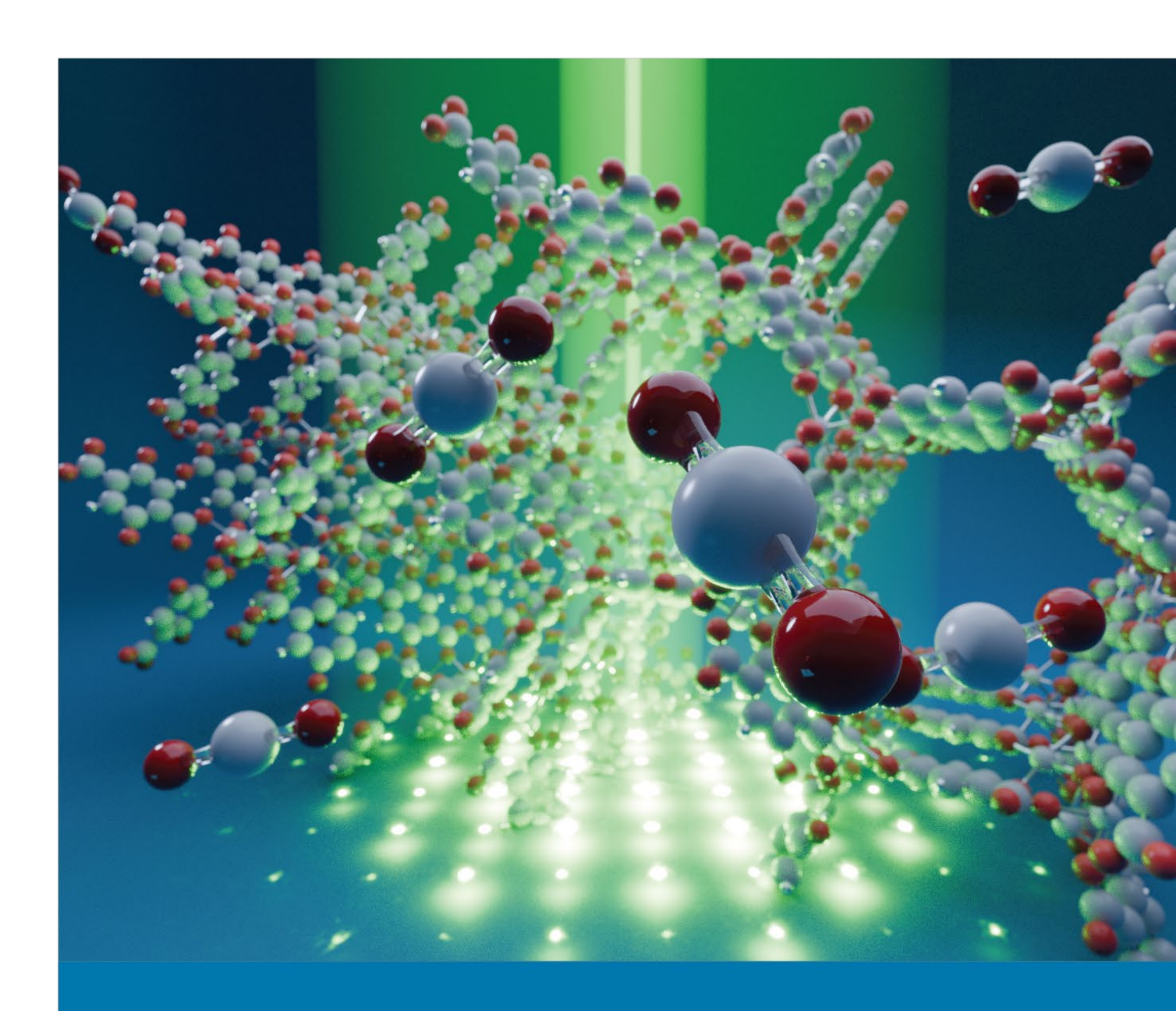
# Transmission electron microscopy studies of catalysts and catalyst carriers for CO<sub>2</sub> absorption and reduction reactions

# **Matthias Quintelier**



Supervisor Prof. Dr. Joke Hadermann

Thesis submitted in fulfilment of the requirements for the degree of Doctor in Physics Faculty of Science | Antwerpen, Month 2025





Faculty of Science
Departement Physics

Transmission electron microscopy studies of catalysts and catalyst carriers for CO<sub>2</sub> absorption and reduction reactions

Transmissie-elektronenmicroscopiestudies van katalysatoren en dragers van katalysatoren voor CO<sub>2</sub>-absorptie- en reductiereacties

> Proefschrift voorgelegd tot het behalen van de graad van Doctor in de Wetenschappen: Fysica aan de Universiteit Antwerpen, te verdedigen door:

> > **Matthias Quintelier**

**Promotor** 

Prof. Dr. Joke Hadermann Antwerpen, 2025

# **Doctoral Committee**

#### Chairman

Prof. Dr. Jacques Tempere, University of Antwerp - Belgium

#### **Promotor**

Prof. Dr. Joke Hadermann, University of Antwerp – Belgium

#### Members

Prof. Dr. Koen Janssens, University of Antwerp – Belgium

Prof. Dr. Stefan Wuttke, AGH University of Krakow - Poland

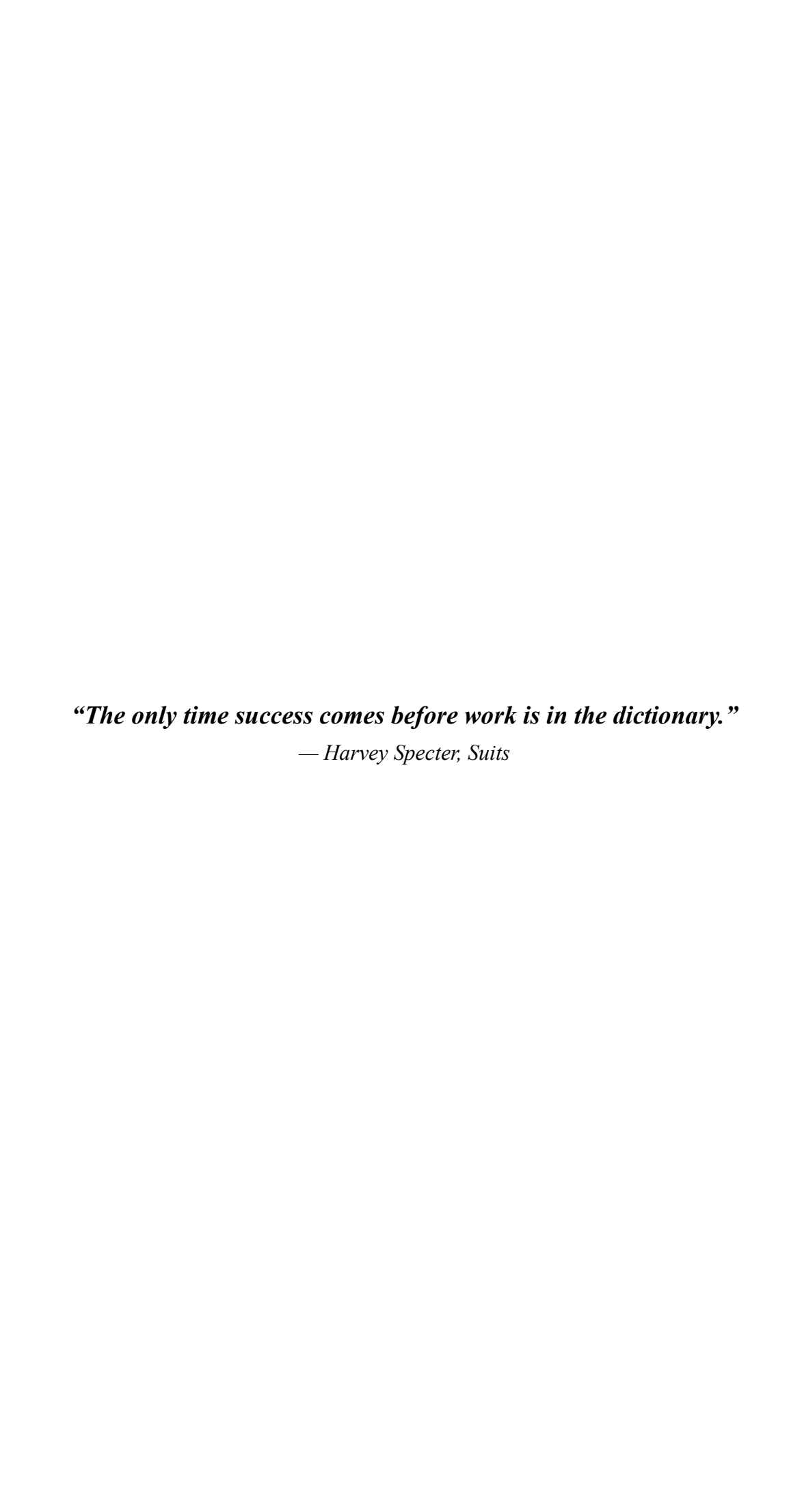
Dr. Paul Klar, University of Bremen – Germany

# **Contact Information**

Matthias Quintelier
University of Antwerp – Department of Physics
EMAT – Electron Microscopy for Materials Science
Groenenborgerlaan 171, B-2020 Antwerp
Belgium
Matthias.Quintelier@uantwerpen.be

©2025 Matthias Quintelier All rights reserved.

De doctoraatsonderzoeker en promotor(en) verklaren dat het doctoraatsonderzoek werd uitgevoerd volgens de principes van de wetenschappelijke integriteit, zoals vermeld in het algemeen doctoraatsreglement en algemeen charter van de doctorandus van UAntwerpen en het integriteitscharter voor doctorandi en promotoren verbonden aan de Universiteit Antwerpen.



# Dankwoord/Acknowledgements

Starting a PhD, doing the research, and writing this thesis have been both a very rewarding and challenging experience, with its share of highs and lows. I couldn't have made this journey without the help of many people, and I want to take the time to thank them here.

Above all, I owe my deepest thanks to my promoter, Professor Dr. Joke Hadermann. Her class on 'Structuur van de vaste stof,' where she showed diffraction with lasers in a way I'll never forget, got me excited about solid-state physics and made me want to do my bachelor thesis with her. During that time, I fell in love with crystallography and electron microscopy. I always felt like we were working together, and that I was not just following orders, which made me even more passionate. This naturally led me to continue my master's thesis with her, and in the end, to begin my PhD under her careful guidance. Her guidance and ability to push me to think differently have helped me grow as a scientist, and I wouldn't be where I am now without her help.

I want to send my deepest thanks and love to my wife Gitte. You've stood by me like a pillar not just during my PhD years but throughout my entire path to becoming a physicist. Your steady support and love made this all happen. Along with Gitte, I want to thank my son Jack and our dogs Hektor<sup>†</sup>, Alfie, Pippa and Madeleine. Even though Jack can't read this yet, and the dogs never will, they've all brought me happiness and comfort when times were rough.

My family deserves my gratitude too. I want to thank Rudi and Birgit, my in-laws, for always believing in me throughout my time at the university. Furthermore, my grandparents, brother and dad have been there for me, backing me up through my studies even when we faced hard times. A special shout-out goes to my godfather Stephan, for pushing me to be my best self and being a source of inspiration.

I would also like to thank my athletics coach, Dirk, as well as all the past and present members of the ATT. They have always believed in me, pushing me to be the best version of myself, and have supported me during many hard times, both professionally and personally.

I'd like to express my heartfelt gratitude to everyone in Joke's group, both past and present: Dr. Maria Batuk, Dr. Stefano Canossa, Dr. Mylene Hendricks, Dr. Romy Poppe, Dr. Daphne Vandemeulebroucke, Saleh Gholam, Sepideh Rahimi, and Amirhossein Hajizadeh. Our conversations have proven priceless, giving me insights, techniques, and tips and tricks to operate the microscopes.

I want to thank all EMAT members, both former and current, with particular appreciation for Dr. Armand Béché, Dr. Lars Riekehr, Dr. Alexander Zintler, and Dr. Saeid Pourbabak. Armand stepped into a mentor role, showing me the technical details of the microscopes and pushing me to excel as a scientist. I also appreciate Lars, Alex, and Saeid for their constant support and help throughout my PhD.

To all of you, my deepest gratitude.

# **Table of contents**

List of a	bbreviations	3
Abstract		4
Preface		6
Voorbes	chouwing	9
Schemat	ic overview of the experimental work performed during this thesis	12
Chapter	1: Basics of the applied techniques	13
1.1.	Transmission electron microscopy	13
1.2.	Electron diffraction	15
1.3.	(HAADF-)STEM	23
1.4.	EDX	24
1.5.	Scanning nanobeam diffraction	25
1.6.	SEM	26
1.7.	Holders	27
1.8.	Sample preparation	31
Chapter	2: MDT dropcasting tool	32
2.1.	Difficulties during in situ sample preparation	32
2.2.	Development of the MDT	33
Conclusi	ion to Chapter 2	38
Chapter	3: Layered double hydroxides	39
3.1.	Introduction to Layered Double Hydroxides	39
3.2.	LDHs studied during this PhD	41
3.3.	Thermal evolution of ZnAl LDH	50
3.4.	CO <sub>2</sub> study of ZnAl LDH	59
Conclusi	ion to Chapter 3	63
Chapter	4: Metal organic frameworks	65
4.1.	Introduction to Metal Organic Frameworks	65
4.2.	MOF-74	
4.2.1.	Optimizing 3D ED acquisition parameters for MOF-74	
4.2.2.	Activation of MOF-74	
4.2.3.	CO <sub>2</sub> study of MOF-74	83
424	Difficulties during in situ experiments on MOF-74	99

4.3.	Biohybrids	91
4.4.	UA-4	
4.5.	Atmospheric studies of UiO-68	
Conclus	sion to Chapter 4	111
Chapter	r 5: ZnO	114
5.1.	Introduction to Zinc Oxide	114
5.2.	Effects of synthesis on morphology	115
5.3.	In situ study of ZnO	118
Conclus	sion to Chapter 5	122
General conclusion to the thesis		
Algemene conclusie van de thesis		
Future prospects		
Scientif	fic contributions during this PhD	144
Referen	nces	129
Append	lix	

# List of abbreviations

3D ED Three dimensional electron diffraction

4AirCRAFT 4 Air carbon recycling for aviation fuel technology

ADP Atomic displacement parameter

BFTEM Bright Field Transmission Electron Microscopy

BSS Blind source separation CCD Charge-coupled device

CO<sub>2</sub>ER CO<sub>2</sub> electrochemical reduction

CO<sub>2</sub>RR CO<sub>2</sub> reduction reactions

cRED Continuous rotation electron diffraction

DMF Dimethylformamide
DED Direct electron detector

EDT Electron diffraction tomography

EDX Energy-dispersive X-ray

HAADF High-angle annular dark field

HRTEM High Resolution transmission electron microscopy

LDH Layered double hydroxide

MEMS Microelectromechanical System

MOF Metal organic framework

NMF Non-negative matrix factorizationPCA Principle component analysisPXRD Powder X-ray diffraction

RHE Reversible Hydrogen Electrode
SAED Selected area electron diffraction

SBU Secondary building unit

SEM Scanning electron microscopy

SNBD Scanning nanobeam electron diffraction
STEM Scanning transmission electron microscopy

SXRD Synchrotron X-ray diffraction

TEM Transmission electron microscopy

UHV Ultra-high vacuum VDF Virtual dark field

# **Abstract**

The increasing concentration of carbon dioxide (CO<sub>2</sub>) in the atmosphere has become a major environmental challenge, driving the need for innovative solutions to mitigate its impact. One promising approach involves the development of advanced catalytic materials that can facilitate CO<sub>2</sub> conversion into valuable products. This thesis explores the structure and functional properties of catalytic materials, particularly layered double hydroxides (LDHs), metal-organic frameworks (MOFs), and ZnO-based catalysts, using transmission electron microscopy (TEM). By combining conventional and *in situ* TEM techniques, this work provides nanoscale insights into how synthesis methods, processing conditions, and environmental exposure influence these materials, with a focus on their applications in CO<sub>2</sub> reduction reactions (CO<sub>2</sub>RR).

While optimizing the *in situ* TEM workflow, a 3D-printed MEMS dropcasting tool (MDT) was developed, which significantly improved sample preparation for these *in situ* experiments.

TEM studies have been performed to determine the structural and compositional characteristics of these materials. For LDHs, the impact of different cation ratios, aging, and mechanical processing on the morphology and crystallinity of the nanoparticles was analyzed using several TEM techniques. Comparing these results to the catalytic efficiency provided a nanoscale explanation for the identification of ZnAl (2:1) LDH as a highly promising CO<sub>2</sub>RR candidate. *In situ* heating experiments for this material showed an environment-dependent decomposition, while CO<sub>2</sub> exposure led to an expansion of LDH layers.

In situ TEM activation experiments of Zn-MOF-74 and Cu-MOF-74 revealed remaining electrostatic potentials, indicating remaining atoms inside the pores, and distinct thermal degradation behaviors. The *in situ* CO<sub>2</sub> adsorption experiments in this work challenge conventional assumptions in literature for Zn-MOF-74 by showing non-linear CO<sub>2</sub> configurations, suggesting the presence of strong adsorption interactions. These strong interactions may contribute to the structural instability of the MOF during desorption. Additionally, enzyme-MOF biohybrids were investigated using various TEM characterization techniques in an effort to achieve the first direct observations of enzymes within the MOF scaffold. This work led to the development of a novel staining approach that enabled the visualization of enzyme encapsulation.

The structural characterization of the novel UA-4 MOF highlighted the challenges of solving complex disordered structures.

ZnO-based catalysts were also characterized using TEM, demonstrating that different synthesis methods resulted in distinct particle morphologies at the nanoscale. Thermal decomposition at 300 °C produced highly active nanorods, while decomposition at 400 °C yielded triangular-shaped particles. In contrast, coprecipitation led to the formation of herringbone-shaped ZnO particles. *In situ* ZnO oxidation studies were hindered by SiO<sub>x</sub> formation on the sample, highlighting experimental challenges when studying oxidation under reactive conditions.

Overall, the detailed TEM characterizations in this thesis offer atomic-scale insights that help connect the catalyst nanoscale structure to performance, contributing to a better understanding and further optimization of materials for CO<sub>2</sub>RR applications. This work not only helps improve catalyst design but also tackles key challenges in using TEM to study dynamic, beam-sensitive materials, providing a solid starting point for future research on functional materials in real-world conditions.

# **Preface**

The global rise in carbon dioxide (CO<sub>2</sub>) emissions has emerged as one of the most pressing environmental challenges of our time. As a greenhouse gas, CO<sub>2</sub> plays an important role in the Earth's climate system by trapping heat in the atmosphere. While this natural process is essential for maintaining our climate, the unprecedented increase in CO<sub>2</sub> levels due to human activities has led to significant and far-reaching consequences. The rapid accumulation of CO<sub>2</sub> in the atmosphere is one of the primary drivers of climate change, contributing to the warming of the planet, rising sea levels, and an increase in the frequency and severity of extreme weather events. The implications of CO<sub>2</sub> emissions are profound, not only for the environment but also for global economies, public health, and social stability. The impact is already being felt worldwide, from the melting polar ice caps to the intensifying wildfires and prolonged droughts. If current trends continue, the consequences will only get worse, leading to irreversible damage to ecosystems and loss of biodiversity.

It is therefore imperative not only to decrease our CO<sub>2</sub> emissions but also to reduce the amount of CO<sub>2</sub> that has already been emitted by human activities. The air transport sector, for instance, is responsible for approximately 2-3% of global CO<sub>2</sub> emissions.

Over the past several years, significant research has been conducted to address and mitigate this CO<sub>2</sub> footprint. One promising European initiative, the 4AirCRAFT project, exemplifies the innovative approaches being pursued in this field. It aims to combine hybrid catalytic conversion and process intensification to convert recycled CO<sub>2</sub> into sustainable and clean liquid fuels that can be used as biofuels for airplanes. The project focuses on three primary goals to achieve this. The first goal is the development of next-generation electrochemical, chemical, and biological catalysts. These advanced catalysts are designed to enhance the efficiency of CO<sub>2</sub> conversion processes. The second goal is the development of novel carrier structures that can support these catalysts effectively. Finally, the project seeks to design and implement a single cascade reactor that operates under milder conditions, specifically at much lower temperatures, which is crucial for improving the overall efficiency and sustainability of the conversion process. This thesis was performed as part of this 4AirCRAFT project.

This work focuses on the investigation of various materials, including electrochemical catalysts and catalyst supports such as layered double hydroxides (LDHs) and metal-organic frameworks (MOFs), as well as ZnO materials, which are all of interest for their potential applications in this quest for CO<sub>2</sub> emission reduction. The research aims to analyze these materials at the nanoscale using a range of transmission electron microscopy (TEM) techniques. Nanoscale studies are particularly useful because it is generally known that the properties of materials at macroscopic scales are often determined by their nanoscale characteristics. By employing both conventional and (*in situ*) TEM techniques, this study seeks to observe the materials under conditions that closely mimic their intended environments, potentially demonstrating insights into their behavior that might be missed when studied at conventional scales or under standard TEM conditions.

The goal of my thesis is to deepen the understanding of the structural and functional properties of advanced catalytic materials, with a particular focus on MOFs and LDHs. By utilizing extensive transmission electron microscopy analysis, I aim to explore how different synthesis methods and environmental conditions affect key characteristics such as morphology, particle size, crystallinity, and elemental composition, which is essential for optimizing these materials for catalytic applications, especially in CO<sub>2</sub> reduction reactions and as catalyst carriers.

The focus of my work lies on *in situ* studies, where I developed and fine-tuned experimental parameters and specialized tools to examine these materials in environments that closely resemble those of their real-world applications. Through these *in situ* experiments, I aim to gain an understanding into critical processes, including the activation of MOF-74, the structural effects of CO<sub>2</sub> absorption, the thermal decomposition of ZnAl LDH and the structural influence of CO<sub>2</sub> absorption on this material. Additionally, I will demonstrate that it is possible to study sensitive MOFs at atmospheric pressure within an electron microscope, preserving their structural integrity without the need for cryogenic conditions. These *in situ* investigations are key to understanding how MOFs and LDHs respond to various environmental conditions, which in turn informs the design and optimization of these materials for practical catalytic use. Ultimately, this thesis seeks to expand the boundaries of knowledge in this field, offering a solid foundation for the more effective and efficient application of MOFs and LDHs in real-world catalytic processes.

In **Chapter 1**, I will introduce the various TEM techniques employed in this work, including details on the hardware such as sample holders and detectors. An outline of the general method used for sample preparation will also be given.

**Chapter 2** will detail the process of optimizing acquisition parameters for *in situ* work with MOFs. A tool (MDT) designed to facilitate sample preparation is developed for this purpose.

In **Chapter 3** I will focus on LDHs, exploring how different synthesis methods influence their properties such as crystallinity, elemental distribution and morphology. Next, I will also present the results of *in situ* experiments conducted on ZnAl LDH, where the impact of the heating atmosphere on the material's thermal decomposition by heating the material both in air and in vacuum was explored. Additionally, CO<sub>2</sub> adsorption studies on these materials were performed to understand how CO<sub>2</sub> absorption influences their structure.

Chapter 4 will cover the investigations conducted on several MOF samples. In this chapter, I investigated various experimental parameters that needed to be optimized for studying the beam sensitive MOFs. For MOF-74, I investigated the activation procedures for Zn-MOF-74 and Cu-MOF-74. The effect of CO<sub>2</sub> adsorption on the crystal structure of Zn-MOF-74 was also examined. For UiO-68, a material highly sensitive to the TEM's vacuum environment, I investigated the possibility of studying this material under gaseous conditions inside the TEM. Additionally, biohybrid materials were studied, which consist of MOFs combined with catalytic enzymes embedded within their pores. Various experiments were conducted to determine the influence of the enzyme on the MOF structure and the positioning of the enzymes within the biohybrid material.

The structure of a novel MOF, UA-4, synthesized using a newly developed method, was also investigated in detail.

Chapter 5 covers the studies on several ZnO-based electrochemical catalysts. The influence of the synthesis method on the particle morphology and elemental composition was studied. Furthermore, I investigated the presence of an aluminum coating on the ZnO particles, which enhances their catalytic effectiveness. Next, I will describe the *in situ* measurements on ZnO, where the effects of activation and CO<sub>2</sub> exposure on particle morphology and crystal structure under elevated temperatures and oxidizing conditions were investigated.

Finally, I will give both an English and Dutch conclusion to this thesis.

# Voorbeschouwing

De wereldwijde toename van koolstofdioxide (CO<sub>2</sub>)-emissies is een van de meest urgente milieuproblemen van deze tijd. Als broeikasgas speelt CO<sub>2</sub> een cruciale rol in het klimaatsysteem van de aarde door warmte vast te houden in de atmosfeer. Hoewel dit natuurlijke proces essentieel is voor het behoud van een leefbaar klimaat, heeft de ongekende stijging van CO<sub>2</sub>-niveaus door menselijke activiteiten geleid tot aanzienlijke en verstrekkende gevolgen. De snelle accumulatie van CO<sub>2</sub> in de atmosfeer is een primaire drijvende kracht achter klimaatverandering, die bijdraagt aan de opwarming van de aarde, stijgende zeespiegels, en een toename in de frequentie en ernst van extreme weersomstandigheden.

De implicaties van ongecontroleerde CO<sub>2</sub>-emissies zijn diepgaand, niet alleen voor het milieu, maar ook voor de wereldeconomieën, de volksgezondheid en de sociale stabiliteit. De impact wordt wereldwijd al gevoeld, van het smelten van de poolkappen tot de intensivering van bosbranden en langdurige droogte. Als de huidige trends zich voortzetten, zullen de gevolgen alleen maar erger worden, wat leidt tot onomkeerbare schade aan ecosystemen en verlies van biodiversiteit.

Het is daarom van groot belang niet alleen onze CO<sub>2</sub>-emissies te verminderen, maar ook de hoeveelheid CO<sub>2</sub> die al door menselijke activiteiten is uitgestoten, terug te dringen. De luchtvaartsector is bijvoorbeeld verantwoordelijk voor ongeveer 2-3% van de wereldwijde CO<sub>2</sub>-emissies. In de afgelopen jaren is er aanzienlijk onderzoek verricht om deze CO<sub>2</sub>-voetafdruk aan te pakken en te verminderen. Een veelbelovend Europees project, het 4AirCRAFT-project, is een goed voorbeeld van onderzoek die op dit gebied worden nagestreefd. Het project heeft tot doel hybride katalytische conversie en procesintensivering te combineren om gerecycleerd CO<sub>2</sub> om te zetten in duurzame en schone brandstoffen die als biobrandstoffen voor vliegtuigen kunnen worden gebruikt. Het project richt zich op drie doelen om dit te bereiken. Het eerste doel is de ontwikkeling van de volgende generatie elektrochemische, chemische en biologische katalysatoren. Deze geavanceerde katalysatoren zijn ontworpen om de efficiëntie van CO<sub>2</sub>-conversieprocessen te verbeteren. Het tweede doel is de ontwikkeling van nieuwe dragerstructuren die deze katalysatoren effectief kunnen ondersteunen.

Ten slotte streeft het project naar het ontwerpen en implementeren van een enkele cascade-reactor die onder mildere omstandigheden opereert, met name bij veel lagere temperaturen, wat cruciaal is voor het verbeteren van de algehele efficiëntie en duurzaamheid van het conversieproces. Deze thesis werd uitgevoerd als onderdeel van dit 4AirCRAFT-project.

Dit werk richt zich op het onderzoeken van verschillende materialen, waaronder elektrochemische katalysatoren en katalysatordragers zoals gelaagde dubbele hydroxiden (LDHs) en metaalorganische kaders (MOFs), evenals ZnO en biohybride materialen, die allemaal van belang zijn voor hun potentiële toepassingen in deze zoektocht naar CO<sub>2</sub>-emissiereductie. Het onderzoek is gericht op het analyseren van deze materialen op nanoschaal met behulp van een reeks transmissieelektronenmicroscopietechnieken (TEM).

Onderzoek op nanoschaal is bijzonder nuttig omdat algemeen bekend is dat de eigenschappen van materialen op macroschaal vaak worden bepaald door hun eigenschappen op nanoschaal.

Door gebruik te maken van verschillende (*in situ*) TEM-technieken, probeert deze studie de materialen te observeren onder omstandigheden die hun beoogde toepassingen nauwkeurig nabootsen, wat mogelijk inzichten kan opleveren in hun gedrag die anders onopgemerkt zouden blijven wanneer ze op conventionele schaal of onder standaard TEM-omstandigheden worden bestudeerd.

Het doel van mijn thesis is het verdiepen van het begrip van de structurele en functionele eigenschappen van geavanceerde katalytische materialen, met een specifieke focus op MOFs en LDHs. Door uitgebreid gebruik te maken van transmissie-elektronenmicroscopie wil ik onderzoeken hoe verschillende synthesemethoden invloed hebben op belangrijke materiaaleigenschappen, zoals morfologie, deeltjesgrootte, kristalliniteit en elementaire samenstelling. Dit onderzoek richt zich op de belangrijke relatie tussen synthesetechnieken, kristalstructuur, morfologie en de daaruit voortvloeiende materiaaleigenschappen, wat essentieel is voor het optimaliseren van deze materialen voor katalytische toepassingen, met name in CO<sub>2</sub>-reductiereacties en als dragers van katalysatoren. De focus van mijn werk ligt op *in situ* studies, waarbij ik experimentele parameters en gespecialiseerde hulpmiddelen heb ontwikkeld en verfijnd om deze materialen te onderzoeken in omgevingen die nauw aansluiten bij hun daadwerkelijke toepassingscondities.

Via deze *in situ* experimenten beoog ik waardevolle inzichten te verkrijgen in cruciale processen, zoals de activering van MOF-74, de structurele effecten van CO<sub>2</sub>-absorptie, de thermische ontleding van ZnAl LDH, en de structurele invloed van CO<sub>2</sub>-absorptie op dit materiaal. Daarnaast zal ik aantonen dat het mogelijk is om gevoelige MOFs bij atmosferische druk te bestuderen binnen een elektronenmicroscoop, waarbij hun structurele integriteit behouden blijft zonder dat cryogene omstandigheden nodig zijn.

Deze *in situ* onderzoeken zijn essentieel om te begrijpen hoe MOFs en LDHs reageren op verschillende omgevingscondities, wat op zijn beurt bijdraagt aan het ontwerp en de optimalisatie van deze materialen voor praktische katalytische toepassingen. Uiteindelijk beoogt deze thesis de grenzen van kennis op dit gebied te verleggen en een solide basis te bieden voor een effectievere en efficiëntere toepassing van MOFs en LDHs in reële katalytische processen.

In **Hoofdstuk 1** bespreek ik de verschillende TEM-technieken die in dit werk zijn toegepast, inclusief details over de hardware, zoals houders en detectoren. Daarnaast geef ik een overzicht van de algemene methode die is gebruikt voor de monstervoorbereiding.

In **Hoofdstuk 2** wordt het proces besproken van het optimaliseren van acquisitieparameters voor *in situ* werk met MOF's. Hier wordt een hulpmiddel geïntroduceerd (de MDT) dat is ontworpen om de monstervoorbereiding voor deze materialen te vergemakkelijken.

In **Hoofdstuk 3** ligt de focus op LDH's, waarbij onderzocht wordt hoe verschillende synthesemethoden invloed hebben op eigenschappen zoals kristalliniteit, elementverdeling en morfologie.

Vervolgens worden de *in situ* experimenten op ZnAl LDH behandeld, waarbij de invloed van de verwarmingsatmosfeer op de thermische ontleding van het materiaal werd bestudeerd door het zowel in lucht als in vacuüm te verhitten. Daarnaast werden CO<sub>2</sub>-adsorptiestudies uitgevoerd om te begrijpen hoe CO<sub>2</sub>-absorptie de structuur van deze materialen beïnvloedt.

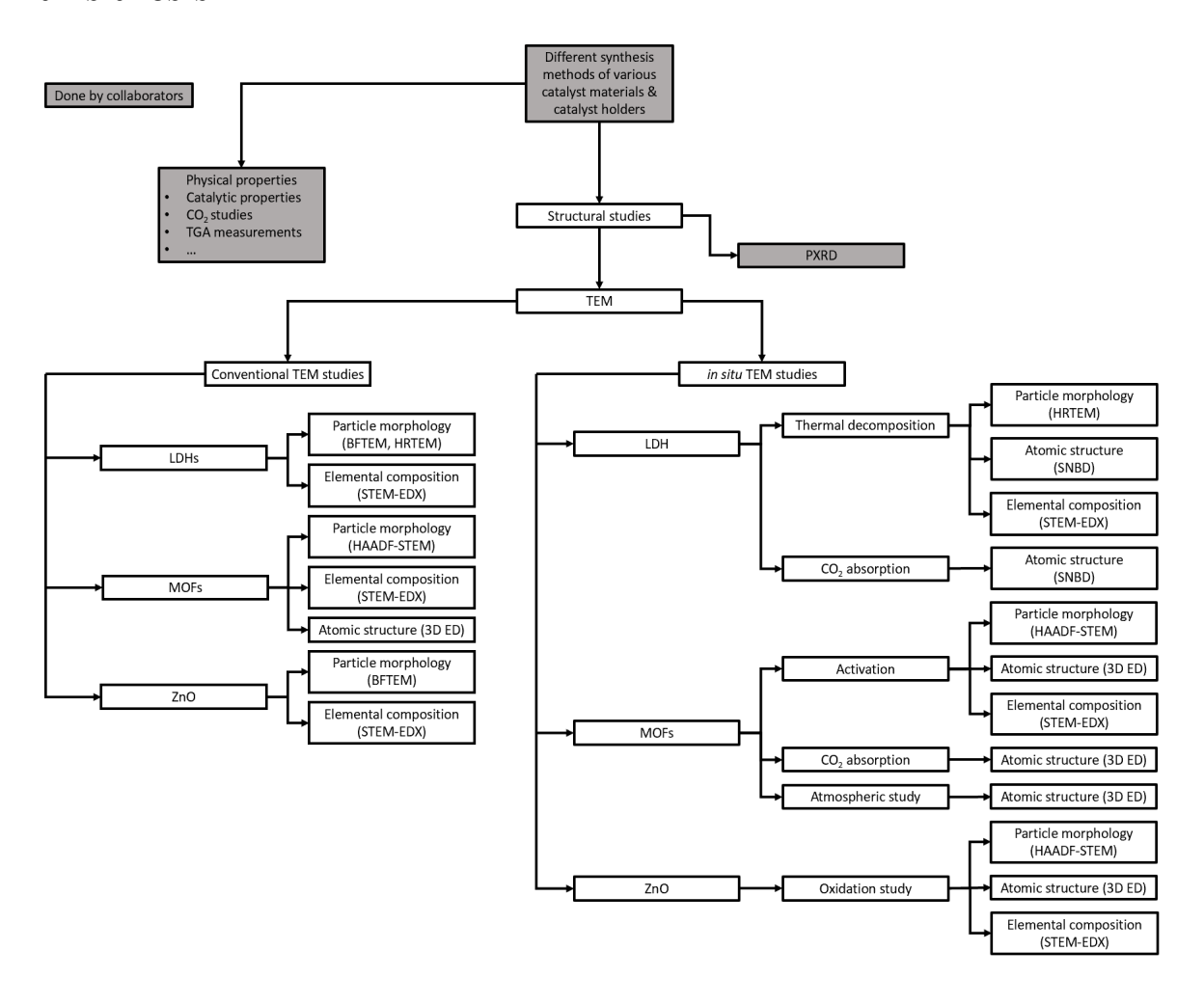
**Hoofdstuk 4** beschrijft het onderzoek dat werd uitgevoerd op verschillende MOF-materialen, die potentieel toepasbaar zijn als katalysatordragers en elektrokatalysatoren. In dit hoofdstuk worden diverse experimentele parameters besproken die geoptimaliseerd moesten worden voor de studie van stralingsgevoelige MOF's. Daarna worden de *in situ* experimenten besproken die zijn uitgevoerd op zowel MOF-74 als UiO-68.

Voor MOF-74 werden de activeringsprocedures voor Zn-MOF-74 en Cu-MOF-74 onderzocht. Ook werden CO<sub>2</sub>-adsorptiestudies uitgevoerd op Zn-MOF-74, waarbij werd gekeken hoe gasabsorptie de kristalstructuur beïnvloedt. Voor UiO-68, een materiaal dat zeer gevoelig is voor het vacuüm van de TEM, werd onderzocht of het mogelijk is om dit materiaal onder gascondities in de TEM te bestuderen. Daarnaast werden biohybride materialen bestudeerd, bestaande uit MOF's gecombineerd met katalytische enzymen die in hun poriën zijn ingebed. Er werden diverse experimenten uitgevoerd om de invloed van het enzym op de MOF-structuur en de positionering van de enzymen binnen het biohybride materiaal te bepalen. Ook de structuur van een nieuw MOF, UA-4, gesynthetiseerd met een nieuw ontwikkelde methode, werd in detail onderzocht.

**Hoofdstuk 5** behandelt de studies op verschillende ZnO-gebaseerde elektrokatalysatoren. De invloed van de synthesemethode op de deeltjesmorfologie en elementaire samenstelling werd onderzocht. Tevens werd de aanwezigheid van een aluminiumcoating op de ZnO-deeltjes bestudeerd, die hun katalytische effectiviteit verhoogt. Vervolgens worden de *in situ* metingen op ZnO beschreven, waarbij de effecten van activering en CO<sub>2</sub>-blootstelling op de deeltjesmorfologie en kristalstructuur onder verhoogde temperaturen en oxiderende omstandigheden werden onderzocht.

Tot slot worden zowel een Engelse als Nederlandse conclusie van deze thesis gegeven.

# Schematic overview of the experimental work performed during this thesis



# Chapter 1: Basics of the applied techniques

# 1.1. Transmission electron microscopy

Transmission electron microscopy (TEM) is the main tool used for the experiments performed in this thesis, encompassing various methodologies and experimental techniques such as selected area electron diffraction (SAED), three-dimensional electron diffraction (3D ED), scanning transmission electron microscopy (STEM) imaging, scanning nanobeam electron diffraction (SNBD), bright-field transmission electron microscopy (BF TEM) imaging, and energy dispersive X-ray (EDX) spectroscopy. All these techniques will be discussed in more detail later. Images of the TEMs used during this work are shown in Figure 1.







Figure 1. Photographs of the used TEMs during this PhD. LTR: FEI Tecnai G2, FEI Tecnai Osiris, FEI Titan.

A transmission electron microscope comprises essential components including an electron gun, electromagnetic lenses, deflection coils, and stigmators. It operates within an ultra-high vacuum environment (~10<sup>-5</sup> Pa) to facilitate the movement of the beam electrons without interference from air molecules. The electron beam is initiated within the electron gun, where electrons escape the cathode material with a velocity determined by the underlying accelerator. Subsequently, a series of condenser lenses direct the beam onto the sample, defining the illumination system. The first condenser lens establishes the spot size or demagnification onto the sample, while subsequent lenses focus or defocus the beam and determine the convergence angle.

A robust objective lens surrounds the sample, serving dual roles within the illumination and imaging systems. This lens focuses the image, projecting the electron beam at a chosen magnification and mode (diffraction or imaging) onto a designated viewing system such as a charged coupled device or high-angle annular dark-field detector. Figure 2 shows a cross section of a TEM, along with a schematic illustration of its main components.



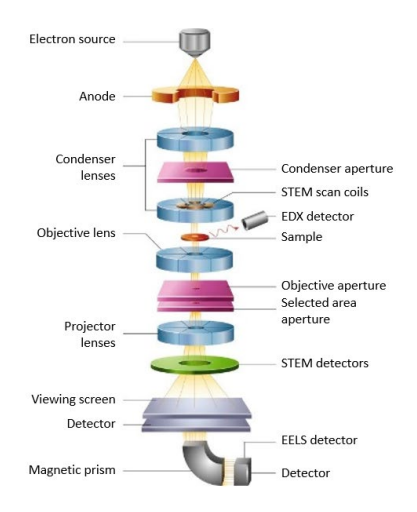


Figure 2. Left: a photograph of a TEM column cut in half, showing the physical structure, including electromagnetic lenses and other components. Right: schematic illustration of the key components of a TEM <sup>1</sup>.

The electron gun generates electrons with controlled kinetic energy. Electromagnetic lenses are employed instead of glass lenses since electromagnetic fields can focus an electron beam, albeit with imperfections resulting in various (spherical and chromatic) aberrations.

These aberrations are inherent to electromagnetic lenses and can distort images, leading to reduced resolution. Stigmators and image and/or probe correctors, exclusive to aberration-corrected microscopes, mitigate these aberrations, achieving resolutions as good as 0.50 Å in direct space. Deflection/scan coils enable beam manipulation, facilitating scanning over specific areas in STEM mode or guiding the beam through the microscope column. The lenses in the illumination system focus the electron beam onto the sample, leading to interactions that generate diffraction patterns in the back focal plane of the objective lens and subsequently form the image in the image plane.

In a TEM, the electron beam is directed at a thin sample, where incident electrons may either pass through unaffected (referred to as direct electrons) or interact with the sample. These interactions result in either elastic or inelastic scattering, which can further be classified as coherent or incoherent, depending on the nature of the scattering event. Other interactions are also possible and are schematically shown in Figure 3. In thin samples, electrons are typically scattered at small angles, whereas in thicker samples, the likelihood of large-angle deviations, including backscattering of up to 180°, increases significantly.

Elastic scattering occurs when electrons are deflected by the Coulomb field of the atomic nucleus or the surrounding electron cloud, with negligible energy loss, effectively conserving their original energy. Inelastic scattering, on the other hand, involves energy transfer from the incoming electrons to the material. This type of interaction mainly occurs between the incoming electrons and the electrons of the sample material. The energy loss during inelastic scattering leads to a longer wavelength for the scattered electrons compared to the incident electrons.

Inelastic interactions can induce a variety of processes, such as the ejection of secondary electrons, emission of X-rays, and the creation of Auger electrons or electron-hole pairs. For example, when an incident electron has enough energy to eject an electron from an atom's inner or outer shell, the atom enters an excited state. As the atom returns to a stable state, the energy difference between the atomic shells may be released as an X-ray or transferred to another electron, which is emitted as an Auger electron. In thicker samples, electrons may not pass through at all, a phenomenon referred to as absorption.

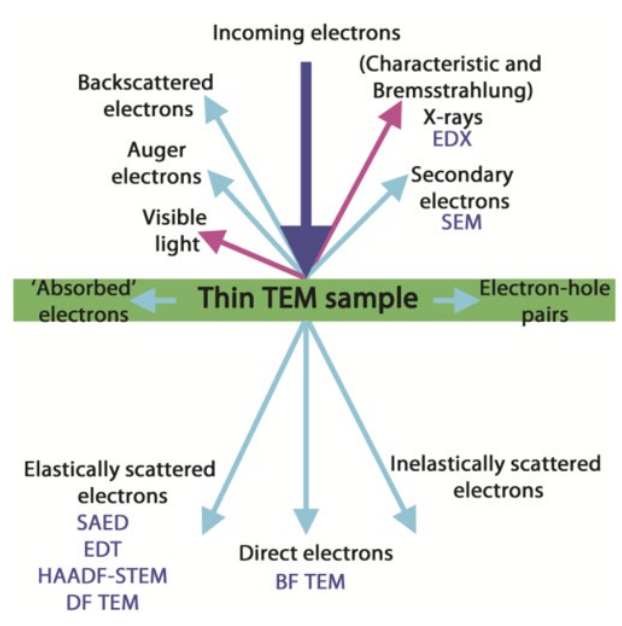


Figure 3. Schematic illustration of the interactions between the incoming electron beam (dark blue) with the sample (green), where the resulting electron signals (light blue) and non-electron signals (pink) used for the techniques in this thesis written in purple are displayed <sup>2</sup>.

### 1.2. Electron diffraction

The main electron microscopy technique used in this thesis is called electron diffraction (ED). ED is based on the detection of elastically scattered electrons. For both selected area electron diffraction (SAED), as well as for continuous rotation electron diffraction (cRED), the form of three-dimensional electron diffraction (3D ED) used in this thesis, a parallel beam interacts with the sample and generates a diffraction pattern that is projected onto a detector, schematically shown in Figure 4. Different types of detectors will be discussed later in this thesis.

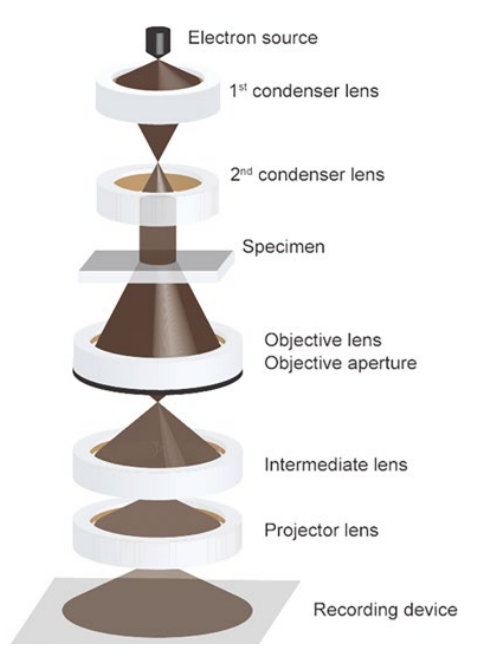


Figure 4. Schematic illustration of the components and operation of a TEM in standard TEM/diffraction mode <sup>3</sup>.

The atomic structure of each crystalline material can be described by a three-dimensional lattice. The simplest repeating unit in a crystal is called a unit cell. Each unit cell is defined with cell length parameters  $\vec{a}$ ,  $\vec{b}$ ,  $\vec{c}$  and angles  $\alpha$ ,  $\beta$  and  $\gamma$ . Each point in the crystal lattice can be described by a lattice vector  $\vec{r}$ , which can be written as a linear combination of the unit cell parameters:

$$\vec{r} = x\vec{a} + y\vec{b} + z\vec{c}$$

Diffraction experiments study the reciprocal space. For electron diffraction experiments, this reciprocal space is the Fourier transform of the electrostatic potentials in the crystal structure in direct space. The reciprocal unit cell can be described by the following equations (with Vthe volume of the unit cell):

$$\vec{a}^* = \frac{\vec{b} \times \vec{c}}{V}, \ \vec{b}^* = \frac{\vec{c} \times \vec{a}}{V}, \ \vec{c}^* = \frac{\vec{a} \times \vec{b}}{V}$$

The relation between real space and reciprocal space orientations is given in Figure 5.

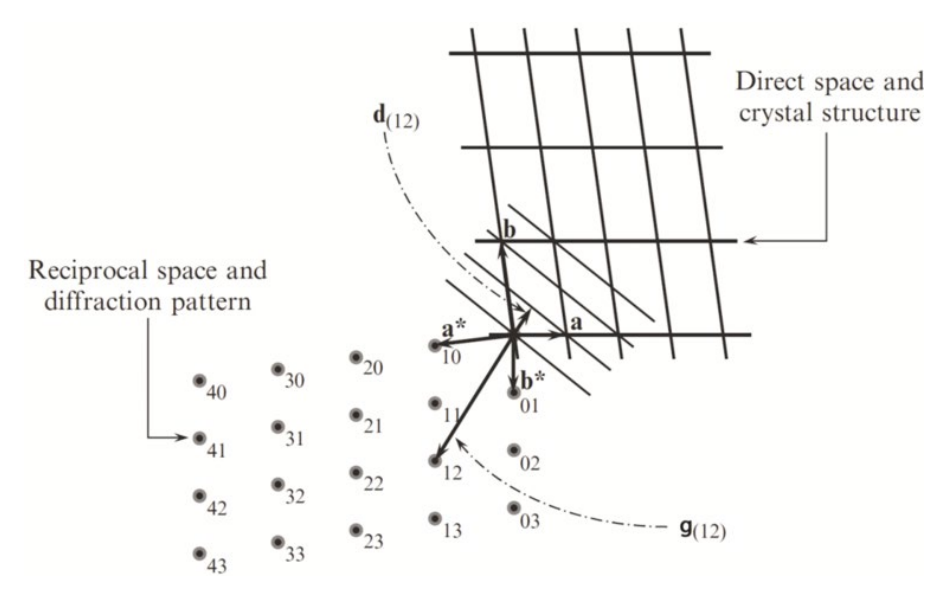


Figure 5. Schematic illustration of the relation between real space and reciprocal space for the two-dimensional case <sup>4</sup>. The planes indicated are the (12) planes, d(12) is the corresponding interplanar distance,  $\vec{g}(12)$  the reciprocal lattice vector to reciprocal lattice point 12.

Each point in this reciprocal space can be described with the Miller indices hkl, which correspond to a set of (hkl) planes in direct space. The reciprocal lattice point can therefore be described with the reciprocal lattice vector  $\vec{g}_{hkl}$ :

$$\vec{g}_{hkl} = h\vec{a}^* + k\vec{b}^* + l\vec{c}^*$$

The relation between this reciprocal lattice vector and the plane in direct space to which it corresponds, means that  $\vec{g}_{hkl}$  is perpendicular to the (hkl) planes with its length being inversely proportional to the distance between these planes  $(d_{hkl})$ :  $|\vec{g}_{hkl}| = 1/d_{hkl}$ .

The incoming parallel electron beam will be diffracted by a set of (hkl) planes and the diffracted electrons will interfere with each other. Constructive interference between these electron waves will only occur when the phase or path difference  $(2d \sin\theta)$  is an integer amount of times the wavelength of the electron, i.e.  $n\lambda$ . This effect is described by the Bragg equation:

$$n\lambda = 2d\sin\theta$$

Figure 6 shows a geometric construction of this Bragg equation.

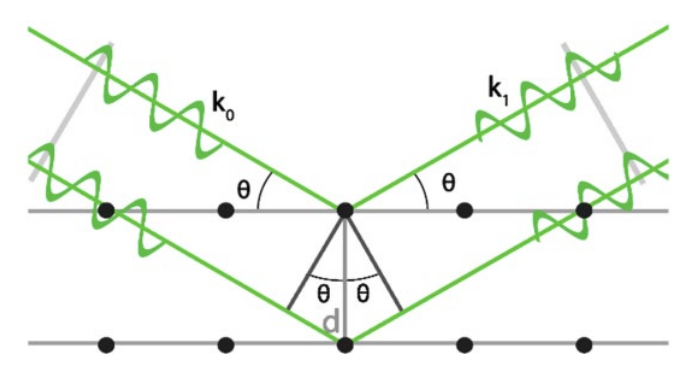


Figure 6. Geometric construction for the Bragg equation in real space, where  $\vec{k}_0$  is the incoming wave and  $\vec{k}_1$  is the diffracted wave <sup>5</sup>. The planes constructed from black atoms at which the electrons diffract are displayed in grey.

Furthermore, if we describe an incident electron by a wave vector  $\vec{k}_0$ , with a length that is equal to  $|\vec{k}_0| = 1/\lambda$ , the length of this vector remains unchanged when the electron is scattered elastically by a set of (hkl) planes. Only the direction changes with a diffraction angle that is defined by  $2\theta$ . The diffracted wave is then defined by the wave vector  $\vec{k}_1$ . When we translate  $\vec{k}_1$  to the starting point of  $\vec{k}_0$ , we obtain the Laue equation:

$$\vec{k}_1 = \vec{k}_0 + \vec{g}$$

Using these two vectors, along with all the possible elastically scattered electrons, with their scattering vectors,  $\vec{k}_1$ , we can define the Ewald sphere. The Ewald sphere has a radius of  $1/\lambda$  and passes through the origin of the reciprocal lattice. Every point in this lattice that intersects with this Ewald sphere, satisfies the Bragg equation and will therefore produce a reflection. A diffraction pattern is therefore the collection of reciprocal lattice points that intersect with the Ewald sphere.

The wavelength of an electron used for electron diffraction in a TEM is extremely small ( $\lambda$  = 0.0251Å when using a 200kV acceleration voltage). The radius of the Ewald sphere therefore is roughly 40 Å<sup>-1</sup> which is very large compared to the distance between the different spots in reciprocal space, see Figure 7. We can therefore approximate this sphere as a flat plane perpendicular to the incident beam, which is why an electron diffraction pattern can be approximated as a two-dimensional intersection of points in reciprocal space. Moreover, since TEM samples are generally very thin, the reciprocal lattice points are elongated in the direction parallel to that of the incident beam.

Therefore, reflections which only vary slightly from the Bragg condition will still be present in diffraction patterns. This small error in the observed positions of reciprocal lattice points is called the excitation error  $\vec{s}$ . When the Ewald sphere rotates, the intersection between the Ewald sphere and the rod will shift in a continuous manner along the rod. The intensity distribution along the rod follows a Gaussian distribution. The consecutive intensities of the resulting reflections during the rotation will therefore follow this distribution.

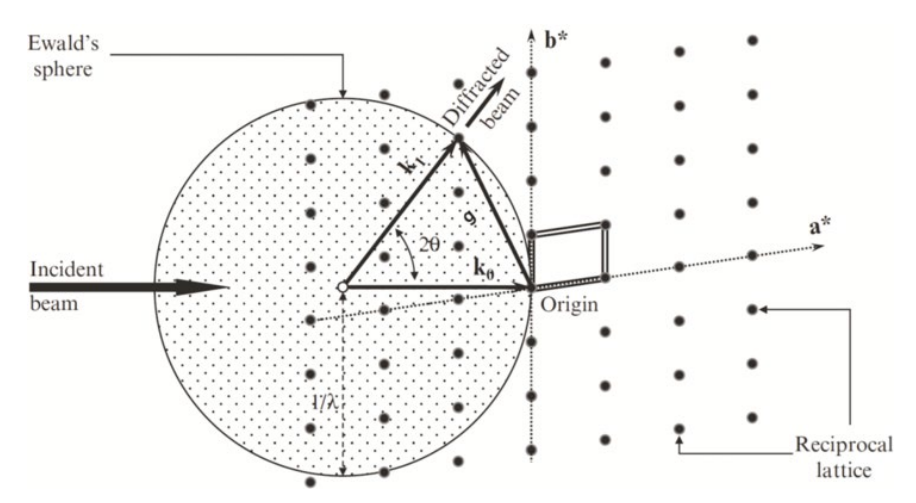


Figure 7. The Ewald sphere construction: reciprocal lattice points that lie on this sphere satisfy the Bragg equation. Double lines mark the unit cell in reciprocal space. This image is taken from Pecharsky et al. <sup>4</sup>.

The aforementioned intensity of the reflection can be expressed by the structure factor  $F_{hkl}$ :

$$F_{hkl} = \sum_{i} f_j \left( \sum_{j} e^{2\pi i (hx_j + ky_j + lz_j)} \right)$$

In this formula,  $f_j$  represents the scattering factor of element i, and  $(x_j, y_j, z_j)$  the real space coordinates of atom j. In the kinematical approach, the intensity of a reflection is  $I_{hkl} = |F_{hkl}|^2$ . In this approach, each electron from the incident beam is assumed to only be scattered once while travelling through the sample. Because of this simple relationship, we can derive the positions of atoms in direct space from the intensities of the reflections in reciprocal space through the use of methods such as direct methods  $^6$ , charge flipping  $^7$ , and simulated annealing  $^8$ . It is possible that for certain atomic positions, the intensity of the resulting reflections is equal to zero ( $I_{hkl} = 0$ ).

These reflections are called extinct and any systematic absence or appearance is described by the reflection conditions, which are tabulated for all 230 space groups in the International Tables for Crystallography Volume A <sup>9</sup>.

However, because of the strong interaction of the electrons from the electron beam with the atoms in the sample, most electrons passing through the material will scatter multiple times. The simple relation between the structure factor and the intensity of reflections is not valid anymore in this case. The chance for multiple scattering increases with the atomic number of the atoms and also increases with sample thickness. Furthermore, multiple scattering can lead to non-zero intensities at lattice points where the reflection conditions predict the absence of intensities.

Two opposite ways to get information about the crystal structure from reciprocal space studies are either through the acquisition of in-zone patterns or through the acquisition of 3D ED data, avoiding in-zone patterns as much as possible.

In a 3D ED experiment, three-dimensional reciprocal space of a material is acquired by rotating the sample around a single random axis and capturing a diffraction pattern at small angle intervals, after which the three-dimensional reciprocal space is reconstructed from these patterns. In the field of proteins, 3D ED is also known as MicroED. 3D ED encompasses several techniques, formerly known under their individual labels such as ADT <sup>10</sup>, EDT <sup>11</sup>, PEDT <sup>12</sup>, RED <sup>13</sup>, and cRED <sup>14</sup>.

A crystallographic zone is a set of planes that shares a common direction, called the zone axis. A zone axis is represented by a vector denoted as  $[u\ v\ w]$ , and the Miller indices of the planes that are part of the zone follow the relationship hu + kv + lw = 0. An in-zone pattern therefore is a pattern taken with the electron beam parallel to the zone axis of a zone. It represents a 2D slice of the 3D reciprocal lattice of the material. In-zone patterns, such as the one shown in Figure 8, give information on the unit cell parameters, symmetry elements of the structure and reflection conditions. Because for in-zone patterns the consecutive parallel planes are all equally in Bragg condition, multiple scattering is facilitated, while for 3D ED data the reduced number of reflections impedes multiple scattering.

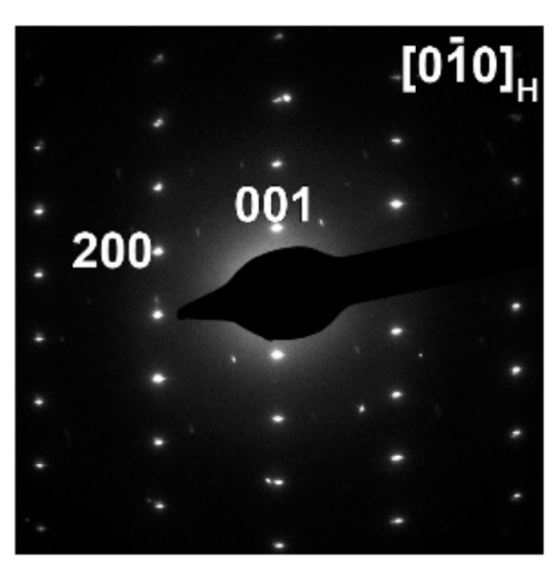


Figure 8. Illustration of an in-zone diffraction pattern 15.

The high amount of multiple scattering in in-zone patterns significantly distorts the relative intensity ratios between the reflections, making the intensities unreliable for quantitative use, whereas the relative intensities from 3D ED can be used for the quantitative solution and refinement of crystal structure <sup>10,16–19</sup>. The 3D reciprocal space is reconstructed using dedicated software such as PETS2 <sup>20</sup>. Then, direct methods, charge flipping or simulated annealing via software such as Jana2020 <sup>21</sup> or Olex2 <sup>22</sup> can be used to solve the crystal structure of the material. A schematic of the 3D ED workflow is shown in Figure 9.

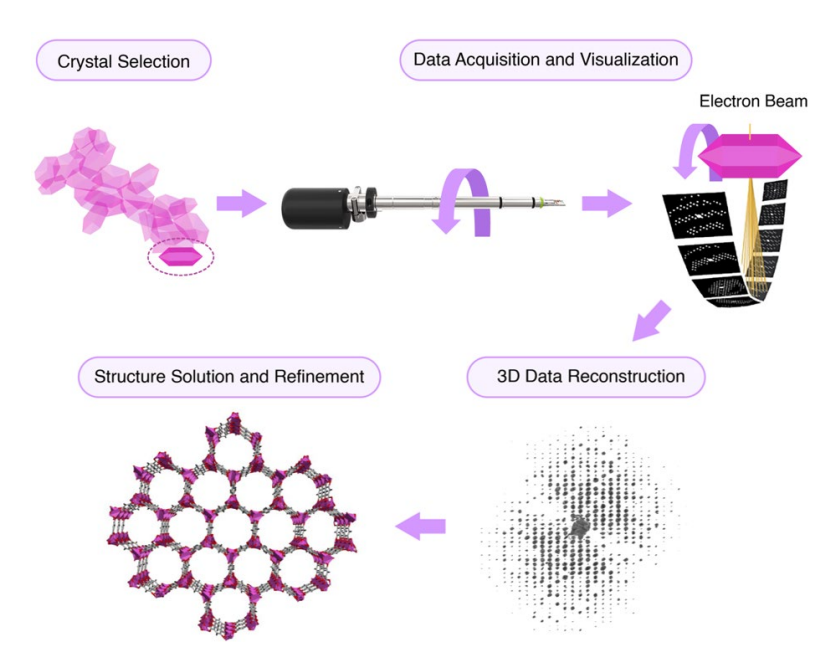


Figure 9. Schematic representation of the workflow of a three-dimensional electron diffraction experiment. This image is based on the figure used in <sup>23</sup>.

Since we tilt the crystal over a random tilt axis during data acquisition, more out-of-zone patterns are obtained than in-zone patterns, reducing the contributions of multiple scattering to the integrated intensities. Furthermore, because we do not need to align the sample to a specific zone axis (a time-consuming step when taking in-zone patterns or high-resolution images), beam damage is reduced. However, the determination of reflection conditions, and thus translational symmetry elements and centering, is more reliable from in-zone patterns, because, although reduced, multiple scattering is still present in 3D ED and causes the appearance of forbidden reflections in all reconstructed sections containing the lattice point. This occurs not only in the zones where the multiple scattering is present, due to the reconstruction method that gathers all representations of a reflection into each reconstructed section. Using in-zone patterns, multiple scattering only causes the appearance of reflections in that same zone.

During a 3D ED acquisition, the crystal can be tilted stepwise, with diffraction patterns taken at each step, typically between 0.1 and 1°. This can be done manually but most research groups using 3D ED have their own in-house codes for automating the acquisition. Even then, stepwise tilting can still be relatively slow, which is not ideal for beam-sensitive materials. The advantage is that the tilt angles are precise, and by using software like FastADT <sup>24</sup>, we can track the crystal position to ensure it stays within the beam during data acquisition.

Another approach is continuous rotation electron diffraction (cRED) <sup>14</sup>. During cRED, the crystal is continuously tilted while diffraction patterns are acquired, integrating the intensities of reflections that are in the Bragg condition during the short time intervals. This method is much faster, and minimizes beam damage which makes it preferable for beam-sensitive materials. Figure 10 shows the difference between stepwise 3D ED and cRED using a schematic of both acquisition methods.

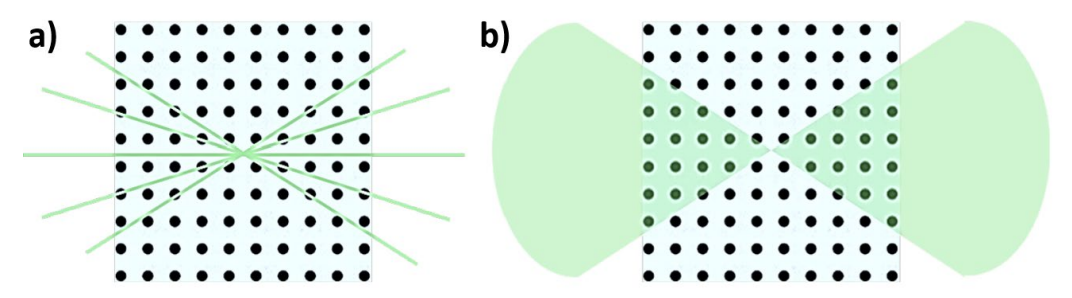


Figure 10. Schematic illustration of a) stepwise and (b) continuous rotation methods for 3D ED data collection <sup>25</sup>.

Once the material's structure is solved, we can refine the structure using different methods. One method is kinematical refinement, which uses the kinematical approximation ( $I = |F|^2$ ). With kinematical refinement, the atoms are conventionally approximated as spheres, which means their atomic displacement parameters (ADPs) are refined isotropically, see Figure 11a. Multiple scattering is not completely eliminated in 3D ED. When a small tilt step size is used, typically below 0.2°, or when techniques such as cRED or precession (not used during this thesis) are applied, the data can be further refined using a more accurate dynamical refinement approach that accounts for multiple scattering effects. Although ADPs can also be modeled using kinematical refinement, with dynamical refinement, we can more reliably model the ADPs of the atoms anisotropically, which means they are described as ellipsoids using six  $U_{ij}$  parameters ( $U_{11}$ ,  $U_{22}$ ,  $U_{33}$ ,  $U_{12}$ ,  $U_{13}$ ,  $U_{23}$ ), shown in Figure 11b. These ADPs provide a more complete description of the distribution of the atoms in the unit cell, including subtle features of motion and disorder.

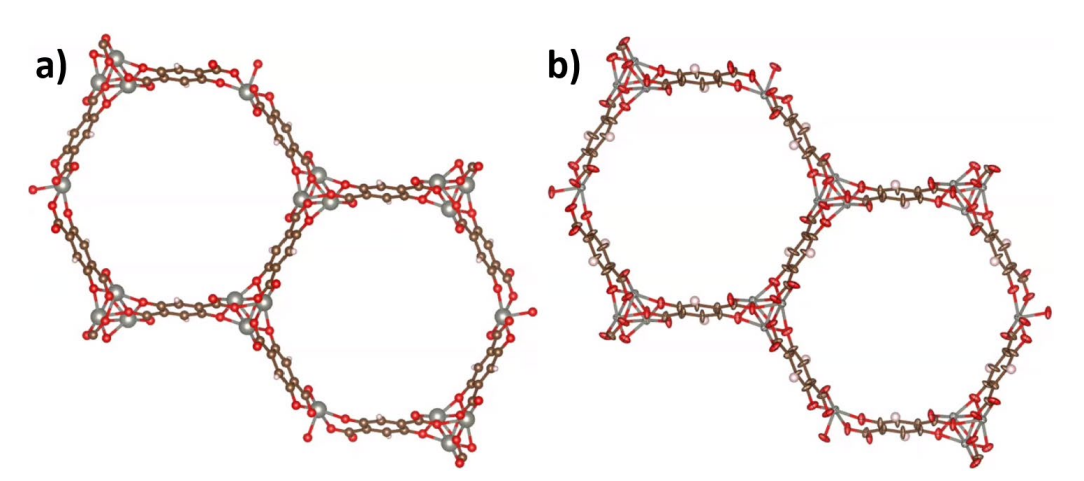


Figure 11. Schematic illustration of a) isotropic ADPs and b) anisotropic ADPs for the Zn-MOF-74 structure.

Using a TEM holder with TEM grids limits the tilt range in 3D ED experiments. Even with specialized tomographic holders, the maximum tilt range is still around 150 degrees, which means part of the reciprocal space cannot be measured.

This unmeasured part is called the "missing wedge". To achieve the best results, the missing wedge should be as small as possible. However, by taking advantage of the material's symmetry, we can reduce the impact of the missing wedge on the refinement quality.

The agreement of the experimental structure factors to the calculated ones using the solved and refined model is measured by the R-factor. This should be as low as possible to indicate a good agreement of the refined structure to the correct structure. The R-factor (often called  $R_1$ ) is calculated by the following formula:

$$R_1 = \frac{\sum ||F_O| - |F_C||}{\sum |F_O|}$$

In this formula,  $F_O$  refers to the observed structure factors, while  $F_C$  corresponds to the calculated structure factors. For electron diffraction, acceptable R-factors are typically below 18%  $^{26}$ . However, the R-factor also depends on various factors such as the complexity of the structure, the size of the missing wedge, and residual dynamical effects. X-ray diffraction, which does not suffer from the missing wedge and in which dynamical effects are negligible in most cases, can achieve R-factors below 5%.

# 1.3. (HAADF-)STEM

Scanning transmission electron microscopy (STEM) involves focusing the electron beam onto the sample and scanning it in a raster pattern using scanning coils. Unlike conventional parallel beam TEM, in STEM the magnification is not determined by the imaging system lenses but by the size of the scanning area. The detectors in STEM imaging measure the intensity of a range of mostly elastically scattered beams, yielding various STEM images such as annular bright field (ABF) and high-angle annular dark-field (HAADF), see Figure 12. In HAADF-STEM imaging, the detector captures high-angle scattered electrons, including coherent diffracted beams and incoherent thermal diffuse scattering. Integration of the signal over a wide angular range results in a mostly incoherent and directly interpretable image. Electrons scattered at high angles experience electron-nucleus interactions, with heavier elements scattering electrons more to higher angles due to stronger Coulomb forces. Consequently, atomic columns containing heavy elements appear brighter, exhibiting Z-dependent contrast approximately proportional to  $\sim Z^{1.6}$ . The inner and outer collection angles for the detector in HAADF STEM are approximately 50 mrad and 200 mrad, respectively. High-angle Rutherford scattering occurs when electrons approach the nucleus, resulting in strong attraction and scattering through larger angles. In HAADF STEM, the detected high-angle Rutherford scattered electrons are incoherent, lacking a phase relationship and orientation dependence, thereby producing no diffraction contrast.

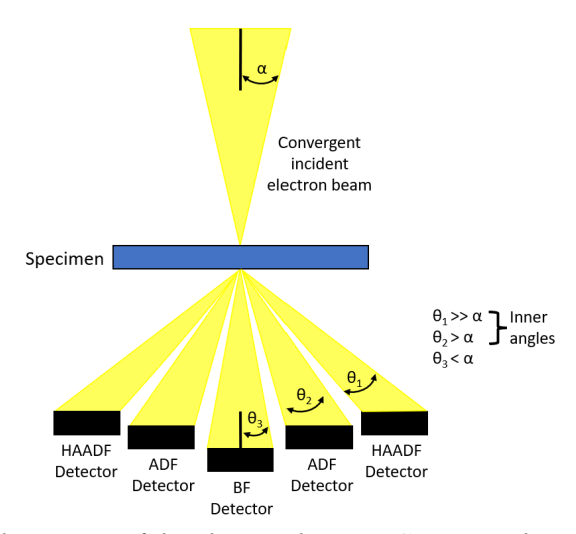


Figure 12. Schematic illustration of the electron beam in STEM mode with the different electron detectors. Figure based on <sup>27</sup>.

One aspect of the STEM technique that is regularly used in this work is the use of Kikuchi lines. Kikuchi lines are band-like patterns seen in STEM diffraction images, created by the interaction of inelastically scattered electrons with a crystalline material. Electrons from the electron beam that undergo inelastic scattering form Kikuchi bands, which appear in diffraction patterns where the conical scattering distributions (known as Kikuchi cones) intersect with the imaging plane. The presence of these lines is a clear sign of crystallinity, as they rely on the ordered structure of a crystal to form. In contrast, amorphous materials, which lack long-range atomic order, do not produce Kikuchi lines. However, even in crystalline materials, these lines may be absent if the sample is very thin, as there may not be enough scattering events to generate them. Kikuchi lines are particularly useful in STEM for precisely orienting a crystal to a specific zone axis. By aligning the electron beam along these bands, we can achieve optimal positioning for high-resolution imaging and diffraction analysis, making them an important tool in crystallographic studies.

#### 1.4. EDX

When electrons undergo inelastic scattering, a reduction in impulse and energy occurs in addition to other interactions between the electrons from the electron beam and atoms of the sample. For example, high-energy electrons hitting atoms within the sample can eject inner-shell electrons (secondary electrons). Subsequently, electrons from outer, higher energy shells may transition to lower energy shells, emitting the energy difference as characteristic X-rays. These energy variances, unique to each element, enable chemical analysis through a technique called energy-dispersive X-ray spectroscopy (EDX), employed in this thesis for material composition analysis.

Additionally, electrons can be deflected by atomic nuclei, emitting energy as X-ray radiation known as Bremsstrahlung.

Although electrons can emit varying amounts of energy, low-energy emissions are more common. Bremsstrahlung X-rays form a continuous energy spectrum, which appears as the background in EDX spectra, whereas characteristic X-rays appear as distinct, discrete peaks. The X-rays are collected by a silicon drift detector (SDD) positioned next to the sample, Figure 13a, and an energy-dispersive spectrometer quantifies the number and energy of emitted X-rays, producing an EDX spectrum.

However, to increase the efficiency of detection, four of these detectors can be symmetrically mounted around the sample, forming the Super-X four detector system used for this thesis (Figure 13b). This configuration enables atomic-resolution STEM-EDX mapping.

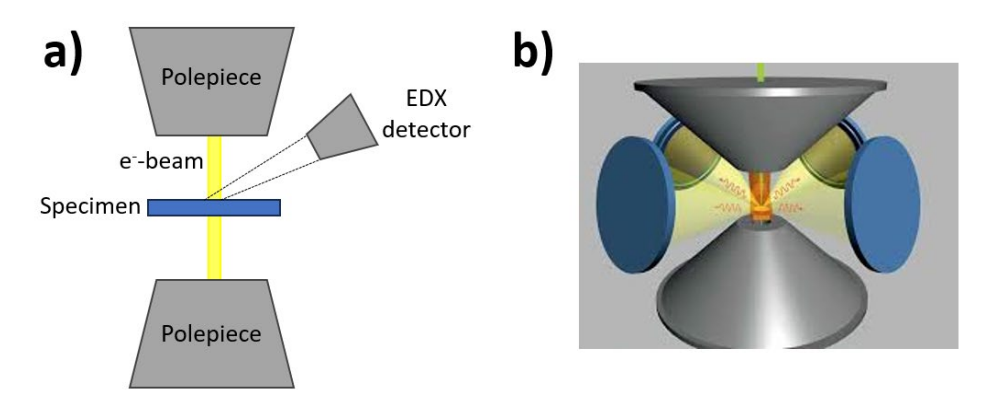


Figure 13. Schematic illustration of the a) EDX detector setup in a TEM and b) a Super-X EDX detector setup <sup>28</sup>.

# 1.5. Scanning nanobeam diffraction

The scanning nanobeam electron diffraction (SNBD) technique combines 4D-STEM with diffraction analysis. By utilizing specific lens settings and apertures, it produces a small (~5 nm) semi-parallel probe with a convergence angle of approximately 0.25 mrad. This probe is scanned across the sample, generating a grid of coordinates (x<sub>real</sub>, y<sub>real</sub>) for each scan position. At each point on this grid, a diffraction pattern is recorded, with the diffraction data represented by coordinates (kx, ky) in reciprocal space. The "four-dimensional" aspect of the technique arises from the combination of real-space and reciprocal-space data. SNBD is a subset of the 4D-STEM techniques: whereas SNBD uses a narrow parallel beam to acquire diffraction data for local crystallographic data, other 4D-STEM techniques including ptychography, center-of-mass analysis and strain mapping all use focused beams.

Data processing for SNBD is often performed using custom Python code based on the python packages Hyperspy <sup>29</sup> and Pyxem <sup>30</sup>.

The primary advantage of this method is its ability to obtain structural information from diffraction data localized to a very small area, making it particularly suited for materials with local periodicity. In contrast, conventional SAED typically involves a much larger probe size, which may not provide the same level of localized detail.

However, a significant drawback of the SNBD technique is the large data volume generated. For instance, a 256x256 scan using a direct electron detector can easily result in data files several gigabytes in size, necessitating careful data storage and conversion strategies.

#### 1.6. SEM

Scanning Electron Microscopy (SEM) employs a focused electron beam with energies typically under 30 keV, which is systematically scanned across the surface of nanomaterials. Figure 14a shows the SEM used during this doctoral research. Unlike transmission techniques, SEM samples are generally large and therefore thick enough to prevent electron transparency, resulting in the absorption of primary electrons. These absorbed electrons undergo multiple scattering processes within the material, creating a small interaction volume inside the sample where the detectable signal is generated. This interaction volume limits the resolution of SEM to approximately 1 nm.

The interactions between the electron beam and the sample produce various signals, schematically illustrated in Figure 14b, that show local surface characteristics, such as topography (through secondary and backscattered electrons) and chemical composition (via backscattered electrons, X-rays, and cathodoluminescence). However, this information is confined to the near-surface region, typically ranging from a few nanometers to a few micrometers depending on the specific signal, and does not offer insight into the material's internal structure. Therefore, SEMs primarily investigate the near-surface structure of a sample, in contrast to TEM, which provides an image of the entire sample's internal structure. Due to the interaction of generated signals (mainly secondary and backscattered electrons) with surface features, SEM images often convey a pseudo-3D effect, resembling those produced by reflected-light microscopy. SEM is widely regarded as user-friendly and is commonly available in research settings, though the resolution of standard SEM instruments typically ranges between 1 and 20 nm.

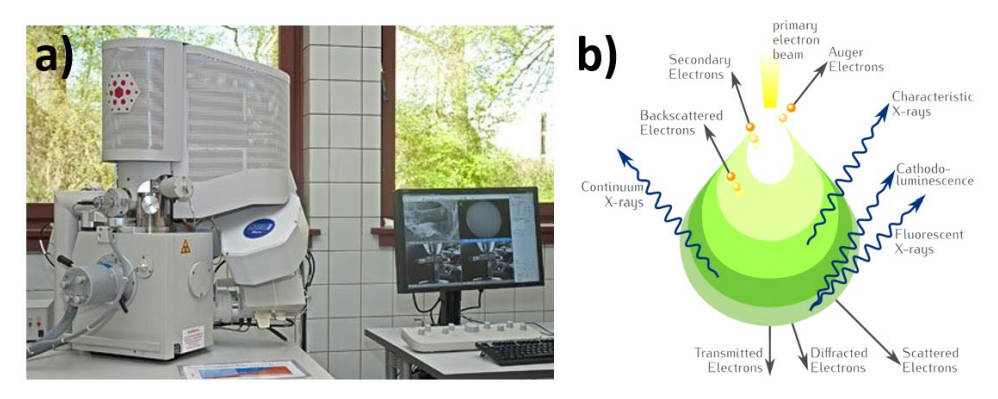


Figure 14. a) Picture of the SEM used during this PhD. b) Schematic illustration of the main interactions of the electron beam with the sample during a SEM experiment <sup>31</sup>.

# 1.7. Holders

During this work, we have used several different types of TEM holders. The current prevalent design of TEM holder is a long rod with a small, flat platform at the top where the sample is placed. This platform, referred to as the holder tip, is engineered with precision to hold the thin specimen securely in place while allowing for various degrees of tilt, rotation, and movement.

For standard 3D ED experiments, a specialized tomography holder (Fischione model 2020) was employed (Figure 15a). This holder offers only one degree of freedom for tilting, but is designed with an extended tilt range of -75 to 75 degrees due to its specially designed holder tip. This design minimizes the missing wedge in reciprocal space. Additionally, the holder is constructed to be lightweight, ensuring more consistent rotation speeds. The primary TEM holder used in this work for EDX measurements, general TEM imaging, and atomic-resolution TEM/HAADF-STEM imaging was a double-tilt holder (Figure 15b). This holder features a black section at the back housing the electronics that enable the second tilt axis, allowing for sample rotation in two directions. It offers a tilt range of -35 to 35 degrees in both tilt directions.

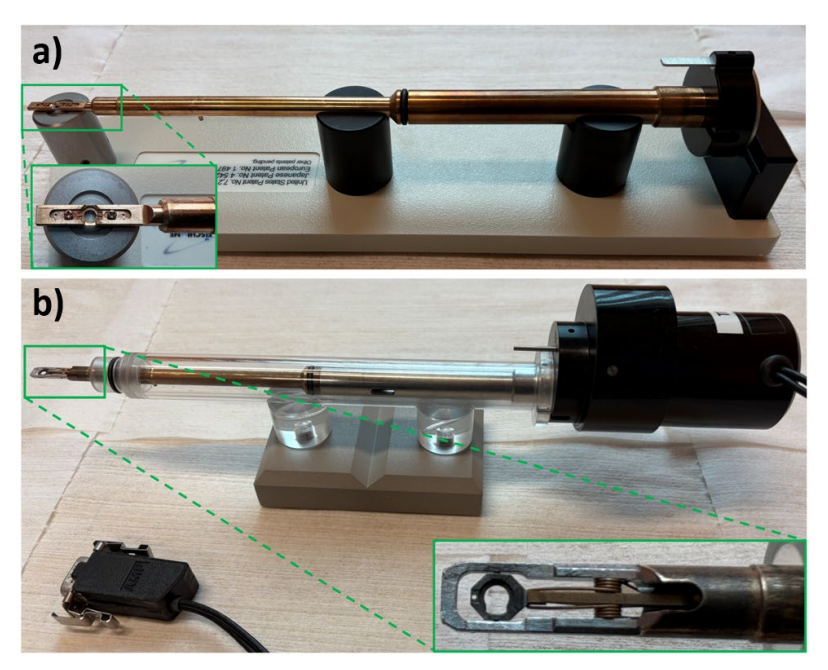


Figure 15. a) Fischione model 2020 tomography holder and b) FEI double tilt holder. The inserts show the holder tips.

For *in situ* experiments conducted at lower temperatures, two different types of holders were utilized. These holders share the same basic design as non-*in situ* holders, but with an additional reservoir at the back that can be filled with liquid nitrogen. Inside the hollow rod of the holder, smaller cold-conducting rods transfer the cold temperature to the tip, enabling it to reach liquid nitrogen temperatures. For 3D ED experiments conducted under cryogenic conditions, a cryogenic tomography holder (Fischione model 2550) was used (Figure 16a).

This holder, like the standard tomography holder, has only one degree of tilt but is equipped with a specially designed tip that allows for an extended tilt range of -75 to 75 degrees.

For SAED experiments at lower temperatures, a cooling holder (Gatan model 915) was employed, shown in Figure 16b. This holder also features a liquid nitrogen reservoir and includes an additional component at the back that houses electronics for a second degree of tilt. Moreover, this holder can operate at any temperature between room temperature and liquid nitrogen temperature. It achieves this by continuously cooling the tip to liquid nitrogen temperatures while simultaneously providing a counter-current that heats the tip. By adjusting the counter-current, a specific working temperature can be precisely selected.

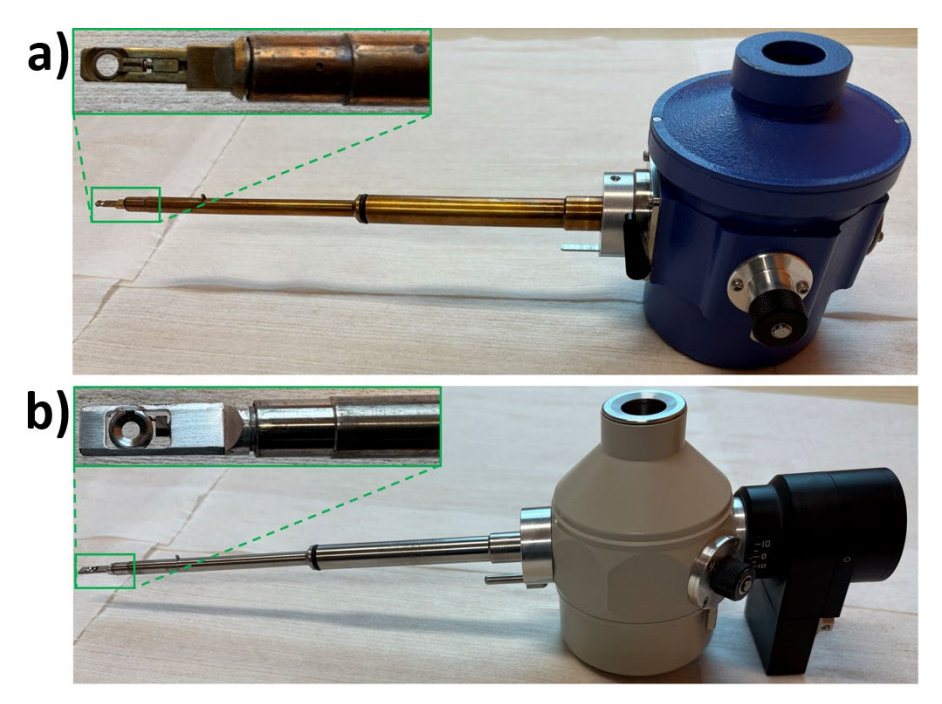


Figure 16. a) Fischione model 2550 cryo tomography holder and b) Gatan model 915 double tilt cooling holder. The inserts show the holder tips.

For *in situ* experiments conducted at elevated temperatures, the DENSsolutions Wildfire holder (Figure 17a) was used. This holder uses heating Microelectromechanical System (MEMS) based chips made from silicon, featuring small electron-transparent Si<sub>3</sub>N<sub>4</sub> windows (Figure 17b). The chips are equipped with heating coils surrounding these windows. When elevated temperatures are required, an electrical current is passed through the heating coils, causing the entire chip—including the windows and any material placed on them—to heat up uniformly. The heat range for experiments with this type of holder is typically between room temperature and 1000°C.



Figure 17. a) DENSsolutions single tilt heating holder. The insert shows the holder tip. b) In situ (gas, bottom) chip. Different elements of the chip are indicated. The insert shows a zoomed in image of the Si<sub>3</sub>N<sub>4</sub> window.

For experiments in gas environments, the DENSsolutions Climate holder (Figure 18) was used. This holder utilizes top and bottom MEMS chips, each equipped with electron-transparent Si<sub>3</sub>N<sub>4</sub> windows, separated by a rubber O-ring for sealing purposes. When the chips are aligned and tightened together with the O-ring (Figure 19a), they form a sealed nanoreactor, effectively isolating the internal environment from the ultra-high vacuum (UHV) of the microscope column.

The bottom chip features two small holes that serve as an inlet and outlet for silica tubes extending from the back to the front of the holder. These tubes allow for gas flow through the nanoreactor. At the back of the holder, specialized valves connect the internal silica tubing to an external gas supply system (GSS), shown in Figure 19b, which can introduce and remove gas from the holder, creating a controlled gas flow. The GSS can introduce either a single gas or a mixture of up to three different gases into the nanoreactor. Additionally, the bottom chip contains heating coils around the windows, enabling experiments at elevated temperatures within the gas-filled environment.



Figure 18. DENSsolutions Climate in situ (gas) holder. The insert shows the holder tip.

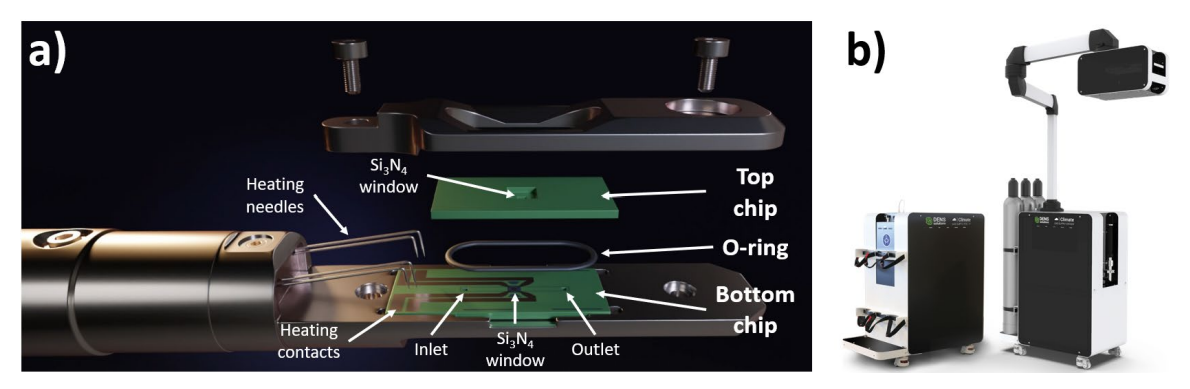


Figure 19. a) Different parts of a closed-cel in situ (gas) TEM holder (DENSsolutions Climate). b) Gas Supply System (GSS).

#### 1.8. Sample preparation

Most of the samples studied during this work were received as dry powders. The different steps of the sample preparation are shown in Figure 20. The powder was dissolved in ethanol. This solution was then placed in an ultrasonic bath, which helps to disperse the powder and break it down into smaller particles suitable for TEM analysis. Note that ultrasonic shaking can potentially damage the structure of the material and was therefore not used for MOFs with longer linkers, such as UA-4, or for the biohybrid materials, as it can damage the enzymes.

A micropipette was used to dropcast a precise amount of the solution onto a TEM grid until the desired particle density was achieved. The TEM grid was then placed on the TEM holder for analysis. The sample preparation method for gas *in situ* experiments is similar to that for standard TEM studies, with the key difference being that dropcasting is performed on the bottom chip instead of a TEM grid. Special care must be taken regarding the size and density of particles during dropcasting. The O-ring between the top and bottom chips creates an opening of approximately 5 µm. If particles are larger than this, or if smaller particles agglomerate into clusters exceeding this size, the chip may break, leading to leaks in the TEM column. Therefore, it is essential to use smaller particles and maintain a relatively low particle density to prevent damage and ensure successful experimentation.

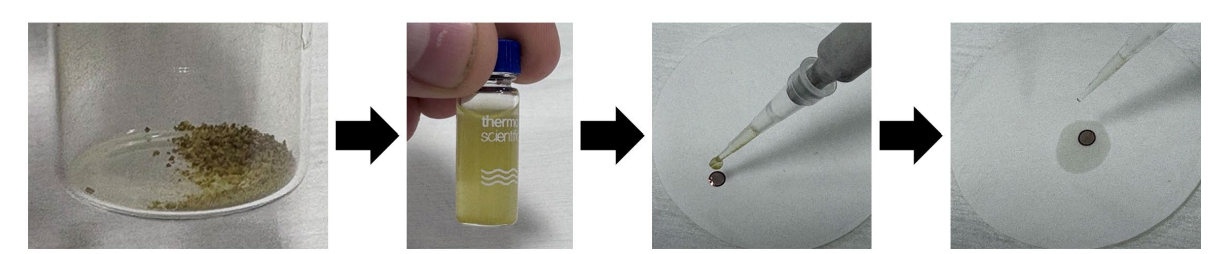


Figure 20. Schematic illustration of the standard method to prepare TEM samples.

# **Chapter 2: MDT dropcasting tool**

This study has been submitted to the journal HardwareX on 19 February 2025 and has been accepted on 13 July 2025.

### 2.1. Difficulties during in situ sample preparation

As part of optimizing *in situ* experiments, efforts were made to improve sample preparation methods. *In situ* experiments require dropcasting directly onto MEMS (Micro-Electro-Mechanical Systems)-based *in situ* chips rather than TEM grids. This method introduces several challenges.

During conventional sample preparation on such MEMS chips for gas phase and liquid phase experiments, a small volume of the sample, dissolved in a suitable solvent, is dropcast onto the Si<sub>3</sub>N<sub>4</sub> windows of the bottom MEMS chip. An O-ring is then placed between the top and bottom chips to create a sealed nanoreactor. However, achieving accurate dropcasting is challenging, often resulting in uneven particle distribution, with particles missing the Si<sub>3</sub>N<sub>4</sub> windows, contaminating the inlet and outlet holes, or settling under the O-ring, which compromises the seal. (Figure 21). These issues can lead to leaks, damage the O-ring, contaminate the inlet or outlet, or conversely, result in no particles being deposited on the windows. Each of these issues results in a failed experiment. The thinness of the Si<sub>3</sub>N<sub>4</sub> windows, while beneficial for resolution, also makes them fragile and prone to breakage, so any correction that requires the user to re-extract the holder, repeat the dropcasting process, and reassemble the setup increases the risk of breaking the window.

To limit droplet spread, solvents with higher surface tension, such as water, can be used. However, a number of materials, including some MOFs, halide perovskites, and alkali metal salts, are water-sensitive and cannot be dissolved in it.

The literature describes various alternative techniques for sample preparation on MEMS devices for *in situ* TEM studies instead of dropcasting. However, these methods often involve complex equipment such as aerosol jet printers <sup>32</sup>, nanocapillaries <sup>33</sup>, double shadow masks <sup>34</sup>, pulsed lasers <sup>35</sup>, or FIB <sup>36</sup>, which may not be suitable for all materials or solvents and are not always readily available in each research laboratory.

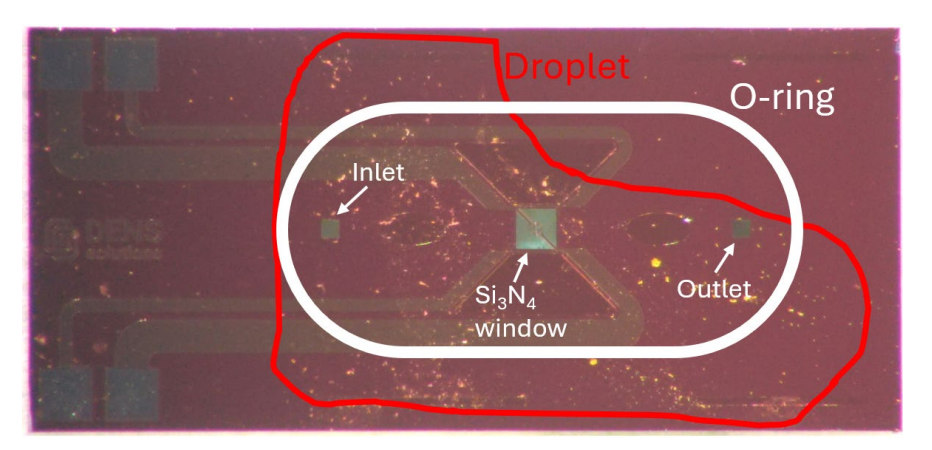


Figure 21. Picture of a MEMS chip with a 2  $\mu$ l droplet of an ethanol/MOF-74 solution dropcasted on it. The droplet size, the inlet/outlet holes, the Si<sub>3</sub>N<sub>4</sub> window, as well as the O-ring position are indicated on the picture.

### 2.2. Development of the MDT

During this thesis, the MEMS-dropcasting tool (MDT) was developed as a simple and cost-effective solution to facilitate dropcasting on MEMS-based chips by confining the droplet to a defined area. The MDT can be reproduced using commonly available 3D printers. It addresses many of the challenges mentioned: it helps to concentrate the particles and solvent on the window, prevents them from spreading to the O-ring and in- and outlets. This reduces sample preparation time and prevents leaks, ultimately making *in situ* gas phase and liquid phase experiments more cost-effective.

The aim of the MDT was to confine the dropcasted solution—regardless of the solvent—onto the MEMS chip, specifically on the electron-transparent viewing windows and within the area sealed by the O-ring (schematically shown in Figure 22). To achieve this, we designed a funnel-like structure that can be placed over the MEMS chip (Figure 23). During dropcasting, this tool guides the droplet to the desired region and contains it while the solvent evaporates, leaving the particles precisely on the viewing window. As the tool is ideally used as a consumable to avoid cross-contamination between experiments, we tested the possibility to manufacture it at low cost using 3D printing. The model shown in Figure 23 was developed in Blender. The 3D printing allows to use a material of choice, however, as demonstrated below, the tool's surface should be as smooth as possible, imposing constraints on the type of printer and nozzles suitable for production.

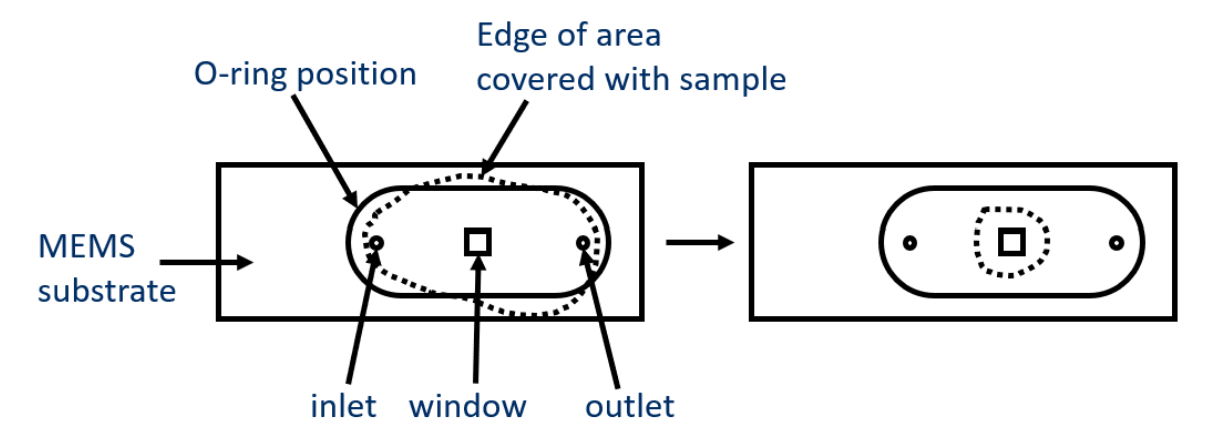


Figure 22. Schematic illustration of the aim of the MDT.

As the Si<sub>3</sub>N<sub>4</sub> windows are highly fragile, the funnel's mouth must be large enough to encircle the window without making contact. The tool must remain stable when placed on the MEMS chip, maintaining its position throughout use. To ensure this, the design has two broad legs on either side to the funnel. The legs and the funnel's mouth are aligned on the same plane to ensure the tool sits perfectly flat on the MEMS chip. The edges, legs, and overall structure of the MDT are sufficiently thick to allow handling with tweezers without bending under the applied force. The testing was done on DENSSolutions Climate chips, which have an asymmetric design. Therefore also the MDT was designed asymmetrically, which can easily be adapted using the Blender design.

For example, the leg closest to the inlet/outlet is positioned far enough away from the window to prevent any liquid that could spill underneath the funnel's mouth from adhering to it, as this could potentially contaminate the inlet/outlet.

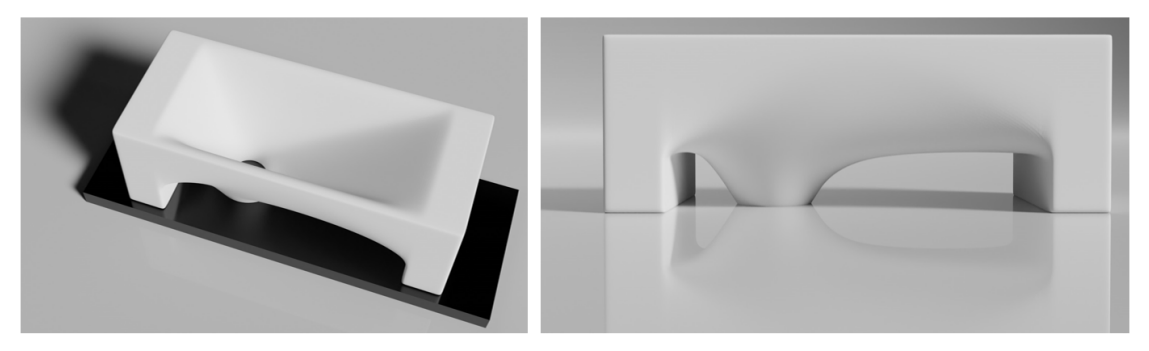


Figure 23. 3D model for the MDT.

Several 3D printer types and materials were tested to identify the optimal combination for dropcasting controlled-size droplets onto MEMS chips.

These printers and materials included: Ultimaker 3 extended 3D printer using polylactic acid (PLA), a stereolithography (SLA) 8K resin printer, a fused deposition modeling (FDM) printer with polyethylene terephthalate glycol (PETG), using a 0.25mm nozzle and 0.7mm layer thickness and an SLA printer utilizing a Formlabs laser system.

Figure 24 compares the results of dropcasting a 3 μl droplet of a solution containing ethanol and MOF-74 particles, with the MDT printed using several different 3D printers and includes the result of dropcasting without the MDT for comparison. For most of the 3D printers tested, except for Ultimaker 3, the droplet confined by the tool remains within the mouth area, avoiding contamination of the O-ring and the inlet/outlet holes, as shown in Figure 24. This figure also provides a higher magnification view of the Si<sub>3</sub>N<sub>4</sub> window area with and without the tool (SLA 8K resin 3D printer). It clearly demonstrates that the use of the tool results in a greater concentration of particles on the windows, improving particle placement efficiency.

Figure 25a illustrates the finalized tool alongside the MEMS chip used for testing. This tool was fabricated using an SLA 8K resin 3D printer and had a 0.5 mm funnel opening. Based on 10 different tries for dropcasting for each tool, this combination produced the most consistent results.

As shown in Figure 25b the tool's mouth encircles the  $Si_3N_4$  window, preventing damage, and the chip's asymmetry has been fully integrated into the design, placing the funnel's mouth more towards one leg of the tool. With this setup, the tool costs  $0.2 \in$  per piece, making it easily replaceable.

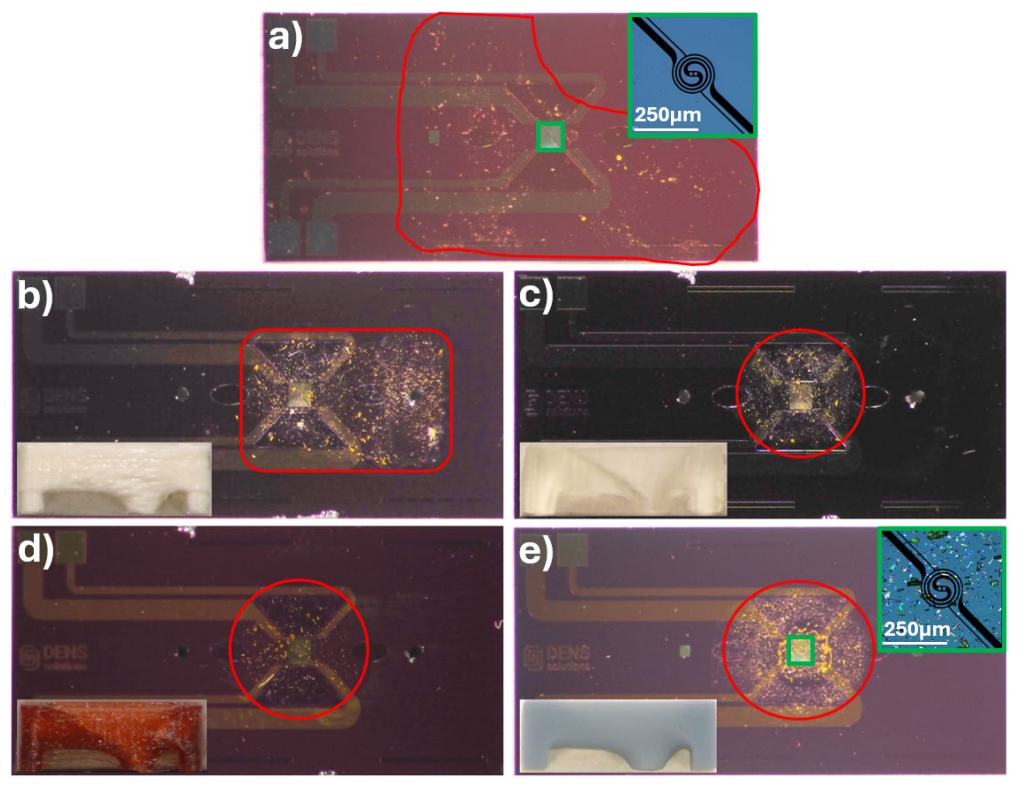


Figure 24. Images of an in situ chip with the printed tool as an inset, showcasing the particle distribution after dropcasting a droplet of the testing solution: a) without the MDT, b) using an Ultimaker 3 Extended 3D printer with PLA material, c) using an SLA printer with a Formlabs laser system, d) using an FDM printer with PETG, utilizing a 0.25mm nozzle and 0.7mm layer thickness, and e) using an SLA 8K resin 3D printer. For panels a) and e), additional insets outlined in green provide magnified views of the Si<sub>3</sub>N<sub>4</sub> window. The edges of the droplets are marked in red, and particles found outside these boundaries were identified as contamination resulting from attempts to clean the chip post-dropcasting.

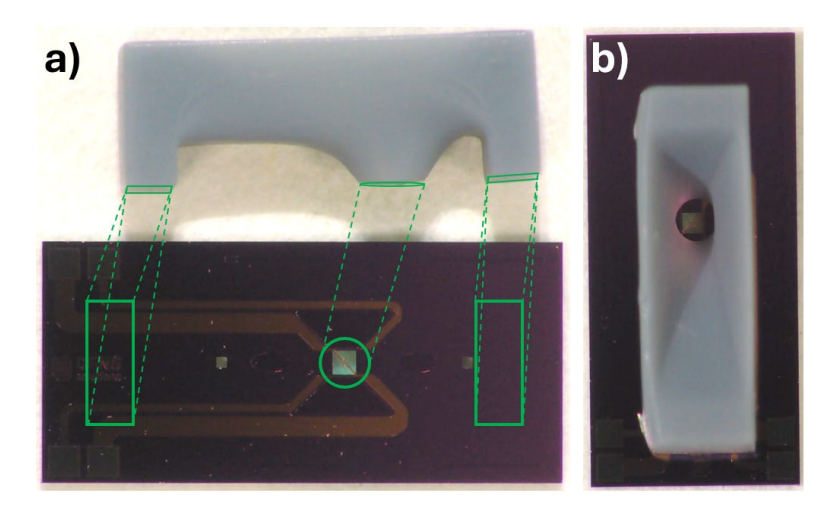


Figure 25. a) Size comparison of the finalized MDT next to a MEMS in situ chip. The intended placement of the tool is indicated on the figure. b) MDT placed on top of the MEMS chip. The mouth of the tool fits just around the  $Si_3N_4$  window.

We observed that some liquid spreads underneath the tool; however, due to surface tension and the small volume of liquid, it adheres to the underside and outer edge of the MDT mouth, preventing further spreading. This behavior is likely caused by minute irregularities on the underside of the tool's mouth.

Because of this spreading, the wall of the tool's mouth should be as thin as possible to minimize the contact area between the tool and the chip. With a larger contact area, the fluid spreads to the larger area underneath the tool's mouth.

To investigate this spilling, SEM images of this region were taken from the tool printed using the SLA 8K resin 3D printer (Figure 26). These images confirm the presence of irregularities on the underside of the tool's mouth. Such imperfections likely disrupt the surface tension of the liquid, allowing it to pass through gaps and counteracting the capillary forces that would otherwise keep the droplet contained. However, as demonstrated, even with these irregularities that were due to the use of a common 3D printer, the droplet still was confined to the targeted area. Lower-end 3D printers may have reduced accuracy, which could introduce sharp edges or irregularities that may lead to window breakage or suboptimal results.

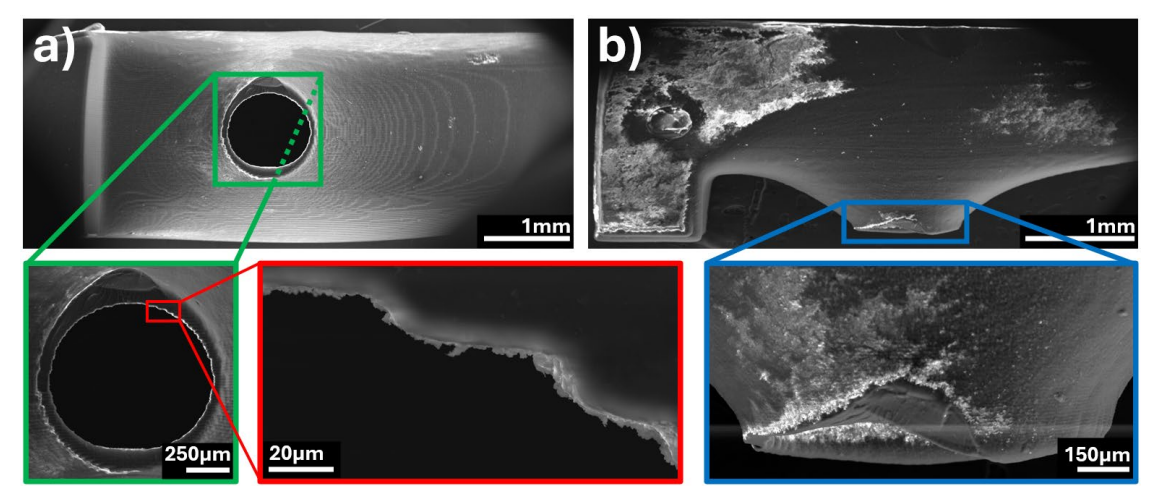


Figure 26. SEM images of the MDT printed using the SLA 8K resin 3D printer in a) top-down and b) side views.

Some *in situ* MEMS chips, particularly those used in liquid experiments involving biasing, feature smaller, rectangular windows. These experiments often require particles to be deposited only on the working electrode, avoiding the counter and reference electrodes.

To address this, we adjusted the tool's design by either reducing the diameter of the funnel mouth or modifying its shape to a rectangle (Figure 27a and b). While this approach successfully prevented particles from depositing on the reference electrode, we could not avoid deposition on the counter electrode (Figure 27c). For the circular, funnel-shaped mouth, the reduced size (0.2 mm) often caused droplets to become trapped due to surface tension, preventing them from passing through.

In the case of the rectangular-shaped funnel, no liquid was able to pass through. Therefore, there is a lower limit to the size of the funnel opening.

While the 0.2 mm opening did not allow liquid to pass through, the 0.5 mm opening of the funnel mouth, used for all other MDTs discussed in this paper, consistently allowed for successful liquid passage.

Although we have not yet succeeded in adjusting the MDT for liquid-biasing chips, further design modifications—particularly to address surface tension issues—may yield better results in the future.

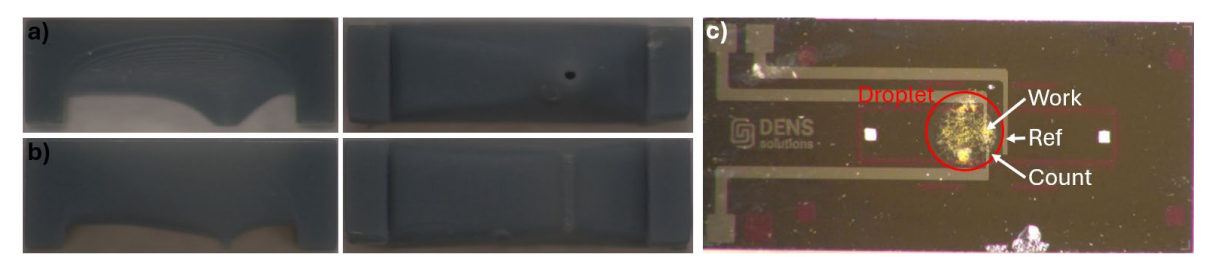


Figure 27. MDT's with an a) smaller and b) rectangular shaped funnel mouth, intended to be used for liquid biasing chips. c) Picture of an in situ liquid biasing chip. The droplet edges, as well as the reference, working and counter electrodes have been indicated on the image.

# **Conclusion to Chapter 2**

This chapter described the development of the MDT. This tool offers a practical and cost-effective solution for improving sample preparation for *in situ* TEM experiments. By confining the droplet to the designated area, the MDT prevented contamination of the O-ring, inlet, and outlet while ensuring a higher concentration of particles on the viewing window. Testing with various 3D printing methods confirmed that the tool is reproducible and effective, though minor surface irregularities influenced liquid containment to some extent. While adaptations for liquid-biasing chips faced challenges related to surface tension and funnel size, the current design significantly improves dropcasting efficiency for *in situ* gas experiments. Although further refinements could potentially further enhance its versatility, the MDT provides a straightforward and reliable method to streamline sample preparation, reducing experimental failure rates and improving overall consistency in *in situ* studies.

## **Chapter 3: Layered double hydroxides**

Parts of this chapter have been published:

Nakazato, R.; Matsumoto, K.; Yamaguchi, N.; Cavallo, M.; Crocella, V.; Bonino, F.; Quintelier, M.; Hadermann, J.; Rosero-Navarro, N. C.; Miura, A.; Tadanaga, K. CO<sub>2</sub> Electrochemical Reduction with Zn-Al Layered Double Hydroxide-Loaded Gas-Diffusion Electrode. Electrochemistry 2023. https://doi.org/10.5796/electrochemistry.23-00080. &

Cavallo, M.; Dosa, M.; Nakazato, R.; Porcaro, N.G.; Signorile M.; Quintelier, M.; Hadermann, J.; Bordiga, S.; Rosero-Navarro N.C.; Tadanaga, K.; Crocellà, V. Insight on Zn-Al LDH as electrocatalyst for CO<sub>2</sub> reduction reaction: An in-situ ATR-IR study. Journal of CO<sub>2</sub> Utilization 2024. https://doi.org/10.1016/j.jcou.2024.102804. &

Nakazato, R., Matsumoto, K., Quintelier, M., Hadermann, J., Rosero-Navarro, N.C., Miura, A., Tadanaga, K. CO<sub>2</sub> Electrochemical Reduction by Zn-Based Layered Double Hydroxides: the Role of Structural Trivalent Metal Ions. Open Ceramics, 2025. https://doi.org/10.1016/j.oceram.2025.100788.

In these works, I have provided the nanoscale characterization of the materials under investigation.

This chapter aims to explore the structural, morphological, and compositional characteristics of layered double hydroxides (LDHs) using TEM, with a particular focus on their potential for CO<sub>2</sub> reduction reactions. Through a combination of synthesis variations, *in situ* heating, and *in situ* gas exposure experiments, we aim to provide nanoscale explanations on how processing conditions and external environments affect LDH structure and morphology, and as a consequence affect properties and catalytic performance.

#### 3.1. Introduction to Layered Double Hydroxides

LDHs are a class of anionic clays that have gained significant attention in materials science due to their unique structural characteristics and wide range of applications. LDHs are represented by the general formula:

$$[M^{2+}_{1-x}M^{3+}_{x}(OH)_{2}]^{x+} \cdot [A^{n-}_{x/n}]^{x-}.mH_{2}O$$
 37

where  $M^{2+}$  and  $M^{3+}$  are divalent and trivalent metal cations, respectively,  $A^{n-}$  are the interlayer anions and x is the fraction of the  $M^{3+}$  cation, defined as  $x = M^{3+} / (M^{2+} + M^{3+})^{37,38}$ . Throughout this work, we will adopt the conventional notation for LDH materials, denoted as  $M^{2+}M^{3+}$  (e.g., ZnAl, where Zn represents the divalent cation and Al the trivalent cation).

The structure of LDHs consists of layers of metal hydroxides, similar to the brucite mineral Mg(OH)<sub>2</sub>, with interlayer spaces filled with anions and water molecules (Figure 28). This layered structure gives LDHs high anion exchange capacities and the ability to intercalate a variety of molecules, making them highly adaptable for numerous applications. The distance between two metal hydroxide layers is known as the basal spacing.

The basal spacing is an important characteristic of the LDH structure, influenced by the type of cations in the structure, as well as the nature and quantity of water molecules and charge-compensating anions within the interlayer spacing <sup>38</sup>.

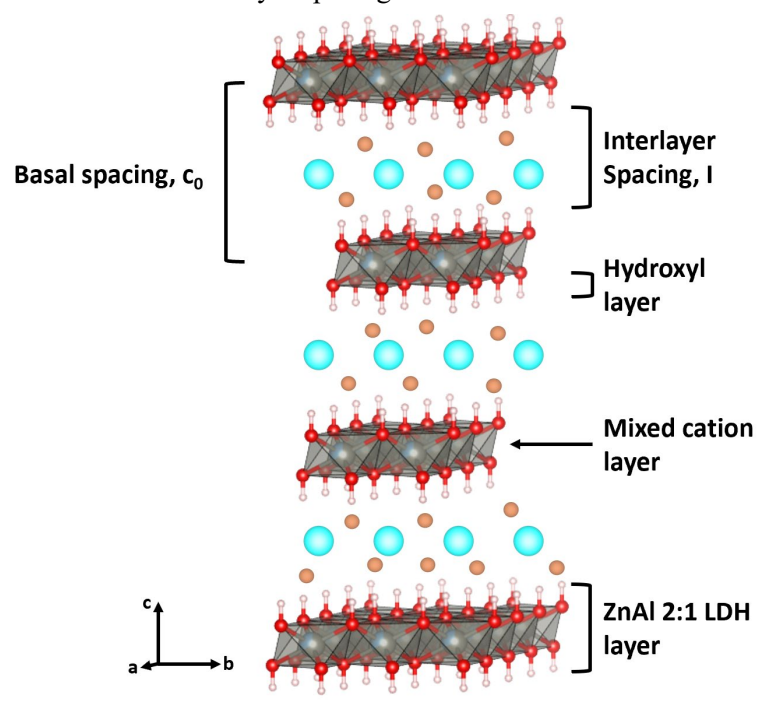


Figure 28. Structure of ZnAl (2:1) LDH. The brown spheres represent interlayer  $H_2O$  and the blue spheres represent interlayer  $CO_3^{2-}$ . The red spheres represent O, the pink ones H and the grey/blue spheres Zn and Al on a shared position.

Due to the versatility of their structure, LDH materials have a wide range of applications, including chemical and physical absorption <sup>39–42</sup>, ion exchange <sup>43,44</sup>, fire retardancy <sup>45,46</sup>, biomedical uses <sup>47,48</sup>, and environmental remediation <sup>49–51</sup>.

Of particular interest in this work is their potential as catalysts for CO<sub>2</sub> reduction reactions (CO<sub>2</sub>RR), specifically in CO<sub>2</sub> electrochemical reductions (CO<sub>2</sub>ER) <sup>37,52–54</sup>. This process, depicted by the chemical reaction below, involves the reduction of CO<sub>2</sub> using electricity to produce CO and OH<sup>-</sup>.

$$CO_2 + H_2O + 2e^- \rightarrow CO + 2OH^- E_o = -0.11V \text{ vs. RHE}$$

Therefore, the standard equilibrium potential for this  $CO_2$  reduction reaction is -0.11 V versus the reversible hydrogen electrode (RHE). This indicates that, under standard conditions, an applied potential more negative than -0.11 V vs. RHE is required to thermodynamically drive the reaction forward.

The electrochemical reduction of CO<sub>2</sub> using electrocatalysts offers a promising way to utilize excess electricity generated from renewable energy sources such as solar and wind power. Moreover, CO produced through this process serves as a raw material for synthesizing methanol and liquid hydrocarbons, which have potential applications as biofuels for aviation, as outlined in the European 4AirCRAFT project, which this thesis work was part of.

### 3.2. LDHs studied during this PhD

The LDH materials with different cations studied in this thesis were synthesized using the coprecipitation method by Dr. Ryosuke Nakazato and Prof. Dr. Kiyoharu Tadanaga from Hokkaido University.

These materials include ZnAl, NiAl, and NiFe LDHs, all prepared with cation ratios of 2 (Zn:Al = Ni:Al = Ni:Fe = 2). The synthesis process is schematically illustrated in Figure 29.

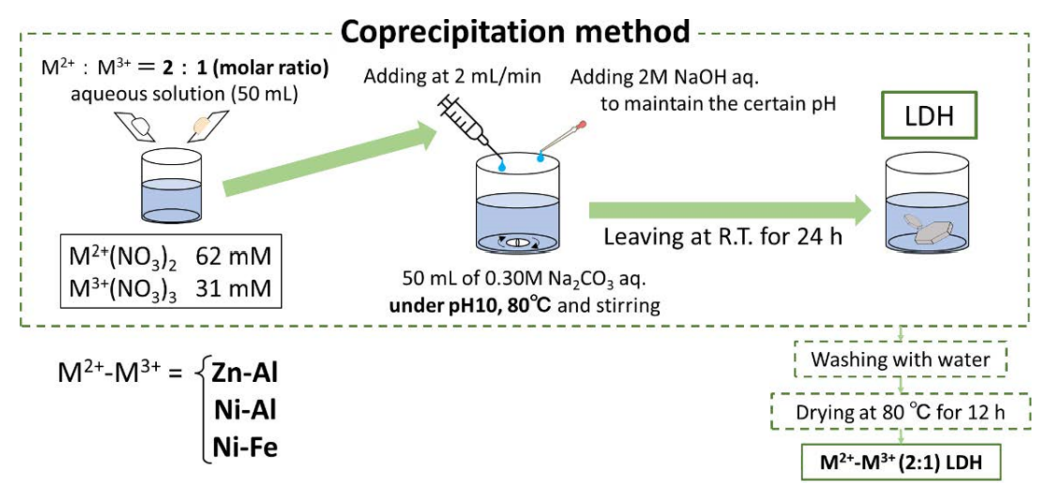


Figure 29. Schematic illustration of the preparation method for different LDH samples <sup>37</sup>.

According to the TEM study, ZnAl consists of crystals with the typical hexagonal platelet morphology (Figure 30). The NiAl and NiFe materials consisted of submicron- to micron-sized aggregates of nanoparticles (representative SAED pattern in Figure 30d). STEM-EDX analysis (Figure 31) shows a homogeneous distribution of the  $M^{2+}$  and  $M^{3+}$  within the particles. The quantitative EDX analysis showed average chemical compositions with molar ratios of Zn/Al = 2.0(3), Ni/Al = 1.8(3) and Ni/Fe = 2.0(2). These results agree with the synthesized products being LDH with the formula  $[M^{2+}_2M^{3+}_1(OH)_6]^+ \cdot [CO_3^{2-}_{0.5}]^-$ .

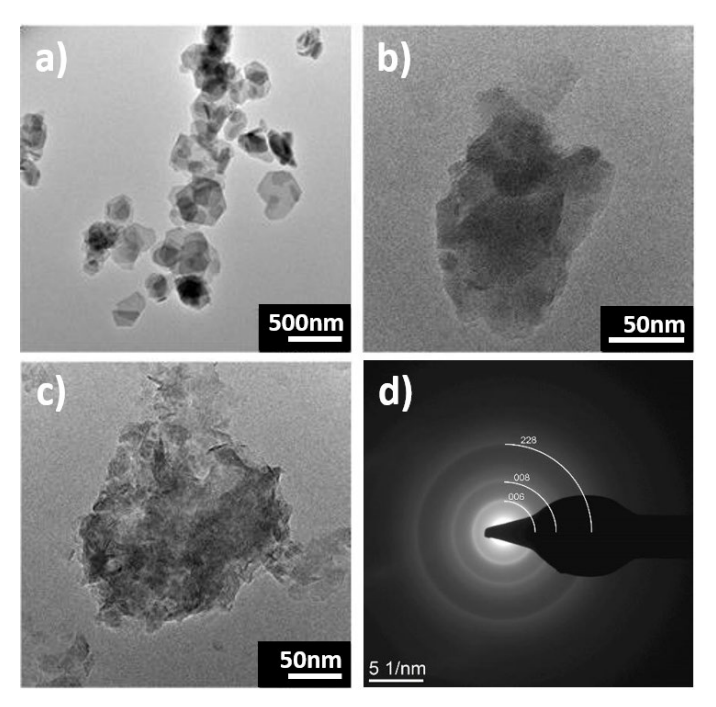


Figure 30. TEM images of a) ZnAl (2:1), b) NiAl (2:1) and c) NiFe (2:1) LDHs. d) Representative SAED pattern of NiFe (2:1) LDH. Several diffraction rings are indexed.

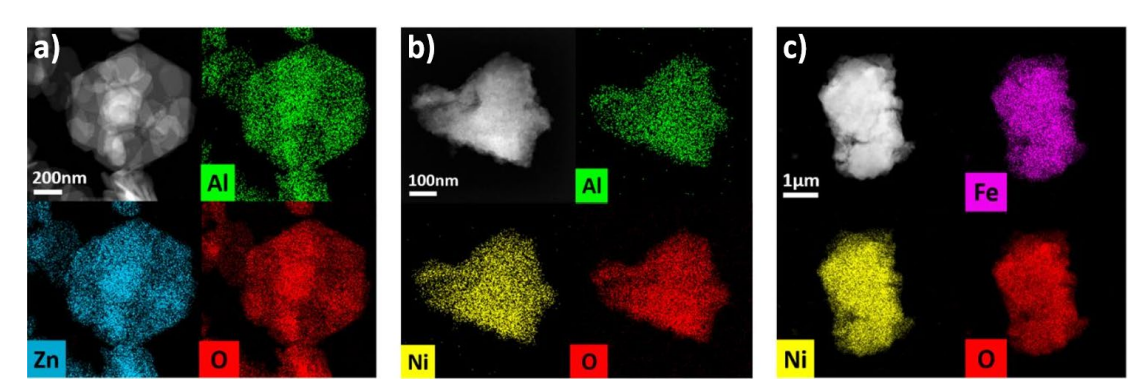


Figure 31. Elemental STEM-EDX maps of a) ZnAl (2:1), b) NiAl (2:1) and c) NiFe (2:1) LDHs. The maps are given in counts.

Our collaborators from Hokkaido University performed experiments to evaluate the Faradaic efficiency of all three samples in order to determine the optimal one for CO<sub>2</sub>RR. Faradaic efficiency is the ratio of the actual product generated in an electrochemical reaction to the theoretical amount predicted from the charge passed. It reflects reaction selectivity and serves as an indicator of energy efficiency, with higher values implying minimal energy loss and better control. It is calculated using the following formula:

Faradaic efficiency (%) = 
$$\frac{z \times n \times F}{Q} \times 100$$

With z being the number of electrons required per molecule of the desired product, n the number of moles of product formed, F is Faraday's constant (96,485 C/mol e<sup>-</sup>), and Q is the total charge passed (C).

Faradaic efficiency in CO<sub>2</sub> reduction is measured by first performing electrolysis under controlled conditions while recording the total charge passed. The reaction products (gaseous or liquid) are then collected and quantified using techniques like gas chromatography or nuclear magnetic resonance. Using the amount of each product and the number of electrons required to form it, Faradaic efficiency is calculated by comparing the charge used to make the product to the total charge passed.

Figure 32a indicates that the ZnAl LDH shows the most potential for this process. After this, the durability of the ZnAl LDH (at an applied potential of -0.96 V vs RHE) was determined (Figure 32b). The partial current density of CO was almost constant (initial: 12.0 mA cm<sup>-2</sup>, end: 11.8 mA cm<sup>-2</sup>) for 6 h, although the Faradaic efficiency of CO gradually decreased slightly (Figure 32c), due to an increase in total current density (initial: 21.1 mA cm<sup>-2</sup>, end: 22.9 mA cm<sup>-2</sup>), indicating the CO-forming activity of Zn-Al LDH was maintained for at least 6 h.

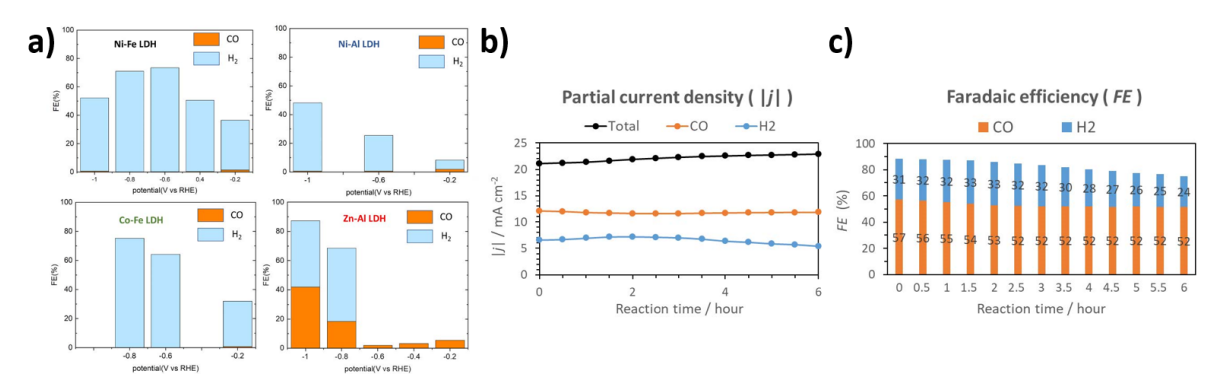


Figure 32. a) Faradaic Efficiency of LDHs with different metal composition. b) & c) Durability of catalytic activity of ZnAl LDH (applied potential: -0.96V vs. RHE).

Although conventional PXRD indicated a perfect ZnAl LDH crystal with no detectable defects or layer variations  $^{37}$ , our low dose HRTEM images (Figure 33) showed that the spacing between consecutive mixed cation layers varied across nanoscale regions, caused by edge dislocations and irregular basal spacings, with an average basal spacing  $c_0 = 7.4(6)$  Å. However, due to the beam sensitivity of the LDH materials, achieving atomic-resolution images was not possible. This basal spacing variation causes a high degree of diffuse scattering in normal SAED patterns (Figure 34a) making standard 3D ED analysis of the crystal structure impossible.

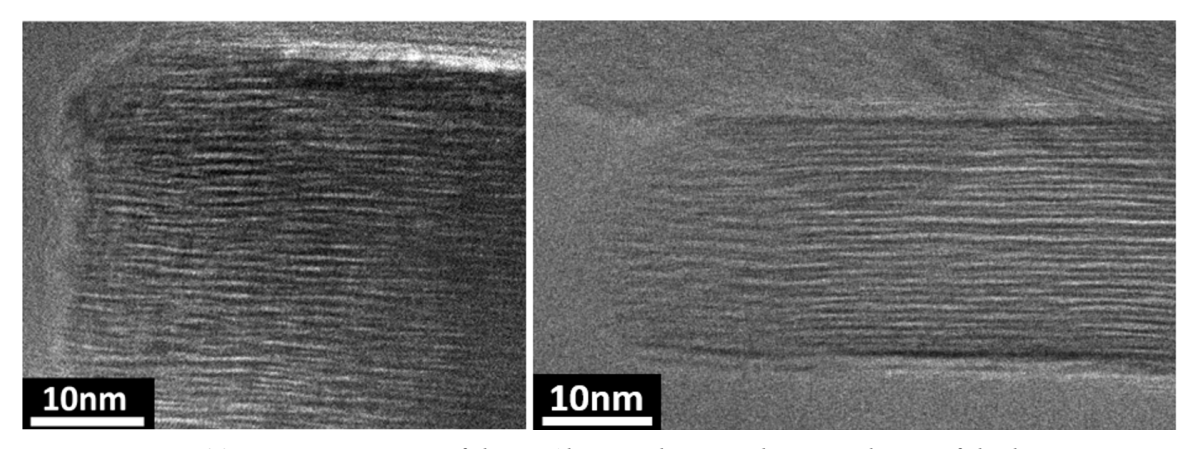


Figure 33. HRTEM images of the ZnAl LDH showing the irregularity of the layers.

Figure 35a shows a representative area from a SNBD scan, displaying particles that contain the c\*-axis on the diffraction patterns. By using a small 5 nm size parallel probe via the SNBD scan technique, we acquire diffraction patterns of localized regions, therefore also minimizing the variation in c\* over the probed area and thus reducing the diffuse scattering in the diffraction patterns (Figure 34b). This allows mapping the average basal spacing per probed 5 nm area and following its trend over the particle (Figure 35b). For regions-of-interest containing the material's c\*-axis, a line profile along the 00l row of reflections in diffraction space was defined for each probe position. This line profile was smoothed by upscaling with a third-order polynomial interpolation between points, and local maxima were identified using a minimum intensity threshold to reduce noise interference. Local maxima corresponding to a similar spacing were considered to belong to a single c\* value. The distances between these local maxima were averaged for each line profile to determine the average basal spacing at each scan point.

This method of basal spacing analysis not only yields an average value but also shows nanoscale variations that cause the diffuse scattering observed in Figure 34a. Specifically, at the edges, the basal spacing is consistently lower than in the core of the particles. Possibly, the vacuum environment inside the TEM column causes the removal of a certain amount of molecules along the edges. The average basal spacing obtained from SNBD is 7.2(2) Å, which matches the basal spacing measured using the HRTEM images.

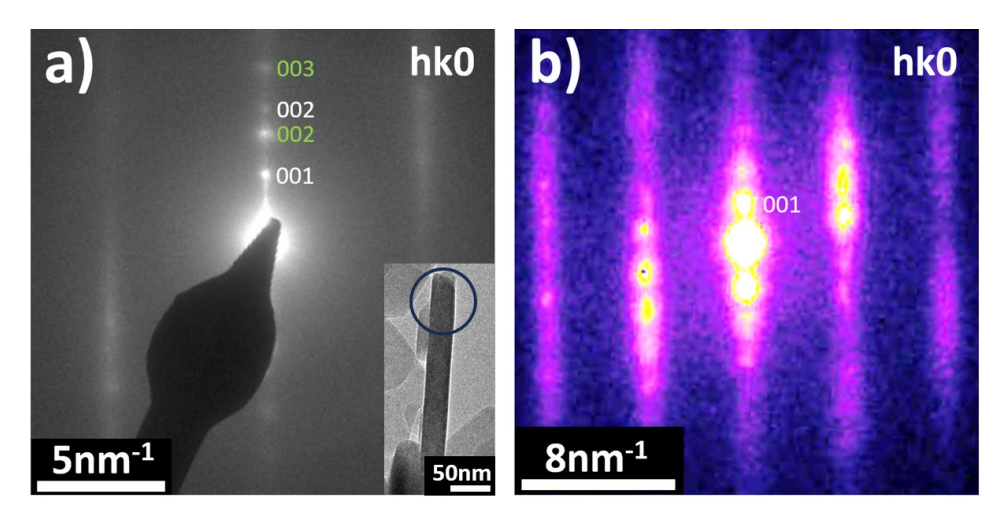


Figure 34. a) SAED pattern taken by using the smallest possible SAED aperture, i.e. 200 nm projected distance. Irregular basal spacings cause the presence of diffuse scattering. Two basal spacings dominate in this SAED image, indexed in white and green. The insert shows the studied particle, along with the area used for the SAED pattern. b) diffraction pattern obtained by using SNBD. The small beam size (~ 5 nm) produces local diffraction patterns, minimizing the diffuse scattering.

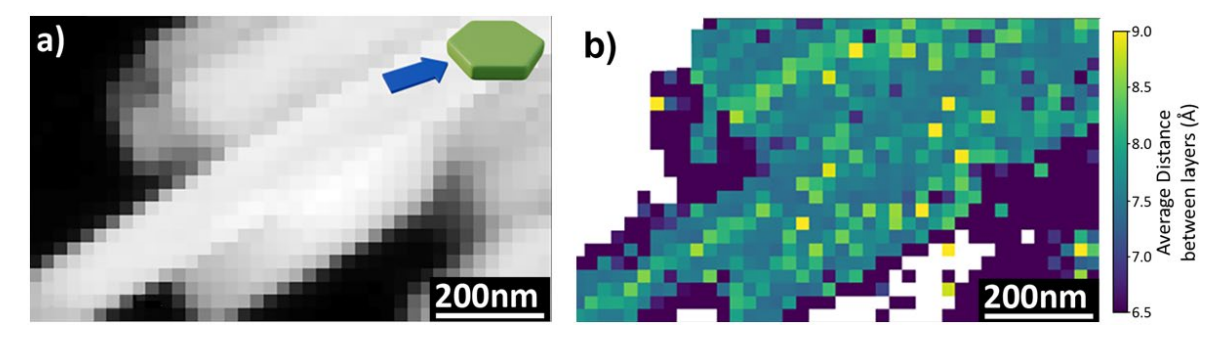


Figure 35. a) SNBD scan showing particles that are lying in an orientation where the diffraction pattern contains the c\*-axis of the material, making it possible to study the basal spacing. The inset shows a schematical representation of the viewing direction. b) Map of the variations in basal spacings per scan point of (a). The map was generated using a self-written python code that utilizes Hyperspy and Pyxem.

Building on these results, several variations of the ZnAl LDH were synthesized with different cation ratios: a new batch of Zn:Al = 2, Zn:Al = 1, and Zn:Al = 0.5. TEM imaging showed that all three samples exhibited the typical hexagonal platelet morphology characteristic of LDHs, as shown in Figure 36.

STEM-EDX analysis showed Zn:Al ratios equal to 2.0(3), 1.6(2), and 1.2(4) for the three samples respectively. Additional STEM-EDX analysis revealed that in the Zn:Al = 0.5 sample, pure Al<sub>2</sub>O<sub>3</sub> particles were also present in the powder. These particles likely absorb a significant portion of the available Al during synthesis, reducing its availability for the formation of LDH particles. This depletion of Al may explain why the resulting LDHs for Zn:Al = 1 and Zn:Al = 0.5 exhibit cation ratios Zn:Al = 1.6(2) and Zn:Al = 1.2(4) instead.

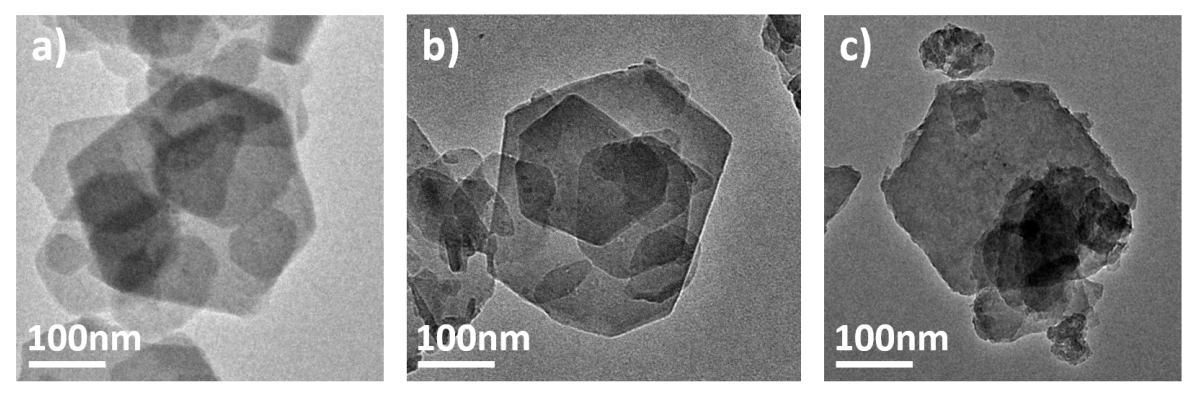


Figure 36. TEM images of a) ZnAl (2:1), b) ZnAl (1:1) and c) ZnAl (1:2) LDHs.

HRTEM imaging was again used to study the cation layers, as shown in Figure 37. The images also indicated an irregular basal spacing in the Zn(1)Al(1) and Zn(1)Al(2) LDH materials. Additionally, structural defects such as edge dislocations were observed in these images, highlighting intrinsic irregularities within the layers.

Average basal spacings manually measured on the HRTEM images (taken over 35 measurements) are Zn(2)Al(1): 7.4(6) Å, Zn(1)Al(1): 6.7(8) Å, and Zn(1)Al(2): 8.0(1.2) Å. The size of the particles decreases when one deviates from the Zn:Al 2:1 ratio. A comparison of the different particle sizes, along with the measured cation ratios, as well as the measured average basal spacings is shown in Figure 38. The difference in basal spacing for LDH materials with different cations can be explained by the nature and ratio of the cations used. For the three ZnAl LDH compositions studied, the variation in basal spacing is likely related to the charge balance required between the metal hydroxide layers and the interlayer anions. In Zn(1)Al(1), the higher content of Al<sup>3+</sup> leads to more positively charged layers, which require a greater concentration of interlayer anions for charge compensation. This stronger electrostatic interaction results in increased attraction between the layers, and thus a smaller basal spacing compared to Zn(2)Al(1).

Despite the higher Al<sup>3+</sup> content in Zn(1)Al(2), the basal spacing is larger compared to Zn(1)Al(1). This could be explained by the increased need for charge compensation, leading to a larger amount of interlayer anions and possibly more structured water molecules trapped between the layers. These species may expand the interlayer distance, counteracting the expected contraction from Coulombic attraction between the layers. However, based on these results alone, no definitive explanation can be given, and it is likely that a combination of factors (such as interlayer composition, water content, and structural rearrangements) plays a role.

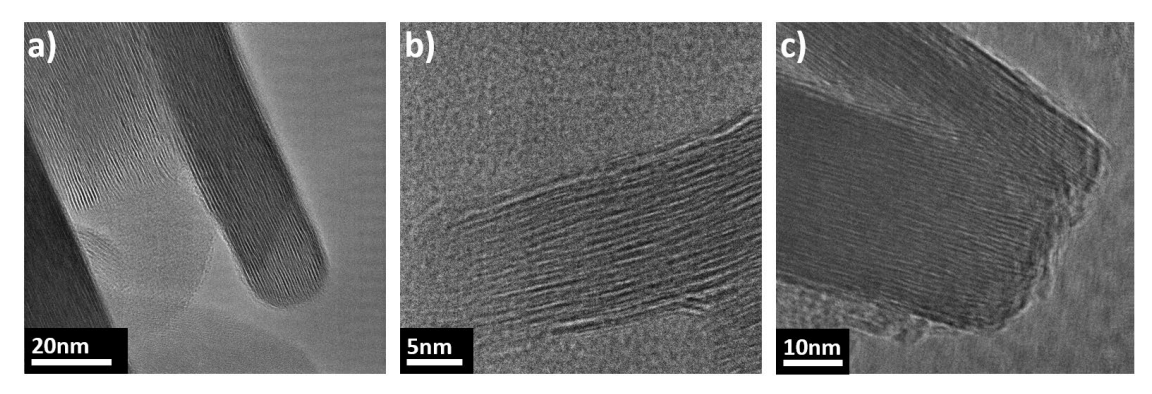


Figure 37. HRTEM images of a) ZnAl (2:1), b) ZnAl (1:1) and c) ZnAl (1:2) LDHs showing the LDH layers.

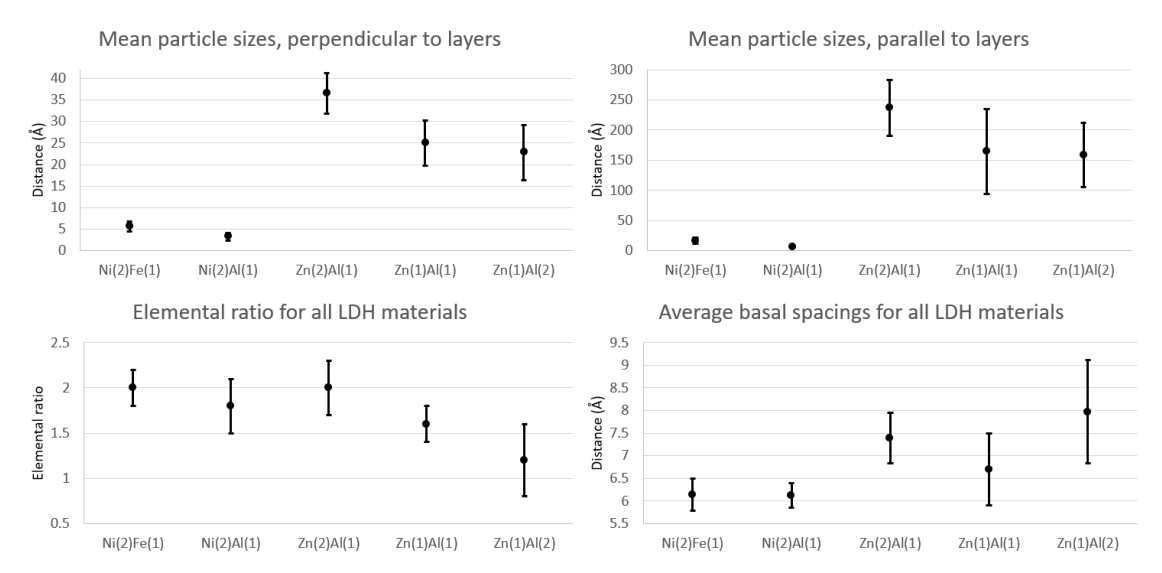


Figure 38. Comparison between LDH with different compositions. The graphs compare size, element ratio and basal spacings.

The evolution of the morphology and microstructure of the ZnAl LDH with targeted 2:1 composition was determined along various synthesis and preparation steps. One of these steps was examining the influence of various stages of aging. From the sample without aging, over a sample with 24 hours of aging at 60 °C to a sample with 12 hours aging at 120 °C, the lateral size of the particles increased from 50-300 nm to 140-375 nm (Figure 39) and the thickness of the platelets from 10-35 nm to 140-375 nm. The sample aged at 120 °C exhibited better defined morphologies and overall thicker particles, as visible on the TEM images. Zn:Al ratios were 1.8(1), 1.63(9) and 2.02(9).

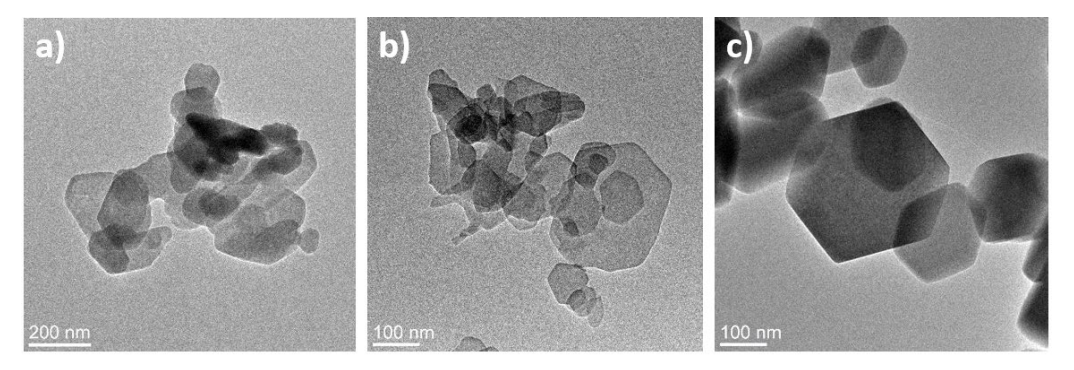


Figure 39. TEM images of the ZnAl LDH with a) no aging, b) 24 h aging at 60 °C and c) 12 h aging at 120 °C.

The influence of grinding on the ZnAl LDH particles was also studied with HRTEM. Our collaborators from Hokkaido University found an increase in Faradaic efficiency towards CO when increasing the grinding time of the ZnAl LDH particles, as is shown in Figure 40.

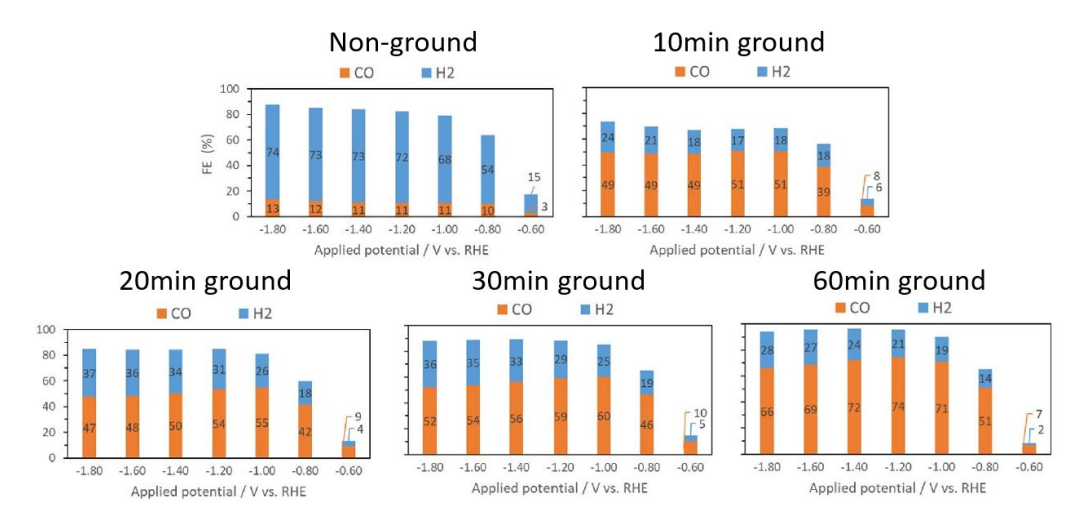


Figure 40. Faradaic efficiency for CO and  $H_2$  of ZnAl LDHs with different grinding times.

HRTEM shows a progressive decline in crystal quality as grinding time increases from 0 minutes to 60 minutes, accompanied by a reduction in both particle size and the number of particles displaying clear metal hydroxide layers over time (Figure 41).

Grinding had a clear impact on particle morphology and crystallinity. At 0 minutes, particles exhibited well-defined hexagonal shapes with the c-axis in the viewing plane and sizes ranging from 100–500 nm. After 10 minutes of grinding, particle sizes decreased to 50–350 nm, and by 20 minutes, the particles began losing their distinct shape and orientation. Significant agglomeration occurred from 20 minutes onward, with indistinct boundaries and agglomerate sizes ranging from 40–150 nm at 20 minutes, 40–400 nm at 30 minutes, and 50–500 nm at 60 minutes. HRTEM images showed that the metal hydroxide layers, initially spanning the full particle size (90–300 nm), progressively broke down with grinding.

After 10 minutes, these layers were reduced to 10–90 nm, shrinking further to 10–30 nm at 20 minutes. At 30 and 60 minutes, only small nanodomains remained, measuring approximately 7 nm and 5 nm, respectively. To ensure these changes reflected actual grinding effects and not artifacts from sample preparation, no ultrasonic treatment was applied during TEM sample preparation. This allowed for accurate observation of the gradual fragmentation and crystallinity loss of the metal hydroxide layers over time.

This reduction in particle size with increased grinding time leads to a significant enhancement in the contact surface area of the ZnAl LDH particles. This larger surface area compared to the untreated particles likely plays an important role in improving the Faradaic efficiency for CO<sub>2</sub>RR. This Faradaic efficiency quantifies the efficiency of charge transfer in an electrochemical process, specifically the percentage of charge used to produce a desired product. As particle sizes decrease and the metal hydroxide layers fragment into smaller nanodomains, more active sites become accessible for the reaction. While these changes reduce overall crystallinity, they highlight the effectiveness of controlled grinding as a strategy to optimize ZnAl LDH materials for CO<sub>2</sub> reduction applications.

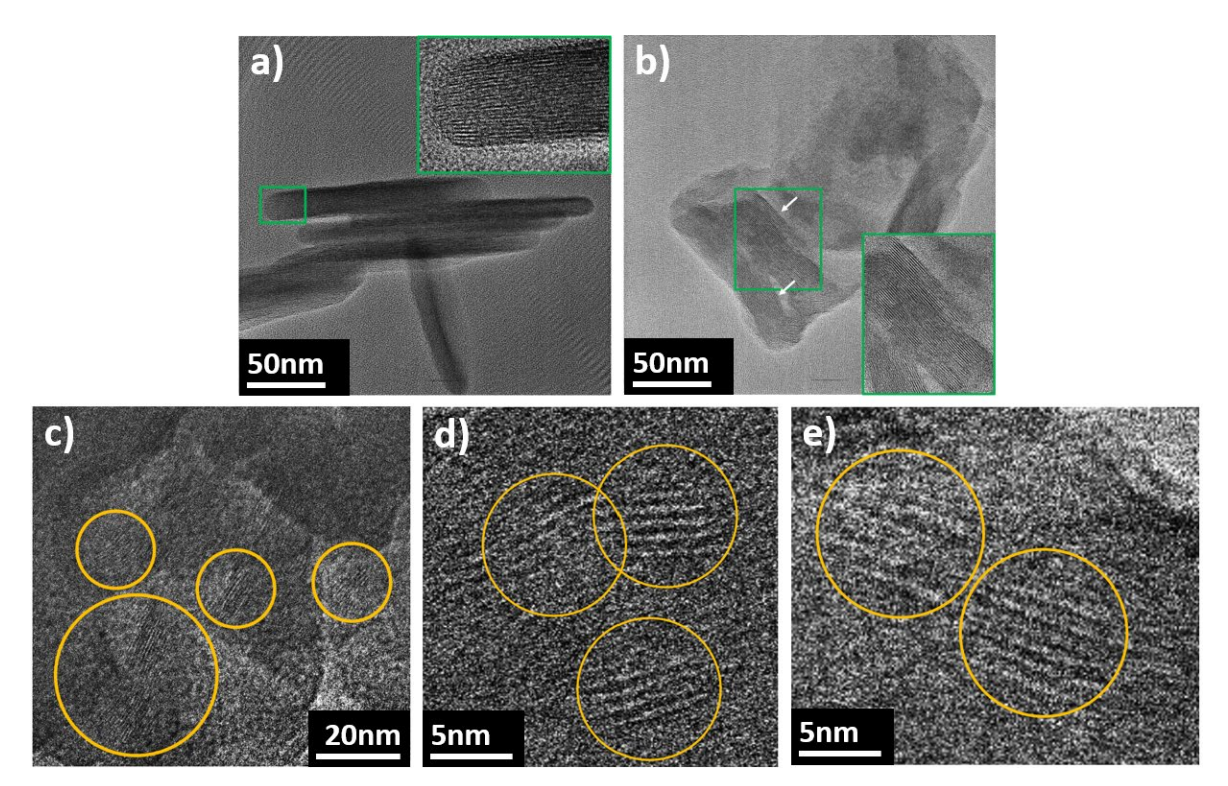


Figure 41. Overview of HRTEM images displaying ZnAl LDH particles with fringes corresponding to metal hydroxide layers at various grinding times: a) no grinding, b) 10 minutes of grinding, c) 20 minutes of grinding, d) 30 minutes of grinding, and e) 60 minutes of grinding. The white arrows in b) indicate particles with clear fringes.

#### 3.3. Thermal evolution of ZnAl LDH

This study has been submitted to the journal ACS Applied Materials & Interfaces on 17 February 2025 and has been accepted on 9 July 2025.

For many applications involving LDH materials, understanding their structural and morphological evolution at elevated temperatures is important, as it directly impacts performance and stability. Investigating the intermediate phases that emerge during any possible thermal transformations offers insight into the underlying mechanisms and allows for more precise control over material properties in targeted applications. An *in situ* heating TEM study on MgAl and NiFe LDHs demonstrated their thermal transformation into α-Al<sub>2</sub>O<sub>3</sub> + MgAl<sub>2</sub>O<sub>4</sub> and NiO + NiFe<sub>2</sub>O<sub>4</sub>, respectively <sup>55</sup>. However, this study was conducted using transmission electron microscopy under high vacuum conditions, whereas most of the applications concerned (catalysis, fire retardancy, environmental remediation, ...) typically occur in ambient atmospheres, decreasing the representativity of the results for real-life applications. Furthermore, the study focused on the end products and neglected the intermediate phases that arise during thermal evolution.

For ZnAl LDH, *ex situ* and *in situ* XRD studies demonstrated that the structure gradually starts to collapse at 120 °C, forming a layered double oxide (LDO), which subsequently transforms into a mixture of ZnO and Al<sub>2</sub>O<sub>3</sub> or ZnO and ZnAl<sub>2</sub>O<sub>4</sub> at higher temperatures <sup>56,57</sup>. However, XRD studies lack the nanoscale positional and morphological information that TEM studies can provide.

In this thesis, *in situ* TEM was used to investigate the thermal behavior of ZnAl (2:1) LDHs in a relevant ambient atmosphere, providing a nanoscale understanding about the changes in crystal structure, morphology, and composition. This approach allows the capture of both the intermediate phases and their positional information throughout the thermal evolution process, offering a thorough nanoscale characterization of ZnAl (2:1) LDH thermal behavior. This knowledge of the thermal decomposition pathway under ambient conditions provides guidance for optimizing the LDH structure to resist degradation, increasing both the lifespan and performance of catalysts under operational conditions. Furthermore, this work shows the distribution of these phases within the particles and the conversion of domains between phases.

The thermal behavior also provides new synthesis pathways for the obtained composites, which are complicated to obtain using the currently known methods.

To investigate the thermal behavior of the LDH material at elevated temperatures, the material was heated *in situ* in both the UHV environment of the TEM, as well as in ambient conditions by using an *in situ* gas holder. For both experiments, the heating curve shown in Figure 42 was used.

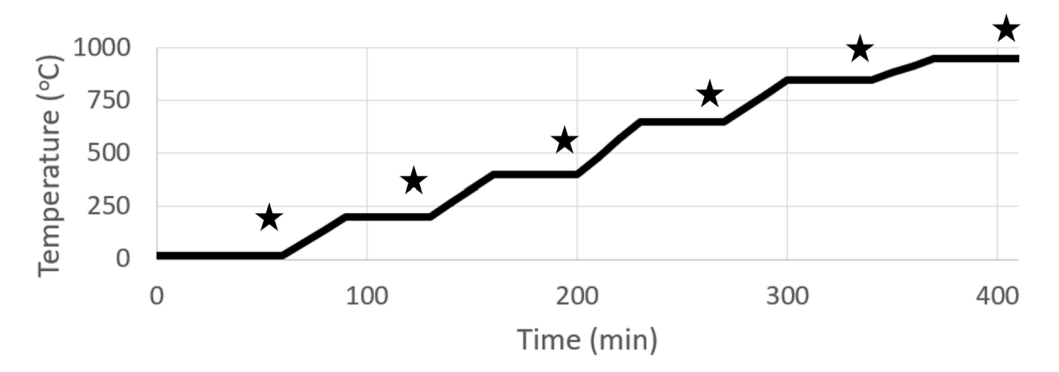


Figure 42. Heating curve followed for all experiments. The stars indicate the temperatures and times where the data was acquired.

When heating the ZnAl LDH particles in vacuum, HAADF-STEM images (Figure 43a) show a slightly rougher appearance at 200 °C than at 20 °C. The average basal spacing at 200 °C has decreased to 5.0(8) Å when measured from HRTEM, while SNBD shows two separate basal spacings, corresponding to 7.27(5) Å and 5.71(5) Å. According to literature, such reduction of the basal spacing is due to the dehydration of the LDH, the decomposition of the CO<sub>3</sub><sup>2-</sup> interlayer anions and the decomposition of the hydroxide layers adjacent to the cation layers <sup>58</sup>. The difference in exact values between the basal spacings at the same temperature from HRTEM versus SNBD could be due to local differences or a particle-to-particle dependence. The basal spacings could not be mapped (as done higher for the pristine material) due to the material's low crystallinity.

SNBD taken along the [001] zone axis shows the same reflections at 200 °C as at 20 °C, indicating that the LDH structure is still retained up to 200 °C. The higher order reflections have become weaker, corresponding to a decrease in crystallinity. Phase mapping using the SNBD data (Figure 44) shows that the LDH structure is homogeneously retained throughout the particle at 200 °C.

Pores start to form at 400 °C, clearly visible on the HAADF-STEM images (Figure 43a), while the phase map at 400 °C shows that the particle has the ZnAl<sub>2</sub>O<sub>4</sub> structure.

Upon further heating, the pores increase in size, and by 650 °C, Al<sub>2</sub>O<sub>3</sub> has appeared within the ZnAl<sub>2</sub>O<sub>4</sub> matrix. At 850 °C, the phase map indicates mostly ZnO within an Al<sub>2</sub>O<sub>3</sub> matrix. Minute traces of the spinel phase ZnAl<sub>2</sub>O<sub>4</sub> are still present and some locations with pure Zn are observed. After heating to 950 °C, no spinel phase was observed anymore, while ZnO has diffused further inwards and aggregated into larger domains.

The phase maps do not show the pores because they are initially smaller than the 5 nm beam used for the scans and for the higher temperatures the pores do not pass all the way through the material. Thus, for each scan point, the diffraction pattern will be that of the remaining material within this 5 nm probe area.

After the full heating curve, the sample was cooled down to 650 °C (as HAADF-STEM imaging at 950 °C was impossible due to the increased beam damage) and high resolution HAADF-STEM images (Figure 43b) were taken while monitoring the Kikuchi lines at a single point to ensure structural stability.

These HAADF-STEM images confirm that the dark regions in Figure 43a are indeed pores. A close-up of the pores is shown in Figure 43b. The changes in the particles during heating were also followed using HRTEM. While at low temperatures only the basal spacings changed, as mentioned above, at 850 °C new crystalline domains appeared on the HRTEM images (Figure 45) with d-spacings corresponding to the interplanar distances between the (110) planes of the Al<sub>2</sub>O<sub>3</sub> structure. This corresponds to the domain formation that was also seen on the SNBD. On the low magnification HAADF-STEM images, the domain formation is not clear, as the pores dominate the appearance of the particle and inherently domains with the same elemental composition and similar thickness will show the same contrast. However, on the atomic resolution HAADF-STEM images, which show the domains along the [001]<sub>Al2O3</sub> zone, the domain formation is clear where different domains overlap and form Moiré patterns.

During heating, we did not observe the formation of LDO that was reported in literature to form at 120 °C <sup>57</sup>. This discrepancy can likely be attributed to the expected poor crystallinity of LDO <sup>59,60</sup>.

In this regard, it is important to note that when diffraction patterns consist of two overlapping patterns from different phases, the phase mapping software assigns the phase of the most intense pattern, which makes nanometer-scaled, poorly crystalline phases difficult to detect.

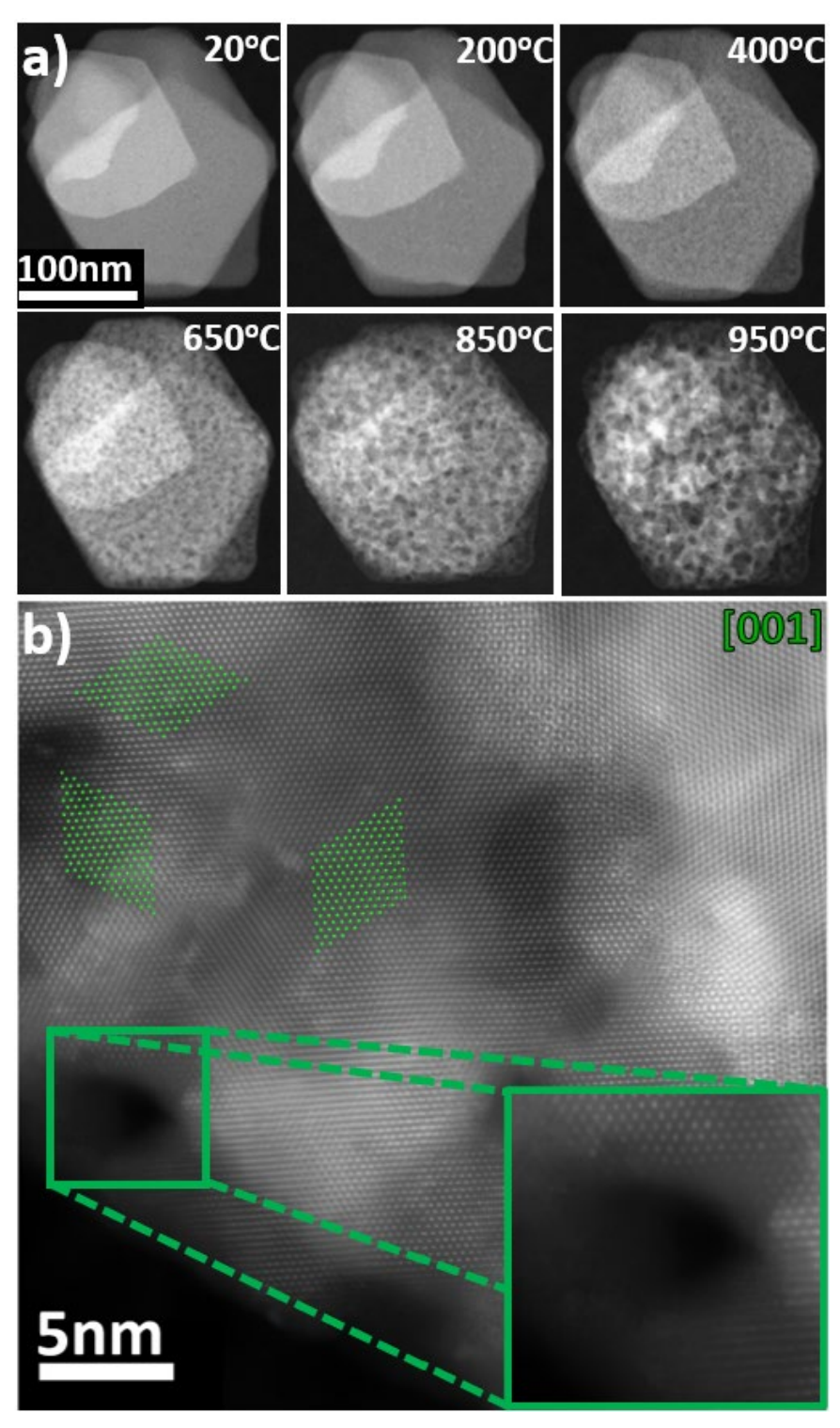


Figure 43. a) HAADF-STEM images showing the morphological changes of an LDH particle. Starting from 400 °C, the morphology changes to a porous structure. b) High magnification HAADF-STEM images of the structure formed after heating ZnAl (2:1) to 950 °C and cooldown to 650 °C in vacuum. The Al<sub>2</sub>O<sub>3</sub> structure viewed along the c-axis has been overlayed in some area's. Al atoms are depicted in green, O atoms have been omitted for clarity. The insert shows one of the formed pores.

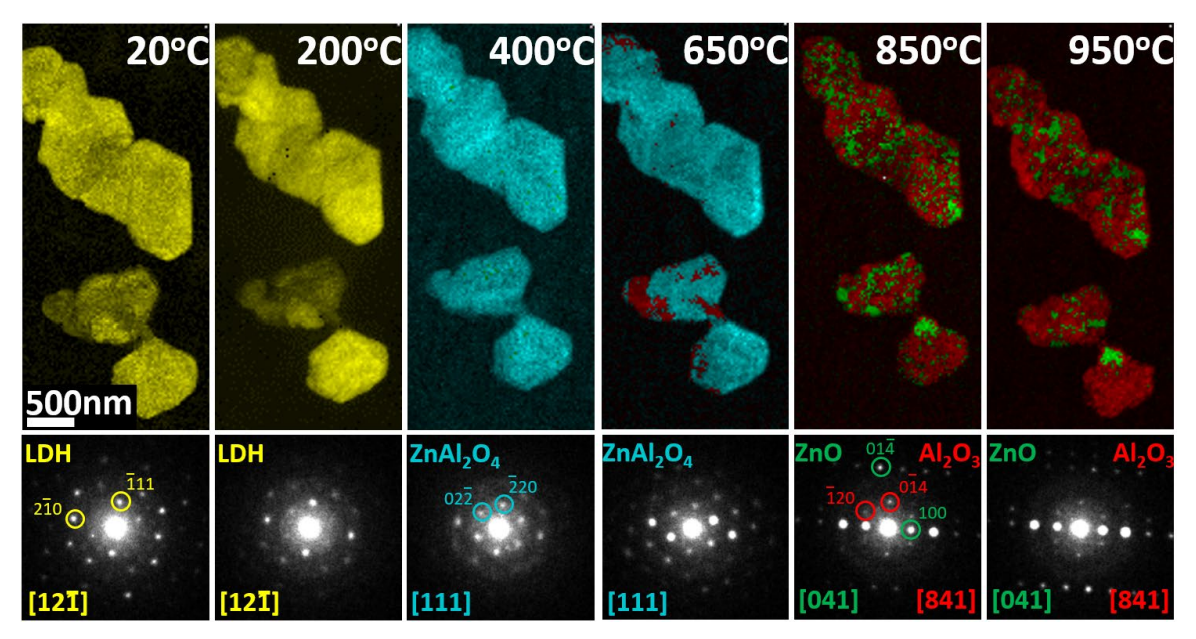


Figure 44. Phase maps of the same particle at the different heating stages. We observe a phase transformation of the LDH structure (yellow) to ZnAl<sub>2</sub>O<sub>4</sub> (light blue) and then further to ZnO (green) in an Al<sub>2</sub>O<sub>3</sub> (red) matrix. The Al<sub>2</sub>O<sub>3</sub> phase is starting to form at 650 °C. The presence of Zn particles (dark blue) at 850 and 950 °C is also observed. Underneath each phase map, a diffraction pattern of the same, representative 5 nm area within the 4D-STEM scan during the heating curve, along with manual indexations of the patterns and zone identifications.

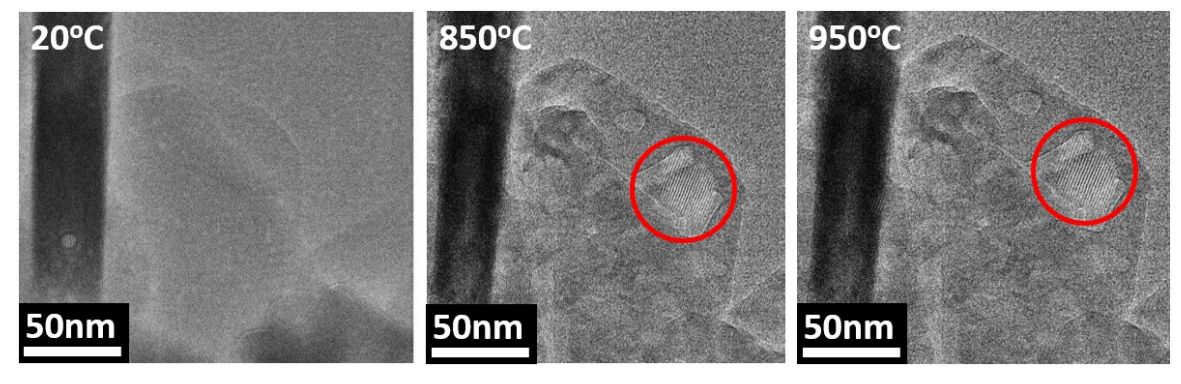


Figure 45. Relevant HRTEM images showing the structural evolution of LDH particles upon heating in vacuum. The images at 850 °C and 950 °C show magnified areas as insets where newly formed crystalline (interplanar distances corresponding to the (110) planes of the Al<sub>2</sub>O<sub>3</sub> structure) domains are visible, indicated by a red circle. The contrast for these images was enhanced by taking the Fourier transform, applying a mask to the two visible spots in the frequency domain, performing an inverse FFT, and overlaying the resulting image with the original one.

After heating, the particles were allowed to cool down, and STEM-EDX measurements were taken (Figure 46a). STEM-EDX exhibited areas rich in Zn and O within a matrix composed of Al and O. For clarity, O was excluded from the maps in Figure 46a.

However, it was not possible to determine the composition of these regions using standard EDX processing techniques due to the Si<sub>3</sub>N<sub>4</sub> background. Therefore, principle component analysis (PCA) combined with non-negative matrix factorization (NMF) analyses, as outlined in <sup>61</sup>, was used.

This confirmed that these regions are indeed Al<sub>2</sub>O<sub>3</sub> and ZnO, and that the pores are not merely regions containing only low-Z elements (Figure 46b and Table 1), which was a possibility that could not be ruled out based on HAADF-STEM images alone. This confirms that ZnO particles form within an Al<sub>2</sub>O<sub>3</sub> matrix as found using SNBD (Figure 44).

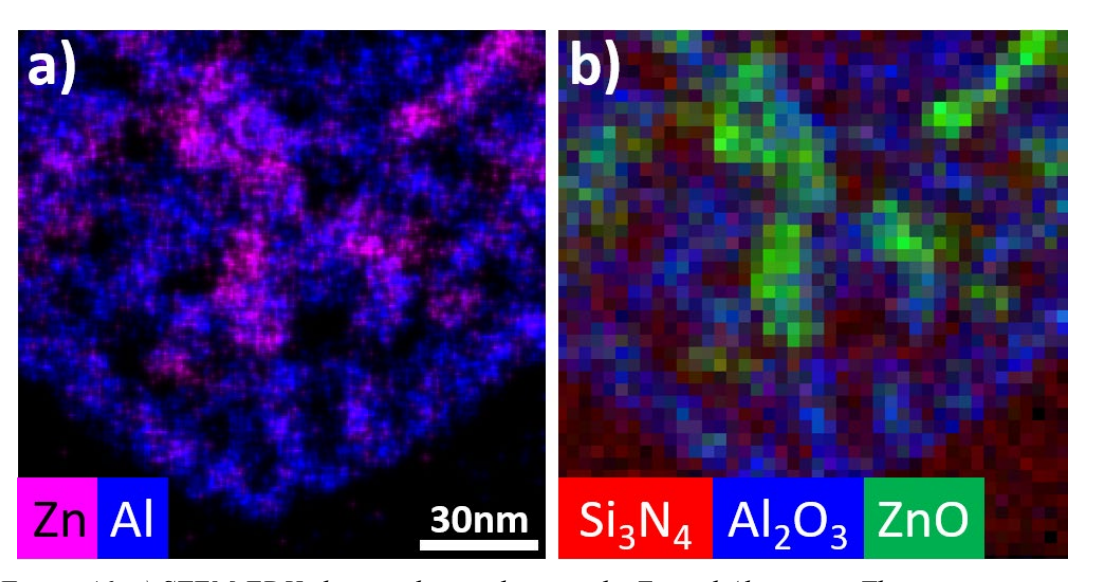


Figure 46. a) STEM-EDX elemental map showing the Zn and Al content. The map is given in counts. b) Component map from NMF analysis.

Table 1. NMF results showing the quantified composition of the three found phases for the thermal decomposition in vacuum. The values are given in atomic percent.

,	Al	Zn	O	C	Cu	N	Si
Component 1 (Si <sub>3</sub> N <sub>4</sub> )	0.1	0.1	3.9	15.1	0.1	35.8	44.9
Component 2 (ZnO)	2.9	34.8	42.5	2.7	6.3	8.7	1.9
Component 3 (Al <sub>2</sub> O <sub>3</sub> )	25.9	0.9	41.5	6.9	0.4	11.8	12.7

To explore the impact of the atmosphere on the structural evolution of the particle, we investigated the crystal structure with the same heating curve, but in ambient air. Heating in air produced a visually similar porous morphology to that observed when heating in vacuum (Figure 47), with the porous structure emerging at 400 °C but being less pronounced than in vacuum. However, as shown furtheron in this section, the phase composition differs.

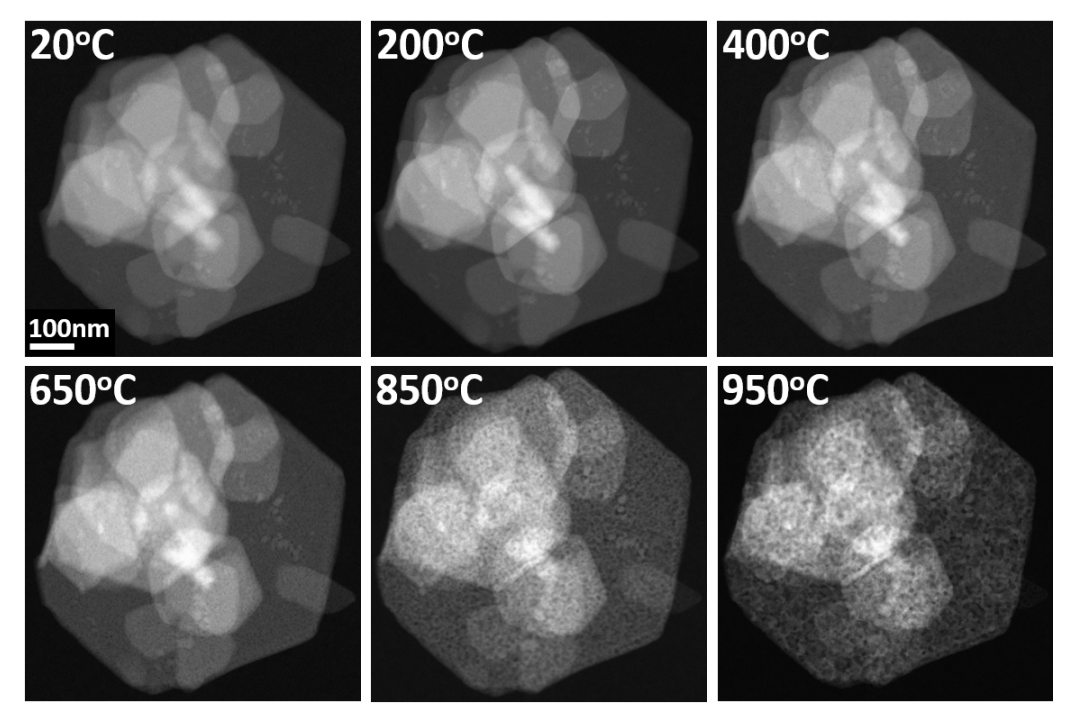


Figure 47. HAADF-STEM images of the morphological changes of an LDH particle. Starting from 400 °C, the morphology changes to a porous structure.

Using SNBD, a manually selected, representative 5 nm area was again followed throughout the heating curve, which showed that the LDH structure is also mostly retained in air up to 200 °C (Figure 48). Phase maps based on an SNBD scan of the entire particle reveal the presence of ZnO domains at 200 °C (Figure 48). The in-house code for mapping the c-parameter could not be applied to these datasets because particles showing the c\*-axis were overlapped by others in different orientations. This overlap produced additional spots in the diffraction patterns, which were visible in the line profiles and affected the measured distances. Furthermore, as observed in datasets taken at 200 °C, the particles' low crystallinity resulted in poorly defined peaks in the line profiles, rendering them unsuitable for analysis using the in-house mapping code.

At 400 °C, the main phase is identified as ZnO by the SNBD technique. At 650 °C,  $ZnAl_2O_4$  domains arise as a secondary phase.

However, if the particles were pure-phase ZnO at 400 °C, this would imply the disappearance and subsequent reappearance of Al. Therefore, to locate the Al, we conducted STEM-EDX analysis at  $400 \, ^{\circ}$ C and  $650 \, ^{\circ}$ C (Figure 49), which shows that Al is uniformly distributed throughout the particle. Since the diffraction patterns correspond to the ZnO crystal structure, the Al atoms should be present as in a  $Zn_{1-x}Al_xO_y$  solid solution.

At 850 °C, ZnAl<sub>2</sub>O<sub>4</sub> dominates the particle, with only a few domains of Zn<sub>1-x</sub>Al<sub>x</sub>O<sub>y</sub> remaining. At 950 °C, only ZnAl<sub>2</sub>O<sub>4</sub> is observed.

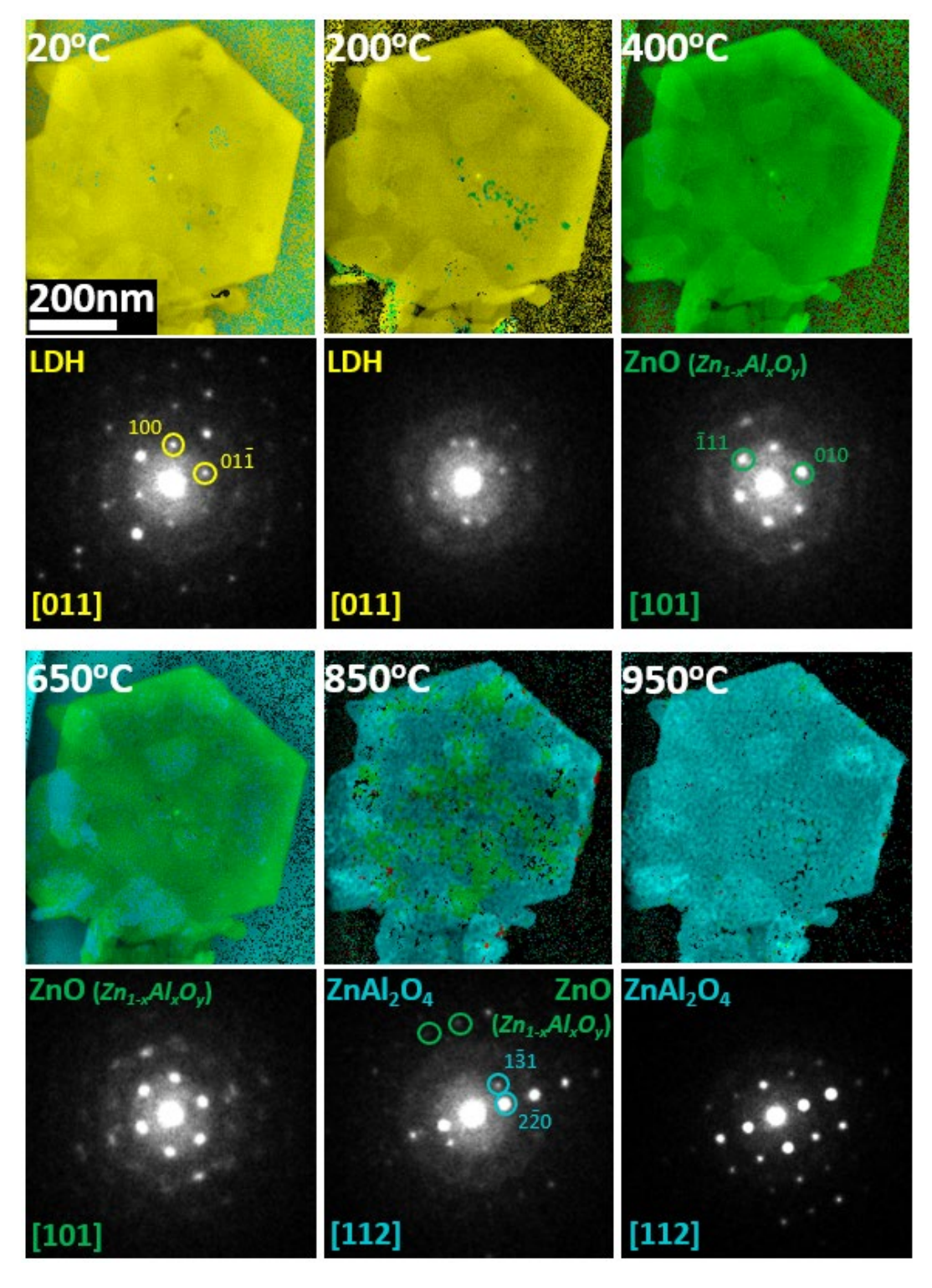


Figure 48. Phase maps based on SNBD data of a particle at the different heating stages. We observe a phase transformation from the LDH structure (yellow) to ZnO (green) to a mixture of ZnO and ZnAl<sub>2</sub>O<sub>4</sub> (light blue) to finally pure ZnAl<sub>2</sub>O<sub>4</sub>. Underneath each phase map, a diffraction pattern of each time the same manually selected 5 nm area within the SNBD during the heating curve, along with manual indexations of the patterns and zone identifications.

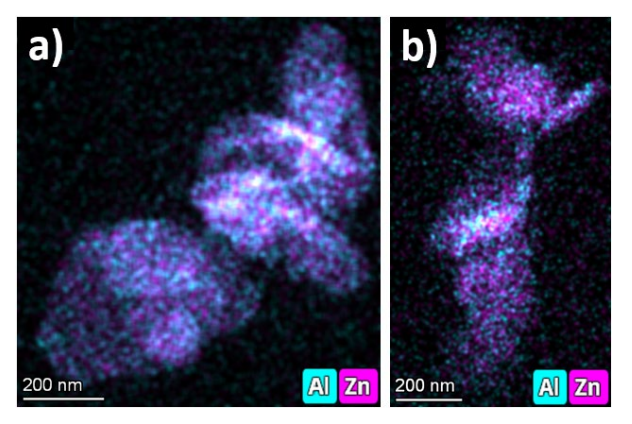


Figure 49. STEM-EDX maps in net counts showing the homogeneous Zn and Al content of particles at (a) 400 and (b) 650 °C.

After the full heating curve in air, STEM-EDX (Figure 50a) shows a homogeneous distribution of Zn, Al, and O over the particles, in agreement with the phase maps showing only a single phase. Standard NMF analysis was unable to separate the Si<sub>3</sub>N<sub>4</sub> signal from the cell windows and the particle signal due to the low number of counts and the high fluorescence of the Zn signal compared to that of Si. Therefore, we employed PCA combined with blind source separation (BSS) using independent component analysis to identify the components in the dataset (Figure 50b and Table 2). This analysis exhibited only a single component, agreeing with ZnAl<sub>2</sub>O<sub>4</sub>, within the particles (Figure 48).

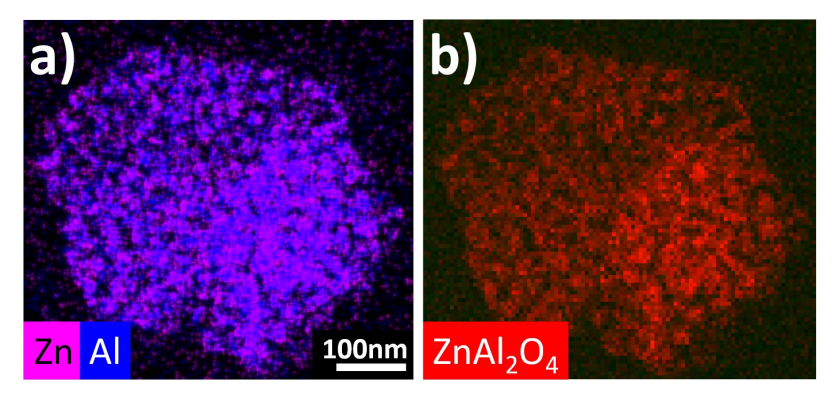


Figure 50. a): STEM-EDX elemental map showing the Zn and Al content. The map is given in counts. b): Component map produced by the BSS analysis. The  $Si_3N_4$  background is not shown as a separate component.

Table 2. BSS results showing the quantified composition of the two found phases for the thermal decomposition in atmospheric conditions. Negative values for some elements result from a combination of noise and fluorescence. The values are given in atomic percent.

	Al	С	Cu	N	O	Si	Zn
Comp1	33.9	2.1	2.4	1.8	44.8	3.3	11.7
$(ZnAl_2O_4)$							
Comp2	-0.3	4.7	0.2	46.8	5.9	42.7	0.0
$(Si_3N_4)$							

### 3.4.CO<sub>2</sub> study of ZnAl LDH

In our next study on LDHs, we investigated the effect of CO<sub>2</sub> absorption and activation on an LDH material using *in situ* TEM. LDH materials are known electrocatalysts for CO<sub>2</sub>RR <sup>37,52–54,62</sup>. We therefore conducted *in situ* TEM studies to investigate their behavior under CO<sub>2</sub> conditions. To our knowledge, no such studies have previously been reported. Both the CO<sub>2</sub> absorption process at the atomic level and the activation process of LDH materials remain unexplored. Similar to the MOF activation process that will be described in Chapter 3.1.1, LDH materials also require activation by heating under vacuum to enable effective gas absorption. This involves clearing the interlamellar spaces of water and carbonate ions (CO<sub>3</sub><sup>2-</sup>) to create active sites for CO<sub>2</sub> binding.

For these experiments, we selected ZnAl (2:1 cation ratio) LDH due to its promising performance in earlier studies, which showed it had the highest potential for CO<sub>2</sub>RR among the LDH materials tested.

Given the challenges associated with 3D ED, as discussed earlier, we used SNBD to investigate the structure of the LDH material based on diffraction data. To examine the influence of (reduced) external pressure on the basal spacing, a SNBD scan was taken while the nanoreactor of the *in situ* holder was pumped to vacuum ( $\sim 1.5 \times 10^{-5}$  mbar). While this pressure is not as low as the UHV conditions of a TEM ( $10^{-6}$  to  $10^{-7}$  mbar), it closely mimics the typical conditions under which LDH materials are studied in TEM.

Next, we studied the activation of the LDH by heating it to 80 °C for 2 hours and 30 minutes under vacuum, after which the sample was cooled down to room temperature again and a second SNBD scan in vacuum conditions was taken. This temperature was maintained throughout the remainder of the experiment, meaning all SNBD scans were conducted at room temperature.

This ensures a consistent basis for comparing all measured basal spacings. Our collaborators from Hokkaido University observed that activating the LDH material above 100 °C leads to structural modifications, therefore we limited the activation temperature to 80 °C. To investigate the effect of ambient pressure on the LDH basal spacing, a third scan was taken while exposing the particles to 1 atm of Ar gas at a flow rate of 1 ml/min for 1 hour.

The holder valves were then closed to maintain a static Ar pressure of 1 atm for 45 minutes, after which another SNBD scan was performed at room temperature.

Finally, to examine the impact of CO<sub>2</sub> absorption on the LDH crystal structure, Ar was replaced with CO<sub>2</sub> at room temperature by subjecting the particles to a continuous flow of CO<sub>2</sub> at 1 atm and 1 ml/min for 1 hour and 30 minutes.

The holder valves were subsequently closed to maintain a static pressure of 1 atm of CO<sub>2</sub> for 30 minutes, at which point a final SNBD scan was performed, at room temperature. Figure 51 shows a schematic illustration of the workflow of this experiment.

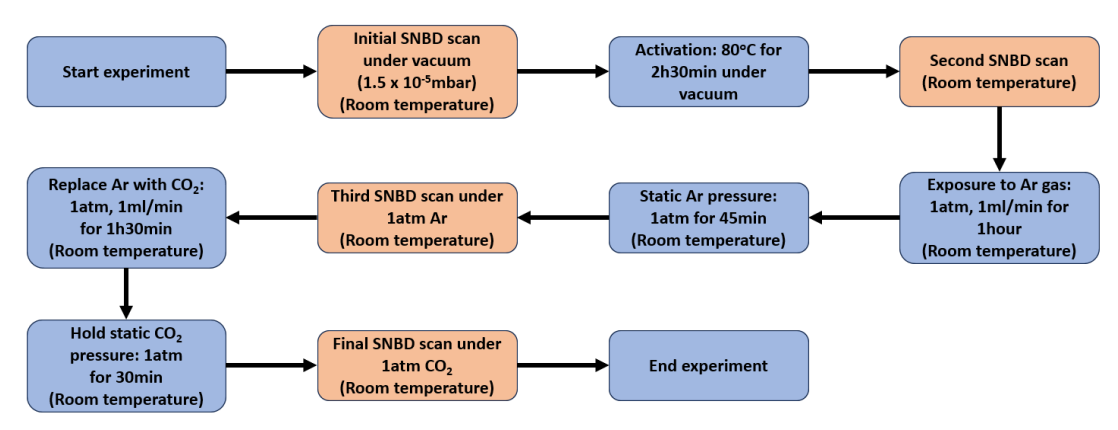


Figure 51. Schematic illustration of the workflow of the in situ CO<sub>2</sub> ZnAl LDH experiment.

As shown in the virtual dark-field images based on SNBD scans in Figure 52, no significant morphological changes are observed in the particles when they are activated, exposed to 1 atm of Ar, or 1 atm of CO<sub>2</sub>. The variations in contrast are a result of how the virtual image is generated from the diffraction patterns.

Since these are virtual dark field images, the contrast is determined by the number and amplitude of reflections present in each pattern, with brighter areas corresponding to a higher total amplitude. Any changes in contrast can be caused by slight particle movement or tilting, which affects the number of recorded reflections. As a result, the contrast variations in these images do not necessarily indicate actual structural changes in the material.

Basal spacing could only be determined for LDH particles oriented with the c\* axis visible in the diffraction pattern. Figure 53 shows a representative diffraction pattern taken from a scan position within the area indicated in green in Figure 52, with the line of reflections corresponding to the c\* axis being marked. A line profile across this line, targeting the main reflections, allows for the investigation of the basal spacing. By fitting Gaussian curves to the intensity of each diffraction spot, the distances between their maxima can be related to the basal spacing at that specific scan position. This fitting was performed manually using the program Fityk <sup>63</sup> to ensure the most accurate results. To ensure the highest accuracy possible for this basal spacing determination, the in-house written Python code was not used here.

This process was repeated for 15 scan points within the green area of Figure 52, and the individual basal spacings were averaged. After activation in vacuum, a slight decrease in basal spacing was observed, from  $c_0 = 7.80(2)$  Å to  $c_0 = 7.76(2)$  Å. While this change is minimal and falls within the error margins, comparison with further changes in basal spacings suggest an effectively occurring systematic change.

This decrease could occur due to the removal of water and carbonate molecules from the interlayer spacing. Upon exposure to 1 atm of Ar gas, the basal spacing increased slightly to  $c_0 = 7.82(2)$  Å.

This expansion may be due to Ar molecules entering the interlayer space and exerting outward pressure, as noble gases do not compress.

When the material was subsequently exposed to 1 atm of  $CO_2$ , the basal spacing increased further to  $c_0 = 7.84(2)$  Å. This additional expansion could be attributed to the larger  $CO_2$  molecules pushing the LDH layers further apart, leading to a slight increase in basal spacing of 0.08(3) Å versus the freshly activated compound. However, at these pressures, the individual  $CO_2$  molecules may also experience repulsive intermolecular forces within the confined space between the LDH layers.

Given that the kinetic diameter of a CO<sub>2</sub> molecule (its effective size during gas-phase collisions) is approximately 3.3 Å <sup>64</sup>, and the interlayer space is only around 4 Å, CO<sub>2</sub> molecules are likely to be in close proximity, potentially leading to intermolecular repulsion.

This slight expansion of the basal spacing has not been observed before. However, CO<sub>2</sub> sorption in LDHs has been described by Reddy *et al.*<sup>65</sup> for calcined MgAl LDH, where it was studied using XRD, FTIR spectroscopy, and thermogravimetric analysis at 200 °C.

In that study, no increase in basal spacing was reported, likely because the experiments were conducted at elevated temperatures of 200, 400, and 600 °C, whereas, in our case, the basal spacings were all measured at room temperature. At the temperatures used in the study by Reddy *et al.*, we have shown in Chapter 2.1 that the LDH structure undergoes calcination and transforms into other phases, eliminating any clearly observable basal spacing.

If we consider these changes in basal spacing, we can also investigate whether similar variations are reflected in the overall particle size in the virtual dark field images shown in Figure 52. Despite the limited resolution of these images, the particle thickness was measured by taking a wide line profile perpendicular to the particles along the c-axis, and then measuring the width of the plateau visible in the line profile, allowing us to assess potential morphological changes in this direction. The direction of the line profile measurement is illustrated in Figure 52. For the thickness of the particles indicated by the red arrows, we observe a change from approximately 560(10) nm in vacuum to 550(10) nm after activation, increasing to 565(10) nm when exposed to 1 atm of Ar gas, and further expanding to 570(10) nm upon CO<sub>2</sub> absorption. Similarly, for the particles marked by the blue arrows in Figure 52, the thickness changed from 570(10) nm to 565(10) nm after activation, increasing to 575(10) nm under 1 atm of Ar and reaching 580(10) nm after CO<sub>2</sub> absorption. Whereas consecutive changes are within measuring errors, the variation over the whole sequence surpasses the error intervals and the various steps are consistent between the different measurements. This change in particle size was observed exclusively in the c-direction and not in the ab-plane of the particles. The only structural parameter affected is therefore the basal spacing.

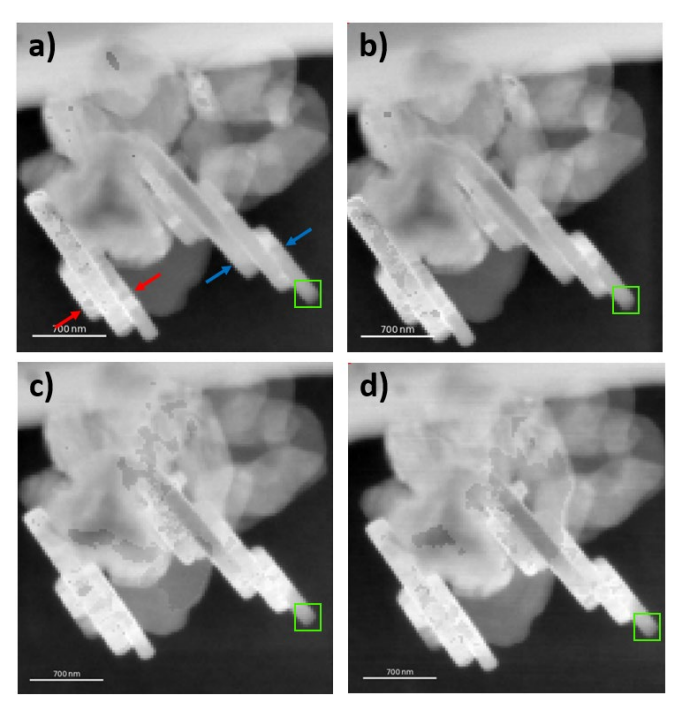


Figure 52. Virtual dark field images based on SNBD scans a) in vacuum, b) after activation in vacuum, c) after exposure to 1 atm of Ar gas and d) after exposure to 1 atm of  $CO_2$  gas. The area used for the basal spacing measurements is indicated by the green box. Particles used for thickness calculations are indicated by the arrows.

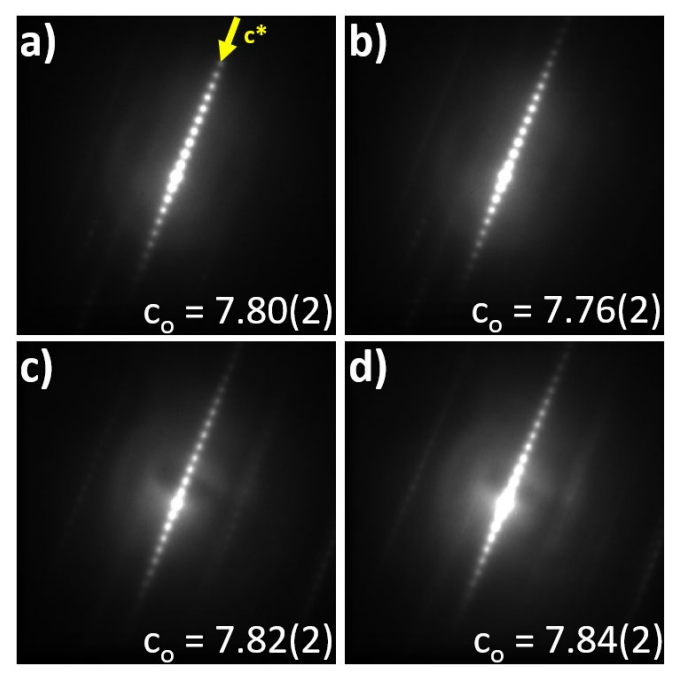


Figure 53. Representative diffraction patterns from the areas of the same particle, indicated in Figure 52. a) in vacuum, b) after activation in vacuum, c) after exposure to 1 atm of Ar gas and d) after exposure to 1 atm of CO<sub>2</sub> gas. The average basal spacing from 15 measurements is provided for each diffraction pattern. The reflections used for the basal spacing calculations are indicated by the yellow arrow.

Unfortunately, due to the challenges associated with this material for 3D ED, as described earlier in this chapter, no further structural information could be obtained regarding the effect of CO<sub>2</sub> absorption. Additionally, since the material is beam-sensitive and must remain undamaged throughout the experiment, beam-intensive techniques such as STEM-EDX or EELS could not be used to gather elemental information at different stages of the experiment.

# **Conclusion to Chapter 3**

In this chapter, the structural characteristics, morphology, and composition of LDH materials were investigated in detail, with a focus on their potential as catalysts for CO<sub>2</sub> reduction reactions. Various synthesis conditions, aging processes, and grinding treatments were explored, revealing their significant influence on nanoscale particle size, basal spacing, and crystallinity. Our TEM findings highlighted how tuning parameters such as cation ratios, aging conditions, and grinding times can enhance material properties. In particular, controlled grinding increases the contact surface area and accessibility of active sites, improving catalytic performance. Furthermore, changing the cations while keeping the synthesis procedure constant resulted in different particle morphologies: Zn and Al led to the formation of single-crystal particles, whereas Ni and Fe, as well as Ni and Al, produced agglomerates of smaller particles. In addition, the choice of cations affects the basal spacing of the LDH materials, with ZnAl (2:1 ratio) exhibiting the largest basal spacing, measured at 8.0(1.2) Å. These results underscore the adaptability of LDH materials and the importance of tailoring their structural and morphological properties for optimal CO<sub>2</sub> reduction applications.

Next, the thermal evolution of ZnAl LDH was examined by heating the material *in situ* under both vacuum and air. Heating the LDH particles in air resulted in a phase transition via Zn<sub>1-x</sub>Al<sub>x</sub>O<sub>y</sub> and Zn<sub>1-x</sub>Al<sub>x</sub>O<sub>y</sub>/ZnAl<sub>2</sub>O<sub>4</sub> into ZnAl<sub>2</sub>O<sub>4</sub>, whereas heating under vacuum led via ZnAl<sub>2</sub>O<sub>4</sub> and ZnAl<sub>2</sub>O<sub>4</sub>/Al<sub>2</sub>O<sub>3</sub> to the formation of ZnO particles within an Al<sub>2</sub>O<sub>3</sub> matrix. The different outcomes under varying atmospheres demonstrate the need to study structural evolution under conditions that reflect real-world applications. Simulating practical environments is an important factor in accurately understanding material behavior and optimizing performance.

Understanding the precise structural evolution of ZnAl LDH during heating is essential for optimizing catalytic and thermal performance, as each phase (whether ZnAl<sub>2</sub>O<sub>4</sub>, Al-doped ZnO, or ZnO in an Al<sub>2</sub>O<sub>3</sub> matrix) has distinct electronic, catalytic, and thermal properties that directly influence material stability, reactivity, and durability. Assuming an incorrect phase transition pathway may lead to the design of materials with unintended phases, resulting in reduced efficiency, faster degradation, or suboptimal performance. Although all these phases are documented in the literature and the known Zn-Al-O phase diagram, the observed microstructure and unique morphologies represent novel findings. These can only be accurately characterized by leveraging the full capabilities of TEM.

Mapping these transformations under different atmospheres enables the development of tailored thermal treatments to reliably achieve the desired phases and improve performance in real-world conditions.

Finally, this chapter presents the *in situ* TEM investigation of LDH materials under CO<sub>2</sub> at room temperature. By using SNBD, subtle differences in interlayer spacing are observed that would otherwise remain undetected in conventional UHV TEM studies. The results show a contraction of the basal spacing after activation in vacuum, followed by a gradual expansion upon exposure to Ar and CO<sub>2</sub> at 1 atm. This expansion is likely caused by the molecular size of CO<sub>2</sub> and possible intermolecular repulsion between the CO<sub>2</sub> molecules within the confined interlayer space. Small but consistent changes in particle thickness along the c-axis further support this structural expansion during gas absorption. Unlike earlier studies conducted at elevated temperatures, where calcination leads to phase transformation, these findings emphasize the importance of studying LDHs under realistic conditions. While the results provide extra information on CO<sub>2</sub>-induced structural changes in LDHs, further research is needed to assess their long-term stability and dynamic behavior under operating conditions.

Other LDH materials, including ZnGa, ZnCr, and FeCo LDHs, were also investigated during this PhD using TEM and STEM-EDX analysis. Additionally, for ZnAl LDH, the influence of various *ex situ* experiments, such as heating to form layered double oxide, reconstructing layered double oxide back to layered double hydroxide, and analyzing samples before and after CO<sub>2</sub>RR, were studied using TEM and STEM-EDX. However, to maintain a focus for this thesis, these measurements have not been included in this work.

# **Chapter 4: Metal organic frameworks**

This chapter aims to explore the structural characterization of metal—organic frameworks (MOFs) using 3D ED. It outlines optimized acquisition strategies for 3D ED of MOFs, highlights the importance of detector selection, and discusses *in situ* studies of MOF activation and gas interaction, with a special focus on the well-known MOF-74. It also examines MOF modifications, such as the development of enzyme—MOF biohybrids, and the structure solution of newly synthesized MOFs such as UA-4. This chapter will demonstrate how electron diffraction can be used to gain insights into MOF behavior at the nanoscale, especially under realistic or application-relevant conditions.

## 4.1. Introduction to Metal Organic Frameworks

MOFs are a class of materials in reticular chemistry that have gained significant attention over the past couple of years <sup>66,67</sup>. MOFs consist of secondary building units (SBUs) that include metal nodes and organic linkers. These nodes and linkers come in different shapes and sizes, as shown in Figure 54 and Figure 55.

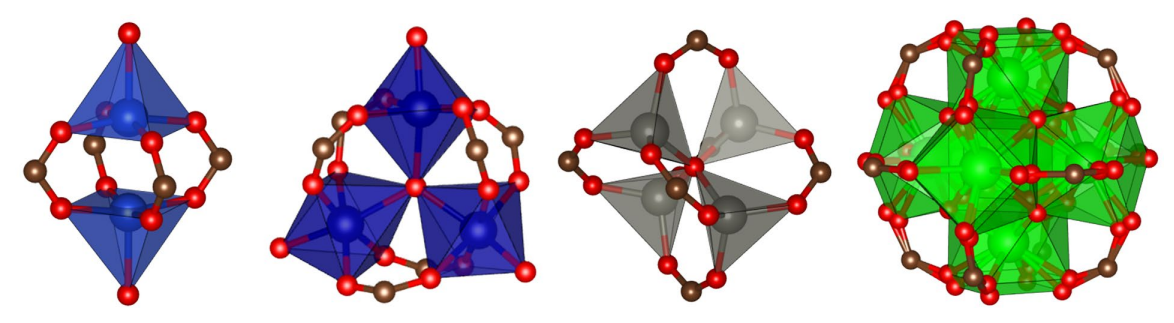


Figure 54. Common metal nodes. From left to right: paddlewheel  $(Cu_2(-CO_2)_4)$ , planar trigonal  $([Cu_3O(-CO_2)_6(H_2O)_3]^+)$ , tetrahedron  $(Zn_4O(-CO_2)_6)$  and octahedron  $(Zr_6O_4(OH)_4(-CO_2)_{12})$  Red spheres represent O and brown spheres C. The spheres in other colors represent metal atoms.

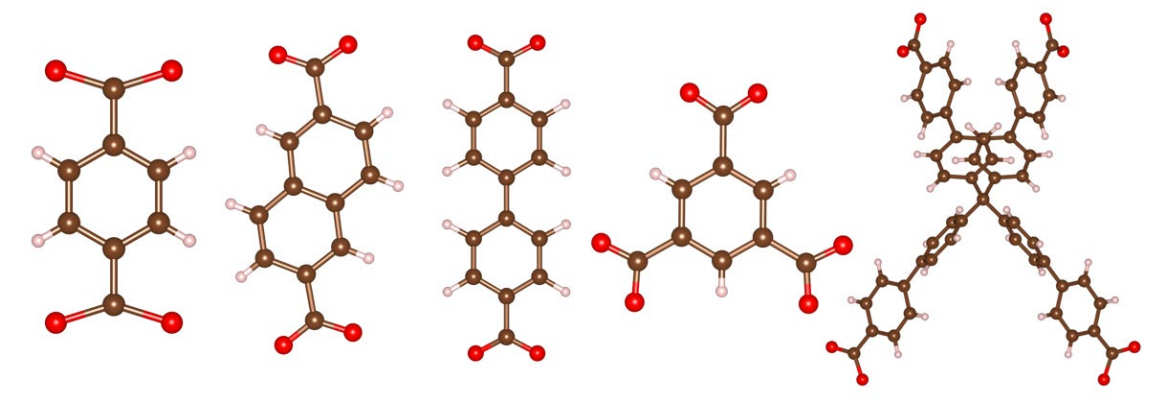


Figure 55. Examples of organic linkers. From left to right: 2,5-dihydroxyterephthalic acid (H<sub>4</sub>dhtp), naphthalene dicarboxylate (NDC), 4,4'-biphenyldicarboxylate (BPDC), benzene-1,3,5-tricarboxylate (BTC) and an extended tetratopic linker based on Tetrakis(4-bromophenyl) ethylene (see Chapter 3.3). Red spheres represent O, pink spheres H and brown spheres C.

The linkers are combined through wet synthesis, allowing control over the resulting structures. This flexibility enables the substitution of different metals into similar node morphologies and the combination of various linkers and nodes, creating a vast range of structures. For example, the same MOF node can be used with different linkers containing additional benzene rings, yielding MOFs with the same topology but larger pores, as shown in Figure 56. Such a series of MOFs is referred to as an isoreticular series.

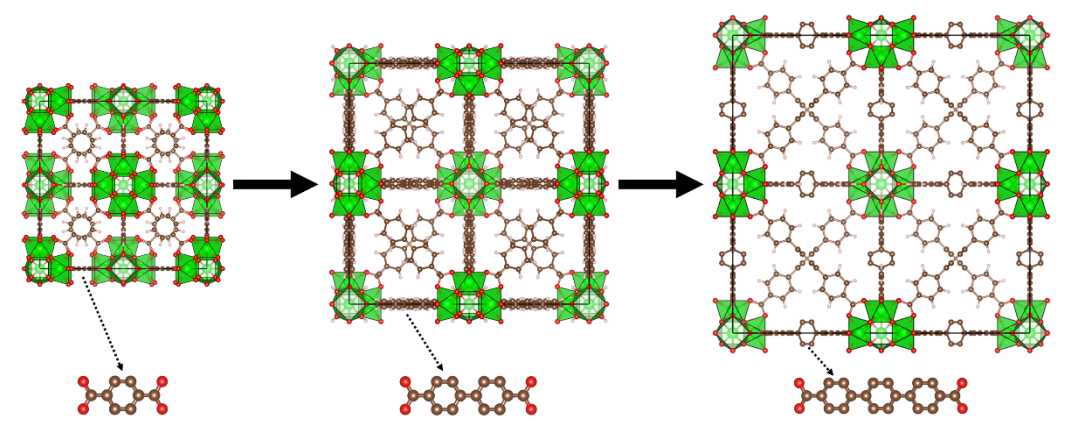


Figure 56. An example of isostructural MOFs: UiO-66, UiO-67, UiO-68 with their respective linkers (H<sub>4</sub>dhtp, BPDC and TPDC). Red spheres represent O, pink spheres H and brown spheres C. Zr atoms are represented by green spheres.

New synthesis methods and novel node and linker morphologies are constantly being developed, resulting in over 100,000 reported MOF structures and more than 500,000 theoretically predicted ones <sup>68</sup>. MOFs are particularly known for their large pore sizes and significant internal surface areas. This structural diversity and flexibility make MOFs suitable for a wide array of applications, ranging from gas storage and separation to catalysis and encapsulation.

For instance, MOF-74 is widely studied for CO<sub>2</sub> capture and separation <sup>69–75</sup>, HKUST-1 is used for methane storage <sup>76,77</sup>, and ZIF-8 is popular for gas separation due to its remarkable chemical stability <sup>78–80</sup>

A unique advantage of MOFs is their potential for post-synthetic modifications <sup>81–83</sup>. This approach allows researchers to tailor the properties of an already-synthesized MOF by adding functional groups, introducing defects, or exchanging metal ions. For instance, amine groups can be introduced post-synthetically to improve gas adsorption <sup>84</sup>, while metal exchange within the nodes can enhance catalytic activity <sup>85</sup>. The ability to engineer defects, such as missing linkers, nodes, or clusters, further extends the versatility of MOFs, as these defects can be beneficial for specific applications, such as enhancing catalytic performance by exposing more active sites <sup>86</sup>.

The sustainability potential of MOFs is especially noteworthy. Their ability to be tailored for specific applications makes them invaluable in addressing global challenges, such as carbon capture and storage, green catalysis, and water purification. MOFs can be functionalized to improve their performance for these purposes.

For example, functional groups such as amines can be grafted onto MOF linkers to enhance CO<sub>2</sub> adsorption capacity <sup>87,88</sup>, making MOFs potentially an important material in reducing greenhouse gas emissions and supporting a greener future.

On the other hand, MOFs are notoriously electron beam-sensitive and, because of this, are often considered to be among the most challenging materials to study using a TEM <sup>89,90</sup>. Several damage mechanisms are responsible for this sensitivity, primarily radiolysis and knock-on damage. Radiolysis occurs when the electron beam ionizes atoms in the MOF structure, breaking bonds and causing structural degradation, while knock-on damage results from the direct displacement of atoms by the beam. Radiolysis tends to dominate at lower acceleration voltages, while knock-on damage becomes more significant at higher voltages. A recent electron diffraction study has shown that the O–C bond between the node and linker is often the first to break under electron irradiation <sup>91</sup>.

A common strategy to mitigate beam sensitivity is the use of cryogenic conditions during TEM imaging. By lowering the temperature, the mobility of radicals produced by radiolysis is reduced, slowing the rate of structural damage and allowing researchers to acquire higher-quality data.

Despite these challenges, numerous TEM studies of MOFs have been reported, focusing on both imaging and (three-dimensional) electron diffraction. Imaging techniques such as low-dose HRTEM <sup>92,93</sup>, low-dose HAADF-STEM <sup>94</sup>, iDPC <sup>95,96</sup>, or iCOM <sup>97</sup> have proven effective, while faster, automated acquisition methods like fast-ADT <sup>98</sup>, cRED <sup>99,100</sup> (both 3D ED methods) or serialED <sup>101</sup> are increasingly used to solve MOF structures. These advances continue to expand our understanding of MOFs and their applications, paving the way for further innovation in the field.

### 4.2.MOF-74

MOF-74 is one of the most extensively studied MOFs worldwide, with potential applications in gas absorption and catalysis, gas separation and storage, drug delivery, gas sensing and detection  $^{102-106}$ . MOF-74 has a well-known structure, consisting of organic H<sub>4</sub>dhtp (2,5-dihydroxyterephthalic acid) linkers and divalent transition metal centers (nodes). Combining these two building blocks results in a 5-c **bnn** net topology (see Figure 57) and gives rise to one-dimensional edge-shared transition metal-based octahedra further connected through the organic linkers to form a three-dimensional framework with large one-dimensional channels aligned along the [001] crystallographic direction. The space group of MOF-74 is  $R\bar{3}$  (trigonal) with unit cell parameters a = 26.18 Å and c = 6.65 Å.

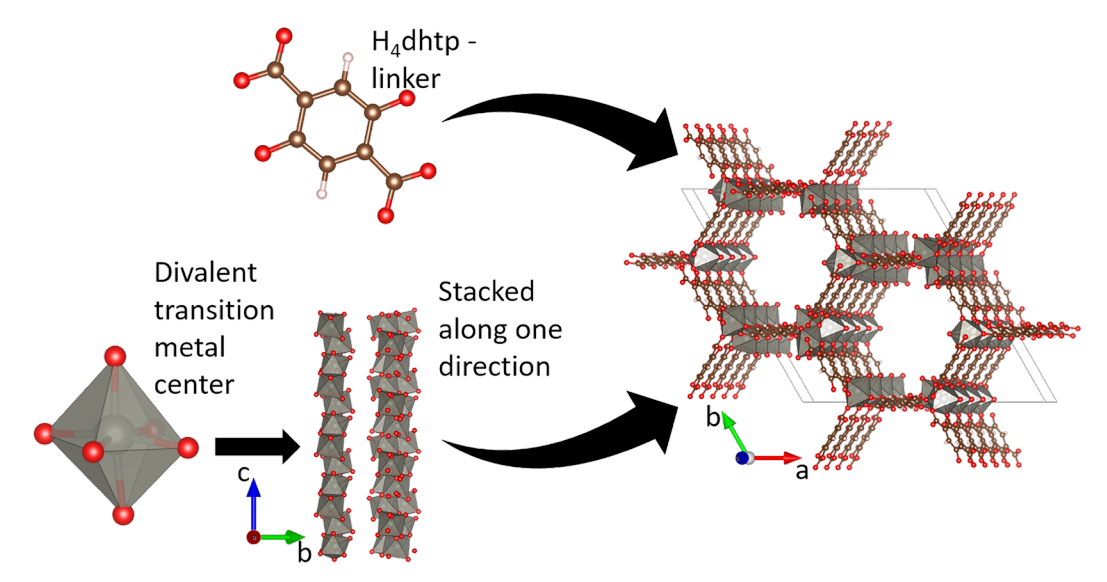


Figure 57. SBUs of the MOF-74 structure. Red atoms represent O, brown ones C, and gray ones divalent transition metal atoms <sup>23</sup>.

#### 4.2.1. Optimizing 3D ED acquisition parameters for MOF-74

Since the targeted *in situ* experiments cannot be combined with cryogenic conditions, it is first necessary to determine whether a valid 3D ED dataset of MOF-74 can be acquired at room temperature. For this investigation, we used Zn-MOF-74, synthesized according to the protocol described in <sup>107</sup>.

A systematic study was first performed to establish "safe" acquisition parameters that would minimize beam damage as much as possible and obtain optimal data. Electron beam damage can be mitigated by either increasing the speed of data acquisition or reducing the dose rate. Standard stepwise data acquisition is unsuitable, as it is often too slow and results in structural damage during the acquisition.

Given that the acquisition speed of cRED is dictated by the combined speeds of the camera and the goniometer of the TEM, this method is particularly suited for studying beam-sensitive materials. Since radiolysis is the dominating beam damage for MOFs <sup>91</sup>, a high acceleration voltage (200kV or 300kV) is preferred for 3D ED experiments on these materials.

The requirement for rapid, low-dose data acquisition imposed restrictions on the choice of suitable cameras/detectors.

Conventional frame-based charge-coupled device (CCD) cameras work by placing a scintillator atop the detector to convert incoming electrons into photons. Once photons are generated, they interact with the silicon pixels by creating electron-hole pairs. After the free charge carriers are generated, they accumulate in each pixel during an integration period. These charges are then transferred sequentially to a readout register, where they are amplified and digitized.

The serial readout process limits the speed of these detectors. The long readout times of these detectors can cause large missing wedges after every acquired frame in the data series. They also have an insufficient signal-to-noise ratio at these low doses. Figure 58a shows a diffraction pattern of MOF-74 taken on a CCD. As we can see here, the readout noise, visible as horizontal streaks on the pattern, is quite pronounced and has almost the same intensity as the reflections. Instead, direct electron detectors (DEDs) are necessary for optimal results. DEDs do not convert incoming fast electrons into photons or an electron cloud. Instead, they directly deposit the electron's energy into the detection layer. This method of detection offers several advantages. Not only is the S/N ratio of these detectors superior to CCDs, the readout is also much faster. Several DEDs were tested for their suitability.

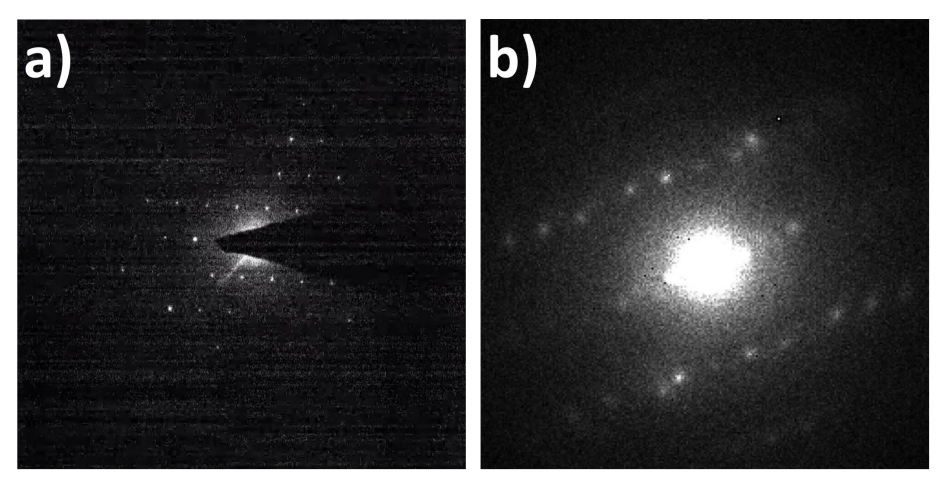


Figure 58. Comparison of diffraction patterns taken during a 3D ED series of MOF-74 using a) a standard CCD camera and b) the Merlin DED.

The first detector tested was the QuantumDetectors Merlin camera, a frame-based detector with a thick silicon detection layer, rendering it beam-hard and suitable for withstanding the direct beam without damage.

It is capable of operating in 24-bit mode, resulting in a large potential dynamic range. Its fast readout time, especially in 12-bit mode (440  $\mu$ s), makes it theoretically suitable for cRED. However, the small physical size of the camera (256  $\times$  256 pixels, each with a pixel size of 55  $\mu$ m) creates limitations when analyzing materials with large unit cell parameters.

To ensure adequate separation of reflections, a longer camera length must be used, causing high-resolution reflections to fall outside the detector's range, as demonstrated in Figure 58b. Consequently, datasets obtained with this camera were suboptimal for complex materials like MOFs. The Gatan K2 DED, with its large size and  $4k \times 4k$  resolution, was also evaluated. However, its thin silicon detection layer makes the camera highly sensitive and prone to damage. To mitigate this, a beamstopper was required to block the central beam, as shown in Figure 59a, which displays a diffraction pattern of MOF-74 taken using a CCD positioned next to the K2 camera.

Unfortunately, the placement of the K2 detector behind the Gatan imaging filter (GIF) introduced an additional magnification factor for the beamstopper, resulting in significant portions of the diffraction pattern being blocked. To address this, I designed a new beamstopper that was then fabricated using micro-laser cutting. The design of this new beamstopper is schematically shown in Figure 59b. This new design was placed closer to the GIF, at the entrance aperture, minimizing the magnification factor and reducing obstruction of the diffraction pattern, as shown in Figure 59c.

Despite these improvements, the required low dose rate made the camera susceptible to Poisson noise, leading to distorted reflection shapes, as shown in Figure 61a. The resulting data had very low peak intensities (< 20 counts), which were insufficient for reliable structure solutions.

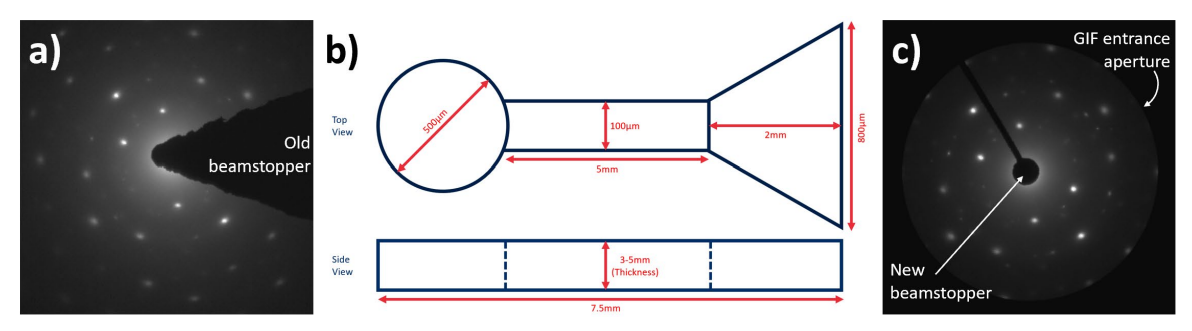


Figure 59.Diffraction patterns taken on a CCD positioned next to the K2 camera and beamstopper design used during a 3D ED series of MOF-74: a) diffraction pattern acquired using the old beamstopper, b) schematic design of the new beamstopper, and c) diffraction pattern acquired using the new beamstopper. In a) and c), the beamstoppers are indicated, and in c), the GIF entrance aperture is also marked.

To improve overall 3D ED data quality at EMAT, I also designed similar beamstoppers for all other compatible microscopes. They were also fabricated using micro-lasercutting and subsequently installed. Their design is shown in Figure 60.

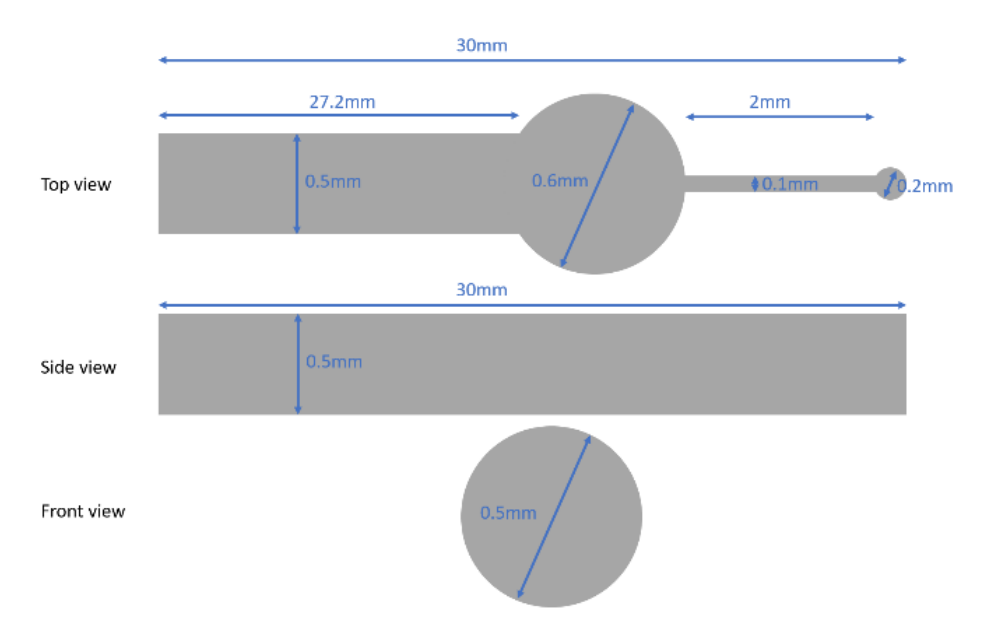


Figure 60. Alternative design of the new beamstopper installed in several compatible microscopes.

The final detector tested was the Amsterdam Scientific CheeTah DED, which proved to be the optimal choice. Unlike frame-based detectors, the CheeTah employs a Timepix chip that records the x- and y-positions, as well as the time of arrival for each electron, with a time resolution of 1.56 ns. This event-based detection ensures an excellent signal-to-noise ratio and high speed. Its physical size  $(512 \times 512 \text{ pixels}, \text{ each with a pixel size of } 55 \,\mu\text{m})$  allows it to record high-resolution reflections at a camera length where reflections remain well-separated, as shown in Figure 61b. This makes the CheeTah camera the best-suited detector available at our research group EMAT for studying the beam-sensitive MOFs.

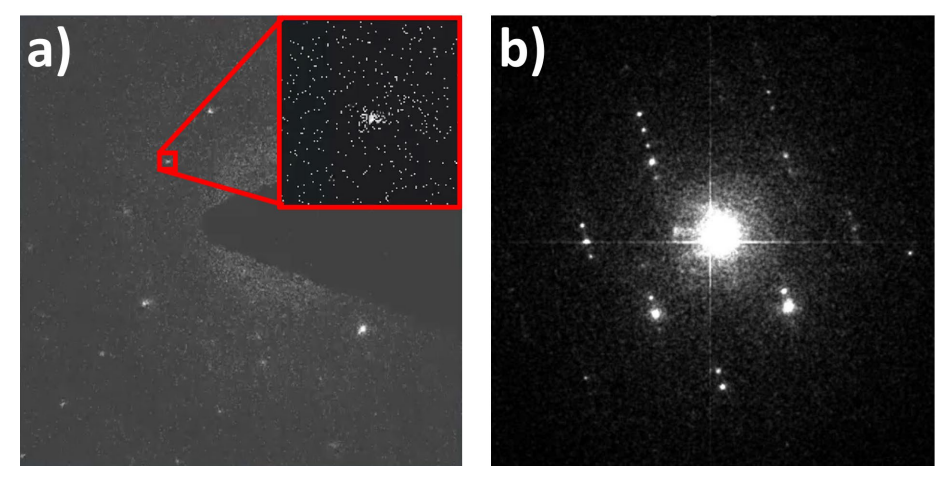


Figure 61.Diffraction patterns of MOF-74 taken during a 3D ED series using a) the K2 DED and b) the CheeTah DED. a) also shows a magnified Bragg reflection to illustrate Poisson noise.

Using the CheeTah camera, cRED data was acquired for Zn-MOF-74 at a speed of 3° per second and 12 frames per second, resulting in an angular step size of 0.26° between frames. For a full 140° tilt range, the acquisition time was approximately 46 seconds. With manual adjustments to the eucentric height, the total irradiation time for the particle was limited to 120 seconds to minimize beam damage. Figure 62 shows a comparison between the known structure from literature 108 and the solved and dynamically refined structure of Zn-MOF-74 based on our cRED data. Table 3 summarizes the acquisition and refinement parameters. Table 11 in the appendix gives all atomic coordinates and anisotropic ADP parameters for our dynamically solved structure. There is a strong agreement between our refined structure and the one previously reported in the literature, which was determined using XRD data collected under cryogenic conditions. The missing features within the pores of our structure correspond to DMF molecules used during the synthesis of the MOF. While these molecules remain immobilized during cryogenic XRD measurements, this is not the case in our room-temperature, UHV experiments. Under ambient conditions, only one DMF molecule remains coordinated to the MOF-74 framework, completing the octahedral geometry of the metal atom of the node, whereas the remaining DMF molecules are mobile and therefore do not contribute to the Bragg intensities. A detailed discussion of this phenomenon is provided in Chapter 4.1.1.

Furthermore, the consistency between our results and the structure reported in the literature demonstrates that reliable acquisition parameters for cRED experiments at room temperature on beam-sensitive MOFs have been successfully established. These optimized conditions are essential for the studies presented throughout the remainder of this thesis.

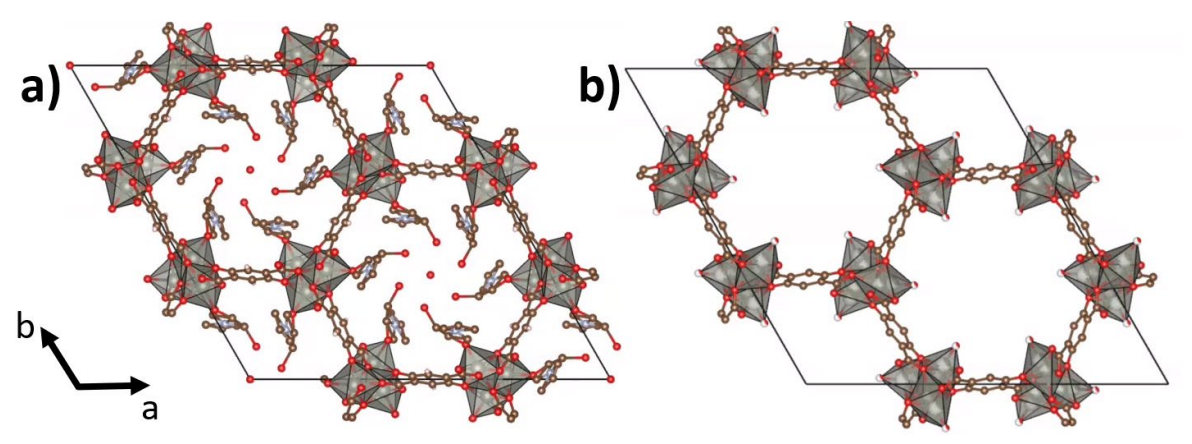


Figure 62. Comparison of the Zn-MOF-74 structure as is known in literature <sup>108</sup> (a) and our 3D ED experiments (b). The missing fragments in the pores when comparing a) to b) are DMF molecules.

Table 3. Comparison between the structural parameters, kinematical refinement results, and dynamical refinement parameters and results for the 3D ED experiment and the structure solution of Zn-MOF-74 from literature <sup>108</sup>, corresponding to the structure shown in Figure 41. The number of used reflections (# refl. used) refers to those included in the dynamical refinement. The maximum resolution (Max res.) value corresponds to the highest resolution achieved in any single frame within the 3D ED dataset.

Zn-MOF-74	Max res. (Å)	$R_{\text{int}} \\$	a (Å)	c (Å)	# refl.	R	wR	R	wR
		(obs)			used	(obs)	(obs)	(all)	(all)
SCXRD	/	/	26.17897	6.65197	1808	7.06	8.43	/	/
			(10)	(5)					
3D ED	0.68	9.99	26.331	6.411	1668	12.64	14.31	14.95	14.44
			(1)	(2)					

#### 4.2.2. Activation of MOF-74

This study has been published: Quintelier, M.; Hajizadeh, A.; Zintler, A.; Gonçalves, B. F.; Fernández de Luis, R.; Esrafili Dizaji, L.; Vande Velde, C. M. L.; Wuttke, S.; Hadermann, J. In situ Study of the Activation Process of MOF-74 Using Three-Dimensional Electron Diffraction. Chemistry of Materials 2024. https://doi.org/10.1021/acs.chemmater.4c01153.

While many TEM studies on MOFs have been conducted, most focus on standard or cryogenic conditions. *In situ* TEM experiments on MOFs are less common. Many of those studies then focusing on heating or synthesis using nanoparticles but these studies lack detailed structural analysis <sup>109–113</sup>. Structural studies using gas- or liquid-phase *in situ* TEM are especially rare, with only one reported so far <sup>114</sup>. Studying MOFs under *in situ* conditions, such as heating, gas exposure, or liquid-phase environments, provides an understanding of their behavior in real-world applications. MOFs are sensitive to external factors like pressure, gas composition, and liquids, which can significantly affect their performance in areas like catalysis, gas storage, and separation. By examining MOFs in conditions similar to their intended use, researchers can better understand their stability and functionality, helping to refine their design for specific applications.

Many MOFs are capable of CO<sub>2</sub> absorption/desorption, but MOF-74 is an excellent candidate in this regard <sup>69–75</sup>. Here, the versatility that MOF-74 has to absorb divalent ions in its structure plays an important role to tune its CO<sub>2</sub> adsorption capacity within the low-pressure regime <sup>115</sup>. Modifying the metal composition in MOF-74 by incorporating elements such as Zn or Cu can enhance the material's CO<sub>2</sub> adsorption efficiency due to the specific interactions between CO<sub>2</sub> molecules and the open metal sites. These tailored interactions not only improve adsorption but also facilitate the catalytic conversion of the adsorbed CO<sub>2</sub> into CO, as the nature of the metal sites plays a crucial role in activating CO<sub>2</sub> for subsequent chemical reactions. This is an important material property considering the significance of CO as a raw material for diverse hydrocarbon-based products <sup>116</sup>.

A critical prerequisite for using MOFs in gas adsorption or guest-interaction studies is their activation, a process necessary to make their pores accessible <sup>117,118</sup>. During synthesis, solvents like N,N-dimethylformamide (DMF), water, ethanol, and unbound linkers often remain bonded to the metal nodes, blocking the pores and preventing guest molecules from entering the framework.

Activation removes these species, creating open metal sites and allowing gases to interact with the MOF. This step is particularly important for MOFs with open metal sites, such as MOF-74, where residual solvents can significantly reduce functionality.

The activation process typically involves a combination of solvent exchange to displace tightly bound synthesis solvents, vacuum treatment to remove volatiles, and heating to fully clear the pores. These steps need to be carefully optimized to avoid damaging the structure, especially in frameworks that are thermally or chemically sensitive. Figure 63 shows a schematic illustration of the activation process of Co-MOF-74.

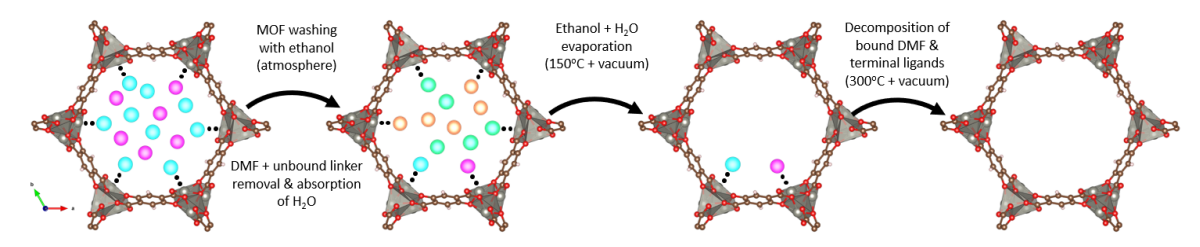


Figure 63. Schematic illustration of the different steps during the activation of Co-MOF-74. Red atoms represent O, brown ones C, grey ones Co, blue ones N, and pink ones H <sup>119</sup>.

So far, the activation of MOF-74 has been studied exclusively using ex situ techniques, primarily PXRD <sup>119–122</sup>. However, PXRD provides a limited perspective when the material consists of nanoscale particles or exhibits significant structural disorder and defects. These limitations are particularly evident in cases where small coherence lengths result in broader PXRD peaks, making data interpretation more challenging due to overlapping peaks and reduced resolution of structural features.

Following a four-day solvent exchange in ethanol, the solution was dropcast onto a heating chip. The *in situ* heating Wildfire (DENSsolutions) holder was used to systematically investigate the activation process of M-MOF-74 (M = Zn, Cu) by using 3D ED. The chip's open design exposes the sample to an ultra-high vacuum within the microscope, which is below  $1.18 \times 10^{-5}$  Pa. This is high vacuum compared to the vacuum typically used for the activation of MOFs in standard conditions (from room pressure to  $10^{-4}$  Pa) but below the vacuum conditions usually employed for activation in some micropore analysis ( $10^{-8}$  Pa)  $^{121,123}$ .

Still, the vacuum applied in the sample holder is high enough to facilitate the removal of the ethanol within the pores. The heating cycle used for both Zn-MOF-74 and Cu-MOF-74 is shown in Figure 64. Both materials were heated overnight at 120 °C, a temperature selected to activate the materials while preserving their structural integrity and aligning with values commonly reported in the literature for this activation step <sup>123,124</sup>. cRED data collection was performed at intervals labeled as 'post', yielding a total of four data series for each particle (20 particles for Zn-MOF-74 and 25 for Cu-MOF-74).

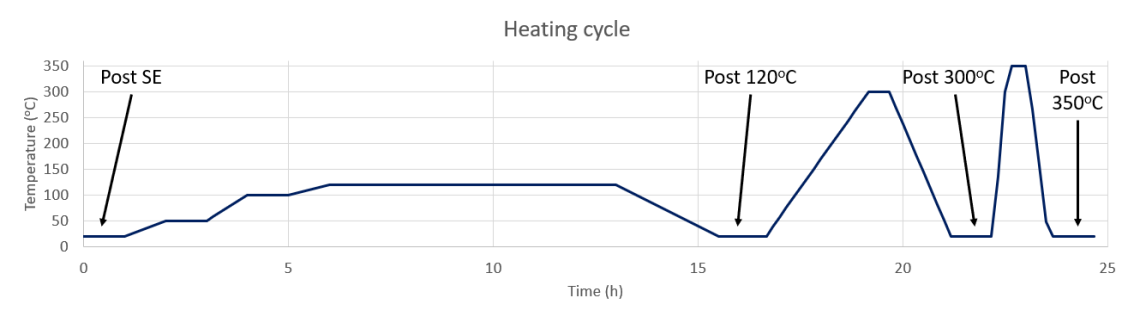


Figure 64. Heating cycle of the experiment. The times where 3D ED series were acquired are indicated. SE stands for solvent exchange.

After the data acquisition, the data were processed using the PETS software, with results summarized in Table 4. Distortion refinements and frame scaling with Laue class  $\bar{3}$  were performed using the hexagonal lattice system. All structure solutions and refinements using Jana and Olex2 are based on our own data, without relying on any pre-existing model.

In Table 4, we observe changes in the cell parameters upon heating, which are attributed to the pliability of the MOF to accommodate changes in the content of the pores. These variations are correlated with the thermal evolution of the cell parameters obtained from thermo-diffraction X-ray experiments performed by collaborators from the Basque Center for Materials (BCMaterials) (Leioa, Basque Country, Spain), with an initial contraction of the framework due to the solvent release, followed by a slight structural thermal expansion, and ending in a fast contraction due to the structural collapse of Zn-MOF-74. Importantly, we observe that the resolution remains the same, and there is only minimal change in R<sub>int</sub>(obs), indicating that the beam damage, if any, is minimal. However, this does not preclude that the beam exposure could generate local defects within the MOF lattice without leading to its structural collapse.

Table 4 displays the R-factors, indicators of the accuracy in structure solution and refinement. These factors, obtained through kinematical refinement using Olex2, are compared with and without incorporating a solvent mask.

The solvent mask, when utilized, enables Olex2 to compute potential solvent-accessible voids while disregarding electron densities or electrostatic potentials within these voids. Table 4 reveals a substantial increase in the R-factor when the solvent mask is not applied.

This difference suggests the persistence of electrostatic potentials within the pores even after completing the entire activation cycle, providing an initial indication of incomplete removal.

While the kinematical refinements in Olex2 indicated the persistence of electrostatic potentials within the pores, JANA2020 lacks an option for utilizing a solvent mask. Consequently, all components within the pores undergo refinement, elevating the R-factors. Table 4 presents the parameters derived from dynamical refinement, alongside the R-factors for the refined structures. The dynamical refinement led to a reduction in the R-factor from 26.03 (R1, Post 350 °C), down to 12.34 (R(obs), Post 350 °C), in comparison to the kinematically refined structures in Olex2 without the use of a solvent mask. Even with residual electrostatic potentials within the pores, R-factors below 15 were achieved through dynamical refinement. Table 11 -Table 15 in the appendix give all atomic coordinates and anisotropic ADP parameters for the dynamically refined structures.

Table 4. Structural parameters for Zn-MOF-74 and Cu-MOF-74. The  $R_{int}$  value for the  $\overline{3}$  Laue class is given. The space group  $R\overline{3}$  was found for every dataset. The data for the non-solvent exchanged (No SE) MOF was taken on a different particle and this structure was solved and kinematically and dynamically refined in Jana. Other structures were solved and kinematically refined in Olex2 and subsequently dynamically refined in Jana. The maximum resolution value corresponds to the highest resolution achieved in any single frame within the 3D ED dataset.

1	Zn-MOF-	-74		Cu-MOF-74			
	No SE*	Post SE	Post 120 °C	Post 300 °C	Post 350 °C	Post SE	Post 120 °C
Max resolution (Å)	0.68	0.75	0.73	0.72	0.75	0.63	0.57
R <sub>int</sub> (obs)	9.99	17.06	18.44	18.92	19.84	14.19	14.45
a (Å)	26.331 (1)	25.4215 (3)	26.7959 (2)	26.805 (8)	25.887 (7)	26.15 (8)	26.248 (7)
c (Å)	6.411 (2)	6.734 (3)	6.630 (7)	6.645 (3)	6.801 (3)	6.32 (3)	6.334 (2)
R1(all) Without solvent mask (Olex2)	n.a.	24.74	26.03	26.30	26.03	n.a.	n.a.
R1(all) With solvent mask (Olex2)	n.a.	12.72	14.96	15.48	14.62	n.a.	n.a.
Number of used reflections (Jana)	1668	1154	1276	1038	1057	454	417
R(obs) Without solvent mask (Jana)	12.64	13.11	14.65	13.59	12.34	13.93	14.49
wR(obs) Without solvent mask (Jana)	14.31	15.24	15.58	14.57	13.48	14.76	15.82
R(all) Without solvent mask (Jana)	14.95	13.92	16.73	14.68	14.07	15.18	15.26
wR(all) Without solvent mask (Jana)	14.44	15.28	15.72	14.61	13.77	14.82	15.84

Figure 65 illustrates a comparison between the as-synthesized MOF structure, resolved through SCXRD under cryogenic conditions, and the solvent-exchanged MOF structure obtained through our 3D ED experiment before the heating cycle. The figure highlights residual electrostatic potentials located in positions closely matching those of DMF within the MOF pores. This comparison is based solely on the positions of the residual electrostatic potentials, as refinement of elemental composition at these sites was not possible for reasons explained below. This observation aligns with expectations from literature that there is still DMF present after the solvent exchange step <sup>123</sup>. Moreover, the figure indicates the presence of additional unidentified electrostatic potentials, shown by the green circles. The effectiveness of 3D ED in discerning nuanced structural variations is underscored by this result. While there appears to be a distinction between the two structures, particularly evident in the octahedral arrangement, this discrepancy arises from the absence of the oxygen atom of the DMF molecule. As the weakest coordination bond in the octahedral coordination sphere around the metal, the DMF is predisposed to partial removal due to the ultra-high vacuum environment of the microscope and the solvent exchange process. Consequently, in Figure 65, it is represented solely as a lingering electrostatic potential, depicted as a red sphere overlapping on the magnified fragment.

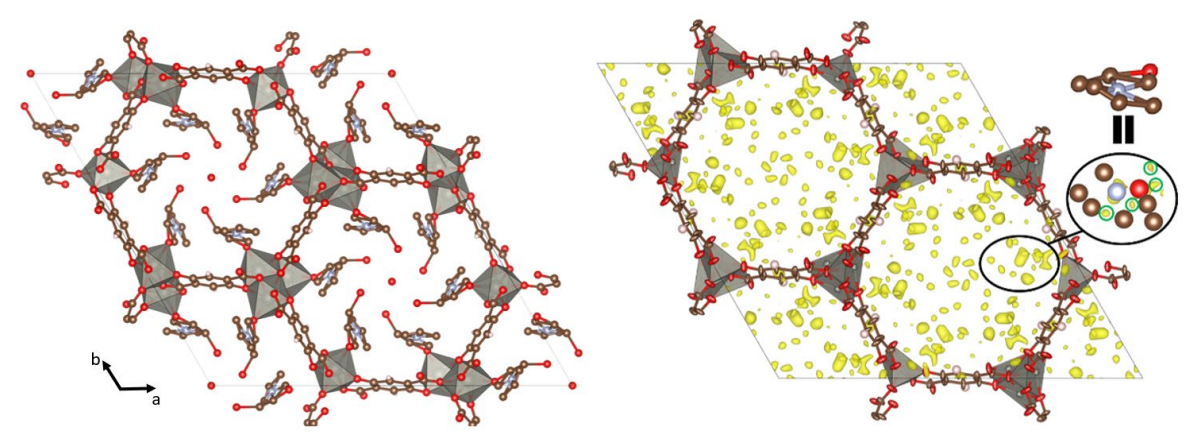


Figure 65. Left: solved structure of as-synthesized Zn-MOF-74, based on SCXRD data taken at cryogenic temperatures. Right: dynamically refined structure of the solvent exchanged MOF, with in yellow the remaining electrostatic potentials (applied lower limit 0.095 eV/ų (2.3σ)) based on the difference Fourier calculation. The positions of the electrostatic potentials in the black oval agree with those of a DMF molecule. The atoms of the refined structure are displayed as their displacement ellipsoids. The green circles around some of the electrostatic potentials indicate unidentified atoms. Red atoms represent O, brown ones C, grey ones Zn, blue ones N and pink ones H

The dynamically refined structures at all stages of the heating cycle are depicted in Figure 66. After heating the sample to 300 °C, open metal sites are visible, since there are no electrostatic potentials left inside the pores within reasonable bond distances from the Zn-atom of the metal node. This indicates the successful activation of the MOF. The MOF retains its crystalline framework even after elevating the temperature to 350 °C.

Importantly, even though it is assumed in literature that the pores are completely empty after heating in vacuum up to  $300\,^{\circ}$ C, the 3D ED data shows the presence of residual electrostatic potentials within the pores.

Adding the ten largest remaining electrostatic potentials from Jana shows a clear decrease at each heating step (Figure 67). This confirms that atoms remain inside the pores after each step, although their amount decreases progressively.

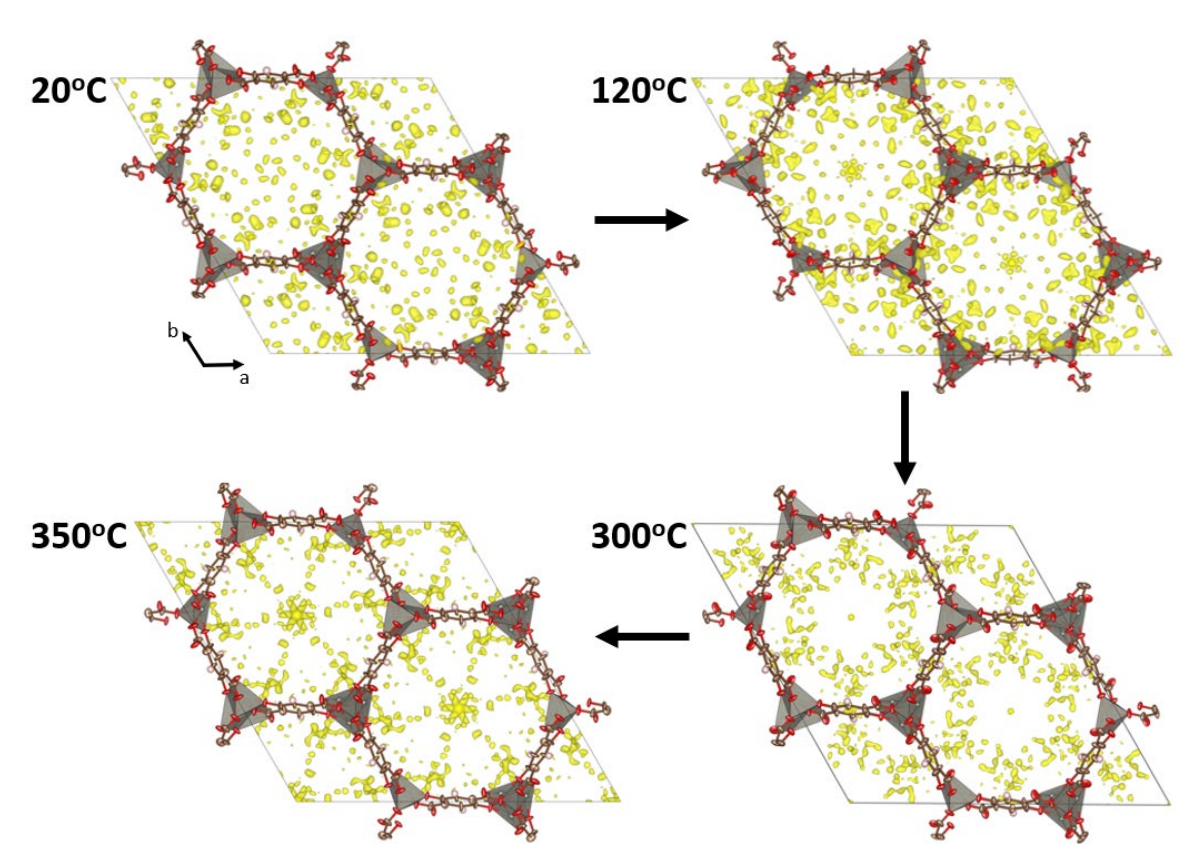


Figure 66. Dynamically refined structures of Zn-MOF-74 at all the heating steps in the heating cycle, showing the remaining electrostatic potentials with values above  $0.095 \text{ eV/Å}^3$  (2.3 $\sigma$ ). The atoms are displayed as their displacement ellipsoids. C-atoms are displayed in brown, O-atoms in red and Zn-atoms in grey. The electrostatic potentials are displayed in yellow.

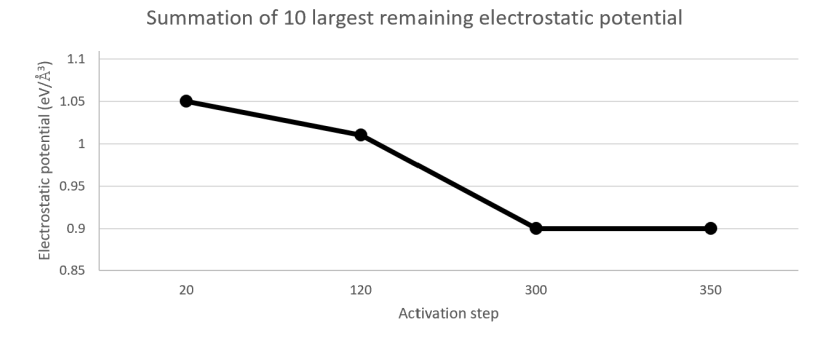


Figure 67. Figure showing the sum of the remaining electrostatic potentials at each heating step.

This difference with literature may be attributed to 3D ED being more sensitive than XRD to small molecules with low occupancies due to the stronger interaction between electrons and atoms, or the higher coherence length requirement in XRD.

As the DMF molecules are only attached through a single coordination bond, they retain rotational freedom inside the pore, therefore reducing the coherence length of the atomic positions of the DMF atoms. Furthermore, the combination of the ultra-high vacuum of the microscope and the solvent exchange causes a low occupancy at these crystallographic positions. The combination of these effects made it impossible for us to refine the elemental composition of the residual electrostatic potentials inside the pores. Unbound linkers, residual ethanol, and general atomic residue are alternative factors, aside from DMF, that can contribute to the presence of these lingering electrostatic potentials. The residual atoms within the pores will likely decrease the efficiency of the gas flow throughout the MOF.

Whereas the SCXRD data for MOFs is normally acquired at cryogenic temperatures, our measurements were conducted at room temperature and elevated temperatures where DMF should be in a 'quasi' liquid form. However, the molecules that can be detected are those that are bonded to the MOF, giving them a more fixed position.

In Figure 68a, the metal octahedron of a dynamically refined structure (see Table 4) from a non-solvent-exchanged Zn-MOF-74 is depicted, with the data acquired at room temperature. The influence of the ultra-high vacuum environment of the microscope is visible, leading to the splitting of the Zn position (from the original position, to two symmetrically independent positions); Zn<sub>1</sub> and Zn<sub>2</sub>.

When the DMF is removed due to the solvent exchange and the placement of the MOF into the ultrahigh vacuum of the microscope, the coordination of the Zn-atom will be reduced by 1. This will shorten all Zn-O bond lengths, therefore creating a different Zn-position ( $Zn_2$ ). The octahedral coordination will then become a pyramidal coordination as shown in Figure 68b. This interpretation is corroborated when refining the occupancies at each position, revealing a close correlation between the occupancies of  $Zn_2$  and  $O_{DMF}$ .

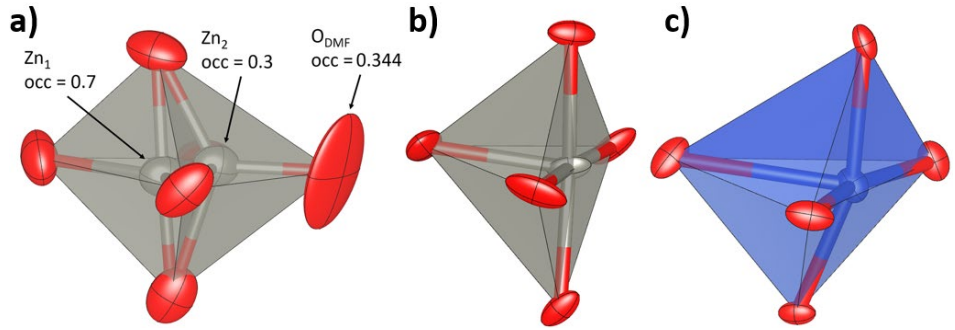


Figure 68. a) Dynamically refined octahedron of a non-solvent exchanged Zn-MOF-74 crystal at room temperature. The refined occupancies of three atomic positions are indicated in the figure, abbreviated by 'occ'. b) & c): Pyramidal structure after heating to 120 °C for the Zn- and Cu-MOF-74 respectively.

Furthermore, we conducted an *in situ* study of the activation procedure for Cu-MOF-74, adhering to the identical heating cycle depicted in Figure 64. Our observations revealed that the sample underwent a transformation to a polycrystalline state after heating it to 300 °C, forming crystalline (as concluded from the observation of Kikuchi lines during the study) nanoparticles, as illustrated in Figure 69. This transition to nanostructured carbon underscores the considerable metal-dependence on the thermal stability of the MOF. Such nanostructured carbons, often made through MOF-mediated synthesis, have potential as electrocatalysts <sup>125</sup>. The thermal dependence of the metal subunits within the MOF-74 family is further corroborated in the thermogravimetric and X-ray thermo-diffraction analyses performed by collaborators from BCMaterials. Based on those measurements, the thermal evolution of the cell parameters for Cu-MOF-74 indicates a sudden collapse of the framework above 130 °C.

To obtain the composition of the particles formed during the activation process (Cu vs CuO), a STEM-EDX experiment was performed using NMF and neural networks using the Python packages Hyperspy and Pyxem to process the data, following the methodology outlined in <sup>61</sup>.

This quantification did not require any previous knowledge about the composition of the material and its results indicate the presence of some other light elements; however, these are likely due to experimental artifacts. The Cu particles, being the heaviest entities in the composition, induce luminescence that results in 'correlated' counts for these light elements. This phenomenon, arising from the physical correlation, cannot be extracted through blind source separation, underscoring the importance of considering such effects in the interpretation of compositional analyses. The results of the BSS analysis (Figure 69 and Table 5) indicate that the newly formed particles consist exclusively of Cu, while the surrounding carbon matrix incorporates all the C and O.

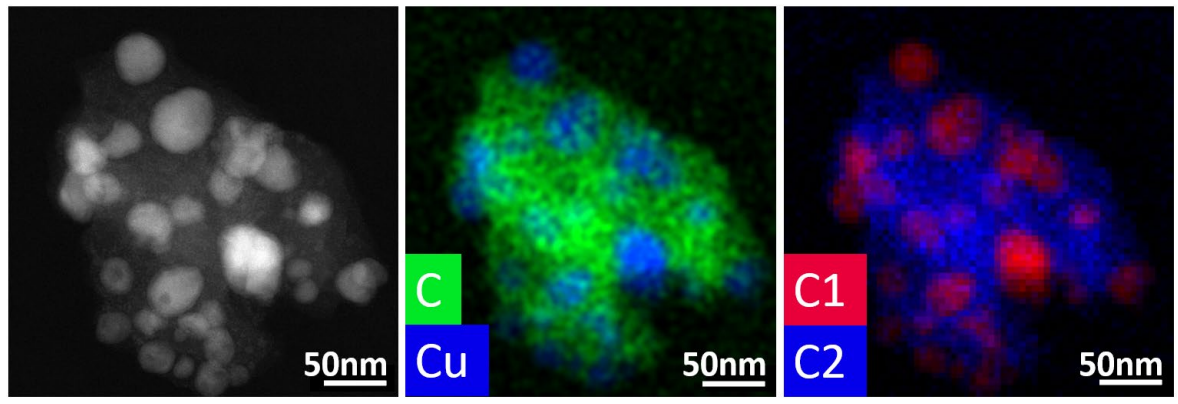


Figure 69. Left: HAADF-STEM image of the newly formed nanostructured carbon. Middle: STEM-EDX map of the nanostructured carbon, given in atomic percent. Right: Image showing the NMF components. Red denotes the first component (Cu-nanoparticles) and blue the second component (C + O matrix), labelled C1 and C2 respectively. The third component (Si<sub>3</sub>N<sub>4</sub>-window) is not shown.

Table 5. Results of the NMF analysis for the three main components. The values are given in atomic

	С	Ca	Cl	Cu	F	N	O	S	Si
Component 1	0.5	0.1	0.3	0.0	0.8	23.4	13.6	0.1	61.1
(Si <sub>3</sub> N <sub>4</sub> -window)									
Component 2	4.1	1.5	1.5	76.1	4.0	2.1	3.8	2.0	4.9
(nanoparticles)									
Component 3	66.3	0.4	0.6	0.3	0.6	3.4	20.8	0.9	6.6
(Carbon matrix)									

Given that the structure of Cu-MOF-74 retained crystallinity only up to 120 °C, the 3D ED analysis focused only on two stages: the structure before heating at 20 °C (Post SE) and the structure after heating to 120 °C (Post 120 °C). PETS processing results for Cu-MOF-74 are given in Table 4. For Cu-MOF-74, the structure was solved using Superflip and kinematically and dynamically refined in the software Jana2020. The dynamical refinement parameters for Cu-MOF-74 are also given in Table 4. Table 16 & Table 15 in the appendix give all atomic coordinates and anisotropic ADP parameters for the dynamically refined structures.

Figure 70 presents the dynamically refined structures for Post SE and Post 120 °C, overlaid with the remaining electrostatic potentials. Minimal presence of DMF and ethanol is discernible at the initiation of the heating cycle. Moreover, the heating cycle up to 120 °C appears to have almost no effect as there is very little DMF and ethanol present to be removed by this process. This suggests that the combination of solvent exchange with the ultra-high vacuum environment of the microscope is sufficient to generate open metal sites and activate Cu-MOF-74. One potential factor contributing to this phenomenon is the elevated Lewis acidity of Cu in comparison to Zn. This heightened Lewis acidity implies that the Cu-O coordination bond connecting the MOF structure and DMF will exhibit greater susceptibility to breakage.

Since the pore content remained largely unchanged, no significant variations in the cell parameters were observed in the cell parameters of the MOF since it is already in a stable state after exposing the particle to the ultra-high vacuum of the microscope.

It is established in the literature that certain MOFs can be activated solely by exposure to vacuum, and the inclusion of a solvent exchange step further facilitates this effect <sup>126</sup>. The observed differences from Zn-MOF-74 can be explained by considering the Zn-O and Cu-O bonds. The Cu-O bond, characterized by both a longer axial bond length (2.15-2.32 Å) and a lower binding energy compared to the Zn-O bond (1.876 Å) <sup>127-129</sup>(~930 eV vs ~1020 eV for Cu-O and Zn-O respectively <sup>130,131</sup>), contributes to the different behaviors.

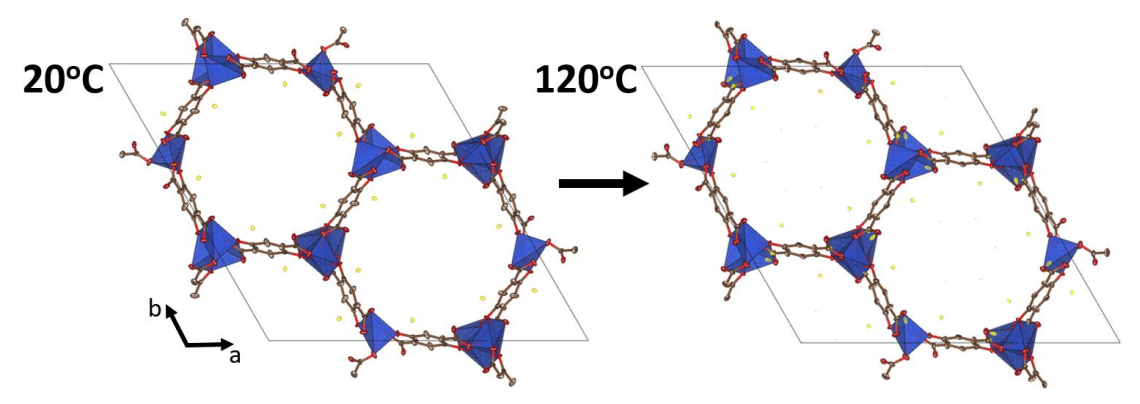


Figure 70. Dynamically refined structures of Cu-MOF-74 at Post SE (20 °C) and Post 120 °C, showing the remaining electrostatic potentials above 0.095 eV/Å<sup>3</sup> (2.3 $\sigma$ ). The atoms are displayed as their displacement ellipsoids. C-atoms are displayed in brown, O-atoms in blue. The electrostatic potentials are displayed in yellow.

The difference in thermal stability between Zn-MOF-74 and Cu-MOF-74 arises from second-order Jahn-Teller distortions within the metal nodes <sup>132,133</sup>. For the refined activated structures, the corresponding polyhedra are shown in Figure 68b and Figure 68c. The pyramidal coordination is created by the removal of the oxygen that was part of the DMF due to the combined effect of solvent exchange and the ultra-high vacuum in the microscope. The resultant second-order Jahn-Teller distortions induce a collapse of the linkers at lower temperatures than when these distortions are absent.

# 4.2.3. CO<sub>2</sub> study of MOF-74

Among the materials capable of CO<sub>2</sub> absorption, MOF-74 is widely studied for its gas sorption properties and structural flexibility. Its adaptability in synthesis, particularly in the choice of metal centers and functional groups, has made MOF-74 a well-suited candidate for CO<sub>2</sub> absorption applications. Many studies have explored its performance, providing observations into its CO<sub>2</sub> uptake under various conditions <sup>69–75,115</sup>.

However, an important knowledge gap remains in understanding how CO<sub>2</sub> absorption directly influences the crystal structure of MOF-74. To date, no *in situ* TEM studies have been conducted to investigate the structural changes during this process. Understanding these changes can provide insights into the interaction between CO<sub>2</sub> and the MOF.

Here, we use *in situ* 3D ED to study the influence of CO<sub>2</sub> absorption on the crystal structure of Zn-MOF-74.

This approach enables us to observe structural changes at the nanometer scale during the absorption process and explore the interaction between CO<sub>2</sub> and Zn-MOF-74, aiming to find the position of absorbed CO<sub>2</sub> within the framework.

The experiment followed a structured workflow to systematically investigate how the material responds to different environmental conditions using 3D ED series acquisitions at various stages.

A schematic illustration of the experiment is shown in Figure 71. First, the nanoreactor was evacuated to a vacuum of  $\sim 1.5 \times 10^{-5}$  mbar, followed by an initial activation step where the material was heated overnight at 120 °C, analogously to the process described in Chapter 4.1.1. After this activation, the first 3D ED series was acquired to test if the activation was successful. Next, the material was exposed to Ar gas at 1 atm with a flow rate of 1 ml/min for 1 hour, followed by a static Ar phase at the same pressure for 30 minutes. A second 3D ED series was then recorded to investigate the effect of ambient pressure on the MOF structure. Afterwards, the material was exposed to  $CO_2$  at 1 atm with a flow rate of 1 ml/min for 1 hour and 30 minutes, followed by a static  $CO_2$  phase at 1 atm for another hour, after which a third 3D ED series was acquired. To further examine the effects of cyclic  $CO_2$  exposure and reactivation, the nanoreactor was pumped to vacuum again, and the material underwent a second activation step, with another overnight heating at 120 °C. After this, a fourth 3D ED series was collected. The material was then re-exposed to  $CO_2$  under the same conditions as before (1 atm, 1 ml/min for 1 hour and 30 minutes) followed by another static  $CO_2$  phase at 1 atm for 1 hour. A fifth 3D ED series was taken at this stage.

Finally, the material was heated once more, this time for 2 hours at 120°C, before undergoing a final static CO<sub>2</sub> phase at 1 atm for 1 hour. The experiment then concludes with a final 3D ED series acquisition. This step-by-step approach provided a detailed look at how the material evolved under vacuum, inert gas exposure, reactivation, and CO<sub>2</sub> absorption, helping to understand its structural behavior under controlled conditions.

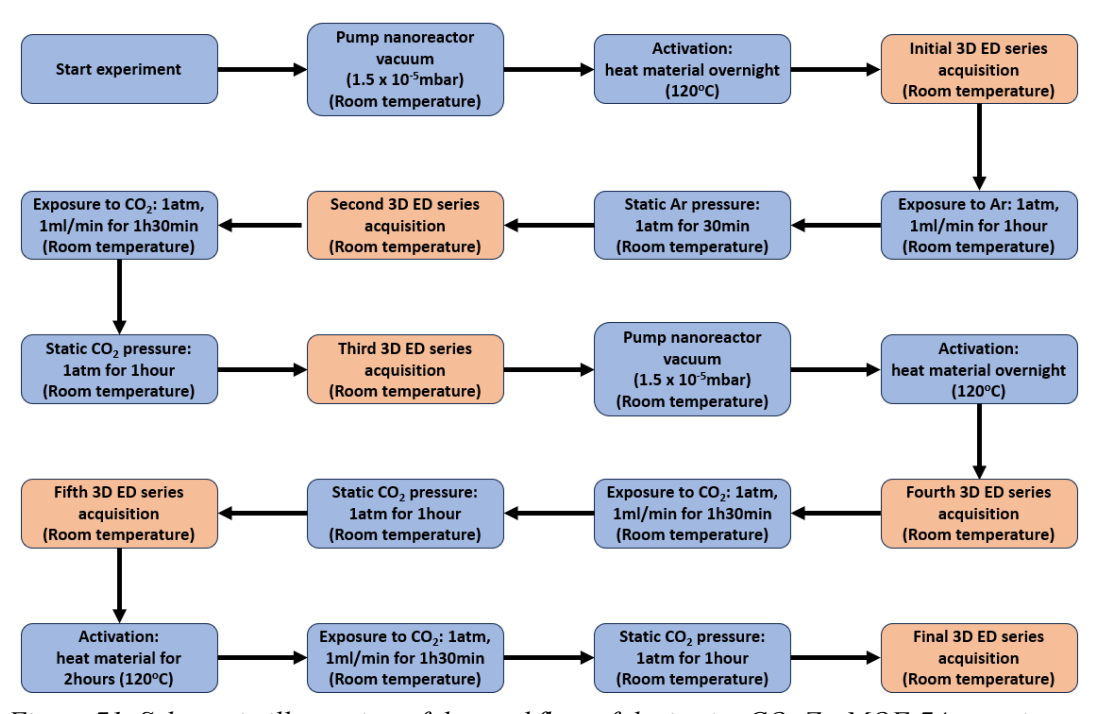


Figure 71. Schematic illustration of the workflow of the in situ CO<sub>2</sub> Zn-MOF-74 experiment.

3D ED analysis showed that the particles remained crystalline up to the third 3D ED acquisition, which was performed at static CO<sub>2</sub> pressure. However, after the second overnight heating cycle, only a few reflections were observed during the entire tilt series, indicating a (partial) collapse of the structure. Among the 11 particles studied, only one located on the Si<sub>3</sub>N<sub>4</sub> windows produced diffraction data with sufficient resolution to analyze any guests in the MOF pores. Unfortunately, data reduction in PETS revealed that, after exposure to Ar, a second particle had moved on top of this well-diffracting particle. This likely occurred because a loosely attached particle on the Si<sub>3</sub>N<sub>4</sub> chip was displaced by the high Ar flow rate and pressure used during exposure. As a result, the data collected at 1 atm of Ar pressure could not be processed, as the diffraction patterns contained overlapping signals from two different reciprocal spaces. This issue was not detected during data acquisition. However, after CO<sub>2</sub> exposure at the same pressure but a higher flow rate, the stray particle was displaced again, restoring the original particle's diffraction and allowing successful data reduction for the dataset taken at 1 atm of static CO<sub>2</sub> pressure.

Table 6 summarizes the unit cell parameters and R<sub>int</sub> values for the two datasets taken after the activation and after CO<sub>2</sub> absorption, respectively. As seen in the Table, CO<sub>2</sub> absorption had no measurable effect on the unit cell dimensions.

Table 6. Results of the data-reduction in PETS for the dataseries taken after activation and after  $CO_2$  exposure. The  $R_{int}$  value for the  $\bar{3}$  Laue class is given. The average and maximum resolution values correspond to the mean resolution across all frames and the highest resolution achieved in any single frame within the 3D ED dataset, respectively.

	Max resolution (Å)	Average resolution (Å)	a (Å)	c (Å)	Mosaicity	R <sub>int</sub> (obs)
After activation	0.85	1.04	26.688	6.869	0.3277	7.97
			(5)	(2)		
After CO <sub>2</sub> exposure	0.90	1.30	26.645	6.873	0.1975	8.73
			(5)	(3)		

Figure 72 presents the dynamically refined structure of the particle after activation. However, refining anisotropic ADPs resulted in unphysical values for one oxygen atom. The ADPs were therefore kept isotropic. As shown in Figure 72a, the activation was not entirely successful, as indicated by the presence of an oxygen atom in the pores, completing the octahedral coordination environment around Zn. This aligns with the findings from the previous chapter, which showed that the standard activation procedure for this MOF is insufficient to fully remove guest molecules and completely empty the pores.

Additionally, an extra oxygen atom was detected inside the pores. Analysis of its interatomic distances revealed that it was too far from neighboring atoms to form a bond.

While it is possible that this atom is part of residual water trapped in the pore, this seems unlikely given that the material underwent overnight heating at 120 °C under vacuum. We currently have no explanation for the presence of this oxygen atom.

The dynamically refined structure after CO<sub>2</sub> exposure is shown in Figure 72b. The refinement confirmed the presence of CO<sub>2</sub>, which is bonded by one of its oxygen atoms at a distance of 2.250(4) Å, closely matching the known *in situ* SCXRD-confirmed distance of 2.261(9) Å <sup>134</sup>. Furthermore, we identified three possible positions within the structure.

Refinement was performed individually for each position by deleting the other two from the model, and additionally using a combined model incorporating all three sites. Table 7 summarizes the relevant R-factors obtained from these refinements.

Table 18 & Table 19 in the appendix give the atomic coordinates and occupancies for all atoms of both datasets. Figure 73 presents the three separate CO<sub>2</sub> positions alongside the combined model, along with the corresponding R(obs) factors from the dynamical refinements.

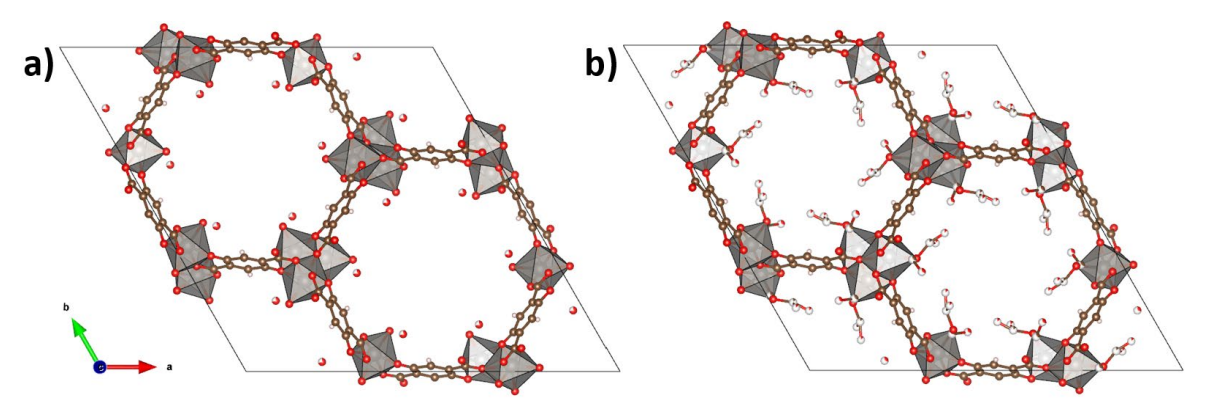


Figure 72. Dynamically refined Zn-MOF-74 structures after a) activation and b) CO<sub>2</sub> exposure.

Table 7. Number of reflections used in the dynamical refinement and the resulting R-factors for each refinement. The individual positions were refined using models in which the other two positions were removed.

	Number of	R(obs)	wR(obs)	R(all)	wR(all)
	reflections used				
After activation	3784	10.93	10.62	21.54	11.65
CO <sub>2</sub> position 1	3191	9.89	9.89	26.15	11.77
CO <sub>2</sub> position 2	3191	8.96	8.49	24.97	10.66
CO <sub>2</sub> position 3	3191	10.51	10.31	26.08	12.14
Combined CO <sub>2</sub> positions	3191	8.88	8.43	24.79	10.49

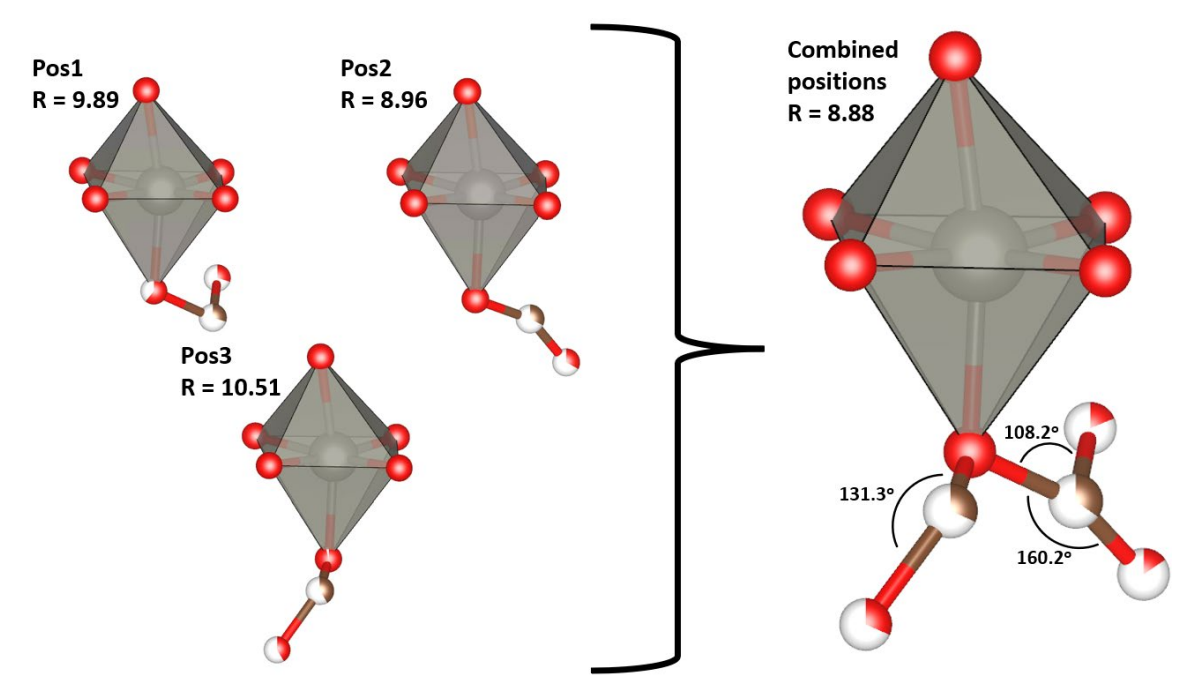


Figure 73. Visualization of the three distinct CO<sub>2</sub> positions, each refined separately using a model containing only that specific site (left), and together using a combined model including all positions (right). The R(obs) values are provided for the refinements of each position. The O-C-O angles are indicated in the combined position image.

CO<sub>2</sub> interactions with metal atoms are well-documented in the literature <sup>135–137</sup>. In MOF-74, it is stated that CO<sub>2</sub> binds to open metal sites through (weak) van der Waals forces (physisorption), where one oxygen atom interacts with the metal center <sup>136,137</sup>. These weak interactions allow CO<sub>2</sub> to maintain its linear structure and facilitate easy desorption.

However, as shown in Figure 73, the CO<sub>2</sub> molecules identified in our dynamically refined structures adopt a non-linear geometry, contradicting theoretical studies assuming a linear configuration  $^{137}$ . While non-linear CO<sub>2</sub> adsorption is possible with van der Waals interactions, as described in  $^{135}$ , when CO<sub>2</sub> forms a  $\pi$ -bond with a metal center, several binding modes are possible.

Given that the bond angle of 108.2° is a large deviation from the 180° linear geometry, this position is considered to be the least likely. While one of the Zn node's octahedral oxygens is relatively close to one CO<sub>2</sub> oxygen (2.707 Å), anionic O–O bonds are highly unlikely in MOF-based CO<sub>2</sub> adsorption, suggesting that this oxygen from the CO<sub>2</sub> may instead originate from residual water in the pores.

The non-linear geometry of Pos2 and Pos3 might be explained by the proximity between the CO<sub>2</sub> molecules and atoms of the MOF structure. In Pos2, the CO<sub>2</sub> carbon is 3.197 Å from an oxygen in the Zn octahedron, while in Pos3, the CO<sub>2</sub> carbon is just 2.595 Å from a Zn octahedron oxygen.

These short distances suggest attractive interactions that could distort the CO<sub>2</sub> geometry, with the stronger interaction in Pos3 likely causing a more pronounced bend compared to the nearly linear configuration in Pos2.

All of this suggests that  $CO_2$  absorption in Zn-MOF-74 is more complex than originally assumed in literature and that other attractive forces resulting from the MOF framework itself, and not just the  $Zn^{2+}$  open metal sites, can potentially distort the linear geometry of the  $CO_2$  molecule.

Furthermore, the interaction between CO<sub>2</sub> and the open Zn<sup>2+</sup> metal sites involves probably more than just van der Waals forces; it might also include donor-acceptor interactions through Lewis acid-base chemistry. The Zn<sup>2+</sup> center, acting as a Lewis acid, can accept electron density, while the oxygen atoms of CO<sub>2</sub>, serving as a Lewis base, can donate electron density through coordination. This results in a partial charge redistribution rather than a full electron transfer, leading to a stronger interaction than pure van der Waals forces. The Zn<sup>2+</sup> ion also polarizes the CO<sub>2</sub> molecule, further stabilizing the adsorption. This polarization allows for attractive forces to act on the carbon atoms of the CO<sub>2</sub> molecule, distorting it from the ideal linear geometry.

The idea of strong CO<sub>2</sub>-Zn bonding is further supported by theoretical studies, where DFT calculations have shown a shift in the density of states upon CO<sub>2</sub> adsorption <sup>137</sup>. However, these calculations typically assume a linear CO<sub>2</sub> geometry, which does not fully align with our experimental observations suggesting a bent configuration.

Similar indications of non-linear CO<sub>2</sub> geometries have also been reported in both an *in situ* neutron diffraction study on Mg-MOF-74 combined with first-principles calculations <sup>138</sup>, as well as an *in situ* synchrotron PXRD study combined with infra-red spectroscopy on Ni-MOF-74 <sup>139</sup>. In these studies, one of the oxygen atoms of the CO<sub>2</sub> molecule was found to coordinate directly to the metal site, similar to our observations, and their refined structure revealed an O-C-O bond angle of 160.5° and 162(3)° for Co-MOF-74 and Mg-MOF-74 respectively, which is almost identical to the angle we found for Pos2. The neutron study suggested that strong electrostatic interactions could polarize the CO<sub>2</sub> molecule while still keeping the interaction within the physisorption range.

However, their DFT calculations predicted a smaller bending angle of about 175° (still indicating a non-linear CO<sub>2</sub> geometry), which they attributed to the assumption of '*frozen phonons*' that removes any molecular motion during the calculation. They further argued that the experimentally observed smaller O-C-O angle was not a true representation of the CO<sub>2</sub> geometry, but rather a result of disorder within the CO<sub>2</sub> molecules, as indicated by their larger ADPs. But, this highlights an important limitation of DFT results, as they are based on idealized models that may not fully capture real experimental and real world conditions. It is also worth noting that the type of metal in the MOF node, in this case Mg instead of Zn, could further influence the CO<sub>2</sub> geometry. In addition, *in situ* SCXRD studies on Co-MOF-74 have shown multiple CO<sub>2</sub> adsorption sites within the framework <sup>134</sup>, similar to our observations for Pos2 and Pos3. While this *in situ* SCXRD experiment was conducted at elevated pressures and assumed a linear CO<sub>2</sub> geometry, the observed CO<sub>2</sub> positions were attributed to favorable interactions between the partially positive carbon atom and oxygen atoms from the MOF linker, as well as interactions between neighboring CO<sub>2</sub> molecules. This explanation closely aligns with the proposed origin of the non-linear CO<sub>2</sub> geometries we observed for Pos2 and Pos3.

However, we do not account for interactions between neighboring CO<sub>2</sub> molecules, as these are assumed to be negligible at our working pressure of 1 atm. Unlike the *in situ* SCXRD study, we do not constrain CO<sub>2</sub> to a linear geometry.

Instead, we attribute the bending to partial polarization of the CO<sub>2</sub> molecule caused by the strong interaction between CO<sub>2</sub> and the MOF, combined with the close proximity of the CO<sub>2</sub> molecule to the MOF framework. These factors were not considered in their analysis.

The observed CO<sub>2</sub> geometries based on our data, as well as the very strong bond between the CO<sub>2</sub> and the MOF might explain why the MOF structure collapsed after the second heating cycle overnight. This heating cycle likely failed because the thermally induced energy could not overcome the strong, non-ideal binding of CO<sub>2</sub> without compromising the structural integrity of the MOF.

The combination of accumulated mechanical strain from distorted guest geometries, incomplete desorption of strongly bound CO<sub>2</sub>, and the resultant perturbation of the metal-ligand coordination network appears to have reached a critical threshold, triggering the observed partial collapse of the framework.

## 4.2.4. Difficulties during in situ experiments on MOF-74

While none of the 11 particles we were tracking survived this heating cycle, literature shows that MOF-74 can be used for several absorption/desorption cycles, although with a decrease in capacity <sup>136,140,141</sup>. Given that these studies are always performed on a large bulk of MOF-74 powder/sample a number of particles might survive the desorption, with the decrease in absorption capability due to the structural collapse of the rest of the particles after the desorption of the CO<sub>2</sub> by heating. While in the first absorption cycle, all particles can absorb CO<sub>2</sub>, some of these particles will collapse after the desorption. These particles then cannot be used for CO<sub>2</sub> absorption anymore, causing the observed decrease in CO<sub>2</sub> absorption capabilities. Follow-up *in situ* 3D ED experiments showed that the structural collapse of MOF-74 particles already occurred after exposing the material to vacuum followed by heating at 120 °C for 30 minutes under vacuum.

These results suggest that the collapse may be caused either by the vacuum conditions themselves (such as an excessively low pressure or a pressure drop applied too quickly) or by the temperature being too high. Further experiments are required to determine which factor is responsible for the observed degradation.

In conclusion, this work shows that CO<sub>2</sub> adopts non-linear configurations upon adsorption in Zn-MOF-74, challenging the commonly assumed linear geometry. The results point to stronger donor-acceptor interactions with Zn<sup>2+</sup> sites, beyond van der Waals forces. The identification of multiple binding geometries reveals a complex adsorption mechanism, and the observed structural collapse after desorption suggests that these strong interactions may cause framework instability. These results refine our understanding of CO<sub>2</sub> adsorption in MOF-74 and provide key takeaways for designing more stable MOFs for CO<sub>2</sub> capture applications.

While the workflow of this *in situ* experiment appears straightforward, in reality, such experiments come with numerous challenges specific to both the setup and the material being studied.

The results presented in this chapter are the outcome of three years of effort, involving multiple attempts to acquire high-quality data suitable for analysis.

Figure 74 shows a Sankey diagram that illustrates the number of attempts made to obtain a successful data acquisition during the *in situ* MOF-74 CO<sub>2</sub> experiment and highlights the various setbacks encountered along the way. One recurring issue was the failure of overnight activation, often due to unexpected disruptions such as power outages or automatic Windows updates that caused the heating system to restart.

Multiple attempts were also made to activate the material in a vacuum pump before transferring the in situ holder to the microscope while keeping the nanoreactor under vacuum. However, this approach frequently led to the breaking of the Si<sub>3</sub>N<sub>4</sub> chips and windows, resulting in leaks that rendered the experiment unusable. This breakage was likely due to the pressure difference exerted on the chips. While they could withstand conditions where the interior remained at 1 atm and the external environment was UHV, the reverse was not possible. This limitation likely stems from the chip manufacturing process, which involves etching, allowing the Si<sub>3</sub>N<sub>4</sub> windows to bulge outward but not inward, ultimately leading to structural failure under reversed pressure conditions. Another challenge was the crystallinity of the MOF particles. While small particles (<1 µm) are typically preferred for 3D ED experiments, MOFs in this size range often exhibited poor crystallinity, leading to suboptimal data. To improve structural quality, MOF particles in the range of 1-2.5 µm were chosen. However, due to the closed-cell design of the in situ holder, the available space between the two chips was limited to just 5 µm. If two larger sized particles ended up stacked on top of each other, they could exert excessive pressure on the Si<sub>3</sub>N<sub>4</sub> windows, causing them to break and leading to leaks. This made sample preparation particularly delicate, requiring a careful balance between selecting sufficiently large particles for 3D ED while ensuring they fit within the available space. Additionally, many of the particles that settled on the Si<sub>3</sub>N<sub>4</sub> windows were too small or poorly crystalline, making them unsuitable for the experiment.

This experiment underscores the challenges of conducting *in situ* TEM experiments, especially with highly sensitive materials like MOFs. Achieving a successful experiment required carefully balancing factors such as sample crystallinity, pressure conditions, and the limited space within the *in situ* holder. Each step of the process played a crucial role, and even seemingly simple workflows were often influenced by multiple interconnected variables. These challenges highlight the need for meticulous planning, precise execution, a small portion of luck and a great deal of perseverance in these *in situ* experiment. While the diagram in Figure 74 only shows the effort for one *in situ* experiment, all *in situ* TEM experiments face their own specific sets of challenges.

# In situ MOF-74 CO<sub>2</sub> experiment Overnight heating failure Chip breakage after heating Chip contamination Chip contamination

Successful data acquisition for single single CO2 absorption cycle



3+ vears

Successful overnight heating

Figure 74. A Sankey diagram illustrating the number of attempts made for a successful data acquisition during the in situ MOF-74 CO<sub>2</sub> experiment, highlighting key issues encountered during the process.

## 4.3. Biohybrids

Attempts 16

MOFs are highly versatile materials, capable of hosting a variety of guests, from nanoparticles to enzymes <sup>142–144</sup>. This flexibility extends to their synthesis, where biocompatible metals can be incorporated, making them ideal for enzyme encapsulation. These enzyme-MOF composites, known as biohybrids, combine the functional versatility of MOFs with the catalytic abilities of enzymes, offering potential for applications such as CO<sub>2</sub> reduction.

While biohybrids have been studied before, existing synthesis methods often involve elevated temperatures that can degrade the enzymes <sup>142,143</sup>. Collaborators from both BCMaterials and Bielefeld University developed a new, room-temperature synthesis technique where the enzyme itself serves as a precursor, and the MOF is grown around it <sup>145</sup>. Initial experiments focused on the MOF Zr-UiO-66 and enzymes Glucose Oxidase (GOx) and Candida Antartica Lipase B (CALB).

To confirm that the enzymes were successfully encapsulated, low-dose HRTEM was performed with a K2 direct electron detector, see Figure 75.

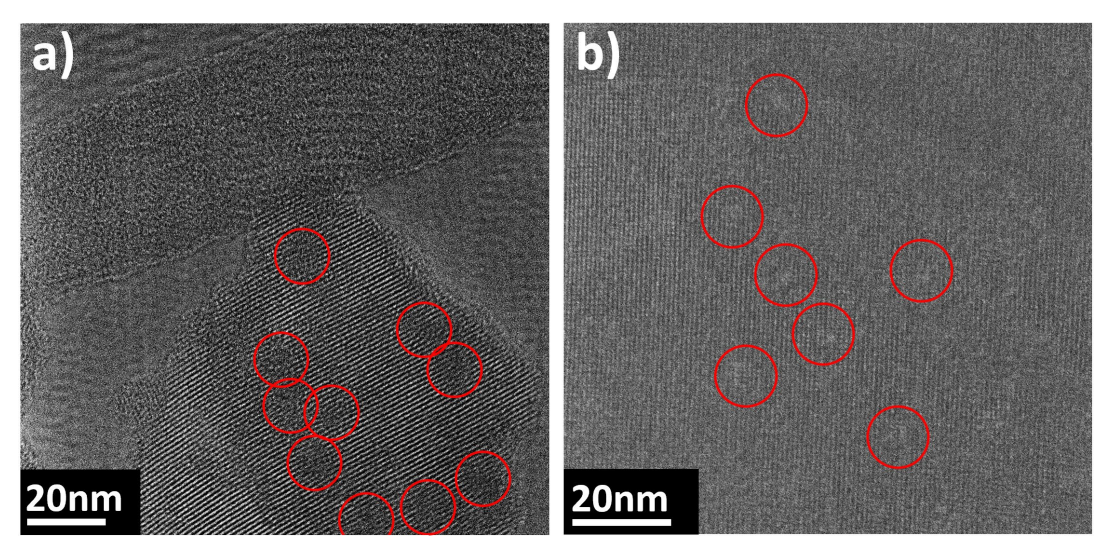


Figure 75. HRTEM images of biohybrid samples consisting of Zr-UiO-66 with the enzymes a) GOx and b) CALB. Areas with slight changes in HRTEM contrast are highlighted with red circles.

Although we observed contrast variations in the images, definitive confirmation using HRTEM was not possible due to the limitations of contrast formation. Enzymes are primarily composed of light elements like carbon and oxygen, which scatter only weakly compared to MOF components such as the zirconium from the nodes. This makes it difficult to differentiate them in HRTEM images, since this is a diffraction-contrast based technique. Techniques like HAADF-STEM, which rely on thickness- and Z-based contrast, were also unsuitable due to the low Z-contrast contribution of the enzyme and the higher risk of damaging both the MOF and the enzyme because of the need for more electron flux for an interpretable signal to noise ratio. As a result, standard TEM techniques could not conclusively confirm the enzyme's presence within the MOF. To address this, the enzymes were stained with a heavy metal that differs from the MOF's metal node, enabling it to stand out in STEM-EDX elemental maps. Our collaborators from BCMaterials prepared biohybrid samples in which each enzyme was stained with a single iron atom. This time, the MOFs Zn-ZIF-8 (ZIF-8@OxdB1) and Zn-MOF-74 (MOF-74@OxdB1) with the enzyme Bacillus sp. strain OxB-1 (OxdB1) were synthesized.

However, STEM-EDX analysis yielded inconclusive results. The observed iron signals (Figure 76) may be the result of stray X-rays. Stray X-rays are secondary X-rays generated when primary X-rays, produced by the interaction between the electron beam and the sample, are scattered within and on the microscope column itself. Since the sample's iron content was extremely low, it was impossible to distinguish between true signals and background signals.

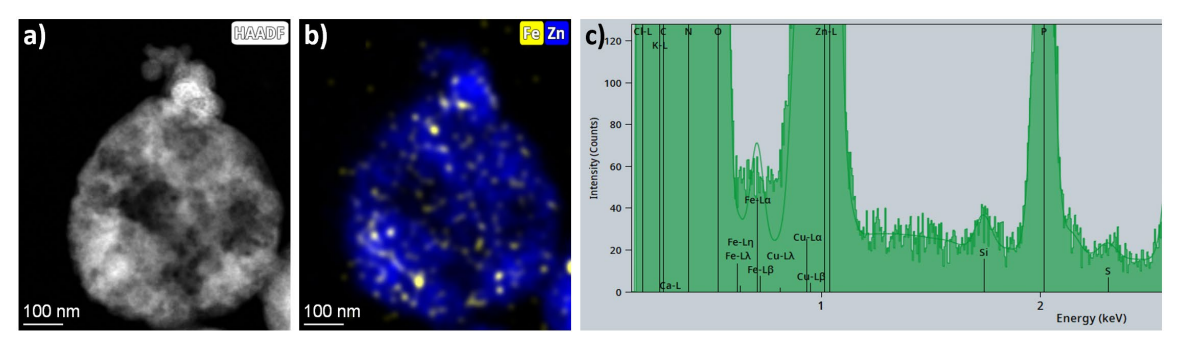


Figure 76. Representative a) HAADF-STEM image of the ZIF-8@OxdB1 biohybrid. b) STEM-EDX map displaying the distribution of Fe and Zn within the particle shown in a), presented in net counts. c) EDX spectrum corresponding to the STEM-EDX map in b), with the individual elemental peaks labeled.

To have an alternative validation of the enzymes' presence in the MOF structure, 3D ED experiments were performed. The crystal structure for ZIF-8 is well known with the cubic spacegroup  $I\bar{4}3m$ , cell parameter a = 16.8303 Å <sup>146,147</sup>. Structural data were successfully obtained and the four studied biohybrid ZIF-8@OxdB1 particles exhibited a slight expansion of the MOF unit cell (Table 8) showing the cell parameters for a representative particle. Table 20 & Table 21 in the appendix give all the atomic coordinates, as well as the occupancies and the ADPs for each atom for both refined structures. The average unit cell parameters for the three studied pure MOF particles were a = 16.857(3) Å, while the average parameters for the four studied biohybrid particles were a = 16.89(2) Å. The enzyme, which takes the monoclinic space group  $P12_11$  in its crystallized form with unit cell parameters a = 48.3 Å, b = 63.8 Å, c = 59.3 Å,  $\alpha = \gamma = 90^{\circ}$  and  $\beta = 94.2^{\circ}$ , exceeds the dimensions of the MOF pores. Its insertion in the MOF might cause an outwards pressure on the framework, elongating the bonds closest to the enzyme, and this elongation might propagate further, resulting in a larger average cell parameter. However, the difference in unit cell parameters is minimal.

Potential artifacts that might influence these cell parameters, such as hysteresis in the microscope lenses, were considered. Careful consideration was given to maintaining consistent lens settings throughout the experiment to minimize these effects. Further analysis included kinematical refinements in Olex2. While the R-factor for the ZIF-8@OxdB1 biohybrid particle (R1 = 14.19) is higher than that of the pure ZIF-8 particle (R1 = 7.97), see Table 8, this difference can likely be attributed to particle-to-particle variability. As shown in Figure 77, the kinematically refined structures of both materials are nearly identical, with only slightly larger cell parameters (Table 8) and generally larger atomic displacement parameters in the biohybrid particle. These differences may suggest that enzyme encapsulation increases atomic motion within the framework, even though the parent MOF structure remains intact. However, based on these results alone (and given the particle-to-particle dependence), no definitive conclusion can be drawn regarding this.

Table 8. Structural parameters and kinematical refinement results for the 3D ED experiment and structure solution of both a pure ZIF-8 and a ZIF-8@OxdB1 biohybrid particle, corresponding to the structure shown in Figure 51. The R<sub>int</sub> value for the m3m Laue class is given. The maximum resolution value corresponds to the highest resolution achieved in any single frame within the 3D ED dataset.

Sample	Max resolution (Å)	a (Å)	Mosaicity	Completeness (%)	$R_{\text{int}} \\$	R1	wR2
					(obs)		
Pure ZIF-8	0.91	16.868	0.18313	93.4	24.65	7.97	20.14
		(4)					
ZIF-8@OxdB1	1.14	16.88	0.55	99.6	12.08	14.19	33.40
		(2)					

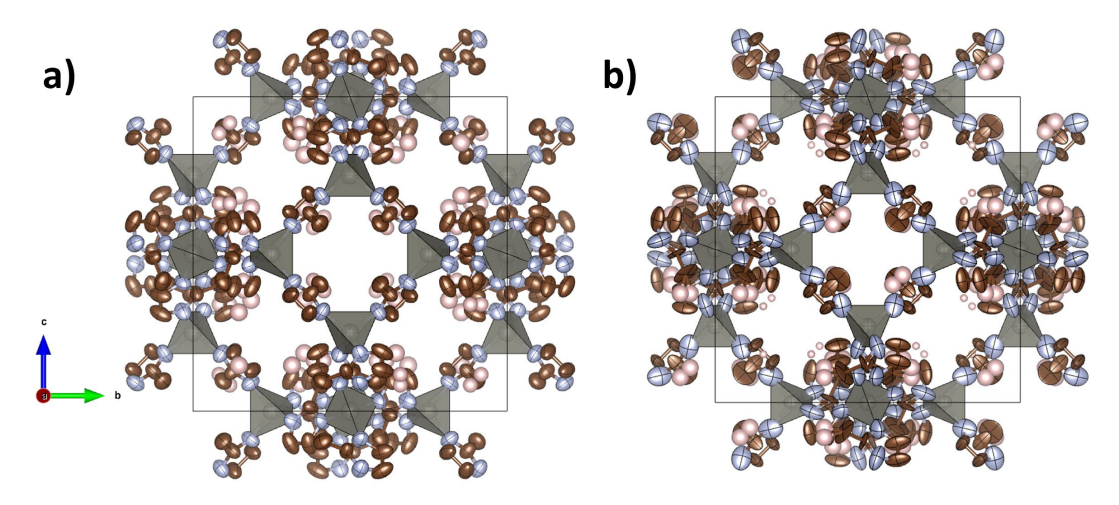


Figure 77. Solved and kinematically refined structures based on 3D ED data for a) pure ZIF-8 and b) ZIF-8@OxdB1 biohybrid samples. N is represented by blue spheres, C by brown spheres, Zn by grey spheres and H by pink spheres.

3D ED analysis was also performed on the MOF-74@OxdB1 biohybrid sample. However, the MOF-74@OxdB1 biohybrid did not show an R-factor increase, which is likely due to dynamical effects being less pronounced in this studied particle. Overall, due to the synthesis process, the biohybrid particles were smaller and therefore also thinner than the pure MOF particles, resulting in reduced dynamical effects. Figure 78 shows the solved and kinematically refined structures for both the pure MOF-74 and MOF-74@OxdB1 biohybrid. The 3D ED analysis did, however, again show the increase in unit cell parameters compared to a pure MOF-74 sample, shown in Table 9. Table 22 & Table 23 in the appendix provide all the atomic coordinates, as well as the occupancies and the ADPs for each atom for both refined structures.

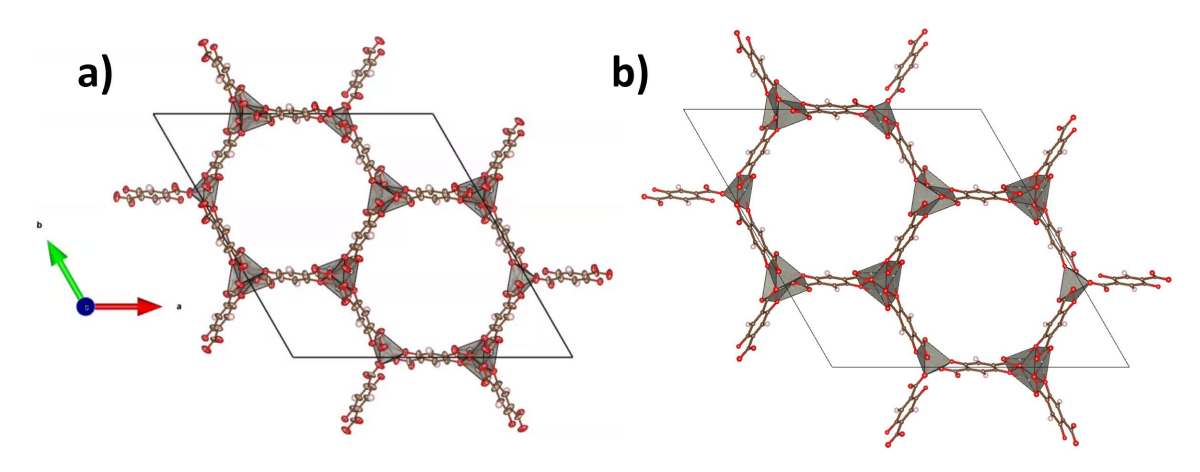


Figure 78. Solved and kinematically refined structures based on 3D ED data for a) pure MOF-74 and b) MOF-74@OxdB1 biohybrid samples.

Table 9. Structural parameters and kinematical refinement results for the 3D ED experiment and structure solution of both pure MOF-74 and a MOF-74@OxdB1 biohybrid particle, corresponding to the structure shown in Figure 78. The  $R_{int}$  value for the  $\overline{3}$  Laue class is given. The maximum resolution value corresponds to the highest resolution achieved in any single frame within the 3D ED dataset.

Sample	Max resolution	a (Å)	c (Å)	Mosaicity	Complete	eness	R <sub>int</sub>	R1 wR2
	(Å)				(%)		(obs)	
Pure MOF-74	0.83	25.406	6.748	0.1432	95.7	20.26	18.3	43.92
		(4)	(1)					
MOF-74	0.83	25.605	6.753	0.10	95.2	14.65	12.4	32.17
@OxdB1		(5)	(2)					

However, the 3D ED analysis offers only indirect support that suggests the enzyme may be present within the biohybrid. To enable direct observation with TEM of the enzymes and their distribution within the MOF, our collaborators at BCMaterials developed a novel staining method. This approach involves washing the biohybrid material with metallic salts that contain heavy metals. Ideally, these salts, and consequently the heavy metals, should adhere to the enzymes since these enzymes obstruct a clear flow through the MOF pores.

To validate this approach, two ZIF-8@OxdB1 biohybrid complexes were washed with Bi- and Pb-based metallic salts. The washing procedure included preparing 5 mM stock solutions of Bi(NO<sub>3</sub>)<sub>3</sub> and Pb(CH<sub>3</sub>COO)<sub>2</sub> by dissolving these salts in DMSO and MeOH, respectively. The ZIF-8@OxdB1 was then immersed in the stock solution and stirred for 30 minutes at room temperature. After immersion, the samples were washed four times in DMSO and MeOH, respectively, by centrifugation. Finally, the samples were evaporated under high vacuum overnight to remove residual solvent.

To confirm whether the salts adhered only to the enzymes, pure ZIF-8 particles were also washed using the same method. During STEM-EDX analysis, the heavy metals should therefore only be detected in the biohybrid materials. Contrast-reversed HAADF-STEM imaging of a pure ZIF-8 particle (Figure 79a) showed no increase in contrast, indicating the absence of heavy elements. However, contrast-reversed HAADF-STEM images of the Pb- and Bi-washed biohybrid samples (Figure 79b and Figure 79c) clearly revealed darker patches of 1-3 nm, indicating the presence of heavy atoms.

STEM-EDX analysis of pure ZIF-8 particles (Figure 80a) showed only the expected elements of ZIF-8, whereas STEM-EDX analysis of the Pb- and Bi-washed biohybrid samples (Figure 80b and Figure 80c) confirmed the presence of Pb and Bi, respectively. Upon closer examination of the elemental maps, these patches indeed corresponded to Bi and Pb locations. Therefore, we can conclude that the incorporation of the enzymes, as well as the washing approach were successful, and this novel staining method provides a clear visual confirmation of the enzyme positions.

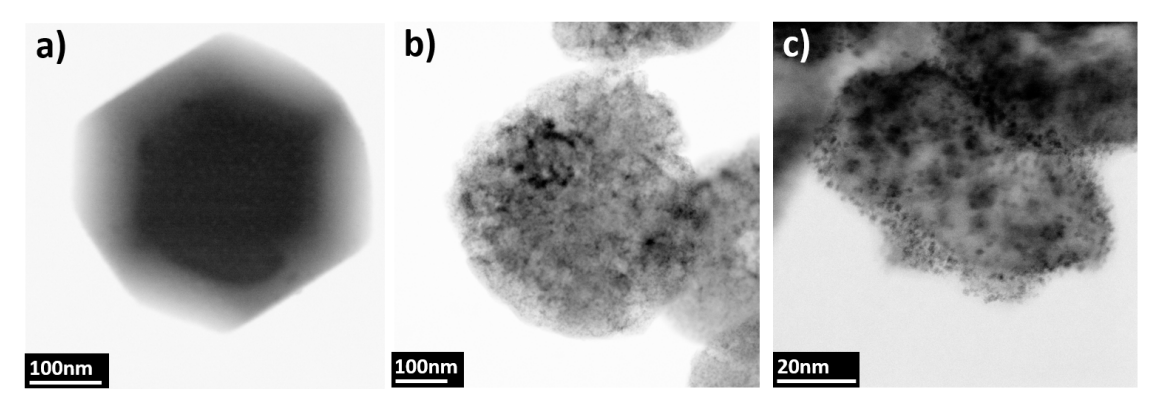


Figure 79. Contrast-reversed HAADF-STEM images of a) a pure ZIF-8 particle, b) a Pb-washed biohybrid ZIF-8@OxdB1 particle and c) a Bi-washed biohybrid ZIF-8@OxdB1 particle. The contrast was reversed to improve visibility.

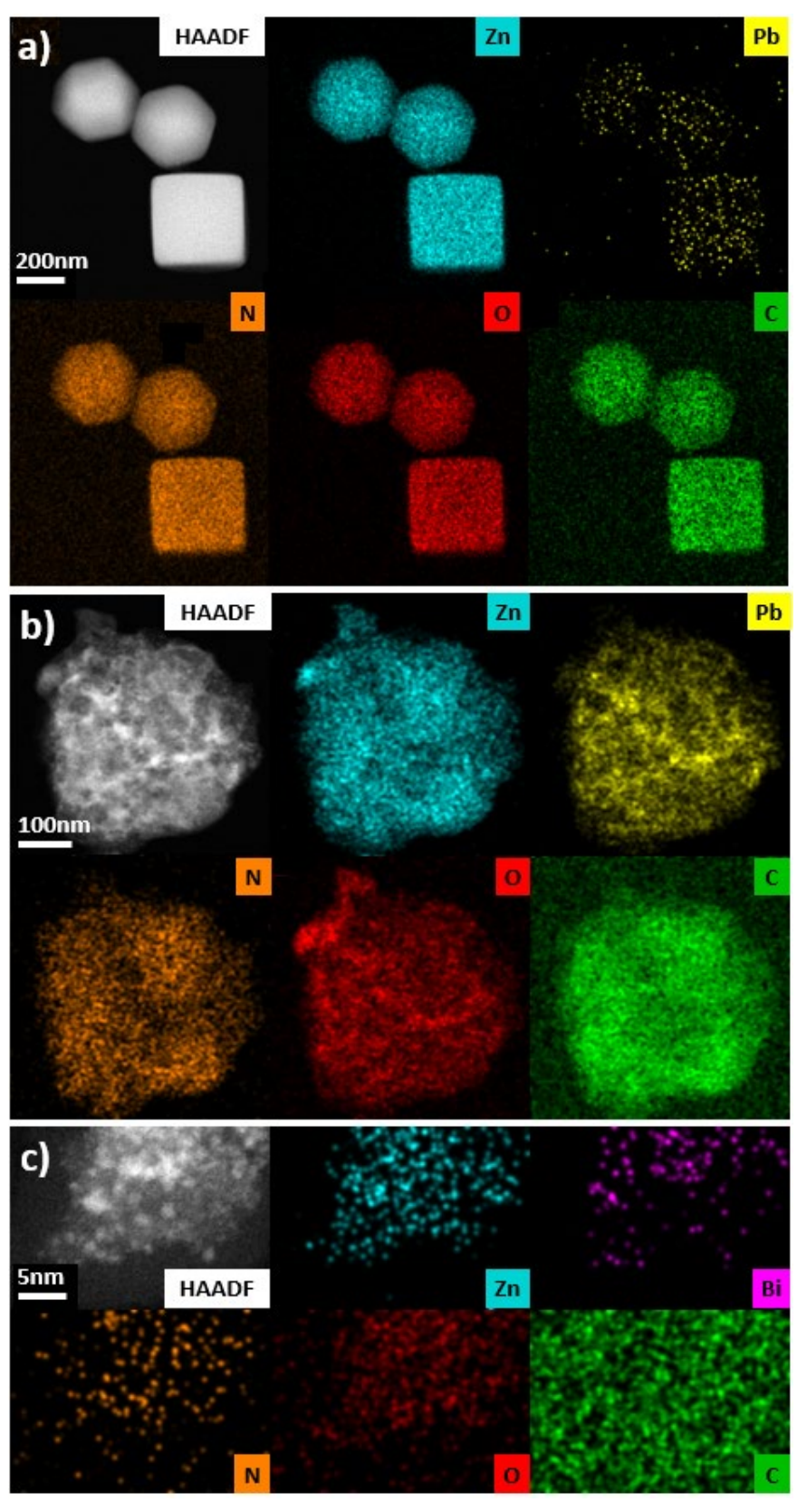


Figure 80. STEM-EDX elemental maps of a) a pure ZIF-8 particle, b) the Pb-washed and c) the Bi-washed biohybrid ZIF-8@OxdB1 sample.

Since this staining approach may be applicable to other materials as well, we investigated its potential for broader use. Three new biohybrid materials were synthesized and stained using the Pb-containing metallic salt. All samples had ZIF-8 as the parent structure, but different enzymes were used: lipase from Thermomyces lanuginosus (TLL), glucose oxidase (GOx), and prostaglandin A1 (PGA1). Figure 81 shows contrast-reversed HAADF-STEM images of the three biohybrid materials. As observed in the figure, the TLL biohybrid showed no increase in contrast, indicating the absence of Pb. The GOx biohybrid exhibited both particles with and without Pb, though the Pb was localized in specific regions and appeared in clusters. In contrast, the PGA1 biohybrid revealed small patches with increased contrast (similar to the ones described earlier), indicating the presence of Pb, which was distributed homogeneously across the particles.

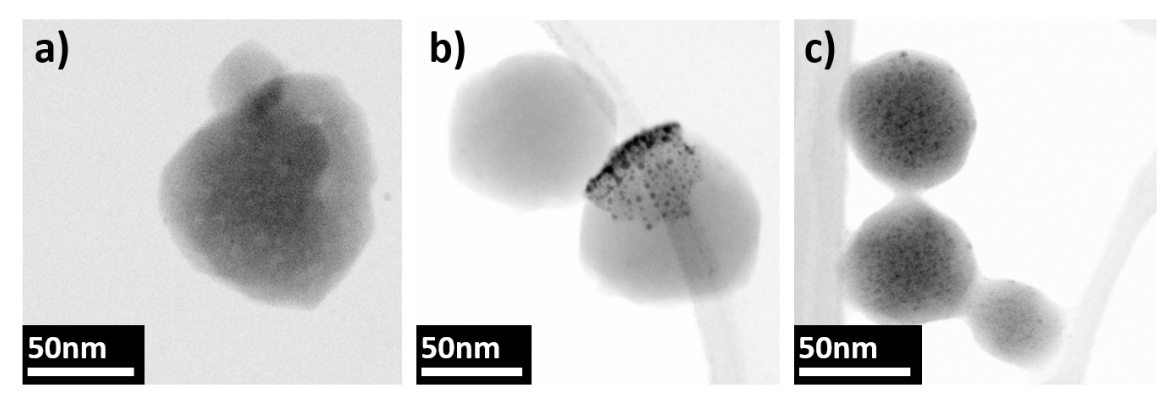


Figure 81. Contrast reversed HAADF-STEM images of the a) ZIF-8 + TLL, b) ZIF-8 + GOx and c) ZIF-8 + PGA1 biohybrids.

To verify these findings, STEM-EDX was used again to examine the Pb content of the particles. As shown in Figure 82a, the TLL biohybrid did not exhibit any detectable Pb content, aside from minor signals attributed to detector/quantification noise. This is further demonstrated in Figure 83a, where there are no detectable Pb-peaks in the EDX-spectrum of this particle. The STEM-EDX measurements of the GOx biohybrid confirmed that Pb was concentrated in specific regions of the particles as shown in Figure 82b, while little to no Pb was detected elsewhere. Figure 83b shows the resulting Pb-peaks in the EDX-spectrum of this particle, indicating the presence of Pb.

The PGA1 biohybrid showed an overall increase in Pb content, which was homogeneously distributed across the particles (Figure 82c), in agreement with the HAADF-STEM images.

Figure 83c shows the resulting Pb-peaks in the EDX-spectrum of this particle. However, some particles contained higher Pb concentrations than others, which can be explained by variations in enzyme loading among individual particles. Due to beam damage, unfortunately, no high-resolution STEM-EDX maps could be obtained.

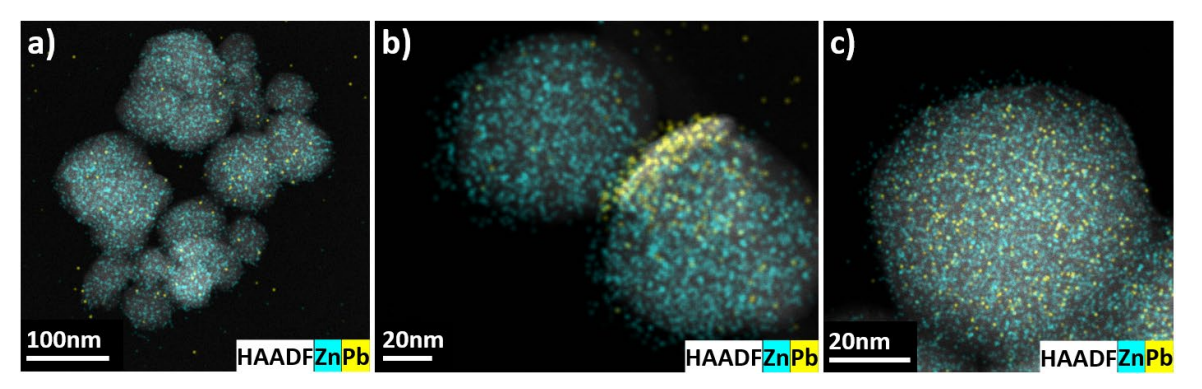


Figure 82. HAADF/Zn/Pb STEM-EDX maps for the a) ZIF-8 + TLL, b) ZIF-8 + GOx and c) ZIF-8 + PGA1 biohybrids. All maps are given in counts.

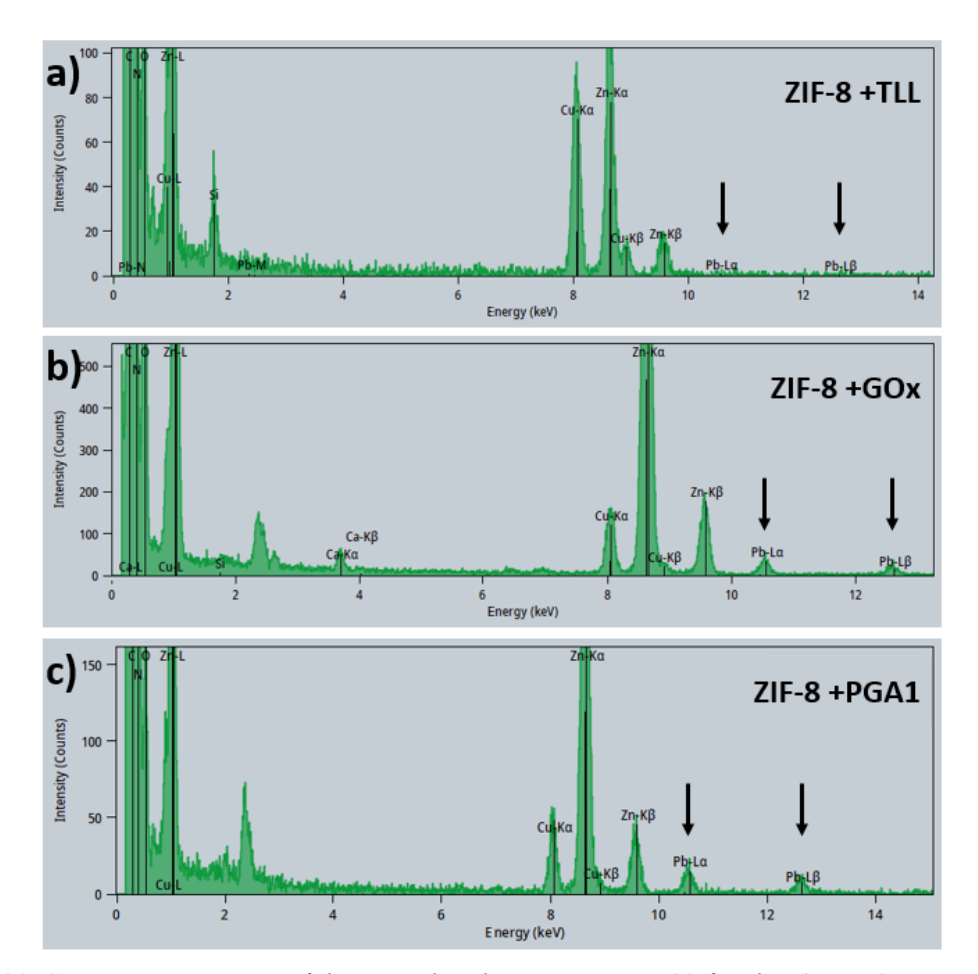


Figure 83. STEM-EDX spectra of the particles shown in Figure 82 for the a) ZIF-8 + TLL, b) ZIF-8 + GOx and c) ZIF-8 + PGA1 biohybrids. The positions of the Pb L $\alpha$ - and L $\beta$ -peaks are indicated by the black arrows.

This variation in Pb content among the three additional biohybrid samples suggests either that enzyme encapsulation was not successful for all samples, indicating an enzyme-dependent effect in this process, or that the washing procedure was ineffective for two of the three samples, also pointing to a possible enzyme dependence.

#### 4.4. UA-4

Several measurements on new MOFs have also been performed in the course of this Ph.D., one of which will be discussed in detail in this section. As discussed earlier, a key advantage of MOFs is the ability to replace shorter linkers with longer ones while preserving the same topology, enabling the creation of mesoporous MOFs with larger pore sizes (provided that the interpenetration is controlled). These materials are particularly valuable for applications such as catalysis and drug delivery, where accommodating bulky molecules and improving mass transport is crucial. However, despite the vast number of MOFs developed to date, synthesizing mesoporous MOFs with large, functionalized pores remains a challenging and costly process. Traditional linker synthesis methods, such as Suzuki, Stille, and Sonogashira couplings, require multiple steps, prefunctionalized starting materials, and expensive palladium-based catalysts, often leading to low yields, unwanted byproducts, and high costs.

To address these challenges, Dr. Leili Esrafili and Prof. Dr. Christophe Vande Velde from the University of Antwerp developed a novel synthesis approach that is both more efficient and cost-effective. This method uses simple organic precursors to generate tetratopic cores, which serve as building blocks for extended linkers. These cores are then functionalized in a one-pot, *in situ* reaction with carboxylated thiophene-based arms, utilizing direct arylation for C–C coupling. Compared to traditional cross-coupling methods, direct arylation offers several advantages, including higher yields, fewer synthetic steps, lower catalyst requirements, and the elimination of organometallic intermediates. The incorporation of thiophene-based linkers further enhances the versatility of this approach, allowing for precise control over functionalization.

Figure 84 shows the extended tetratopic organic linker used as an SBU in a new MOF called UA-4. The Zr-based MOF was synthesized under solvothermal conditions using modulators such as trifluoroacetic acid, acetic acid, and formic acid.

This innovative strategy simplifies the synthesis of mesoporous MOFs while providing a scalable and efficient route for designing functional materials with tunable properties.

Figure 84. Extended linker of the UA-4 MOF.

However, structural characterization of the synthesized UA-4 MOF proved to be challenging. Dr. Esrafili performed PXRD and Dr. Stefano Canossa from ETH Zurich performed synchrotron XRD analysis, but both methods gave only reflections up low resolution. This is evident in Figure 85a, where the PXRD pattern shows a significant background signal (starting at  $2\theta > 15^{\circ}$ ) and only weak diffraction peaks in this angular range. Similarly, the synchrotron XRD patterns, shown in Figure 85b, exhibit low resolution, with an absence of reflections at the outer edges of the detector. The limited resolution in both PXRD and synchrotron XRD data can be attributed to poor crystallinity of the material or the presence of multiple phases, including both crystalline and amorphous components. Amorphous particles contribute to the elevated background in PXRD. Despite these limitations, Dr. Canossa was able to identify a hexagonal unit cell with parameters a = b = 39.1798 Å, c = 15.8714 Å,  $\alpha = \beta = 90^{\circ}$ , and  $\gamma = 120^{\circ}$ , corresponding to the space group P6/m, as shown in Figure 85c. While this unit cell suggests a large ~40 Å pore, closer examination reveals gaps in the linker positions, indicating that the found structure is incomplete. Additionally, the Zr-nodes appear disordered, further complicating the structural characterization of the material.

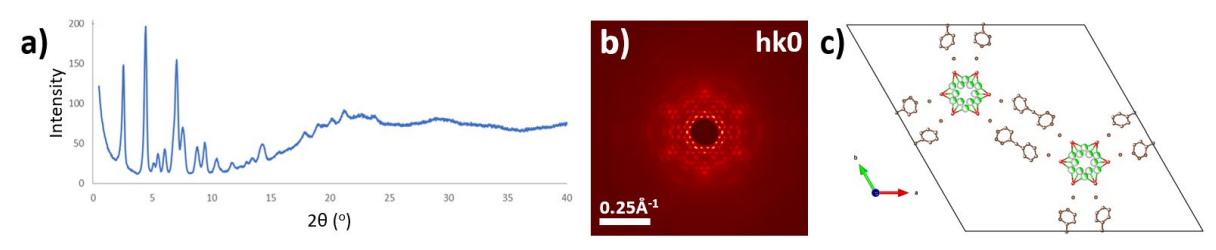


Figure 85. a) PXRD pattern of UA-4. b) Reconstructed hk0 section from synchrotron XRD data. c) Solved unit cell based on synchrotron XRD data.

To further resolve the structure of the UA-4 MOF, multiple 3D ED experiments were performed at room temperature using the cRED acquisition technique, as part of this thesis. Low magnification TEM imaging analysis combined with ED confirmed the presence of two distinct phases: particles lacking defined morphology and showing no Bragg reflections, thus labelled amorphous, and crystalline particles with well-defined edges and clear Bragg reflections (Figure 86). Particle sizes ranged from 500 nm to 2.5 µm for both particle types.

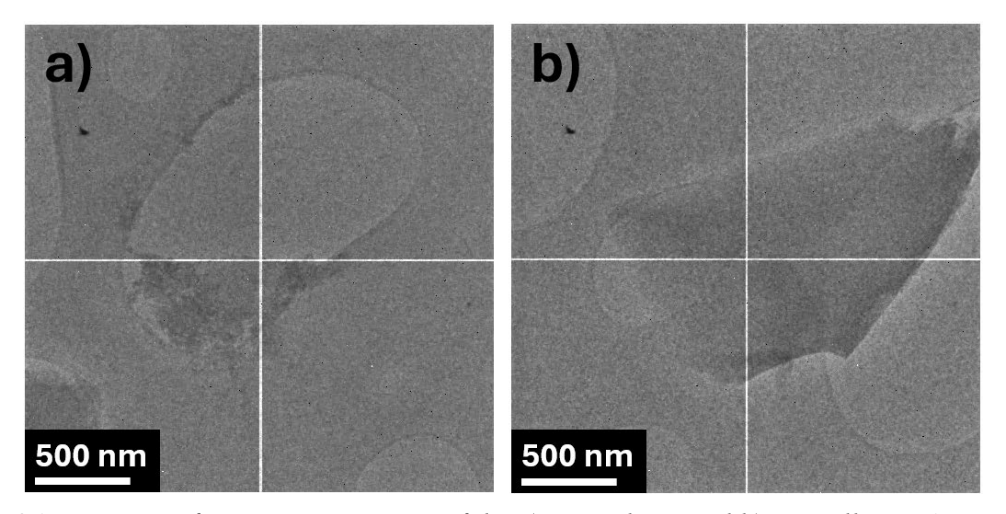


Figure 86. Low magnification TEM images of the a) amorphous and b) crystalline UA-4 particles. The bright cross in the images is an artefact of the detector, appearing at the junction where the four detector chips are connected.

Data processing in PETS identified the same hexagonal unit cell previously determined from synchrotron XRD data. In the 3D ED datasets, the resolution also remained exceptionally low, averaging around 3.5 Å, which is comparable to, or even lower than, typical protein crystallography resolutions. Table 10 presents the key parameters of the data reduction in PETS such as the unit cell parameters, average resolution, mosaicity, and  $R_{\rm int}$  values for all datasets.

The low  $R_{int}$  values are a result of the poor resolution and therefore the limited number of reflections. In contrast, higher-resolution reflections often deviate more, which can increase the  $R_{int}$  value. To enhance the likelihood of successfully solving the structure by increasing the completeness of the reciprocal space, the seven individual datasets were merged into a single combined dataset.

Table 10. Key structural parameters obtained from data reduction in PETS for each individual particle, as well as for the merged dataset combining all individual particles. The R<sub>int</sub> value for the 6/m Laue class is given. The average and maximum resolution values correspond to the mean resolution across all frames and the highest resolution achieved in any single frame within the 3D ED dataset, respectively.

Particle	Average	Max	a (Å)	c (Å)	Mosaicity	Completeness	$R_{\mathrm{int}}$
#	res.	res.				(%)	(obs)
	(Å)	(Å)					
1	3.70	1.89	39.84	15.23	0.1	84.5	9.03
			(4)	(1)			
2	2.86	1.67	39.97	15.225	0.1	79.8	12.23
			(2)	(5)			
3	3.33	1.69	39.65	15.413	0.1	87.0	9.87
			(4)	(8)			
4	3.70	1.69	40.74	15.21	0.1	81.4	10.30
			(3)	(2)			
5	3.13	1.67	39.60	15.326	0.1	90.7	11.34
			(3)	(5)			
6	3.33	1.67	40.49	14.961	0.1	90.9	11.92
			(2)	(6)			
7	2.44	1.67	40.56	15.08	0.1	89.0	12.23
			(2)	(6)			
Merged	3.45	1.69	40.0887	15.185	0.15	99.0	8.95
			(7)	(2)			

While Jana2020 successfully supported the P6/m space group for both individual datasets and the merged dataset, conventional structure solution methods in Jana2020 and Olex2, such as charge flipping, superflip, intrinsic phasing, and direct methods, were unsuccessful in solving the unit cell of the material. These approaches produced unrealistic unit cells, likely due to the overall low resolution of the data.

Inspired by techniques commonly used in protein crystallography, where low-resolution data is a known challenge <sup>148–150</sup>, an alternative approach was explored using the program SIR2019 <sup>151</sup>. This software applies a structure solution method called Simulated Annealing (SA)<sup>8</sup>, which operates similarly to molecular replacement in protein studies <sup>152–154</sup>. SA allows the incorporation of prior knowledge about the material (such as unit cell dimensions, space group, and expected unit cell content) to solve and refine the structure. The method can also use predefined structural fragments (known components of the unit cell) to improve the accuracy of the solution. The predefined fragments are placed within the unit cell, and their positions are adjusted through random movements, similar to Monte Carlo simulations. At each step, the R-factor is calculated to evaluate the fit of the structure.

If the R-factor decreases, the simulation temperature is gradually reduced, thereby decreasing the magnitude of the structural adjustments. This iterative process continues, refining the structure step by step until the lowest possible R-factor is achieved, leading to a more accurate structural solution. Since no prior information was available regarding the Zr-node in the UA-4 structure, a known and structurally simple Zr-node (see Figure 87a) was used as an initial fragment.

For the second fragment, the known linker structure, shown in Figure 84, was used in the structure solution process. The cif/mol-file for the linker was created from the chemical drawing shown in Figure 87b using the program ChemSketch <sup>155</sup>.

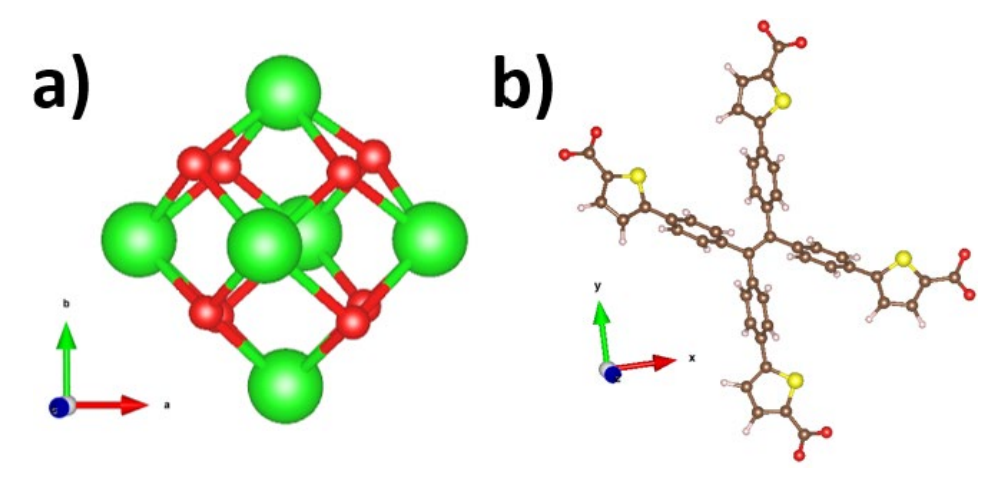


Figure 87. a) Zr-node used as the first fragment in the SA calculations. b) synthesized linker used as the second fragment in the SA calculations. O atoms are represented as red spheres, Zr atoms as green spheres, C atoms as brown spheres, and S atoms as yellow spheres. H atoms are depicted as pink spheres.

Furthermore, SA allows for certain degrees of freedom to be incorporated into the structure solution process. For the UA-4 structure, these included adjustments to the xyz positions of both fragments as a whole, as well as their rotational movements. Additionally, internal distortions were permitted for specific bonds in the second fragment, allowing the eight hexagonal rings (four phenyl and four thiophenyl rings) to rotate freely. The unit cell dimensions were kept fixed, and since both synchrotron XRD data and JANA2020 analysis confirmed the P6/m space group, this symmetry was maintained throughout the SA simulations.

Despite the limited resolution of the 3D ED data, a solution was obtained (Figure 88) using the P6/m space group, yielding an R-factor of 45.61, which is considered to be high and is caused by the low resolution. However, comparison with the unit cell obtained from synchrotron XRD data reveals strong similarities. The 3D ED based model appears more complete, as it does not exhibit the structural voids seen in the synchrotron-derived model. Given this agreement, it is plausible that the correct structure of the UA-4 MOF has been identified.

Additional refinements to the model are still possible, particularly regarding the Zr node. In the P6/m structure solution, the Zr atoms exhibit a high degree of disorder, as shown in Figure 89a.

While such disorder in MOF nodes has been reported <sup>156–158</sup>, some oxygen atoms in the structure are positioned unrealistically close to neighboring atoms.

Removing these oxygen atoms results in the modified node shown in Figure 89b. To assess its viability, an SA structure solution was performed using this adjusted node. The overall unit cell remained unchanged, though a slight increase in the R-factor to 45.76. Despite this minor increase, the revised structure is more chemically and physically reasonable than the original since all atoms in the node are at feasible distances from each other.

However, closer examination still reveals several chemically and physically unrealistic features: both the metal node and the linker exhibit an unusually high degree of disorder (Figure 88), far beyond what has been previously reported in the literature for MOF structures  $^{156-158}$ . Additionally, the interatomic distances in several regions of the structure are too short, suggesting unrealistic atomic positions. A closer examination of the linker suggests that much of its observed disorder stems from the imposed mirror plane (m) in the P6/m space group during SA simulations. When changing the space group of the structure to P6 (the same space group but without mirror symmetry) the linker adopts the configuration expected from synthesis (Figure 88).

P6/m and P6 have identical reflection conditions and Laue symmetry, making it impossible to differentiate between them using standard synchrotron XRD. The distinction can be made using 3D ED if dynamical refinement can be performed, which cannot be done in the current case because of the low resolution of the data. Crystallographic convention dictates selecting the highest symmetry space group (P6/m) when multiple space group options are possible and there is no clear reason to do otherwise. Here, the clear improvement in the chemical and physical plausibility of the model suggests that P6 is the more realistic choice.

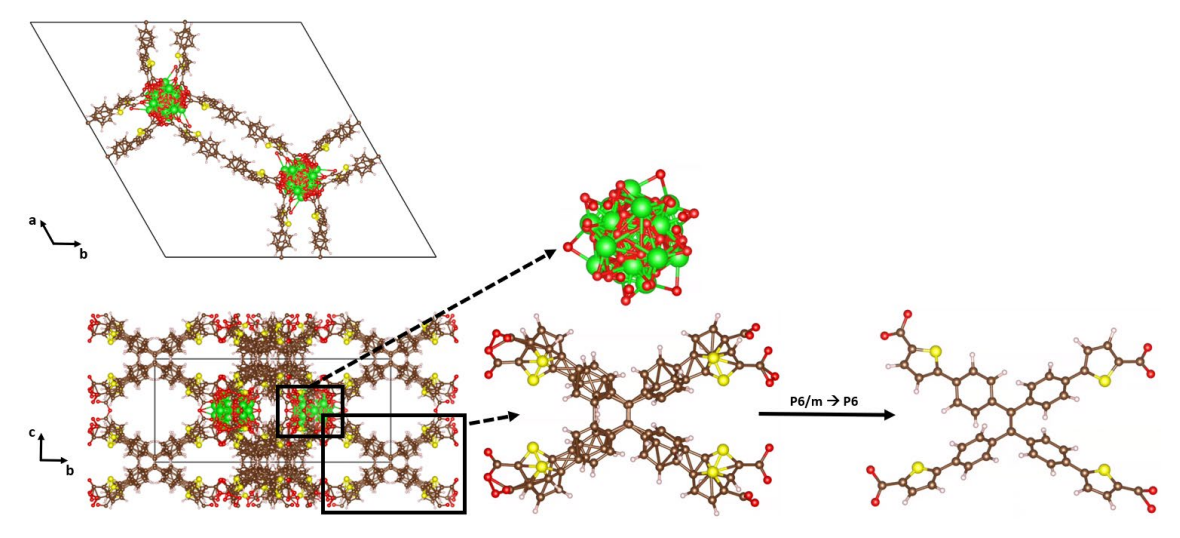


Figure 88. Initial solved structure by the SA in P6/m along with magnified images of the found Zr-node and the linker, as well as the linker in P6. Green spheres represent Zr, brown ones C, yellow ones S and red ones O.

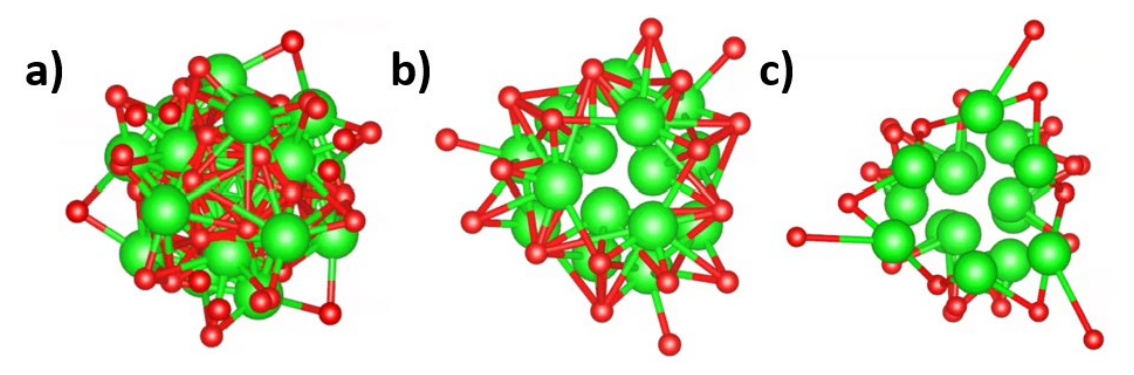


Figure 89. a) original P6/m Zr-node found by the SA. b) P6/m node with unfeasible O-atoms removed. c) P6 node with unfeasible O-atoms removed. Green spheres represent Zr, red ones O.

Final improvements can be made by considering the space group information previously discussed. Placing the Zr-node, without the extra oxygen atoms, in space group P6 instead of P6/m yields the configuration shown in Figure 89c. SA simulations using this P6 node produced a nearly identical overall structure with an R-factor of 48.30, as shown in Figure 90. Table 24 in the appendix provides the atomic coordinates for all atoms within this unit cell. Although the R-factor is slightly higher, this structure exhibits less disorder and contains no unrealistic interatomic distances. While this final structure is the most reasonable model for UA-4, there remains the possibility that the Zr-node is significantly more disordered or adopts an alternative configuration.

However, given the low resolution of the 3D ED data, further experimental confirmation of the exact nature of the Zr-node is currently not possible.

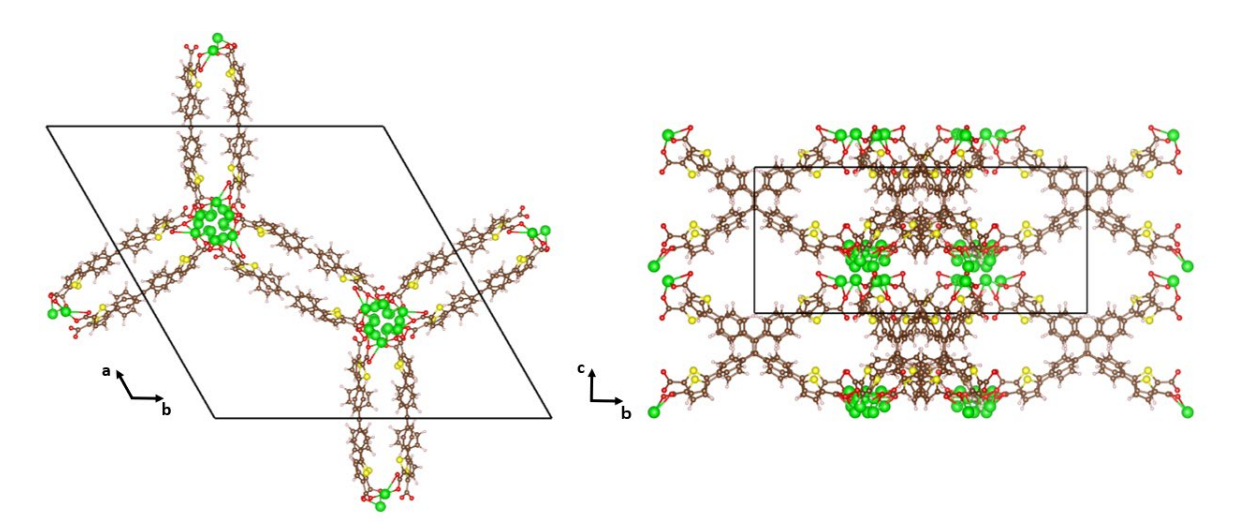


Figure 90. Final structure solution for UA-4 using the P6 space group.

A further refinement step could involve referencing known Zr-nodes in the literature, taking into account the empty space left when removing the Zr-node while keeping the linkers in place (Figure 91). However, no viable node has been identified so far.

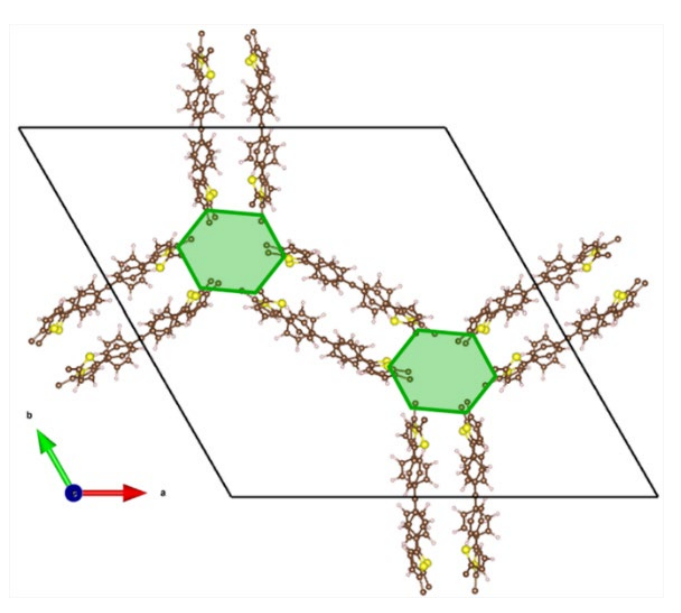


Figure 91. Illustration of the empty space left, indicated by the green hexagon, when removing the Zr-node while keeping the linkers in place.

Given the overall high R-factor, the accuracy of the proposed structure may be called into question. However, PXRD analysis provides validation of this model. Since the absolute cell parameters determined by 3D ED often show slight deviations from the actual values due to distortions caused by electromagnetic lenses, the cell parameters of our model were adjusted to match those obtained from PXRD. Compared to the original 3D ED parameters (a = b = 40.0887(7) Å, c = 15.185(2) Å,  $\alpha = \beta = 90^{\circ}$ ,  $\gamma = 120^{\circ}$ ), the optimized parameters are: a = b = 39.75 Å, c = 16.122 Å, c = 6.122 Å, c = 16.122 Å, c =

#### Experimental vs simulated PXRD patterns

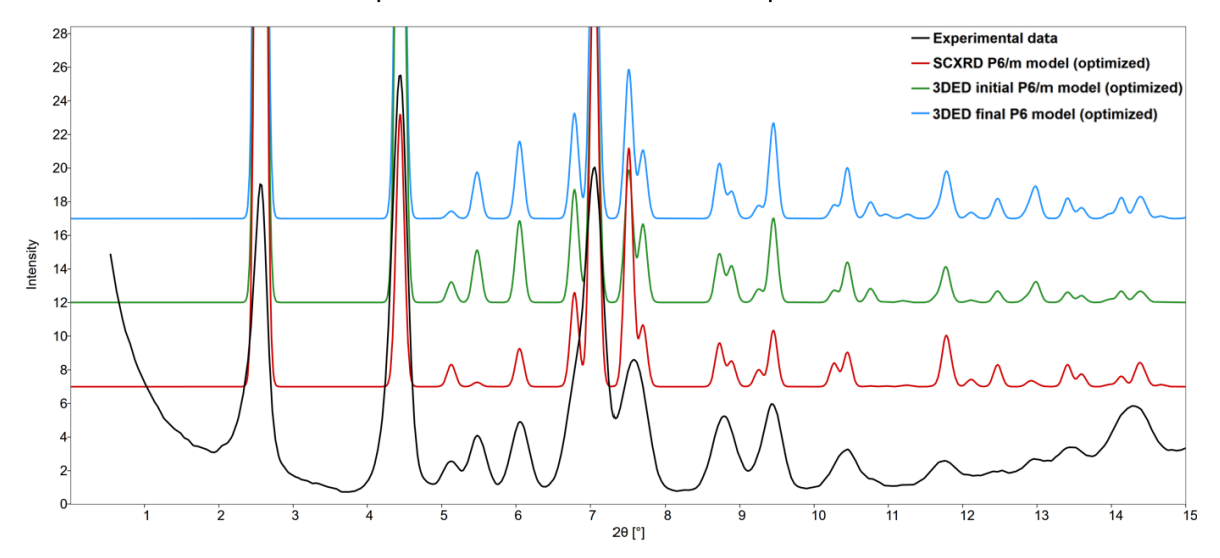


Figure 92. Experimental and simulated (initial P6/m and final P6 models, with optimized unit cell parameters) PXRD patterns of UA-4.

The low crystallinity and limited resolution observed in the 3D ED data could be due to linker rotations <sup>159,160</sup>. The linker consists of eight hexagonal rings (four phenyl and four thiophenyl), each of which can undergo a full 180° rotation, as schematically illustrated in Figure 93. When considering a large number of unit cells, these rotations result in an average structure where atomic positions are effectively smeared over the full 180° range.

This average structure creates an apparent mirror plane, aligning with the P6/m space group, even though the local structure may actually conform to P6. This could explain the difficulty in determining the correct space group in both synchrotron XRD and 3D ED analyses. Furthermore, these continuous linker rotations significantly reduce spatial periodicity, leading to diffraction patterns with inherently low resolution. Because of this low resolution, further structural refinements were not possible.

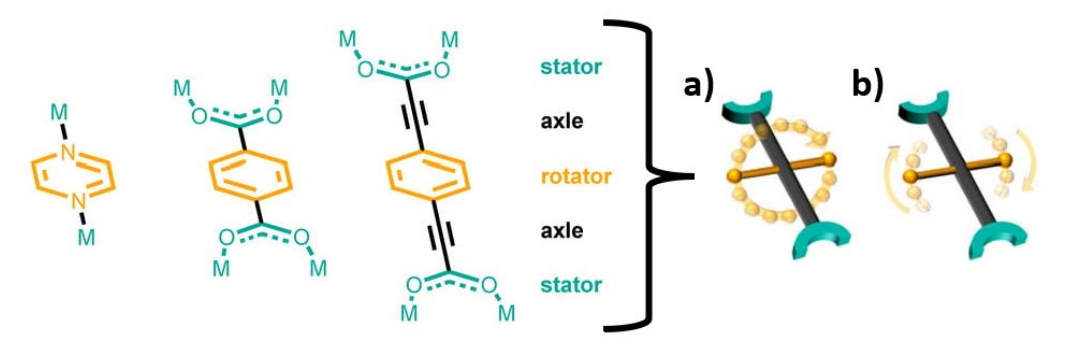


Figure 93. Schematic illustration of common types of axles MOF rotor linkers, as well as an illustration of two types of rotational linker dynamics: a) complete and b) rotation. Figure adapted from <sup>160</sup>.

### 4.5. Atmospheric studies of UiO-68

This chapter has been published as part of a paper on the use of closed cells for TEM on vacuum sensitive samples: Rahimisheikh S.; Hajizadeh A.; Quintelier M.; Stulens S.; Hardy A.; Hadermann J. Crystal structure of submicron-sized sulfur particles using 3D ED obtained in atmospheric conditions. Acta crystallographica Section C 2025. https://doi.org/10.1107/S2053229625000130.

A significant challenge in studying MOFs with a TEM is the UHV environment inside the instrument. During synthesis, MOFs are often immersed in a liquid, such as DMF, that remains within their pores after preparation. When MOF samples are introduced into the TEM's UHV conditions, the resulting pressure difference causes the liquid within the pores to rapidly evaporate. This evaporation creates surface tension that exerts a strong pulling force on the MOF's structure. Depending on the liquid used, this tension can be so severe that it pulls the MOF's linkers apart from the parent framework, causing the structure to collapse. While some methods exist to improve the stability of the MOF with regards to the application, they rarely improve the vacuum sensitivity of the MOF <sup>161</sup>.

To mitigate this issue, cryogenic conditions are frequently employed. By freezing the residual solvent within the MOF pores, structural collapse caused by evaporation is prevented. Alternatively, a systematic solvent exchange process can be employed, replacing the initial solvent with others of progressively lower surface tension  $^{162}$ . A possible exchange sequence might be: DMF  $\rightarrow$  methanol  $\rightarrow$  acetone  $\rightarrow$  dichloromethane  $\rightarrow$  hexane  $\rightarrow$  perfluoropentane.

If available, supercritical CO<sub>2</sub> can also be used in the exchange process. However, even these strategies cannot guarantee stability in the UHV environment of the TEM.

Cryogenic conditions, while useful for preserving these vacuum-sensitive MOFs during TEM experiments, limit the range of experiments that can be conducted. To enable a wider range of studies, a proof-of-concept experiment was therefore performed using the MOF UiO-68, shown in Figure 94, which is known to be vacuum-sensitive.

This MOF consists of Zr-nodes connected by 4-[4-(4-carboxyphenyl)phenyl]benzoic acid (H<sub>2</sub>TPDC) linkers, with the space group  $Fm\bar{3}m$  and cell parameters a = 32.60 Å <sup>163</sup>. Using the *in situ* gas holder, UiO-68 was studied under atmospheric conditions, allowing the sample to remain in its assynthesized state without requiring cryogenic conditions. This method not only avoids UHV-induced collapse but also opens the possibility for *in situ* gas studies that are otherwise impossible with cryogenic setups.

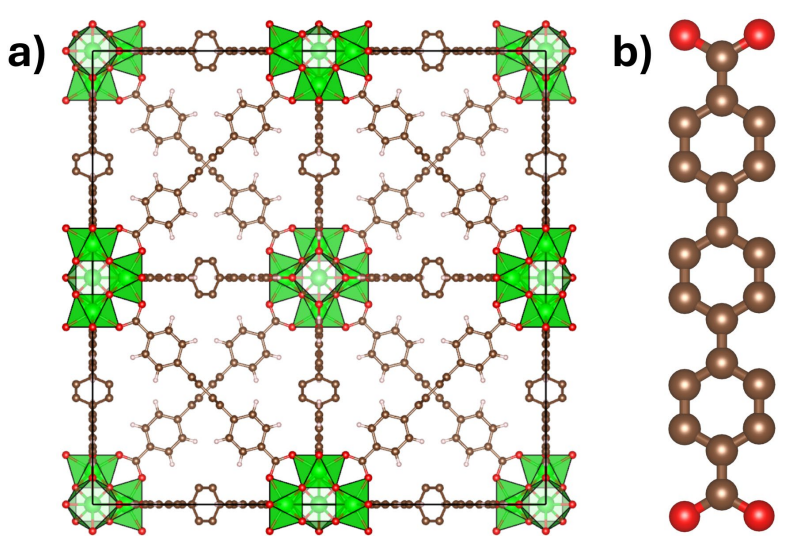


Figure 94. Illustration of a) the structure of UiO-68 and b) its  $H_2TPDC$  linker.

Figure 95 compares the diffraction patterns of the same UiO-68 particle under UHV and atmospheric air conditions after 60 seconds of exposure. Under UHV, no diffraction was observed, indicating structural collapse. However, in atmospheric air, low-resolution diffraction patterns were obtained. Despite the limited resolution, these results represent a step forward in studying vacuum-sensitive MOFs. It is unclear whether the low resolution is inherent to the material at room temperature, or whether the 3D ED study still reduces the resolution despite the lack of vacuum. The low resolution could stem from non-optimal synthesis, resulting in poor crystallinity. Alternatively, the structure's limited periodicity may result from independent rotations of the three benzene rings in the H<sub>2</sub>TPDC linker, similar to the linker behavior observed in the UA-4 MOF discussed in Chapter 4.3.

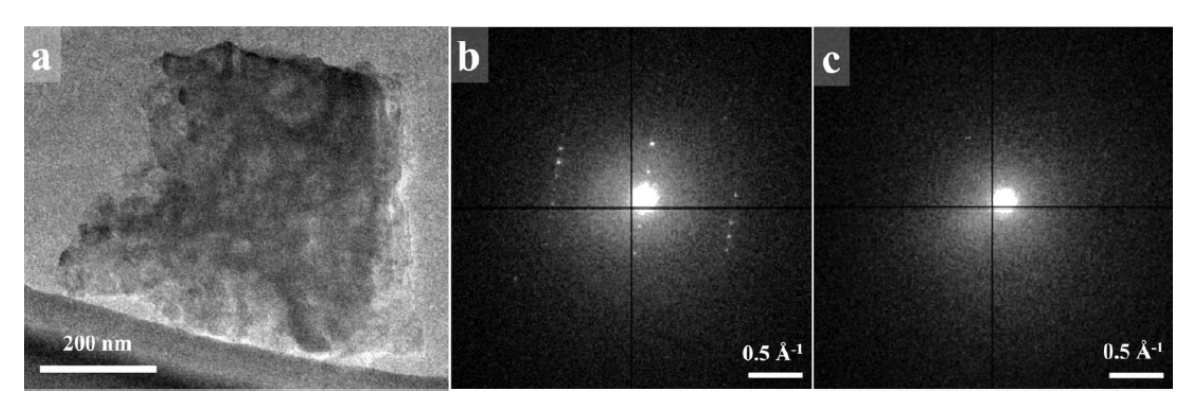


Figure 95. (a) real space image of the studied UiO-68 particle. (b and c) Diffraction patterns after 60 seconds of exposure of the same particle taken at atmospheric (b) and UHV conditions (c).

Furthermore, we observed that some UiO-68 particles degraded more rapidly in atmospheric air than expected based on previous experience with other MOFs. This degradation may be due to the interaction (radiolysis) between the electron beam and the moisture in the air: high-energy electrons can ionize water molecules, producing reactive radicals such as hydroxyl radicals, which can attack and degrade the MOF framework <sup>164–166</sup>.

To address this, a 3D ED experiment on UiO-68 under an argon atmosphere at 1 bar was conducted, simulating normal atmospheric pressure but without exposure to moisture. The nanoreactor was flushed with Ar for one hour at high flow and pressure, then sealed to maintain static conditions.

Despite these precautions, almost all particles showed little to no diffraction. Using SNBD, only a few small regions ( $\sim$ 10 nm) were identified that produced diffraction, and even these patterns were lost upon rotation of the particle.

Several factors may explain the lack of diffraction in these experiments. The ethanol used for dissolving the sample during preparation could have evaporated from within the MOF pores, causing structural damage. To test this hypothesis, the experiment was repeated using DMF instead of ethanol, as DMF has a higher boiling point (153 °C) and is also the solvent used during the material's synthesis. However, similar results were obtained, ruling out the solvent evaporation issue. Another potential cause could be the flushing process with Ar gas.

It is possible that the gas flow displaces the DMF molecules from the MOF pores. As these molecules leave the MOF structure, they may exert a pulling force on the linkers, as described earlier, leading to structural collapse.

To date, the exact cause of this structural collapse remains unclear. While factors like the use of ethanol or DMF during sample preparation, or the flushing process with Ar have been suggested, none can be definitively identified as the primary reason.

# **Conclusion to Chapter 4**

In this chapter, several MOFs were investigated, starting with MOF-74. This MOF served as a model system for determining optimal acquisition parameters for 3D ED experiments aimed at minimizing beam damage in beam-sensitive materials. The parameters established in this process are applied throughout the remaining MOF studies in this thesis. As part of the optimization, multiple detectors were tested and custom beam stoppers were designed, fabricated, and installed.

Next, the activation of M-MOF-74 (M = Cu, Zn) was studied *in situ*. For Zn-MOF-74, heating to 300 °C successfully generated open metal sites on the metal nodes, indicating effective activation. Surprisingly, heating to 350 °C did not fully clear the MOF pores as previously reported in the literature. Instead, residual electrostatic potentials were observed, suggesting the presence of remaining species that may hinder gas flow during CO<sub>2</sub> absorption. During heating, changes in unit cell parameters were observed, attributed to the inherent flexibility of the MOF.

The dynamic positions of DMF molecules, combined with solvent exchange and ultra-high vacuum conditions, result in low occupancies at the remaining sites with positive electrostatic potentials.

These positions resemble those of DMF, but their elemental composition cannot be refined due to insufficient occupancy. At higher temperatures (300 °C and 350 °C), the remaining potentials might be due to unbound linkers, residual ethanol, or atomic residue. In contrast, Cu-MOF-74 exhibits a faster activation. Open metal sites were formed immediately after solvent exchange and exposure to ultra-high vacuum, rendering further heating to 120 °C relatively ineffective.

This rapid activation is attributed to the weaker Cu-O bond compared to Zn-O, which makes the Cu-O bond between the MOF structure and DMF more easily breakable, along with Cu's greater Lewis acidity. Additionally, Cu-MOF-74 formed an amorphous carbon matrix with small Cu nanoparticles after heating to 300 °C. This difference in thermal stability is linked to Cu's higher Lewis acidity and second-order Jahn-Teller distortions within the metal octahedra of Cu-MOF. These findings show the varied activation dynamics and behaviors of different metal-based MOFs, providing insights into the activation of MOF-74 that could inform future MOF applications and design.

Building on this, the influence of CO<sub>2</sub> adsorption on the structure of Zn-MOF-74 was studied *in situ* using 3D ED. This work provided the first experimental evidence of CO<sub>2</sub> positions within Zn-MOF-74, revealing that CO<sub>2</sub> adopts non-linear configurations upon adsorption, contradicting previous assumptions of a linear geometry. Our findings suggested that the interaction involves more than weak van der Waals forces, incorporating donor-acceptor interactions between CO<sub>2</sub> and Zn<sup>2+</sup> sites. The identification of two distinct viable CO<sub>2</sub> binding geometries highlights the complexity of the adsorption mechanism. The CO<sub>2</sub> geometries can be explained by the close proximity of the CO<sub>2</sub> carbon atom to oxygen atoms within the MOF framework. The strong interaction with the Zn atom likely polarizes the CO<sub>2</sub> molecule, enabling additional interactions between the CO<sub>2</sub> and the surrounding framework. Additionally, the observed structural collapse after CO<sub>2</sub> desorption suggests that strong CO<sub>2</sub>-MOF interactions may contribute to framework instability, explaining the decline in CO<sub>2</sub> uptake over multiple cycles reported in the literature.

Several enzyme–MOF biohybrid samples were also examined, where catalytic enzymes were encapsulated within a MOF framework. Multiple attempts were made to directly observe the position of the enzymes within the MOF framework. During this process, a novel staining method was developed using metallic salts to selectively label the enzymes. This technique proved effective in locating the enzymes within the MOF. Combined with results from our 3D ED experiments, which show (despite the difference only being minimal) that the biohybrid samples consistently exhibited larger unit cell parameters, likely due to the enzyme exerting pressure on the MOF framework, we can conclude that both the enzyme encapsulation and the staining method were successful.

A new MOF, UA-4, made using a novel synthesis method, is also investigated using 3D ED. The structural characterization of this MOF proves to be highly challenging due to its poor crystallinity, as indicated by PXRD, synchrotron XRD, and 3D ED data.

Despite this limitation, a hexagonal unit cell could be identified. Structure solution using simulated annealing with predefined structural fragments resulted in a plausible structure.

The observed low resolution in diffraction data was likely caused by dynamic linker rotations, which reduced long-range periodicity, further complicating structural determination.

Finally, an atmospheric *in situ* TEM study was carried out on UiO-68. Despite several challenges, this proof-of-concept experiment demonstrates that *in situ* gas environments could be used to study vacuum-sensitive MOFs without the limitations of cryogenic conditions. While diffraction data could be obtained under ambient conditions, structural damage is still observed, possibly caused by interactions between the electron beam and moisture molecules present in the surrounding air. This approach will allow us to study structural evolutions of vacuum sensitive MOFs in their assynthesized state and under *in situ* gas conditions.

## Chapter 5: ZnO

This chapter has been published: Rodríguez-Jara E.; Cavallo M.; Nakazato R.; Quintelier M.; Matsumoto K.; Hadermann J.; Mosa J.; Bonino F.; Tadanaga K.; Aparicio M.; Rosero-Navarro NC. Zinc oxides by thermal decomposition synthesis and parameters affecting electrocatalyst activity for CO<sub>2</sub> reduction reaction. Open Ceramics 2025. https://doi.org/10.1016/j.oceram.2024.100733. In these works, I have provided the nanoscale characterization of the materials under investigation.

This chapter aims to investigate the relation between the structure and morphology and catalytic properties of ZnO nanomaterials for application in CO<sub>2</sub>RR, as achieved after various different syntheses as well as after changes in environment.

### 5.1. Introduction to Zinc Oxide

Precious metals like gold, silver, platinum, and their derivatives have long been used in CO<sub>2</sub> reduction reactions (CO<sub>2</sub>RR), producing valuable products such as carbon monoxide, hydrogen, formic acid, and ethylene <sup>167</sup>. However, their high cost limits their use in large-scale applications. Similarly, while elements like cobalt have shown great potential as CO<sub>2</sub>RR electrocatalysts, their availability is limited, often leading to geopolitical challenges. As a result, the development of electrocatalysts from more abundant and affordable metals has become an important focus in research. Metals such as copper, bismuth, nickel, iron, and zinc are particularly promising due to their cost-effectiveness, availability, and performance potential.

Among these, zinc oxide (ZnO) has shown potential as an efficient electrocatalyst for CO<sub>2</sub>RR <sup>168</sup>. ZnO-based materials are especially notable for their ability to enhance electrocatalytic activity. Faradaic efficiency for CO production during CO<sub>2</sub>RR has been reported across a wide range, from 20% to 80%, depending on the material's structure, synthesis method, and surface modifications <sup>169–171</sup>. This broad variability highlights the importance of optimizing ZnO's properties to improve its performance.

As part of this work, our collaborators Elías Rodríguez and Dr. Carolina Rosero from ICS-CSIC (Madrid, Spain) explored new synthesis methods for ZnO, focusing on thermal decomposition and coprecipitation. This approach offers a low-cost, scalable, and environmentally friendly alternative to conventional techniques. Within this thesis, I investigated using TEM how the different heating rates and temperatures used during synthesis influence the morphology and elemental distribution of ZnO-based materials.

By linking these structural features to their physicochemical properties and electrocatalytic performance in CO<sub>2</sub>RR, this work contributes to the development of more efficient ZnO-based electrocatalysts.

Beyond CO<sub>2</sub>RR, ZnO has a wide range of applications in electronics, as it is used for sensors <sup>172</sup>, transparent conducting films <sup>173</sup>, and light-emitting diodes <sup>174</sup> due to its semiconducting properties. ZnO also plays a key role in photocatalysis <sup>175</sup>, especially for breaking down organic pollutants under UV light, making it useful for environmental remediation.

Its biocompatibility and antimicrobial properties also make it an excellent candidate for medical applications, such as wound dressings and drug delivery systems <sup>176,177</sup>.

According to literature, ZnO has a wurtzite crystal structure, characterized by a hexagonal lattice with unit cell parameters of a = b = 3.351 Å, c = 5.226 Å,  $\alpha = \beta = 90^{\circ}$ ,  $\gamma = 120^{\circ}$  with space group  $P6_3mc^{178}$  (Figure 96).

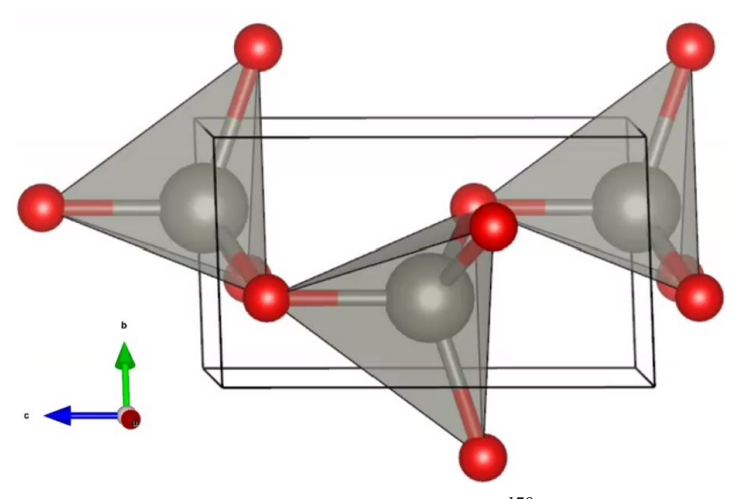


Figure 96. ZnO structure <sup>178</sup>.

### 5.2. Effects of synthesis on morphology

Two ZnO materials were synthesized through thermal decomposition of zinc acetate dihydrate  $(Zn(CH_3CO_2)\cdot 2H_2O)$  in stagnant air with 54% relative humidity for three hours, varying the treatment temperature between 300 °C and 400 °C. A third ZnO material was prepared by a coprecipitation method, in which zinc acetate dihydrate was mixed with methanol and stirred at 60 °C for 24 hours while KOH was added dropwise. The resulting solution was washed with methanol to obtain ZnO particles.

The HAADF-STEM images (Figure 97) show distinct morphological differences between the particles synthesized using the different methods. The crystalline or amorphous nature was determined using the observation or absence of Kikuchi lines. Thermal decomposition at 300 °C yielded needle-shaped nanorod ZnO particles accompanied by shapeless amorphous nanoparticles. STEM-EDX analysis indicated a homogeneous ZnO composition with a Zn:O ratio of 50(3):50(3) throughout the particles.

Thermal decomposition at 400 °C resulted in triangular-shaped crystalline particles with a Zn:O ratio of 54(1):46(1) along with amorphous nanoparticles with a Zn:O ratio of 53(1):47(1). In contrast, the coprecipitation method produced herringbone-shaped crystalline ZnO particles with a Zn:O ratio of 50(1):50(1), as shown in Figure 97c, accompanied by amorphous particles with a Zn:O ratio of 33(1):67(1).

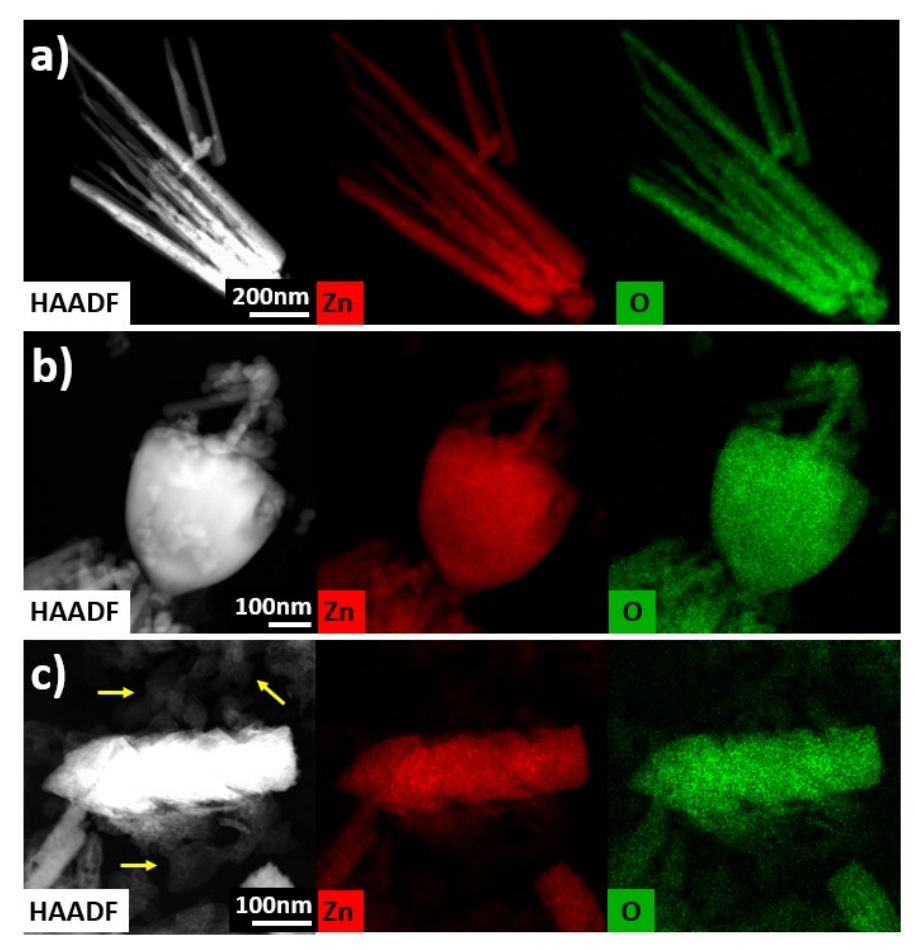


Figure 97. HAADF-STEM images and Zn & O STEM-EDX elemental maps for ZnO samples synthesized by: a) nanorods resulting from thermal decomposition at 300 °C, b) triangular-shaped particles resulting from thermal decomposition at 400 °C and c) herringbone-shaped particles along with amorphous particles (indicated by yellow circles), resulting from coprecipitation, which are indicated by the yellow arrows. The EDX maps are shown in counts.

Figure 98 shows the electrocatalytic activity for CO<sub>2</sub>RR of the different samples. These experiments demonstrated that particles synthesized through thermal decomposition at 300 °C (Figure 97a) exhibit the highest catalytic activity for converting CO<sub>2</sub> to CO, followed by those made at 400 °C (Figure 97b). In contrast, the particles synthesized via the coprecipitation method (Figure 97c) show the lowest activity. The superior performance of the 300 °C thermal decomposition particles may be attributed to their nanorod morphology, which provides a larger contact surface area compared to the particles made with the other synthesis techniques, enhancing their efficiency for CO<sub>2</sub>RR.

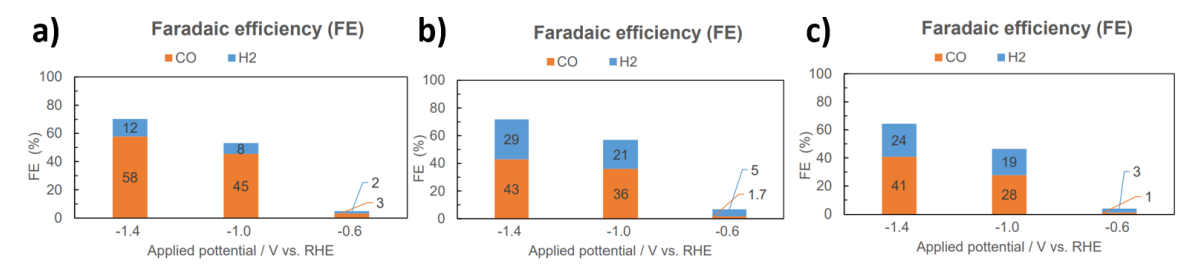


Figure 98. Faradaic efficiency for CO and  $H_2$  of ZnO synthesized by thermal decomposition at a)  $300 \,^{\circ}\text{C}$ , b)  $400 \,^{\circ}\text{C}$  and c) coprecipitation.

After identifying the optimal synthesis method for ZnO particles with the highest catalytic activity, these particles were further modified to enhance their performance. Given aluminum's known high catalytic activity for CO<sub>2</sub>RR <sup>179–181</sup>, the collaborators attempted to coat the ZnO nanorod particles with aluminum using aluminum-tri-sec-butoxide. The coating process involved stirring aluminum-tri-sec-butoxide with isopropanol, followed by dropcasting the solution onto the ZnO particles.

The coated particles were analyzed using atomic resolution HAADF-STEM and STEM-EDX. HAADF-STEM imaging showed that the coating process did not alter the overall size or morphology of the ZnO particles. STEM-EDX confirmed the presence of the aluminum coating, although it was inhomogeneously distributed, as shown in Figure 99a. The coating appeared both in bulk sections atop the particles and as a thin layer along their edges. The edge coating was approximately 4.5–5 nm thick and displayed a non-uniform distribution. Elemental analysis identified the edge coating as Al<sub>2</sub>O<sub>3</sub>, and atomic resolution HAADF-STEM images showed a crystalline structure with a thickness of 2-5 atomic layers, as shown in Figure 99b.

Subsequent electrocatalytic measurements showed an increase in Faradaic efficiency for CO, improving from 58% for pure ZnO nanorods to 74% for the Al-coated particles.

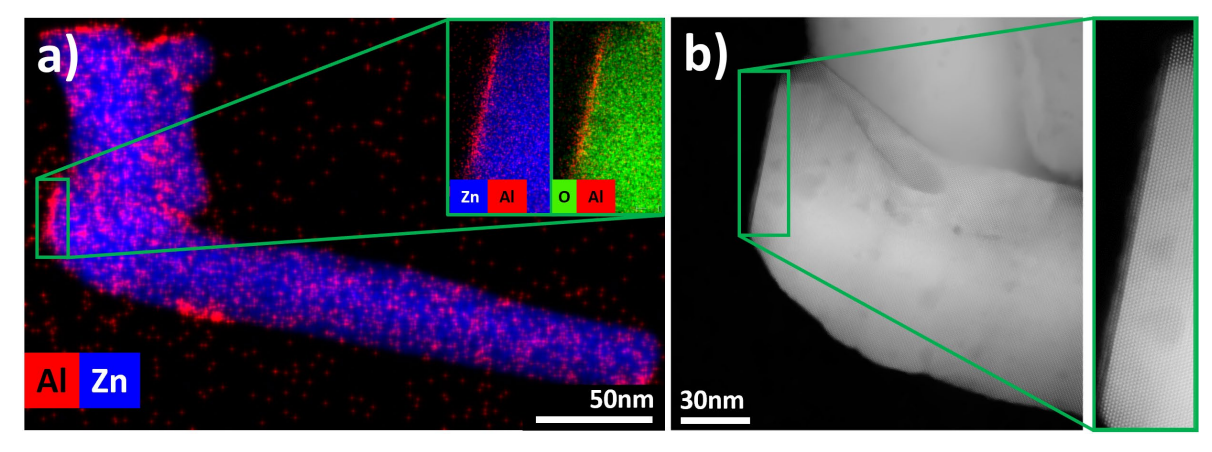


Figure 99. a) Al/Zn STEM-EDX map of the entire particle shown in b). The insets display the Zn/Al and O/Al STEM-EDX maps of the same magnified edge. The map is shown in counts. b) High-resolution HAADF-STEM image of a ZnO edge with an inset magnifying the first few atomic layers of the edge, where a thin amorphous coating can be observed atop the sharp ZnO edge.

### 5.3. *In situ* study of ZnO

After identifying the synthesis method that yielded the highest Faradaic efficiency (nanorod ZnO particles produced by thermal decomposition at 300 °C) the next step was to investigate the effect of CO<sub>2</sub> exposure on these particles.

Before studying CO<sub>2</sub> interactions, the ZnO material needed to undergo a specific pre-treatment, similar to the activation process used for MOFs (discussed in Chapter 4.1.1), but adapted for ZnO. This involved gradually heating the material to 500 °C, holding it at that temperature for three hours, and then exposing it to two cycles of 60 mbar O<sub>2</sub> gas for 20 minutes each, followed by rapid cooling. This procedure is intended to remove residual impurities from the ZnO particles, though its impact on their morphology and structure is unknown in literature. Once activated *in situ*, the material was exposed to CO<sub>2</sub> to assess any potential structural or morphological changes.

To study these changes, HAADF-STEM, 3D ED, and SNBD were used at different stages (before heating, after cooling following O<sub>2</sub> exposure, and after CO<sub>2</sub> exposure) to allow a detailed investigation of possible transformations.

HAADF-STEM was used to examine the overall particle morphology and particle surfaces for modifications, 3D ED to provide insight into overall structural changes and SNBD to assess the crystallinity of any new surface layers that form. A schematic overview of the entire experimental workflow is shown in Figure 100. STEM-EDX was also attempted to obtain elemental information at each stage, but due to the closed-cell design of the *in situ* holder and the metal top lid sealing the nanoreactor (see Figure 19a), combined with the small particle size, the X-ray signal was too weak to allow for reliable elemental identification.

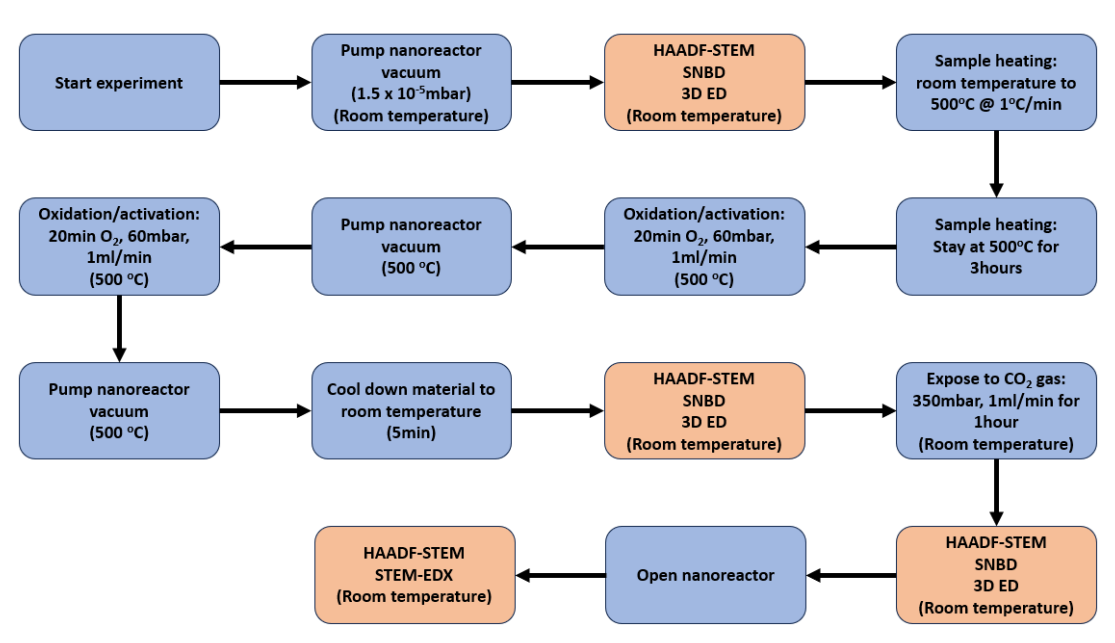


Figure 100. Schematic illustration of the workflow of the in situ ZnO study.

Figure 101 shows HAADF-STEM images of a representative ZnO particle at three stages: before O<sub>2</sub> treatment, after O<sub>2</sub> treatment, and after CO<sub>2</sub> exposure. After the O<sub>2</sub> treatment, an approximately 15nm thick amorphous-looking layer appears around the ZnO particle, as indicated by the white arrows, and remains present even after CO<sub>2</sub> exposure.

The SNBD scans also suggest that this layer is likely amorphous, as no measurable diffraction pattern was detected at those scan positions. Additionally, analysis of the 3D ED data collected at each stage of the experiment revealed no changes in structure. All datasets consistently showed the known wurtzite ZnO unit cell, with unit cell parameters of a = b = 3.35 Å, c = 5.226 Å,  $\alpha = \beta = 90^{\circ}$ , and  $\gamma = 120^{\circ}$ .

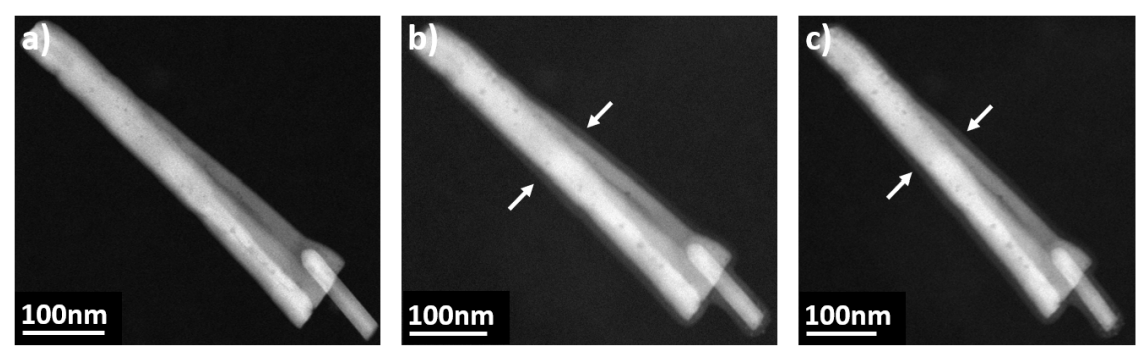


Figure 101. HAADF-STEM images of the ZnO material a) before heating and exposure to  $O_2$ , b) after heating and exposure to  $O_2$  and c) after exposure to  $CO_2$ . The formed layer is indicated in b) and c).

While it might initially seem that the layer formation is solely a result of the O<sub>2</sub> treatment and it is the only structural change occurring during this process, it closely resembles the SiO layer formation described in <sup>182</sup>. This study showed the formation of a SiO layer following the interaction of a sample with an oxidizing environment at elevated temperatures, conditions similar to those used in this experiment. The resulting layer forms around the entire particle, preventing further oxidation or other reactions. This process is reminiscent of strong metal-support interactions<sup>183–185</sup> where a strong interaction between nanoparticles and their support leads to the encapsulation of the metal by a thin layer derived from the support material. In our case, a similar interaction appears to occur between the Si<sub>3</sub>N<sub>4</sub> window, the ZnO particle, and the O<sub>2</sub> gas.

To verify this, the nanoreactor was opened, and the material was studied using an open cell setup, which included only a single Si<sub>3</sub>N<sub>4</sub> window. By removing the second window, more X-rays could be detected from the material, making STEM-EDX analysis possible. Figure 102 shows the HAADF-STEM image of the particle from Figure 101, alongside the corresponding Zn/Si STEM-EDX elemental maps. The elemental map shows an increased concentration of Si around the particle, precisely where the amorphous edge is located, confirming that the layer contains Si.

A line profile across the particle, shown in Figure 102c, further supports this observation, showing an increase in Si and O content at the amorphous layer. Oxygen is detected across the entire width of the line profile, which is unexpected since the  $Si_3N_4$  window should not inherently contain this level of oxygen.

This suggests that a thin  $SiO_x$  layer may have formed on the  $Si_3N_4$  window itself, with the highest concentration near the particle, likely due to localized reactivity. However, it is also important to consider that the O signal across the particle could be influenced by exposure to ambient air after opening the nanoreactor. This, however, would not fully explain the pronounced increase in oxygen near the edges of the particle.

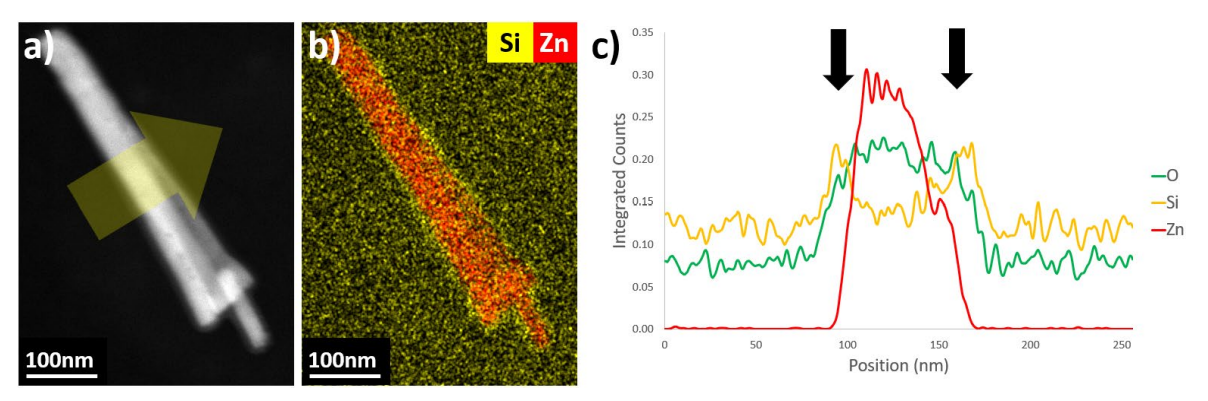


Figure 102. a) HAADF-STEM image of the particle. b) Zn/Si STEM-EDX elemental map. The map is given in counts. c) Line profile taken across the area indicated in a). The position of the  $SiO_x$  edge around the particle is indicated using black arrows.

We can therefore conclude that the formed layer is indeed  $SiO_x$ , resulting from an interaction between the  $Si_3N_4$  window, the  $O_2$  gas, and the ZnO particle. This indicates that the layer was not solely formed due to the  $O_2$  treatment of the particle, and it likely prevented any reactions with the  $CO_2$ . To determine whether the  $SiO_x$  layer forms only at the edges of the ZnO particles or as a complete coating around the particle, PCA combined with NMF analysis was applied to the STEM-EDX data. This method could separate the EDX signal into three distinct components: the ZnO particle, the  $Si_2N_4$  background, and the  $SiO_x$  layer.

As shown in Figure 103, the ZnO signal (Figure 103a) corresponds to the particle, while the  $Si_3N_4$  signal (Figure 103b) reflects the expected background from the  $Si_3N_4$  window. The  $SiO_x$  signal (Figure 103c) shows a clear increase at the particle edges, indicating the presence of an  $SiO_x$  layer. A line profile across the particle (Figure 103d) further confirms this, displaying a distinct  $SiO_x$  edge. However, the signal in the area of the particle does not return to the baseline intensity found next to the particles, suggesting that the  $SiO_x$  layer forms a coating over the entire particle.

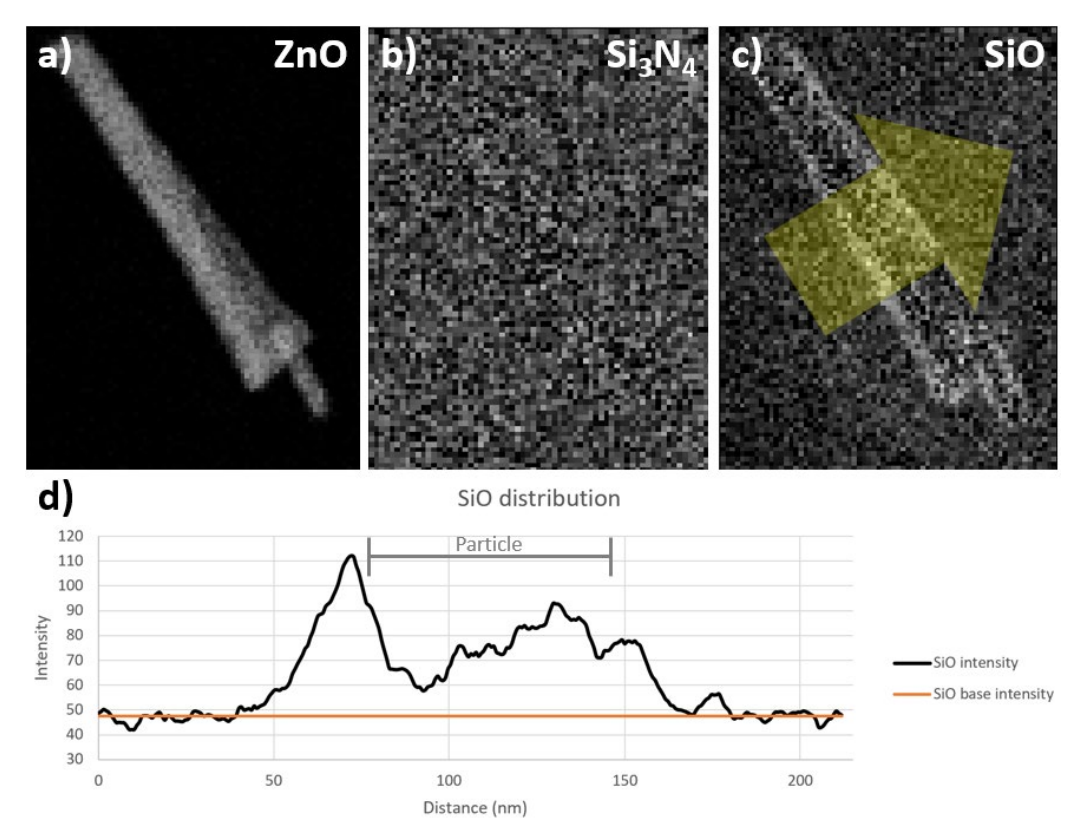


Figure 103. Results of the PCA combined with NMF analysis. The signals shown are a) ZnO, b)  $Si_3N_4$ , and c)  $SiO_x$ . d) shows a lineprofile taken across the line shown in c). The area of the particles is indicated in d).

This phenomenon has been extensively studied within our group, as it has consistently occurred whenever oxidizing conditions were applied to the (metal oxide) materials investigated <sup>182</sup>. While it was initially considered a sample-specific issue, this *in situ* ZnO experiment demonstrates that the problem is broader than previously assumed. Attempts to mitigate this effect, such as coating the Si<sub>3</sub>N<sub>4</sub> window with graphene or amorphous carbon, have shown some promising results, but no definitive solution has yet been found. Other manufacturers of chips/in situ holders have also encountered a similar issue and have solved it by slightly changing the composition of their windows. Therefore, we conclude that with the current instrumentation, reliably studying the evolution of the ZnO crystal structure upon oxidation in O<sub>2</sub> or CO<sub>2</sub> *in situ* is not possible due to interference from SiO<sub>x</sub> layer formation. This conclusion highlights another difficulty during *in situ* TEM experiments.

## **Conclusion to Chapter 5**

This chapter explores the TEM characterization of the nanoscale morphology and elemental distribution, alongside the synthesis and electrocatalytic performance of ZnO-based materials for CO<sub>2</sub> reduction reactions. The focus is on the study of morphology and surface modifications as a function of synthesis methods, and their link to improved catalytic activity. ZnO nanorods synthesized at 300 °C showed the highest CO<sub>2</sub>RR activity, likely due to their increased surface area, as confirmed by TEM imaging. Building on this, aluminum coatings were introduced to further improve performance, leading to a significant increase in Faradaic efficiency. STEM-EDX elemental analysis confirmed the presence of an inhomogeneous Al<sub>2</sub>O<sub>3</sub> coating, with a crystalline layer approximately 3–5 atoms thick. While these modifications enhanced catalytic activity, the coating process remains inconsistent and requires further refinement for uniform deposition.

The *in situ* study of ZnO under oxidizing conditions was hindered by the formation of a SiO<sub>x</sub> coating around the particles after O<sub>2</sub> exposure. This coating, caused by a reaction between the Si<sub>3</sub>N<sub>4</sub> window, ZnO, and O<sub>2</sub> gas, prevents further interactions and mirrors SiO<sub>x</sub> formation reported in previous studies. Structural analysis using SNBD confirmed that the ZnO retains its wurtzite structure throughout, with no detectable changes apart from the amorphous surface layer. STEM-EDX verified the presence of Si and O, confirming that the coating originates from the Si<sub>3</sub>N<sub>4</sub> support rather than the ZnO itself. No definitive solution has been found yet to prevent this SiO<sub>x</sub>, making it currently impossible to study ZnO transformations during oxidation using the available *in situ* TEM equipment, without interference from SiO<sub>x</sub> formation.

### General conclusion to the thesis

This thesis presents experiments that used transmission electron microscopy (TEM) to gain insights into the structure and behavior of materials used in catalysis, with a particular focus on CO<sub>2</sub> reduction reactions (CO<sub>2</sub>RR). The crystal structure and morphology of layered double hydroxides (LDHs), metal-organic frameworks (MOFs), and ZnO-based catalysts are investigated to better understand their suitability and performance in CO<sub>2</sub>RR applications. Our results link synthesis methods and processing conditions, via crystal structure and nanoscale morphology, to the physical properties and catalytic performance.

At the start of these studies, I developed a 3D-printed dropcasting tool (MDT) that improved sample preparation for *in situ* TEM by enhancing particle distribution and minimizing contamination. This simple and cost-effective tool helped reduce experimental costs. Furthermore, I designed new beam stoppers which were fabricated and implemented into the microscopes and used in this study.

LDHs were studied in detail, showing how factors like cation ratio, aging, and grinding strongly affect morphology, crystallinity, and performance. ZnAl (2:1) LDH showed the highest potential for CO<sub>2</sub>RR, and *in situ* experiments highlighted how thermal behavior heavily depends on the surrounding atmosphere. *In situ* TEM studies using CO<sub>2</sub> at room temperature for this material showed subtle structural changes, including an expansion of the basal spacing.

MOF-74 served as a model system for optimizing low-dose 3D ED acquisition parameters, which were later applied to other beam-sensitive MOFs. *In situ* activation experiments showed different behaviors for Zn- and Cu-based MOFs, with Cu-MOF-74 activating faster but forming Cu nanoparticles in amorphous carbon at elevated temperatures. *In situ* CO<sub>2</sub> adsorption experiments on Zn-MOF-74 revealed non-linear binding geometries and framework collapse after desorption, pointing to stronger interactions and previously unrecognized CO<sub>2</sub> coordination geometries.

Enzyme-MOF biohybrids were also studied using a novel metallic salt staining method, allowing direct visualization of enzyme encapsulation. Combined with 3D ED data showing expanded unit cells, these results confirmed successful encapsulation and introduce a new approach for studying such systems.

A newly synthesized MOF (UA-4) was also structurally characterized, despite significant disorder which complicated the structure solution.

Finally, *in situ* gas experiments on UiO-68 demonstrated that vacuum-sensitive MOFs can be studied without cryogenic conditions.

ZnO-based catalysts were optimized through various synthesis routes and surface treatments, with nanorods formed at 300 °C showing the best performance. Aluminum coatings further improved efficiency, though coating consistency remains a challenge. *In situ* studies were unsuccessful due to the formation of a SiO<sub>x</sub> layer, caused by interactions with the microscope's Si<sub>3</sub>N<sub>4</sub> support grid.

## Algemene conclusie van de thesis

Deze thesis beschrijft experimenten waarbij transmissie-elektronenmicroscopie (TEM) werd gebruikt om inzicht te krijgen in de structuur en het gedrag van materialen die worden gebruikt in katalyse, met een bijzondere focus op CO<sub>2</sub>-reductiereacties (CO<sub>2</sub>RR). De kristalstructuur en morfologie van layered double hydroxides (LDHs), metaal-organische roosters (MOFs) en op ZnO-gebaseerde katalysatoren werden onderzocht om hun geschiktheid en prestaties voor CO<sub>2</sub>RR-toepassingen beter te begrijpen. Onze resultaten leggen een verband tussen synthesemethoden en verwerkingscondities, via kristalstructuur en morfologie op nanoschaal, met de fysische eigenschappen en katalytische prestaties.

Aan het begin van deze studies ontwikkelde ik een 3D-geprinte dropcasting-tool (MDT) die de monstervoorbereiding voor *in situ* TEM verbeterde door een betere verdeling van de deeltjes en minder contaminatie. Deze eenvoudige en kostenefficiënte tool verlaagde de experimentele kosten aanzienlijk. Daarnaast ontwierp ik nieuwe beamstoppers die vervolgens gefabriceerd en in de microscopen geïntegreerd werden en gebruikt zijn in dit onderzoek.

LDHs werden in detail bestudeerd, waarbij werd aangetoond dat factoren zoals de kationenverhouding, veroudering en malen een grote invloed hebben op de morfologie, kristalliniteit en prestaties. ZnAl (2:1) LDH toonde het grootste potentieel voor CO<sub>2</sub>RR, en *in situ* experimenten benadrukten dat het thermisch gedrag sterk afhangt van de omgevingsatmosfeer. *In situ* TEM-experimenten met CO<sub>2</sub> bij kamertemperatuur voor dit materiaal toonden subtiele structurele veranderingen, waaronder een toename van de basale afstand.

MOF-74 werd gebruikt als modelmateriaal voor het optimaliseren van low-dose 3D ED-acquisitieparameters, die later werden toegepast op andere bundelgevoelige MOFs. *In situ* activatie-experimenten lieten verschillende gedragingen zien voor Zn- en Cu-gebaseerde MOFs, waarbij Cu-MOF-74 sneller activeerde maar bij verhoogde temperaturen Cu-nanodeeltjes in amorfe koolstof vormde. *In situ* CO<sub>2</sub>-adsorptie-experimenten op Zn-MOF-74 onthulden niet-lineaire bindingsgeometrieën en instorting van het rooster na desorptie, wat wijst op sterkere interacties en eerder niet-herkende CO<sub>2</sub>-coördinatiegeometrieën.

Ook enzym-MOF-biohybriden werden onderzocht met behulp van een nieuwe kleuringstechniek op basis van metaalzouten, waarmee directe visualisatie van enzyminkapseling mogelijk werd. Gecombineerd met 3D ED-data die een toename in de eenheidscel aantonen, bevestigden deze resultaten de succesvolle inkapseling en introduceerden ze een nieuwe benadering voor de studie van dergelijke systemen.

Een nieuw gesynthetiseerde MOF (UA-4) werd eveneens structureel gekarakteriseerd, ondanks aanzienlijke wanorde die de structuurinterpretatie bemoeilijkte.

Tot slot toonden *in situ* gasexperimenten op UiO-68 aan dat vacuümgevoelige MOFs bestudeerd kunnen worden zonder gebruik van cryogene omstandigheden.

ZnO-gebaseerde katalysatoren werden geoptimaliseerd via verschillende syntheseroutes en oppervlaktebehandelingen, waarbij nanostaven gevormd bij 300 °C de beste prestaties leverden. Aluminiumcoatings verbeterden de efficiëntie verder, hoewel de consistentie van de coating nog een uitdaging blijft. *In situ* studies waren niet succesvol vanwege de vorming van een SiO<sub>x</sub>-laag, veroorzaakt door interacties met het Si<sub>3</sub>N<sub>4</sub>-rooster van de microscoop.

## **Future prospects**

Although this PhD project concludes with this thesis, there are still many opportunities for further research. The work presented here provides a strong foundation for future *in situ* studies on both LDH and MOF materials.

For both types of materials, the impact of gas adsorption beyond CO<sub>2</sub> (such as other industrially relevant gases) remains largely unexplored and offers interesting research potential.

In LDHs, it's known that they can recover their layered structure after high-temperature treatment, but this process has not yet been observed with *in situ* TEM. Using a vaporizer connected to a gas holder, *in situ* TEM could track both the heating and the reconstruction process at the nanoscale, potentially giving valuable insights in this process.

This research also demonstrated that *in situ* 3D ED is a reliable technique to study MOF activation and structural changes during CO<sub>2</sub> adsorption. Similar studies could now be extended to other MOFs, such as HKUST-1 and UiO-66.

Moreover, many MOFs respond to moisture or hydrogen with a structural "breathing" effect, which *in situ* 3D ED could help examine in greater detail.

Linker exchange in MOFs is another promising application of *in situ* 3D ED. Although this experiment was attempted during this PhD using a liquid holder, technical issues prevented it's success. With continued improvements in holders, this experiment could be repeated.

Advances in automation, detectors, and data processing will improve the speed, quality, and reliability of 3D ED data. These developments will not only enhance *in situ* measurements but also 3D ED experiments in general. This will enable studies on MOF linker functionalization and more detailed guest molecule behavior studies.

Finally, improved *in situ* holders may resolve current issues like the SiO<sub>x</sub> layer formation in our ZnO experiment, opening new paths for studying oxidation processes.

## Scientific contributions during this PhD

### Published articles

- Quintelier, M., Perkisas, T., Poppe, R., Batuk, M., Hendrickx, M. and Hadermann, J.,
   2021. Determination of Spinel Content in Cycled Li<sub>1.2</sub>Ni<sub>0.13</sub>Mn<sub>0.54</sub>Co<sub>0.13</sub>O<sub>2</sub> Using Three-Dimensional Electron Diffraction and Precession Electron Diffraction. *Symmetry*, 13(11),
   p.1989.\*
- Quintelier, M., Canossa, S. and Hadermann, J., 2021. The strength of TEM for research into correlated disorder. *Belgian Journal of Physics—September*, p.30-37.\*\* Invited paper as Winner of the Belgian Physical Society best Master thesis award 2021.
- Quintelier, M., Hajizadeh, A., Zintler, A., Gonçalves, B.F., Fernández de Luis, R., Esrafili Dizaji, L., Vande Velde, C.M., Wuttke, S. and Hadermann, J., 2024. *In situ* Study of the Activation Process of MOF-74 Using Three-Dimensional Electron Diffraction. *Chemistry of Materials*, 36(15), pp.7274-7282.
- Quintelier, M., Zintler, A., Nakazato, R., Rosero-Navarro, N.C., Tadanaga, K. and Hadermann, J., 2025. Influence of atmospheric conditions on the structural evolution upon heating of the ZnAl layered double hydroxide: a comprehensive *in situ* TEM study. *ACS Applied Materials & Interfaces*. https://doi.org/10.1021/acsami.5c03313.
- Nakazato, R., Matsumoto, K., Yamaguchi, N., Cavallo, M., Crocellà, V., Bonino, F.,
   Quintelier, M., Hadermann, J., Rosero-Navarro, N.C., Miura, A. and Tadanaga, K., 2023.
   CO<sub>2</sub> Electrochemical Reduction with Zn-Al Layered Double Hydroxide-Loaded Gas-Diffusion Electrode. *Electrochemistry*, 91(9), pp.097003-097003.
- Cavallo, M., Dosa, M., Nakazato, R., Porcaro, N.G., Signorile, M., <u>Quintelier, M.</u>, Hadermann, J., Bordiga, S., Rosero-Navarro, N.C., Tadanaga, K. and Crocellà, V., 2024. Insight on Zn-Al LDH as electrocatalyst for CO<sub>2</sub> reduction reaction: An in-situ ATR-IR study. *Journal of CO<sub>2</sub> Utilization*, 83, p.102804.
- Rodríguez-Jara, E., Cavallo, M., Nakazato, R., <u>Quintelier, M.</u>, Matsumoto, K., Hadermann, J., Mosa, J., Bonino, F., Tadanaga, K., Aparicio, M. and Rosero-Navarro, N.C., 2024. Zinc oxides by thermal decomposition synthesis and parameters affecting electrocatalyst activity for CO<sub>2</sub> reduction reaction. *Open Ceramics*, p.100733.
- Rahimisheikh, S., Hajizadeh, A., Quintelier, M., Stulens, S., Hardy, A. and Hadermann, J.,
   2025. Crystal structure of submicron-sized sulfur particles using 3D ED obtained in atmospheric conditions. *Acta Chryst. C*, 81, 56-6.
- Nakazato, R., Matsumoto, K., Quintelier, M., Hadermann, J., Rosero-Navarro, N.C., Miura, A., Tadanaga, K., 2025. CO<sub>2</sub> Electrochemical Reduction by Zn-Based Layered Double Hydroxides: the Role of Structural Trivalent Metal Ions. *Open Ceramics*. p.100788

<sup>\*</sup>Publication based on work performed during the bachelorthesis.

<sup>\*\*</sup>Publication based on work performed during the masterthesis.

#### Published abstracts

- Quintelier, M., Canossa, S., Hendrickx, M., Poppe, R. and Hadermann, J., 2021. Characterization of the correlated disorder in Ge<sub>2</sub>Bi<sub>4</sub>Te<sub>7</sub>. Acta Crystallographica Section A: Foundations and Advances, 77, pp.C309-C309.
- Quintelier, M., Hajizadeh, A., Zintler, A., Goncalves, B., de Luis, R., Esrafili, L., Vande Velde, C. M. L., Wuttke, S. & Hadermann, J., 2024. *In situ* study of the activation process of MOF-74 using three-dimensional electron diffraction. *Acta Crystallographica Section A: Foundations and Advances*, 80, e303.
- Annys, A., Robert, H., **Quintelier, M.**, Hadermann, J. and Verbeeck, J., 2024. Dose fractionation and alternative scanning strategies for beam damage mitigation in event-driven 4D-STEM. In *BIO Web of Conferences* (Vol. 129, p. 05016). EDP Sciences.

#### Submitted manuscripts

- <u>Matthias Quintelier</u> and Joke Hadermann. MDT: A simple tool to facilitate dropcasting on in situ TEM MEMS chips. Submitted to *HardwareX* on 19 February 20, Accepted on 13 July 2025.
- Ruben Palacio, Daniela Jaramillo, Elías Rodríguez-Jara, Ryosuke Nakazato, <u>Matthias Quintelier</u>, Keeko Matsumoto, Joke Hadermann, Kiyoharu Tadanaga and Nataly Carolina Rosero-Navarro. Electrocatalytic CO<sub>2</sub> reduction to produce efficient and controlled syngas on highly dispersed NiFe on N-doped porous carbonaceous support. Submitted to *Carbon* on 13 July 2025.

#### Manuscripts in preparation

- <u>Matthias Quintelier</u>, Jacopo Andr, Roberto Fernández de Luis, Stefan Wuttke and Joke Hadermann. *In situ* 3D ED study of the CO<sub>2</sub> absorption in Zn-MOF-74.
- Leilli Esrafili Dizaji\*, <u>Matthias Quintelier\*</u>, Paul B. Klar, Stefano Canossa, Joke Hadermann and Christophe Vande Velde. Designing Linkers, Crafting Pores: Shortcut Strategies for Synthesis of Mesoporous Zr-MOFs and Advanced Characterization. \*Equal contributions.
- Daphne Vandemeulebroucke, Amirhossein Hajizadeh, Saleh Gholam, <u>Matthias Quintelier</u>, Maria Batuk, and Joke Hadermann. *In situ* 3D ED Uncovers Order/Disorder for Intermediate Oxygen Deficient Phases of (Ca,Sr)(Fe,Mn)O<sub>3-δ</sub> upon High-Temperature Reduction in Gas and Vacuum.
- Kazunari Arai, Jingxin Xia, Taito Murakami, Artem Abakumov, <u>Matthias Quintelier</u>, Joke Hadermann, Emilia Morosan, Motoaki Hirayama, Mathias Rambaud, Takafumi Yamamoto, and Hiroshi Kageyama. Anion-cation disorder in layered antimonides A<sub>2</sub>Zn<sub>1-x</sub>Sb<sub>3+x</sub> (A = Zr, Hf, x = 0.3-0.4).

- Ryosuke Nakazato, Keeko Matsumoto, Noboru Yamaguchi, Margherita Cavallo, Valentina Crocella, Francesca Bonino, <u>Matthias Quintelier</u>, Joke Hadermann, Nataly Carolina Rosero-Navarro, Akira Miura and Kiyoharu Tadanaga. Electrocatalytic Gas-Phase Carbon Dioxide Reduction Reaction with Zn-Al Layered Double Hydroxide-Loaded Gas-Diffusion electrode.
- Rafaella T. Buratto, Melodj Dosa, <u>Matthias Quintelier</u>, Joke Hadermann, Francesca Bonino, Valentina Crocellà, Joaquin Coronas, Jonas Gurauskis. Zeolite ZSM-5 synthesis within alumina scaffolds with hierarchical porosity obtained via robocasting.
- A manuscript is currently in preparation detailing the influence of grinding on the CO<sub>2</sub>RR efficiency of ZnAl LDH, incorporating the results discussed earlier in this thesis. First author: Ryosuke Nakazato.
- A manuscript is currently in preparation detailing the influence of the Al coating on ZnO material and its efficiency for CO<sub>2</sub>RR, incorporating the results discussed earlier in this thesis. First author: Elías Rodríguez-Jara.

#### **Oral Presentations**

- "Quantification of phase ratios within crystallites on a nanometer scale from 3D ED".
   Seminar within the international Core-to-Core project on Mixed Anion Research for Energy Conversion, October 2022, online.
- "3D ED INVESTIGATION OF THE ACTIVATION PROCESS OF MOF-74", BCS-12 conference, 2023, Brussels, Belgium.
- "In situ study of the activation process of MOF-74 using three-dimensional electron diffraction.", ECM34 conference, 2024, Padova, Italy.

#### Posters

- "TEM studies for ab initio structure determination of LDHs and MOFs for the absorption and conversion of CO<sub>2</sub>", We meet again SCK visits UAntwerp, 2022, University of Antwerp.
- "3D ED INVESTIGATION OF THE ACTIVATION PROCESS OF Zn-MOF-74, NanoLab day Universiteit van Antwerpen, 2023, University of Antwerp.
- "3D ED INVESTIGATION OF THE ACTIVATION PROCESS OF Zn-MOF-74", BCS-12 conference, 2023, Brussels, Belgium. Winner of the best poster prize award.

### References

- (1) Inkson, B. J. Scanning Electron Microscopy (SEM) and Transmission Electron Microscopy (TEM) for Materials Characterization. In *Materials Characterization Using Nondestructive Evaluation (NDE) Methods*; Elsevier Inc., 2016; pp 17–43. https://doi.org/10.1016/B978-0-08-100040-3.00002-X.
- (2) Carolien Callaert. Characterization of Defects, Modulations and Surface Layers in Topological Insulators and Structurally Related Compounds. PhD thesis, University of Antwerp, Antwerp, 2020.
- (3) Van Aert, S.; De Backer, A.; Martinez, G. T.; Den Dekker, A. J.; Van Dyck, D.; Bals, S.; Van Tendeloo, G. Advanced Electron Crystallography through Model-Based Imaging. *IUCrJ* **2016**, *3*, 71–83. https://doi.org/10.1107/S2052252515019727.
- (4) Pecharsky, V. K.; Zavalij, P. Y. Fundamentals of Powder Diffraction and Structural Characterization of Materials; Springer US, 2005. https://doi.org/10.1007/978-0-387-09579-0.
- (5) Marc De Graef. Introduction to Conventional Transmission Electron Microscopy. *Mater Res Bull* **2003**, *38* (13), 1781–1782. https://doi.org/10.1016/s0025-5408(03)00178-8.
- (6) Sinkler, W.; Bengu, E.; Marks, L. D. Application of Direct Methods to Dynamical Electron Diffraction Data for Solving Bulk Crystal Structures. *Acta Crystallogr A* 1998, 54 (5), 591–605. https://doi.org/10.1107/S0108767398001664.
- (7) Oszlányi, G.; Sütő, A. The Charge Flipping Algorithm. *Acta Crystallogr A* **2008**, *64* (1), 123–134. https://doi.org/10.1107/S0108767307046028.
- (8) van Laarhoven, P. J. M.; Aarts, E. H. L. Simulated Annealing. In *Simulated Annealing: Theory and Applications*; Springer Netherlands: Dordrecht, **1987**; pp 7–15. https://doi.org/10.1007/978-94-015-7744-1\_2.
- (9) Arnold, H.; Billiet, Y.; Buerger, M. J.; Burzlaff, H.; Donnay, J. D. H.; Hahn, T.; Klapper, H.; Koch, E.; Konstantinov, P. B.; Langlet, G. A.; Mu, U.; Wondratschek, H.; Zimmermann, H. *International Tables for Crystallography*; **1983**; Vol. A.
- (10) Kolb, U.; Gorelik, T.; Otten, M. T. Towards Automated Diffraction Tomography. Part II-Cell Parameter Determination. *Ultramicroscopy* **2008**, *108* (8), 763–772. https://doi.org/10.1016/j.ultramic.2007.12.002.
- (11) Gemmi, M.; Oleynikov, P. Scanning Reciprocal Space for Solving Unknown Structures: Energy Filtered Diffraction Tomography and Rotation Diffraction Tomography Methods. *Z Kristallogr Cryst Mater* **2013**, *228* (1), 51–58. https://doi.org/10.1524/zkri.2013.1559.
- (12) Boullay, P.; Palatinus, L.; Barrier, N. Precession Electron Diffraction Tomography for Solving Complex Modulated Structures: The Case of Bi<sub>5</sub>Nb<sub>3</sub>O<sub>15</sub>. *Inorg Chem* **2013**, *52* (10), 6127–6135. https://doi.org/10.1021/ic400529s.

- (13) Zhang, D.; Oleynikov, P.; Hovmöller, S.; Zou, X. Collecting 3D Electron Diffraction Data by the Rotation Method. *Zeitschrift für Kristallographie* **2010**, *225* (2–3), 94–102. https://doi.org/10.1524/zkri.2010.1202.
- Yuan, S.; Qin, J.-S.; Xu, H.-Q.; Su, J.; Rossi, D.; Chen, Y.; Zhang, L.; Lollar, C.; Wang, Q.; Jiang, H.-L.; Son, D. H.; Xu, H.; Huang, Z.; Zou, X.; Zhou, H.-C. Ti<sub>8</sub>Zr<sub>2</sub>O<sub>12</sub>(COO)<sub>16</sub> Cluster: An Ideal Inorganic Building Unit for Photoactive Metal–Organic Frameworks. ACS Cent Sci 2018, 4 (1), 105–111. https://doi.org/10.1021/acscentsci.7b00497.
- (15) Quintelier, M.; Perkisas, T.; Poppe, R.; Batuk, M.; Hendrickx, M.; Hadermann, J. Determination of Spinel Content in Cycled Li<sub>1.2</sub>Ni<sub>0.13</sub>Mn<sub>0.54</sub>Co<sub>0.13</sub>O<sub>2</sub> Using Three-Dimensional Electron Diffraction and Precession Electron Diffraction. *Symmetry (Basel)* **2021**, *13* (11), 1–17. https://doi.org/10.3390/sym13111989.
- (16) Gemmi, M.; Mugnaioli, E.; Gorelik, T. E.; Kolb, U.; Palatinus, L.; Boullay, P.; Hovmöller, S.; Abrahams, J. P. 3D Electron Diffraction: The Nanocrystallography Revolution. *ACS Cent Sci* **2019**, *5* (8), 1315–1329. https://doi.org/10.1021/acscentsci.9b00394.
- (17) Gemmi, M.; Lanza, A. 3D Electron Diffraction Techniques. *Acta Crystallogr B Struct Sci Cryst Eng Mater* **2019**, *39*. https://doi.org/10.1107/S2053230X16011663.You.
- (18) Cichocka, M. O.; Ångström, J.; Wang, B.; Zou, X.; Smeets, S. High-Throughput Continuous Rotation Electron Diffraction Data Acquisition via Software Automation. *J Appl Crystallogr* **2018**, *51* (6), 1652–1661. https://doi.org/10.1107/S1600576718015145.
- (19) Kolb, U.; Krysiak, Y.; Plana-Ruiz, S. Automated Electron Diffraction Tomography -Development and Applications. *Acta Crystallogr B Struct Sci Cryst Eng Mater* 2019, 75, 463–474. https://doi.org/10.1107/S2052520619006711.
- (20) Palatinus, L.; Brázda, P.; Jelínek, M.; Hrdá, J.; Steciuk, G.; Klementová, M. Specifics of the Data Processing of Precession Electron Diffraction Tomography Data and Their Implementation in the Program PETS2.0. Acta Crystallogr B Struct Sci Cryst Eng Mater 2019, 75, 512–522. https://doi.org/10.1107/S2052520619007534.
- (21) Petrícek, V.; Dušek, M.; Palatinus, L. Crystallographic Computing System JANA2006: General Features. *Zeitschrift fur Kristallographie* **2014**, *229* (5), 345–352. https://doi.org/10.1515/zkri-2014-1737.
- (22) Dolomanov, O. V.; Bourhis, L. J.; Gildea, R. J.; Howard, J. A. K.; Puschmann, H. OLEX2: A Complete Structure Solution, Refinement and Analysis Program. *J Appl Crystallogr* **2009**, *42* (2), 339–341. https://doi.org/10.1107/S0021889808042726.
- (23) Quintelier, M.; Hajizadeh, A.; Zintler, A.; Gonçalves, B. F.; Fernández de Luis, R.; Esrafili Dizaji, L.; Vande Velde, C. M. L.; Wuttke, S.; Hadermann, J. *In Situ* Study of the Activation Process of MOF-74 Using Three-Dimensional Electron Diffraction. *Chemistry of Materials* **2024**. https://doi.org/10.1021/acs.chemmater.4c01153.

- (24) Plana-Ruiz, S.; Krysiak, Y.; Portillo, J.; Alig, E.; Estradé, S.; Peiró, F.; Kolb, U. Fast-ADT: A Fast and Automated Electron Diffraction Tomography Setup for Structure Determination and Refinement. *Ultramicroscopy* **2020**, *211*. https://doi.org/10.1016/j.ultramic.2020.112951.
- (25) Laura Samperisi. Three-Dimensional Electron Diffraction for Studying Order, Disorder and Flexibility in Metalorganic Frameworks. PhD thesis, Stockholm University, Stockholm, 2022.
- (26) Commission on Electron Crystallography. CIF Meeting for ED. In *CIF meeting for ED*; Padua, Italy, **2024**.
- (27) Williams, D. B.; Carter, C. B. *Transmission Electron Microscopy: A Textbook for Materials Science*; Springer, **2009**.
- (28) Allen, L. J.; D'Alfonso, A. J.; Freitag, B.; Klenov, D. O. Chemical Mapping at Atomic Resolution Using Energy-Dispersive X-Ray Spectroscopy. *MRS Bull* **2012**, *37* (1), 47–52. https://doi.org/10.1557/mrs.2011.331.
- (29) de la Peña, F.; Prestat, E.; Lähnemann, J.; Tonaas Fauske, V.; Burdet, P.; Jokubauskas, P.; Furnival, T. Hyperspy/Hyperspy: V2.2.0. **2024**. https://zenodo.org/records/16850 (accessed 2025-04-14).
- (30) Johnstone, D.; Crout, P.; Francis, C.; Nord, M.; Laulainen, J.; Høgås, S.; Opheim, E.; Prestat, E.; Martineau, B.; Bergh, T.; Cautaerts, N.; Wiik Ånes, H.; Smeets, S.; Johan Femoen, V.; Ross, A.; Broussard, J.; Huang, S.; Collins, S.; Furnival, T.; Jannis, D.; Hjorth, I.; Jacobsen, E.; Danaie, M.; Herzing, A.; Poon, T.; Dagenborg, S.; Bjørge, R.; Iqbal, A.; Morzy, J.; Doherty, T.; Ostasevicius, T.; Inge Thorsen, T.; von Lany, M.; Tovey, R.; Vacek, P. Pyxem/Pyxem: V0.19.1. https://pyxem.readthedocs.io/en/latest/index.html (accessed 2025-04-14).
- (31) Vaccoat. What is an Electron Microscope?
- (32) Morzy, J. K.; Sartor, A.; Dose, W. M.; Ou, C.; Kar-Narayan, S.; De Volder, M. F. L.; Ducati, C. Aerosol Jet Printing as a Versatile Sample Preparation Method for Operando Electrochemical TEM Microdevices. *Adv Mater Interfaces* **2022**, *9* (20). https://doi.org/10.1002/admi.202200530.
- (33) Tarnev, T.; Cychy, S.; Andronescu, C.; Muhler, M.; Schuhmann, W.; Chen, Y. Eine Universelle, Auf Nanokapillaren Basierende Methode Zur Katalysatorimmobilisierung Für Die Flüssigzell-Transmissionselektronenmikroskopie. *Angewandte Chemie* **2020**, *132* (14), 5634–5638. https://doi.org/10.1002/ange.201916419.
- (34) Alphonse, C. M. E.; Garlapati, M. M.; Hilke, S.; Wilde, G. Double Shadow Masking Sample Preparation Method for *In-situ* TEM Characterization. *Nano Select* **2020**, *I* (4), 413–418. https://doi.org/10.1002/nano.202000063.
- (35) Baig, M. K.; Atiq, S.; Bashir, S.; Riaz, S.; Naseem, S.; Soleimani, H.; Yahya, N. Pulsed Laser Deposition of SmCo Thin Films for MEMS Applications. *Journal of Applied Research and Technology* **2016**, *14* (5), 287–292. https://doi.org/10.1016/j.jart.2016.06.005.

- (36) Srot, V.; Straubinger, R.; Predel, F.; van Aken, P. A. Preparation of High-Quality Samples for MEMS-Based In-Situ (S)TEM Experiments. *Microscopy and Microanalysis* **2023**, *29* (2), 596–605. https://doi.org/10.1093/micmic/ozad004.
- (37) Nakazato, R.; Matsumoto, K.; Yamaguchi, N.; Cavallo, M.; Crocella, V.; Bonino, F.; Quintelier, M.; Hadermann, J.; Rosero-Navarro, N. C.; Miura, A.; Tadanaga, K. CO<sub>2</sub> Electrochemical Reduction with Zn-Al Layered Double Hydroxide-Loaded Gas-Diffusion Electrode. *Electrochemistry* **2023**. https://doi.org/10.5796/electrochemistry.23-00080.
- (38) Evans, D. G.; Slade, R. C. T. Structural Aspects of Layered Double Hydroxides. *Struct Bond* **2005**, *119*, 1–87. https://doi.org/10.1007/430 005.
- (39) Xu, X.; Shi, S.; Tang, Y.; Wang, G.; Zhou, M.; Zhao, G.; Zhou, X.; Lin, S.; Meng, F. Growth of NiAl-Layered Double Hydroxide on Graphene toward Excellent Anticorrosive Microwave Absorption Application. *Advanced Science* **2021**, 8 (5). https://doi.org/10.1002/advs.202002658.
- (40) Tang, Z.; Qiu, Z.; Lu, S.; Shi, X. Functionalized Layered Double Hydroxide Applied to Heavy Metal Ions Absorption: A Review. *Nanotechnology Reviews*. De Gruyter Open Ltd January 1, **2020**, pp 800–819. https://doi.org/10.1515/ntrev-2020-0065.
- (41) Liu, R.; Frost, R. L.; Martens, W. N. Absorption of the Selenite Anion from Aqueous Solutions by Thermally Activated Layered Double Hydroxide. *Water Res* **2009**, *43* (5), 1323–1329. https://doi.org/10.1016/j.watres.2008.12.030.
- (42) Feng, Y.; Li, D.; Wang, Y.; Evans, D. G.; Duan, X. Synthesis and Characterization of a UV Absorbent-Intercalated Zn-Al Layered Double Hydroxide. *Polym Degrad Stab* **2006**, *91* (4), 789–794. https://doi.org/10.1016/j.polymdegradstab.2005.06.006.
- (43) Olfs, H. W.; Torres-Dorante, L. O.; Eckelt, R.; Kosslick, H. Comparison of Different Synthesis Routes for Mg-Al Layered Double Hydroxides (LDH): Characterization of the Structural Phases and Anion Exchange Properties. *Appl Clay Sci* **2009**, *43* (3–4), 459–464. https://doi.org/10.1016/j.clay.2008.10.009.
- (44) Chubar, N.; Gilmour, R.; Gerda, V.; Mičušík, M.; Omastova, M.; Heister, K.; Man, P.; Fraissard, J.; Zaitsev, V. Layered Double Hydroxides as the next Generation Inorganic Anion Exchangers: Synthetic Methods versus Applicability. *Advances in Colloid and Interface Science*. Elsevier B.V. July 1, **2017**, pp 62–80. https://doi.org/10.1016/j.cis.2017.04.013.
- (45) Hu, X.; Zhu, X.; Sun, Z. Fireproof Performance of the Intumescent Fire Retardant Coatings with Layered Double Hydroxides Additives. *Constr Build Mater* **2020**, *256*. https://doi.org/10.1016/j.conbuildmat.2020.119445.
- (46) Matusinovic, Z.; Wilkie, C. A. Fire Retardancy and Morphology of Layered Double Hydroxide Nanocomposites: A Review. *Journal of Materials Chemistry*. Royal Society of Chemistry September 28, **2012**, pp 18701–18704. https://doi.org/10.1039/c2jm33179a.

- (47) Hu, T.; Gu, Z.; Williams, G. R.; Strimaite, M.; Zha, J.; Zhou, Z.; Zhang, X.; Tan, C.; Liang, R. Layered Double Hydroxide-Based Nanomaterials for Biomedical Applications. *Chem Soc Rev* **2022**, *51* (14), 6126–6176. https://doi.org/10.1039/D2CS00236A.
- (48) Kuthati, Y.; Kankala, R. K.; Lee, C. H. Layered Double Hydroxide Nanoparticles for Biomedical Applications: Current Status and Recent Prospects. *Applied Clay Science*. Elsevier Ltd August 1, **2015**, pp 100–116. https://doi.org/10.1016/j.clay.2015.04.018.
- (49) Lu, Y.; Li, X.; Jing, X.; Huang, Y.; Qiang, Y.; Cao, G.; Qin, R.; Cao, Q.; Cao, J.; Lee, S. C. Applications of Layered Double Hydroxide Nanomaterials in Environmental Remediation: Synthesis, Structural Modification and Performance Enhancement. Surfaces and Interfaces. Elsevier B.V. September 1, 2024. https://doi.org/10.1016/j.surfin.2024.104902.
- (50) Ahmed, M. A.; Mohamed, A. A. A Systematic Review of Layered Double Hydroxide-Based Materials for Environmental Remediation of Heavy Metals and Dye Pollutants. *Inorganic Chemistry Communications*. Elsevier B.V. February 1, **2023**. https://doi.org/10.1016/j.inoche.2022.110325.
- (51) Forano, C. Environmental Remediation Involving Layered Double Hydroxides. In *Interface Science and Technology*; Aubiere Cedex, **2004**; Vol. 1, pp 425–458. https://doi.org/10.1016/S1573-4285(04)80050-4.
- (52) Dewangan, N.; Hui, W. M.; Jayaprakash, S.; Bawah, A. R.; Poerjoto, A. J.; Jie, T.; Jangam, A.; Hidajat, K.; Kawi, S. Recent Progress on Layered Double Hydroxide (LDH) Derived Metal-Based Catalysts for CO<sub>2</sub> Conversion to Valuable Chemicals. *Catal Today* **2020**, *356*, 490–513. https://doi.org/10.1016/j.cattod.2020.06.020.
- (53) Zhang, T.; Shang, H.; Zhang, B.; Yan, D.; Xiang, X. Ag/Ultrathin-Layered Double Hydroxide Nanosheets Induced by a Self-Redox Strategy for Highly Selective CO<sub>2</sub> Reduction. *ACS Appl Mater Interfaces* **2021**, *13* (14), 16536–16544. https://doi.org/10.1021/acsami.1c02737.
- (54) Serafini, M.; Mariani, F.; Fasolini, A.; Brandi, E. T.; Scavetta, E.; Basile, F.; Tonelli, D. Electrosynthesized CuMgAl Layered Double Hydroxides as New Catalysts for the Electrochemical Reduction of CO<sub>2</sub>. *Adv Funct Mater* **2023**, *33* (29). https://doi.org/10.1002/adfm.202300345.
- (55) Hobbs, C.; Jaskaniec, S.; McCarthy, E. K.; Downing, C.; Opelt, K.; Güth, K.; Shmeliov, A.; Mourad, M. C. D.; Mandel, K.; Nicolosi, V. Structural Transformation of Layered Double Hydroxides: An *in Situ* TEM Analysis. *NPJ 2D Mater Appl* **2018**, *2* (1). https://doi.org/10.1038/s41699-018-0048-4.
- (56) Liu, J.; Song, J.; Xiao, H.; Zhang, L.; Qin, Y.; Liu, D.; Hou, W.; Du, N. Synthesis and Thermal Properties of ZnAl Layered Double Hydroxide by Urea Hydrolysis. *Powder Technol* **2014**, *253*, 41–45. https://doi.org/10.1016/j.powtec.2013.11.007.
- (57) Asghar, H.; Maurino, V.; Iqbal, M. A. Development of Highly Photoactive Mixed Metal Oxide (MMO) Based on the Thermal Decomposition of ZnAl-NO<sub>3</sub>-LDH. *Eng* **2024**, *5* (2), 589–599. https://doi.org/10.3390/eng5020033.

- (58) Matsuda, K.; Okuda, A.; Iio, N.; Tarutani, N.; Katagiri, K.; Inumaru, K. Chemical and Structural Transformations of M-Al-CO<sub>3</sub> Layered Double Hydroxides (M = Mg, Zn, or Co, M/Al = 2) at Elevated Temperatures: Quantitative Descriptions and Effect of Divalent Cations. *Inorg Chem* **2024**, *63* (34), 15634–15647. https://doi.org/10.1021/acs.inorgchem.4c01186.
- (59) Wang, C.; Zhang, R.; Miao, Y.; Xue, Q.; Yu, B.; Gao, Y.; Han, Z.; Shao, M. Preparation of LDO@TiO<sub>2</sub> Core–Shell Nanosheets for Enhanced Photocatalytic Degradation of Organic Pollution. *Dalton Transactions* 2021, 50 (48), 17911–17919. https://doi.org/10.1039/D1DT03302F.
- (60) Jin, L.; Zhou, X.; Wang, F.; Ning, X.; Wen, Y.; Song, B.; Yang, C.; Wu, D.; Ke, X.; Peng, L. Insights into Memory Effect Mechanisms of Layered Double Hydroxides with Solid-State NMR Spectroscopy. *Nat Commun* 2022, *13* (1), 6093. https://doi.org/10.1038/s41467-022-33912-7.
- (61) Rossouw, D.; Burdet, P.; De La Peña, F.; Ducati, C.; Knappett, B. R.; Wheatley, A. E. H.; Midgley, P. A. Multicomponent Signal Unmixing from Nanoheterostructures: Overcoming the Traditional Challenges of Nanoscale X-Ray Analysis via Machine Learning. *Nano Letters*. American Chemical Society April 8, 2015, pp 2716–2720. https://doi.org/10.1021/acs.nanolett.5b00449.
- (62) Ram Reddy, M. K.; Xu, Z. P.; Lu, G. Q.; Da Costa, J. C. D. Layered Double Hydroxides for CO<sub>2</sub> Capture: Structure Evolution and Regeneration. *Ind Eng Chem Res* **2006**, *45* (22), 7504–7509. https://doi.org/10.1021/ie060757k.
- (63) Wojdyr, M. Fityk: A General-Purpose Peak Fitting Program. *J Appl Crystallogr* **2010**, *43* (5), 1126–1128. https://doi.org/10.1107/S0021889810030499.
- (64) Kentish, S. E.; Scholes, C. A.; Stevens, G. W. Carbon Dioxide Separation through Polymeric Membrane Systems for Flue Gas Applications. *Recent Patents on Chemical Engineering* 2010, 1 (1), 52–66. https://doi.org/10.2174/1874478810801010052.
- (65) Ram Reddy, M. K.; Xu, Z. P.; Lu, G. Q.; Da Costa, J. C. D. Layered Double Hydroxides for CO<sub>2</sub> Capture: Structure Evolution and Regeneration. *Ind Eng Chem Res* **2006**, *45* (22), 7504–7509. https://doi.org/10.1021/ie060757k.
- (66) Freund, R.; Canossa, S.; Cohen, S. M.; Yan, W.; Deng, H.; Guillerm, V.; Eddaoudi, M.; Madden, D. G.; Fairen-Jimenez, D.; Lyu, H.; Macreadie, L. K.; Ji, Z.; Zhang, Y.; Wang, B.; Haase, F.; Wöll, C.; Zaremba, O.; Andreo, J.; Wuttke, S.; Diercks, C. S. 25 Years of Reticular Chemistry. *Angewandte Chemie* 2021, No. April. https://doi.org/10.1002/ange.202101644.
- (67) Furukawa, H.; Cordova, K. E.; O'Keeffe, M.; Yaghi, O. M. The Chemistry and Applications of Metal-Organic Frameworks. *Science* (1979) **2013**, 341 (6149). https://doi.org/10.1126/science.1230444.

- (68) Moosavi, S. M.; Nandy, A.; Jablonka, K. M.; Ongari, D.; Janet, J. P.; Boyd, P. G.; Lee, Y.; Smit, B.; Kulik, H. J. Understanding the Diversity of the Metal-Organic Framework Ecosystem. *Nat Commun* **2020**, *11* (1). https://doi.org/10.1038/s41467-020-17755-8.
- (69) Choi, I.; Jung, Y. E.; Yoo, S. J.; Kim, J. Y.; Kim, H. J.; Lee, C. Y.; Jang, J. H. Facile Synthesis of M-MOF-74 (M=Co, Ni, Zn) and Its Application as an Electrocatalyst for Electrochemical CO<sub>2</sub> Conversion and H<sub>2</sub> Production. *Journal of Electrochemical Science and Technology* **2017**, 8 (1), 61–68. https://doi.org/10.5229/JECST.2017.8.1.61.
- (70) Millward, A. R.; Yaghi, O. M. Metal-Organic Frameworks with Exceptionally High Capacity for Storage of Carbon Dioxide at Room Temperature. *J Am Chem Soc* **2005**, *127* (51), 17998–17999. https://doi.org/10.1021/ja0570032.
- (71) Britt, D.; Furukawa, H.; Wang, B.; Glover, T. G.; Yaghi, O. M. Highly Efficient Separation of Carbon Dioxide by a Metal-Organic Framework Replete with Open Metal Sites. *Proc Natl Acad Sci U S A* **2009**, *106* (49), 20637–20640. https://doi.org/10.1073/pnas.0909718106.
- (72) McDonald, T. M.; Lee, W. R.; Mason, J. A.; Wiers, B. M.; Hong, C. S.; Long, J. R. Capture of Carbon Dioxide from Air and Flue Gas in the Alkylamine-Appended Metal-Organic Framework Mmen-Mg 2(Dobpdc). *J Am Chem Soc* 2012, 134 (16), 7056–7065. https://doi.org/10.1021/ja300034j.
- (73) McDonald, T. M.; Mason, J. A.; Kong, X.; Bloch, E. D.; Gygi, D.; Dani, A.; Crocellà, V.; Giordanino, F.; Odoh, S. O.; Drisdell, W. S.; Vlaisavljevich, B.; Dzubak, A. L.; Poloni, R.; Schnell, S. K.; Planas, N.; Lee, K.; Pascal, T.; Wan, L. F.; Prendergast, D.; Neaton, J. B.; Smit, B.; Kortright, J. B.; Gagliardi, L.; Bordiga, S.; Reimer, J. A.; Long, J. R. Cooperative Insertion of CO<sub>2</sub> in Diamine-Appended Metal-Organic Frameworks. *Nature* **2015**, *519* (7543), 303–308. https://doi.org/10.1038/nature14327.
- (74) Cho, H. Y.; Yang, D. A.; Kim, J.; Jeong, S. Y.; Ahn, W. S. CO 2 Adsorption and Catalytic Application of Co-MOF-74 Synthesized by Microwave Heating. In *Catalysis Today*; **2012**; Vol. 185, pp 35–40. https://doi.org/10.1016/j.cattod.2011.08.019.
- (75) Valenzano, L.; Civalleri, B.; Chavan, S.; Palomino, G. T.; Areán, C. O.; Bordiga, S. Computational and Experimental Studies on the Adsorption of CO, N<sub>2</sub>, and CO<sub>2</sub> on Mg-MOF-74. *Journal of Physical Chemistry C* **2010**, *114* (25), 11185–11191. https://doi.org/10.1021/jp102574f.
- (76) Denning, S.; Majid, A. A. A.; Crawford, J. M.; Wells, J. D.; Carreon, M. A.; Koh, C. A. Methane Storage Scale-up Using Hydrates & Metal Organic Framework HKUST-1 in a Packed Column. *Fuel* **2022**, *325*. https://doi.org/10.1016/j.fuel.2022.124920.
- (77) Denning, S.; Majid, A. A. A.; Lucero, J. M.; Crawford, J. M.; Carreon, M. A.; Koh, C. A. Metal-Organic Framework HKUST-1 Promotes Methane Hydrate Formation for Improved Gas Storage Capacity. ACS Appl Mater Interfaces 2020, 12 (47), 53510–53518. https://doi.org/10.1021/acsami.0c15675.

- (78) Koyuturk, B.; Altintas, C.; Kinik, F. P.; Keskin, S.; Uzun, A. Improving Gas Separation Performance of ZIF-8 by [BMIM][BF4] Incorporation: Interactions and Their Consequences on Performance. *Journal of Physical Chemistry C* **2017**, *121* (19), 10370–10381. https://doi.org/10.1021/acs.jpcc.7b00848.
- (79) James, J. B.; Lin, Y. S. Thermal Stability of ZIF-8 Membranes for Gas Separations. *J Memb Sci* **2017**, *532*, 9–19. https://doi.org/10.1016/j.memsci.2017.02.017.
- (80) Lai, Z. Development of ZIF-8 Membranes: Opportunities and Challenges for Commercial Applications. *Curr Opin Chem Eng* **2018**, 20, 78–85. https://doi.org/10.1016/j.coche.2018.03.002.
- (81) Chen, T.; Zhao, D. Post-Synthetic Modification of Metal-Organic Framework-Based Membranes for Enhanced Molecular Separations. *Coordination Chemistry Reviews*. Elsevier B.V. September 15, **2023**. https://doi.org/10.1016/j.ccr.2023.215259.
- (82) Shultz, A. M.; Sarjeant, A. A.; Farha, O. K.; Hupp, J. T.; Nguyen, S. T. Post-Synthesis Modification of a Metal-Organic Framework to Form Metallosalen-Containing MOF Materials. *J Am Chem Soc* **2011**, *133* (34), 13252–13255. https://doi.org/10.1021/ja204820d.
- (83) Song, Y. F.; Cronin, L. Postsynthetic Covalent Modification of Metal-Organic Framework (MOF) Materials. *Angewandte Chemie International Edition*. June 9, **2008**, pp 4635–4637. https://doi.org/10.1002/anie.200801631.
- (84) Bahamon, D.; Anlu, W.; Builes, S.; Khaleel, M.; Vega, L. F. Effect of Amine Functionalization of MOF Adsorbents for Enhanced CO<sub>2</sub> Capture and Separation: A Molecular Simulation Study. *Front Chem* **2021**, *8*. https://doi.org/10.3389/fchem.2020.574622.
- (85) Gao, F.; Yan, R.; Shu, Y.; Cao, Q.; Zhang, L. Strategies for the Application of Metal-Organic Frameworks in Catalytic Reactions. *RSC Advances*. Royal Society of Chemistry March 31, **2022**, pp 10114–10125. https://doi.org/10.1039/d2ra01175a.
- (86) Zhou, S.; Ban, T.; Li, T.; Gao, H.; He, T.; Cheng, S.; Li, H.; Yi, J.; Zhao, F.; Qu, W. Defect Engineering in Ce-Based Metal-Organic Frameworks toward Enhanced Catalytic Performance for Hydrogenation of Dicyclopentadiene. ACS Appl Mater Interfaces 2024, 16 (29), 38177–38187. https://doi.org/10.1021/acsami.4c08040.
- (87) Soleimani, B.; Niknam Shahrak, M.; Walton, K. S. The Influence of Different Functional Groups on Enhancing CO<sub>2</sub> Capture in Metal-Organic Framework Adsorbents. *Journal of the Taiwan Institute of Chemical Engineers*. Taiwan Institute of Chemical Engineers October 1, **2024**. https://doi.org/10.1016/j.jtice.2024.105638.
- (88) Kazemi, S.; Safarifard, V. Carbon Dioxide Capture in MOFs: The Effect of Ligand Functionalization. *Polyhedron*. Elsevier Ltd November 1, **2018**, pp 236–251. https://doi.org/10.1016/j.poly.2018.07.042.
- (89) Chen, Q.; Dwyer, C.; Sheng, G.; Zhu, C.; Li, X.; Zheng, C.; Zhu, Y. Imaging Beam-Sensitive Materials by Electron Microscopy. *Advanced Materials*. Wiley-VCH Verlag April 1, **2020**. https://doi.org/10.1002/adma.201907619.

- (90) Wiktor, C.; Meledina, M.; Turner, S.; Lebedev, O. I.; Fischer, R. A. Transmission Electron Microscopy on Metal-Organic Frameworks-a Review. *J Mater Chem A Mater* **2017**, *5* (29), 14969–14989. https://doi.org/10.1039/c7ta00194k.
- (91) Banerjee, P.; Kollmannsberger, K. L.; Fischer, R. A.; Jinschek, J. R. Mechanism of Electron-Beam-Induced Structural Degradation in ZIF-8 and Its Electron Dose Tolerance. *J Phys Chem A* **2024**, *128* (48), 10440–10451. https://doi.org/10.1021/acs.jpca.4c06391.
- (92) Wiktor, C.; Turner, S.; Zacher, D.; Fischer, R. A.; Tendeloo, G. Van. Imaging of Intact MOF-5 Nanocrystals by Advanced TEM at Liquid Nitrogen Temperature. *Microporous and Mesoporous Materials* 2012, 162, 131–135. https://doi.org/10.1016/j.micromeso.2012.06.014.
- (93) Li, X.; Wang, J.; Liu, X.; Liu, L.; Cha, D.; Zheng, X.; Yousef, A. A.; Song, K.; Zhu, Y.; Zhang, D.; Han, Y. Direct Imaging of Tunable Crystal Surface Structures of MOF MIL-101 Using High-Resolution Electron Microscopy. *J Am Chem Soc* 2019, 141 (30), 12021–12028. https://doi.org/10.1021/jacs.9b04896.
- (94) Zheng, A.; Yin, K.; Pan, R.; Zhu, M.; Xiong, Y.; Sun, L. Research Progress on Metal–Organic Frameworks by Advanced Transmission Electron Microscopy. *Nanomaterials*. MDPI June 1, **2023**. https://doi.org/10.3390/nano13111742.
- (95) Liu, B.; Chen, X.; Huang, N.; Liu, S.; Wang, Y.; Lan, X.; Wei, F.; Wang, T. Imaging the Dynamic Influence of Functional Groups on Metal-Organic Frameworks. *Nat Commun* **2023**, *14* (1). https://doi.org/10.1038/s41467-023-40590-6.
- (96) Shen, B.; Chen, X.; Shen, K.; Xiong, H.; Wei, F. Imaging the Node-Linker Coordination in the Bulk and Local Structures of Metal-Organic Frameworks. *Nat Commun* **2020**, *11* (1). https://doi.org/10.1038/s41467-020-16531-y.
- (97) Li, G.; Zhang, H.; Han, Y. 4D-STEM Ptychography for Electron-Beam-Sensitive Materials. *ACS Central Science*. American Chemical Society December 28, **2022**, pp 1579–1588. https://doi.org/10.1021/acscentsci.2c01137.
- (98) Rhauderwiek, T.; Zhao, H.; Hirschle, P.; Döblinger, M.; Bueken, B.; Reinsch, H.; De Vos, D.; Wuttke, S.; Kolb, U.; Stock, N. Highly Stable and Porous Porphyrin-Based Zirconium and Hafnium Phosphonates-Electron Crystallography as an Important Tool for Structure Elucidation. *Chem Sci* **2018**, *9* (24), 5467–5478. https://doi.org/10.1039/c8sc01533c.
- (99) Samperisi, L.; Jaworski, A.; Kaur, G.; Lillerud, K. P.; Zou, X.; Huang, Z. Probing Molecular Motions in Metal-Organic Frameworks by Three-Dimensional Electron Diffraction. *J Am Chem Soc* **2021**, *143* (43), 17947–17952. https://doi.org/10.1021/jacs.1c08354.
- (100) Samperisi, L.; Zou, X.; Huang, Z. Three-Dimensional Electron Diffraction: A Powerful Structural Characterization Technique for Crystal Engineering. *CrystEngComm*. Royal Society of Chemistry March 18, **2022**, pp 2719–2728. https://doi.org/10.1039/d2ce00051b.

- (101) Huang, Z.; Willhammar, T.; Zou, X. Three-Dimensional Electron Diffraction for Porous Crystalline Materials: Structural Determination and Beyond. *Chemical Science*. Royal Society of Chemistry January 28, **2021**, pp 1206–1219. https://doi.org/10.1039/d0sc05731b.
- (102) Schnabel, J.; Ettlinger, R.; Bunzen, H. Zn-MOF-74 as PH-Responsive Drug-Delivery System of Arsenic Trioxide. *ChemNanoMat* **2020**, *6* (8), 1229–1236. https://doi.org/10.1002/cnma.202000221.
- (103) Strauss, I.; Mundstock, A.; Treger, M.; Lange, K.; Hwang, S.; Chmelik, C.; Rusch, P.; Bigall, N. C.; Pichler, T.; Shiozawa, H.; Caro, J. Metal-Organic Framework Co-MOF-74-Based Host-Guest Composites for Resistive Gas Sensing. ACS Appl Mater Interfaces 2019, 11 (15), 14175–14181. https://doi.org/10.1021/acsami.8b22002.
- (104) Bhadra, B. N.; Yoo, D. K.; Jhung, S. H. Carbon-Derived from Metal-Organic Framework MOF-74: A Remarkable Adsorbent to Remove a Wide Range of Contaminants of Emerging Concern from Water. *Appl Surf Sci* **2020**, *504* (October 2019), 144348. https://doi.org/10.1016/j.apsusc.2019.144348.
- (105) Chen, S.; Li, X.; Duan, J.; Fu, Y.; Wang, Z.; Zhu, M.; Li, N. Investigation of Highly Efficient Adsorbent Based on Ni-MOF-74 in the Separation of CO<sub>2</sub> from Natural Gas. *Chemical Engineering Journal* **2021**, *419* (February). https://doi.org/10.1016/j.cej.2021.129653.
- (106) Xiao, T.; Liu, D. The Most Advanced Synthesis and a Wide Range of Applications of MOF-74 and Its Derivatives. *Microporous and Mesoporous Materials*. Elsevier B.V. July 15, **2019**, pp 88–103. https://doi.org/10.1016/j.micromeso.2019.03.002.
- (107) Liao, Y.; Zhang, L.; Weston, M. H.; Morris, W.; Hupp, J. T.; Farha, O. K. Tuning Ethylene Gas Adsorption via Metal Node Modulation: Cu-MOF-74 for a High Ethylene Deliverable Capacity. *Chemical Communications* **2017**, *53* (67), 9376–9379. https://doi.org/10.1039/c7cc04160h.
- (108) Tranchemontagne, D. J.; Hunt, J. R.; Yaghi, O. M. Room Temperature Synthesis of Metal-Organic Frameworks: MOF-5, MOF-74, MOF-177, MOF-199, and IRMOF-0. *Tetrahedron* **2008**, *64* (36), 8553–8557. https://doi.org/10.1016/j.tet.2008.06.036.
- (109) Xu, D.; Pan, Y.; Chen, M.; Pan, Q.; Zhu, L.; Xue, M.; Zhang, D.; Fang, Q.; Qiu, S. Synthesis and Application of a MOF-Derived Ni@C Catalyst by the Guidance from an in Situ Hot Stage in TEM. *RSC Adv* **2017**, *7* (42), 26377–26383. https://doi.org/10.1039/C7RA03162A.
- (110) Mücke, D.; Liang, B.; Wang, Z.; Qi, H.; Dong, R.; Feng, X.; Kaiser, U. In-Situ Imaging of Heat-Induced Phase Transition in a Two-Dimensional Conjugated Metal-Organic Framework. *Micron* 2024, 184, 103677. https://doi.org/10.1016/j.micron.2024.103677.
- (111) Van Vleet, M. J.; Weng, T.; Li, X.; Schmidt, J. R. In Situ, Time-Resolved, and Mechanistic Studies of Metal–Organic Framework Nucleation and Growth. *Chem Rev* **2018**, *118* (7), 3681–3721. https://doi.org/10.1021/acs.chemrev.7b00582.

- (112) Patterson, J. P.; Abellan, P.; Denny, M. S.; Park, C.; Browning, N. D.; Cohen, S. M.; Evans, J. E.; Gianneschi, N. C. Observing the Growth of Metal–Organic Frameworks by in Situ Liquid Cell Transmission Electron Microscopy. *J Am Chem Soc* **2015**, *137* (23), 7322–7328. https://doi.org/10.1021/jacs.5b00817.
- (113) Xiao, L.; Wang, G.; Huang, X.; Zhou, S.; Zhou, R.; Jiang, Y.; Liu, S.; Li, G.; Zheng, H.; Sun, S.-G.; Liao, H.-G. Efficient CO<sub>2</sub> Reduction MOFs Derivatives Transformation Mechanism Revealed by In-Situ Liquid Phase TEM. *Appl Catal B* **2022**, *307*, 121164. https://doi.org/10.1016/j.apcatb.2022.121164.
- (114) Ling, Y.; Sun, T.; Guo, L.; Si, X.; Jiang, Y.; Zhang, Q.; Chen, Z.; Terasaki, O.; Ma, Y. Atomic-Level Structural Responsiveness to Environmental Conditions from 3D Electron Diffraction. *Nat Commun* **2022**, *13* (1), 6625. https://doi.org/10.1038/s41467-022-34237-1.
- (115) Choe, J. H.; Kim, H.; Hong, C. S. MOF-74 Type Variants for CO<sub>2</sub> Capture. *Mater Chem Front* **2021**, *5* (14), 5172–5185. https://doi.org/10.1039/D1QM00205H.
- (116) Trickett, C. A.; Helal, A.; Al-Maythalony, B. A.; Yamani, Z. H.; Cordova, K. E.; Yaghi, O. M. The Chemistry of Metal-Organic Frameworks for CO<sub>2</sub> Capture, Regeneration and Conversion. *Nat Rev Mater* **2017**, *2* (8). https://doi.org/10.1038/natrevmats.2017.45.
- (117) Gropp, C.; Canossa, S.; Wuttke, S.; Gándara, F.; Li, Q.; Gagliardi, L.; Yaghi, O. M. Standard Practices of Reticular Chemistry. *ACS Cent Sci* **2020**, *6* (8), 1255–1273. https://doi.org/10.1021/acscentsci.0c00592.
- (118) Howarth, A. J.; Peters, A. W.; Vermeulen, N. A.; Wang, T. C.; Hupp, J. T.; Farha, O. K. Best Practices for the Synthesis, Activation, and Characterization of Metal—organic Frameworks. *Chemistry of Materials* **2017**, *29* (1), 26–39. https://doi.org/10.1021/acs.chemmater.6b02626.
- (119) Liang, X.; Wang, P.; Li, C.; Yuan, M.; Shi, Q.; Dong, J. The Activation of Co-MOF-74 with Open Metal Sites and Their Corresponding CO/N<sub>2</sub> Adsorptive Separation Performance. *Microporous and Mesoporous Materials* **2021**, *320* (January), 111109. https://doi.org/10.1016/j.micromeso.2021.111109.
- (120) Akeremale, O. K.; Ore, O. T.; Bayode, A. A.; Badamasi, H.; Adedeji Olusola, J.; Durodola, S. S. Synthesis, Characterization, and Activation of Metal Organic Frameworks (MOFs) for the Removal of Emerging Organic Contaminants through the Adsorption-Oriented Process:

  A Review. *Results Chem* **2023**, *5* (January), 100866. https://doi.org/10.1016/j.rechem.2023.100866.
- (121) Otun, K. O. Temperature-Controlled Activation and Characterization of Iron-Based Metal-Organic Frameworks. *Inorganica Chim Acta* **2020**, *507* (March), 119563. https://doi.org/10.1016/j.ica.2020.119563.
- (122) Mondloch, J. E.; Karagiaridi, O.; Farha, O. K.; Hupp, J. T. Activation of Metal-Organic Framework Materials. *CrystEngComm* **2013**, *15* (45), 9258–9264. https://doi.org/10.1039/c3ce41232f.

- (123) Liang, X.; Wang, P.; Li, C.; Yuan, M.; Shi, Q.; Dong, J. The Activation of Co-MOF-74 with Open Metal Sites and Their Corresponding CO/N<sub>2</sub> Adsorptive Separation Performance. *Microporous and Mesoporous Materials* **2021**, *320* (January), 111109. https://doi.org/10.1016/j.micromeso.2021.111109.
- (124) Flores, J. G.; Obeso, J. L.; Martínez-Jiménez, V.; Martín-Guaregua, N.; Islas-Jácome, A.; González-Zamora, E.; Serrano-Espejel, H.; Mondragón-Rodríguez, B.; Leyva, C.; Solís-Casados, D. A.; Ibarra, I. A.; Peralta, R. A.; Aguilar-Pliego, J.; Antonio de los Reyes, J. Evaluation of the Catalytic Activity of Zn-MOF-74 for the Alcoholysis of Cyclohexene Oxide. RSC Adv 2023, 13 (39), 27174–27179. https://doi.org/10.1039/D3RA03122E.
- (125) Oar-Arteta, L.; Wezendonk, T.; Sun, X.; Kapteijn, F.; Gascon, J. Metal Organic Frameworks as Precursors for the Manufacture of Advanced Catalytic Materials. *Materials Chemistry Frontiers*. Royal Society of Chemistry September 1, **2017**, pp 1709–1745. https://doi.org/10.1039/c7qm00007c.
- (126) Zhang, X.; Chen, Z.; Liu, X.; Hanna, S. L.; Wang, X.; Taheri-Ledari, R.; Maleki, A.; Li, P.; Farha, O. K. A Historical Overview of the Activation and Porosity of Metal-Organic Frameworks. *Chem Soc Rev* **2020**, *49* (20), 7406–7427. https://doi.org/10.1039/d0cs00997k.
- (127) Huang, C. H.; Jan, Y. L.; Chuang, W. J.; Lu, P. T. Investigation of Approaches to Control the Compositions of Zn(Se,OH) Buffers Prepared by Chemical Bath Deposition Process for Cu(In,Ga)Se<sub>2</sub> (CIGS) Solar Cells. *Crystals (Basel)* **2018**, 8 (9). https://doi.org/10.3390/cryst8090343.
- (128) Ali, A.; Hussain, S.; Bhatti, H. S.; Shabbir, B. Study of Structural, Electronic, and Conducting Properties of  $Cu_{2-x}Mn_xO$  ( $0 \le x \le 0.07$ ) System. *Results Phys* **2021**, *25*, 104224. https://doi.org/10.1016/j.rinp.2021.104224.
- (129) Persson, I.; Lundberg, D.; Bajnóczi, É. G.; Klementiev, K.; Just, J.; Sigfridsson Clauss, K. G. V. EXAFS Study on the Coordination Chemistry of the Solvated Copper(II) Ion in a Series of Oxygen Donor Solvents. *Inorg Chem* **2020**, *59* (14), 9538–9550. https://doi.org/10.1021/acs.inorgchem.0c00403.
- (130) Kamarulzaman, N.; Kasim, M. F.; Chayed, N. F. Elucidation of the Highest Valence Band and Lowest Conduction Band Shifts Using XPS for ZnO and Zn<sub>0.99</sub>Cu<sub>0.01</sub>O Band Gap Changes. *Results Phys* **2016**, *6* (May), 217–230. https://doi.org/10.1016/j.rinp.2016.04.001.
- (131) Sung, M. M.; Kim, Y. Self-Assembled Monolayers of Alkanethiols on Clean Copper Surfaces. *Bull Korean Chem Soc* **2001**, *22* (7), 748–752.
- (132) Molina, M. A.; Manjón-Sanz, A.; Sánchez-Sánchez, M. On the Contribution of Pair Distribution Function (PDF) to the Characterization of Nanocrystalline MOFs: The Case of M-MOF-74. *Microporous and Mesoporous Materials* 2021, 319 (January). https://doi.org/10.1016/j.micromeso.2021.110973.

- (133) Flores, J. G.; Aguilar-Pliego, J.; Martin-Guaregua, N.; Ibarra, I. A.; Sanchez-Sanchez, M. Room-Temperature Prepared Bimetallic Nanocrystalline MOF-74 as Catalysts in the Aerobic Oxidation of Cyclohexene. *Catal Today* **2022**, *394–396* (June 2021), 295–303. https://doi.org/10.1016/j.cattod.2021.08.025.
- (134) Gonzalez, M. I.; Mason, J. A.; Bloch, E. D.; Teat, S. J.; Gagnon, K. J.; Morrison, G. Y.; Queen, W. L.; Long, J. R. Structural Characterization of Framework–Gas Interactions in the Metal–Organic Framework Co<sub>2</sub> (Dobdc) by in Situ Single-Crystal X-Ray Diffraction. *Chem Sci* 2017, 8 (6), 4387–4398. https://doi.org/10.1039/C7SC00449D.
- (135) Aresta, M.; Dibenedetto, A.; Quaranta, E. *Reaction Mechanisms in Carbon Dioxide Conversion*; Springer Berlin Heidelberg: Berlin, Heidelberg, **2016**. https://doi.org/10.1007/978-3-662-46831-9.
- (136) Choe, J. H.; Kim, H.; Hong, C. S. MOF-74 Type Variants for CO<sub>2</sub> Capture. *Mater Chem Front* **2021**, *5* (14), 5172–5185. https://doi.org/10.1039/D1QM00205H.
- (137) Kazemi, A.; Pordsari, M. A.; Tamtaji, M.; Manteghi, F.; Ghaemi, A.; Rohani, S.; Goddard, W. A. Environmentally Friendly Synthesis and Morphology Engineering of Mixed-Metal MOF for Outstanding CO<sub>2</sub> Capture Efficiency. *Chemical Engineering Journal* 2025, 505. https://doi.org/10.1016/j.cej.2024.158951.
- (138) Wu, H.; Simmons, J. M.; Srinivas, G.; Zhou, W.; Yildirim, T. Adsorption Sites and Binding Nature of CO<sub>2</sub> in Prototypical Metal—Organic Frameworks: A Combined Neutron Diffraction and First-Principles Study. *J Phys Chem Lett* **2010**, *I* (13), 1946–1951. https://doi.org/10.1021/jz100558r.
- (139) Dietzel, P. D. C.; Johnsen, R. E.; Fjellvåg, H.; Bordiga, S.; Groppo, E.; Chavan, S.; Blom, R. Adsorption Properties and Structure of CO<sub>2</sub> Adsorbed on Open Coordination Sites of Metal-Organic Framework Ni<sub>2</sub>(Dhtp) from Gas Adsorption, IR Spectroscopy and X-Ray Diffraction. *Chemical Communications* **2008**, No. 41, 5125–5127. https://doi.org/10.1039/b810574j.
- (140) Lin, X.; Zeng, W.; Liu, M.; Zhong, Q.; Su, T.; Gong, L.; Liu, Y. Amino-Modified Mg-MOF-74: Synthesis, Characterization and CO<sub>2</sub> Adsorption Performance. *Environmental Engineering Research* **2022**, *28* (1), 210569–0. https://doi.org/10.4491/eer.2021.569.
- Zuluaga, S.; Fuentes-Fernandez, E. M. A.; Tan, K.; Xu, F.; Li, J.; Chabal, Y. J.; Thonhauser,
  T. Understanding and Controlling Water Stability of MOF-74. *J Mater Chem A Mater* 2016,
  4 (14), 5176–5183. https://doi.org/10.1039/C5TA10416E.
- (142) Lian, X.; Fang, Y.; Joseph, E.; Wang, Q.; Li, J.; Banerjee, S.; Lollar, C.; Wang, X.; Zhou, H.-C. Enzyme–MOF (Metal–Organic Framework) Composites. *Chem Soc Rev* **2017**, *46* (11), 3386–3401. https://doi.org/10.1039/C7CS00058H.

- (143) Hsu, P. H.; Chang, C. C.; Wang, T. H.; Lam, P. K.; Wei, M. Y.; Chen, C. T.; Chen, C. Y.; Chou, L. Y.; Shieh, F. K. Rapid Fabrication of Biocomposites by Encapsulating Enzymes into Zn-MOF-74 via a Mild Water-Based Approach. ACS Appl Mater Interfaces 2021, 13 (44), 52014–52022. https://doi.org/10.1021/acsami.1c09052.
- (144) Lu, G.; Li, S.; Guo, Z.; Farha, O. K.; Hauser, B. G.; Qi, X.; Wang, Y.; Wang, X.; Han, S.; Liu, X.; Duchene, J. S.; Zhang, H.; Zhang, Q.; Chen, X.; Ma, J.; Loo, S. C. J.; Wei, W. D.; Yang, Y.; Hupp, J. T.; Huo, F. Imparting Functionality to a Metal-Organic Framework Material by Controlled Nanoparticle Encapsulation. *Nat Chem* 2012, 4 (4), 310–316. https://doi.org/10.1038/nchem.1272.
- (145) Yang, J.; Zaremba, O.; Andreo, J.; Gröger, H.; Wuttke, S. Unravelling the Potential of Crude Enzyme Extracts for Biocatalyst Entrapment in Metal–Organic Frameworks. *ACS Nano* **2025**. https://doi.org/10.1021/acsnano.4c18266.
- (146) Lee, Y. R.; Jang, M. S.; Cho, H. Y.; Kwon, H. J.; Kim, S.; Ahn, W. S. ZIF-8: A Comparison of Synthesis Methods. *Chemical Engineering Journal* **2015**, *271*, 276–280. https://doi.org/10.1016/j.cej.2015.02.094.
- (147) Karagiaridi, O.; Lalonde, M. B.; Bury, W.; Sarjeant, A. A.; Farha, O. K.; Hupp, J. T. Opening ZIF-8: A Catalytically Active Zeolitic Imidazolate Framework of Sodalite Topology with Unsubstituted Linkers. *J Am Chem Soc* 2012, 134 (45), 18790–18796. https://doi.org/10.1021/ja308786r.
- (148) Schröder, G. F.; Levitt, M.; Brunger, A. T. Super-Resolution Biomolecular Crystallography with Low-Resolution Data. *Nature* **2010**, *464* (7292), 1218–1222. https://doi.org/10.1038/nature08892.
- (149) Wlodawer, A.; Minor, W.; Dauter, Z.; Jaskolski, M. Protein Crystallography for Non-crystallographers, or How to Get the Best (but Not More) from Published Macromolecular Structures. *FEBS J* **2008**, *275* (1), 1–21. https://doi.org/10.1111/j.1742-4658.2007.06178.x.
- (150) Carpenter, E. P.; Beis, K.; Cameron, A. D.; Iwata, S. Overcoming the Challenges of Membrane Protein Crystallography. *Current Opinion in Structural Biology*. October **2008**, pp 581–586. https://doi.org/10.1016/j.sbi.2008.07.001.
- (151) Burla, M. C.; Caliandro, R.; Carrozzini, B.; Cascarano, G. L.; Cuocci, C.; Giacovazzo, C.; Mallamo, M.; Mazzone, A.; Polidori, G. Crystal Structure Determination and Refinement via SIR2014. *J Appl Crystallogr* 2015, 48 (1), 306–309. https://doi.org/10.1107/S1600576715001132.
- (152) Scapin, G. Molecular Replacement Then and Now. *Acta Crystallogr D Biol Crystallogr* **2013**, 69 (11), 2266–2275. https://doi.org/10.1107/S0907444913011426.
- (153) Evans, P.; McCoy, A. An Introduction to Molecular Replacement. In *Acta Crystallographica Section D: Biological Crystallography*; **2007**; Vol. 64, pp 1–10. https://doi.org/10.1107/S0907444907051554.
- (154) Rossmann, M. G. The Molecular Replacement Method; 1990; Vol. 46.

- (155) Advanced Chemistry Development, Inc. (ACD/Labs). ChemSketch. Toronto, ON, Canada.
- (156) Koschnick, C.; Stäglich, R.; Scholz, T.; Terban, M. W.; von Mankowski, A.; Savasci, G.; Binder, F.; Schökel, A.; Etter, M.; Nuss, J.; Siegel, R.; Germann, L. S.; Ochsenfeld, C.; Dinnebier, R. E.; Senker, J.; Lotsch, B. V. Understanding Disorder and Linker Deficiency in Porphyrinic Zirconium-Based Metal—Organic Frameworks by Resolving the Zr<sub>8</sub>O<sub>6</sub> Cluster Conundrum in PCN-221. *Nat Commun* 2021, *12* (1). https://doi.org/10.1038/s41467-021-23348-w.
- (157) Cliffe, M. J.; Wan, W.; Zou, X.; Chater, P. A.; Kleppe, A. K.; Tucker, M. G.; Wilhelm, H.; Funnell, N. P.; Coudert, F. X.; Goodwin, A. L. Correlated Defect Nanoregions in a Metal-Organic Framework. *Nat Commun* **2014**, *5*. https://doi.org/10.1038/ncomms5176.
- (158) Meekel, E. G.; Goodwin, A. L. Correlated Disorder in Metal-Organic Frameworks. *CrystEngComm*. Royal Society of Chemistry April 28, **2021**, pp 2915–2922. https://doi.org/10.1039/d1ce00210d.
- (159) Yue, S.; Oh, C.; Nandy, A.; Terrones, G. G.; Kulik, H. J. Effects of MOF Linker Rotation and Functionalization on Methane Uptake and Diffusion. *Mol Syst Des Eng* **2023**, *8* (4), 527–537. https://doi.org/10.1039/d2me00237j.
- (160) Gonzalez-Nelson, A.; Coudert, F. X.; van der Veen, M. A. Rotational Dynamics of Linkers in Metal–Organic Frameworks. *Nanomaterials*. MDPI AG March 1, **2019**. https://doi.org/10.3390/nano9030330.
- (161) Ding, M.; Cai, X.; Jiang, H. L. Improving MOF Stability: Approaches and Applications. *Chemical Science*. Royal Society of Chemistry **2019**, pp 10209–10230. https://doi.org/10.1039/c9sc03916c.
- (162) Manning, J. R. H.; Donval, G.; Tolladay, M.; Underwood, T. L.; Parker, S. C.; Düren, T. Identifying Pathways to Metal–Organic Framework Collapse during Solvent Activation with Molecular Simulations. *J Mater Chem A Mater* 2023, 11 (47), 25929–25937. https://doi.org/10.1039/D3TA04647H.
- (163) Ye, X.; Liu, D. Metal-Organic Framework UiO-68 and Its Derivatives with Sufficiently Good Properties and Performance Show Promising Prospects in Potential Industrial Applications. *Crystal Growth and Design*. American Chemical Society August 4, **2021**, pp 4780–4804. https://doi.org/10.1021/acs.cgd.1c00460.
- (164) Wu, H.; Friedrich, H.; Patterson, J. P.; Sommerdijk, N. A. J. M.; de Jonge, N. Liquid-Phase Electron Microscopy for Soft Matter Science and Biology. *Advanced Materials* **2020**, *32* (25). https://doi.org/10.1002/adma.202001582.
- (165) Ponomarev, A. V.; Ershov, B. G. The Green Method in Water Management: Electron Beam Treatment. *Environ Sci Technol* **2020**, *54* (9), 5331–5344. https://doi.org/10.1021/acs.est.0c00545.

- (166) Watson, C.; Janik, I.; Zhuang, T.; Charvátová, O.; Woods, R. J.; Sharp, J. S. Pulsed Electron Beam Water Radiolysis for Submicrosecond Hydroxyl Radical Protein Footprinting. *Anal Chem* 2009, 81 (7), 2496–2505. https://doi.org/10.1021/ac802252y.
- (167) Leonzio, G.; Hankin, A.; Shah, N. CO<sub>2</sub> Electrochemical Reduction: A State-of-the-Art Review with Economic and Environmental Analyses. *Chemical Engineering Research and Design*. Institution of Chemical Engineers August 1, **2024**, pp 934–955. https://doi.org/10.1016/j.cherd.2024.07.014.
- (168) Luo, W.; Zhang, Q.; Zhang, J.; Moioli, E.; Zhao, K.; Züttel, A. Electrochemical Reconstruction of ZnO for Selective Reduction of CO<sub>2</sub> to CO. *Appl Catal B* **2020**, *273*. https://doi.org/10.1016/j.apcatb.2020.119060.
- (169) Geng, Z.; Kong, X.; Chen, W.; Su, H.; Liu, Y.; Cai, F.; Wang, G.; Zeng, J. Oxygen Vacancies in ZnO Nanosheets Enhance CO<sub>2</sub> Electrochemical Reduction to CO. *Angewandte Chemie International Edition* **2018**, *57* (21), 6054–6059. https://doi.org/10.1002/anie.201711255.
- (170) Han, K.; Ngene, P.; de Jongh, P. Structure Dependent Product Selectivity for CO<sub>2</sub> Electroreduction on ZnO Derived Catalysts. *ChemCatChem* **2021**, *13* (8), 1998–2004. https://doi.org/10.1002/cctc.202001710.
- (171) Xue, L.; Zhang, A.; Wu, J.; Wang, Q.; Liu, Y.; Zhao, Y.; Liu, S.; Liu, Z.; Li, P.; Zeng, S. Surface Modification and Reconstruction of ZnO Hollow Microspheres for Selective Electroreduction of CO<sub>2</sub> to CO. *J Alloys Compd* **2021**, 882. https://doi.org/10.1016/j.jallcom.2021.160703.
- (172) Hongsith, N.; Wongrat, E.; Kerdcharoen, T.; Choopun, S. Sensor Response Formula for Sensor Based on ZnO Nanostructures. *Sens Actuators B Chem* **2010**, *144* (1), 67–72. https://doi.org/10.1016/j.snb.2009.10.037.
- (173) Lee, J.-H.; Ko, K.-H.; Park, B.-O. Electrical and Optical Properties of ZnO Transparent Conducting Films by the Sol-Gel Method; 2003; Vol. 247.
- (174) Choi, Y. S.; Kang, J. W.; Hwang, D. K.; Park, S. J. Recent Advances in ZnO-Based Light-Emitting Diodes. *IEEE Trans Electron Devices* **2010**, *57* (1), 26–41. https://doi.org/10.1109/TED.2009.2033769.
- (175) Lee, K. M.; Lai, C. W.; Ngai, K. S.; Juan, J. C. Recent Developments of Zinc Oxide Based Photocatalyst in Water Treatment Technology: A Review. *Water Research*. Elsevier Ltd January 1, **2016**, pp 428–448. https://doi.org/10.1016/j.watres.2015.09.045.
- (176) Huang, X.; Zheng, X.; Xu, Z.; Yi, C. ZnO-Based Nanocarriers for Drug Delivery Application: From Passive to Smart Strategies. *International Journal of Pharmaceutics*. Elsevier B.V. December 20, 2017, pp 190–194. https://doi.org/10.1016/j.ijpharm.2017.10.008.
- (177) Xiong, H. M. ZnO Nanoparticles Applied to Bioimaging and Drug Delivery. *Advanced Materials* **2013**, *25* (37), 5329–5335. https://doi.org/10.1002/adma.201301732.
- (178) Aminoff, G. Ueber Lauephotogramme Und Struktur von Zinkit. Zeitschrift fuer Kristallographie, Kristallgeometrie, Kristallphysik, Kristallchemie 1921, 56, 495–505.

- (179) Weetman, C.; Bag, P.; Szilvási, T.; Jandl, C.; Inoue, S. CO<sub>2</sub> Fixation and Catalytic Reduction by a Neutral Aluminum Double Bond. *Angewandte Chemie International Edition* **2019**, *58* (32), 10961–10965. https://doi.org/10.1002/anie.201905045.
- (180) Zeng, J.; Castellino, M.; Fontana, M.; Sacco, A.; Monti, N. B. D.; Chiodoni, A.; Pirri, C. F. Electrochemical Reduction of CO<sub>2</sub> With Good Efficiency on a Nanostructured Cu-Al Catalyst. Front Chem 2022, 10. https://doi.org/10.3389/fchem.2022.931767.
- (181) Ma, Z.; Wang, B.; Yang, X.; Ma, C.; Wang, W.; Chen, C.; Liang, F.; Zhang, N.; Zhang, H.; Chu, Y.; Zhuang, Z.; Xu, H.; Wang, Y.; Liu, J. P-Block Aluminum Single-Atom Catalyst for Electrocatalytic CO<sub>2</sub> Reduction with High Intrinsic Activity. *J Am Chem Soc* **2024**. https://doi.org/10.1021/jacs.4c11326.
- (182) Vandemeulebroucke, D.; Batuk, M.; Hajizadeh, A.; Wastiaux, M.; Roussel, P.; Hadermann, J. Incommensurate Modulations and Perovskite Growth in La<sub>x</sub>Sr<sub>2-x</sub>MnO<sub>4-δ</sub> Affecting Solid Oxide Fuel Cell Conductivity. *Chemistry of Materials* **2024**, *36* (5), 2441–2449. https://doi.org/10.1021/acs.chemmater.3c03199.
- (183) Tang, H.; Wei, J.; Liu, F.; Qiao, B.; Pan, X.; Li, L.; Liu, J.; Wang, J.; Zhang, T. Strong Metal–Support Interactions between Gold Nanoparticles and Nonoxides. *J Am Chem Soc* **2016**, *138* (1), 56–59. https://doi.org/10.1021/jacs.5b11306.
- (184) Xu, M.; Peng, M.; Tang, H.; Zhou, W.; Qiao, B.; Ma, D. Renaissance of Strong Metal—Support Interactions. *J Am Chem Soc* **2024**, *146* (4), 2290–2307. https://doi.org/10.1021/jacs.3c09102.
- (185) Wang, H.; Wang, L.; Xiao, F.-S. New Routes for the Construction of Strong Metal—Support Interactions. *Sci China Chem* **2022**, *65* (11), 2051–2057. https://doi.org/10.1007/s11426-022-1356-3.

## **Appendix**

Atomic coordinates and anisotropic ADP parameters for the refined structures discussed in chapters 4.1 and 4.1.1. regarding MOF-74 and the *in situ* activation of this MOF.

Table 11. Atomic coordinates, occupancies and anisotropic ADP values for the non-solvent exchanged 7n-MOF-74. Space group:  $R_2^{-1}$ . Cell parameters: a = 26.331(1).  $A_1 c = 6.411(2)$ .

exchanged Zn-MOF-74. Space group: R3. Cell parameters: $a = 26.331(1) \text{ Å}$ , $c = 6.411(2) \text{ Å}$ .										
	X	y	Z	Occ	U11	U22	U33	U12	U13	U23
Zn	0.63903	0.68412	-0.00811	0.7	0.05346	0.04187	0.05709	0.02488	-	0.00299
1	6				9	5	8	7	0.00713	8
									7	
Zn	0.60524	0.68109	0.02489	0.3	0.05346	0.04187	0.05709	0.02488	-	0.00299
2	3	3	3		9	5	8	7	0.00713	8
									7	
C1	0.65976	0.78738	0.46869	1	0.07369	0.04671	0.03570	0.02934	0.00626	0.00992
	3		8		9	7	8		8	4
C2	0.65292	0.74284	0.62665	1	0.08427	0.06122	0.04172	0.05287	0.01266	0.01329
	3	4	7		6	7	7	1	9	4
C3	0.67935	0.78872	0.26060	1	0.08073	0.06095	0.04386	0.05050	-	0.00273
	8	4	1		4	2	5	6	0.00045	1
									8	
C4	0.68710	0.83529	0.12683	1	0.08948	0.02879	0.06374	0.03651	-	0.01064
	9	1	8		6		8	2	0.00192	5
									1	
O1	0.69018	0.74798	0.17889	1	0.10094	0.06172	0.06163	0.05251	0.01776	0.01747
	1	6	2		6	2	2	5	3	6
O2	0.54541	0.68574	0.17129	0.34	0.32828	0.19530	0.24205	0.24333	0.14031	0.09336
	7	6	7	4	5	6	3	7	6	5
О3	0.68026	0.71453	0.60246	1	0.09828	0.06832	0.06544	0.05871	0.00411	0.01457
	5		2		2	5	7	1	1	7
O4	0.62255	0.73454	0.78462	1	0.12803	0.05546	0.04958	0.05815	0.01208	0.01103
	6	2			6	7	6	9	1	5

Table 12. Atomic coordinates, occupancies and anisotropic ADP values for the Post SE Zn-MOF-74. Space group:  $R\bar{3}$ . Cell parameters: a = 25.4215(3) Å, c = 6.734(3) Å.

	X	v .	Z	Oc	U11	U22	U33	U12	U13	U23
		J	2	c	011	922	900	012	010	020
Zn	0.68690	0.63898	0.52668	1	0.02279	0.03566	0.01917	0.01478	0.00126	0.00366
1	9	4	9			7	1	5	7	8
C1	0.55565	0.54508	0.57589	1	0.02196	0.02493	0.01257	-	-	-
	8	6	9			7	9	0.00296	0.00254	0.00192
								9	2	3
C2	0.48490	0.50115	0.30597	1	0.02945	0.02645	0.01764	-	-	0.00061
	4	4	3		7	6	7	0.00944	0.00529	7
								8	7	

C3	0.57795	0.59465	0.23685	1	0.01551	0.03350	0.01048	0.00143	-	0.00422
	5	1	1		2	8		5	0.00166	5
									8	
C4	0.53928	0.54689	0.37889	1	0.02417	0.03421	0.01707	0.00354	0.00354	-
	8	6	2		2	6	9	2	7	0.00895
										4
O1	0.60641	0.58514	0.65496	1	0.03504	0.03454	0.01774	0.00294	0.00308	0.00359
	9	9	2		2	8		3	4	3
O2	0.56173	0.59307	0.06501	1	0.04286	0.02723	0.02703	-	-	0.00727
	3	6	1		9	5	5	0.00220	0.00174	3
								6	3	
О3	0.62802	0.63445	0.29665	1	0.03332	0.03345	0.03387	-	-	0.01291
	2	8	9		4	8	7	0.00367	0.00850	5
								4	1	
H1	0.47424	0.50185	0.15416	1	/	/	/	/	/	/
	5	3	6							

Table 13. Atomic coordinates, occupancies and anisotropic ADP values for the Post 120 Zn-MOF-74. Space group:  $R\overline{3}$ . Cell parameters: a=26.7959(2) Å, c=6.630(7) Å.

	X	y	Z	Oc	U11	U22	U33	U12	U13	U23
				c						
Zn	0.28515	0.30577	0.19450	1	0.03621	0.03697	0.00754	0.02698	0.00302	0.00283
1	4	2	5		9	1	5	6	5	
C1	0.24392	0.31676	0.57090	1	0.01595	0.04222	0.00713	0.01145	0.00536	0.00103
	5	5	9		4	5	2		2	8
C2	0.15195	0.31684	0.64127	1	0.02462	0.09862	0.00365	0.04751	-	-
	6		1		9	3	9	9	0.00056	0.00479
									3	7
C3	0.22305	0.34389	0.90968	1	0.02578	0.06690	0.00505	0.03388	-	-
	9		2		7	6	5	4	0.00960	0.01122
									1	5
C4	0.20634	0.32636	0.70674	1	0.02967	0.04676	0.00667	0.02080	0.00214	0.00518
		9	3		3		7	5	5	6
01	0.22796	0.30227	0.39798	1	0.03202	0.06071	0.01151	0.03384	-0.00786	-
	9	9			2	4	7	3		0.01131
										3
O2	0.27410	0.35461	0.98889	1	0.02061	0.05018	0.01186	0.02015	-	-
	1	4	2		1		9	9	0.00140	0.00302
									3	8
О3	0.29469	0.32668	0.62788	1	0.03729	0.07228	0.03058	0.03040	-	-
	8	8	3		3	8		8	0.00433	0.03107
									3	6
H1	0.14738	0.30265	0.46673	1	/	/	/	/	/	/
	6	6	5							

Table 14. Atomic coordinates, occupancies and anisotropic ADP values for the Post 300 Zn-MOF-74. Space group:  $R\overline{3}$ . Cell parameters: a = 26.805(8) Å, c = 6.645(3) Å.

	X	у	Z	Oc	U11	U22	U33	U12	U13	U23
				c						
Zn	0.69386	0.71448	0.19360	1	0.03862	0.02725	0.01087	0.01945	-	-0.00199
1	6	3	2			5	8	2	0.00252	
									3	
C1	0.68218	0.75414	0.56913	1	0.05458	0.02279	0.00914	0.02001	0.00537	-
		9	9		5	3	1	4	9	0.00062
										7
C2	0.65022	0.81862	1.02449	1	0.06408	0.03243	0.00425	0.02912	-	0.00034
	6	8	2		2	1	6	3	0.00561	8
									5	
C3	0.65657	0.77712	0.90746	1	0.05787	0.03444	0.01245	0.03261	-	-
	3	6	4		4	3	3	1	0.00228	0.00010
									2	4
C4	0.67213	0.79245	0.70943	1	0.06949	0.03477	0.00394	0.04088	0.00458	0.00376
	1		4		6	3	1	5	3	6
01	0.70006	0.77346	0.39736	1	0.07009	0.05563	0.01512	0.04334	0.01318	-
	5		8		1	4		6	6	0.00443
										6
O2	0.64563	0.72574	0.98762	1	0.05193	0.02354	0.01578	0.02021	0.00386	-
	8	9	5		1	8	6	4	3	0.00289
										2
О3	0.67168	0.70549	0.62529	1	0.07537	0.03437	0.02798	0.03906	0.02693	0.01205
	2	9	2		9	4	3	3	8	8
Н1	0.63607	0.80719	1.17512	1	/	/	/	/	/	/
	3		9							

Table 15. Atomic coordinates, occupancies and anisotropic ADP values for the Post 350 Zn-MOF-74. Space group:  $R\overline{3}$ . Cell parameters: a = 25.887(7) Å, c = 6.801(3) Å.

	74. Space group: R3. Cell parameters: $a = 25.88/(7) A$ , $c = 6.801(3) A$ .										
	X	У	Z	Oc	U11	U22	U33	U12	U13	U23	
				c							
Zn	0.68723	0.63911	0.52650	1	0.02255	0.03252	0.01628	0.01332	-	0.00232	
1	7	4	5		3	8	1	7	0.00062	8	
									6		
C1	0.55634	0.54623	0.57751	1	0.02118	0.02416	0.01836	-	-0.00894	-	
	3	8			9	9	4	0.00045		0.00539	
								7		9	
C2	0.48416	0.50062	0.30591	1	0.02975	0.02122	0.01063	-	-	-	
	4	1	7		6	9	1	0.00732	0.00264	0.00178	
								6	9	2	
C3	0.57877	0.59395	0.23635	1	0.01678	0.04191	0.00563	0.00098	-	0.00354	
	5	8	3		4			6	0.00075		
									5		

C4	0.53927	0.54609	0.37548	1	0.04951	0.04551	0.00611	0.01501	0.00494	0.00333
	5		8		1	3		2	4	5
O1	0.60798	0.58729	0.65350	1	0.01764	0.03283	0.01477	-	0.00195	0.00191
	2	7	1		6	6	8	0.00275	6	8
								2		
O2	0.56107	0.59375	0.06353	1	0.03430	0.03047	0.01893	-	-	0.00265
	2	3	8		9	7	7	0.00258	0.00148	
								6	6	
О3	0.62758	0.63356	0.29160	1	0.02801	0.03912	0.03027	-	-	0.01657
		1	1		8	9		0.00697	0.00474	4
								4	4	
H1	0.47286	0.50209	0.15702	1	/	/	/	/	/	/
	7		2							

Table 16. Atomic coordinates, occupancies and anisotropic ADP values for the Post SE Cu-MOF-74. Space group:  $R\overline{3}$ . Cell parameters: a = 26.15(8) Å, c = 6.32(3) Å.

	X	у	Z	Oc	U11	U22	U33	U12	U13	U23
				c						
Cu	-0.27969	0.01511	0.84321	1	0.01959	0.01809	0.01387	0.00627	0.00184	0.00206
1		4	6		8	7	3	2	4	6
C1	-	0.16237	0.37176	1	0.04527	0.01657	0.00423	0.00556	-	0.00112
	0.15050	2	2		9		9	8	0.00273	7
	9								1	
C2	-	-	0.75920	1	0.01153	0.02295	0.01420	0.00707	-	-
	0.31951	0.10945	2		7	1	1	7	0.00162	0.00813
	7	9							4	6
C3	-0.24727	0.07691	0.46111	1	0.01159	0.02192	0.01328	0.00965	0.00003	0.00073
		1	7			8	3	4	6	6
C4	-	0.12170	0.30301	1	0.02022	0.02937	0.00676	0.00775	0.00280	0.00774
	0.20591	7	6		3	1	2	6	9	
	7									
O1	-	-	0.67387	1	0.02998	0.01439	0.01783	0.01606	0.00311	0.00218
	0.30797	0.05731	8		8	9	1	8	6	5
	6	7								
O2	-	0.06745	0.62585	1	0.01609	0.02043	0.01628	0.00195	-	0.00135
	0.22456		6		5	6	3	9	0.00177	1
	3								2	
О3	-	0.05117	0.43702	1	0.01311	0.03660	0.01167	0.00497	0.00145	-
	0.30350	7	7			8	8	6	2	0.00032
	6									6

Table 17. Atomic coordinates, occupancies and anisotropic ADP values for the Post 120 Cu-MOF-74. Space group:  $R\overline{3}$ . Cell parameters: a=26.248(7) Å, c=6.334(2) Å.

x y z Oc U11 U22 U33 U12 U13 U23

c

Cu	-0.27979	0.01516	0.84340	1	0.02026	0.01975	0.01256	0.00735	0.00197	0.00136
1		1	7		8	8	4	4	6	
C1	-0.15042	0.16219	0.37133	1	0.03250	0.02288	0.01087	0.01897	0.00107	0.00848
		7	2		3	1	2	5	2	4
C2	-	-	0.75792	1	0.01920	0.01614	0.01329	0.00520	-	-
	0.31916	0.10883	1		3	8	2	5	0.00019	0.00136
	1	1							8	2
C3	-	0.07725	0.46108	1	0.01451	0.01772	0.01145	0.00279	-	0.00063
	0.24627	4	2			5	6	7	0.00406	2
	9								5	
C4	-0.20474	0.12169	0.30224	1	0.02620	0.02614	0.00439	0.00208	0.00674	0.00610
		6	8		4		7	8	3	7
O1	-	-0.05664	0.67445	1	0.02504	0.01241	0.01356	0.01136	0.00525	0.00348
	0.30746		4		3	1		6	6	6
	5									
O2	-	0.06665	0.62529	1	0.01951	0.02116	0.01313	0.00495	-	0.00372
	0.22520		7		5	4		6	0.00176	6
	6								5	
О3	-	0.05118	0.43674	1	0.01963	0.02736	0.01160	0.00134	-	-
	0.30298		4		6	4	1		0.00017	0.00106
	9								6	9

Atomic coordinates for the refined structures discussed in chapter 4.1.2. regarding the *in situ* CO<sub>2</sub> study using MOF-74.

Table 18. Atomic coordinates and occupancies for the vacuum Zn-MOF-74 structure. Space group:  $R\overline{3}$ . Cell parameters: a = 26.688(5) Å, c = 6.869(2) Å.

	X	у	Z	Occ	
Zn	0.70318	0.72078	0.1789	1	
C1	0.6775	0.8895	0.7508	1	
C2	0.6836	0.7549	0.5734	1	
C3	0.6725	0.7926	0.7140	1	
C4	0.6844	0.8475	0.6391	1	
O1	0.7015	0.7731	0.3965	1	
O2	0.6899	0.9393	0.6687	1	
O3	0.6752	0.7047	0.6351	1	
O4	0.541761	0.655282	0.702155	1	
O5	0.55145	0.696297	0.292631	0.71	
Н	0.528018	0.493451	0.872452	1	

Table 19. Atomic coordinates and occupancies for the  $CO_2$  absorbed Zn-MOF-74 structure. Space group:  $R\bar{3}$ . Cell parameters: a = 26.645(5) Å, c = 6.873(3) Å.

	X	у	Z	Occ	
Zn	0.68412	0.62974	0.5120	1	
C1	0.4211	0.4042	0.7553	1	

C2	0.5558	0.5452	0.5843	1
C3	0.4585	0.4529	0.6075	1
C4	0.5159	0.4981	0.6917	1
O1	0.6064	0.5813	0.6636	1
O2	0.4390	0.4048	0.9373	1
O3	0.3702	0.3621	0.6939	1
O4	0.678331	0.553049	0.353969	1
Н	0.518369	0.485312	0.869154	1
Cpos1and2	0.483018	0.606812	0.72723	0.346
Cpos3	0.55448	0.65821	0.47501	0.277
Opos1	0.427422	0.576927	0.735699	0.157
Opos2	0.46715	0.60797	1.00082	0.189
Opos3	0.5485	0.69684	0.29927	0.277

Atomic coordinates for the refined structures discussed in chapter 4.2. regarding the biohybrid materials.

Table 20. Atomic coordinates, occupancies and anisotropic ADP values for the pure ZIF-8 MOF.

Space group:  $1\overline{4}3m$  Cell parameters: a = 16.868(4) Å

	X	У	Z	Occ	U11	U22	U33	U12	U13	U23
Zn	1.00	0.50	0.75	1	0.102	0.102	0.099	0.000	0.000	0.000
N	0.9677	0.4104	0.6832	1	0.090	0.084	0.104	-0.028	0.014	-0.011
C1	1.0119	0.3743	0.6257	1	0.058	0.082	0.082	-0.027	0.010	-0.010
C2	0.8972	0.3698	0.6892	1	0.152	0.079	0.091	-0.016	0.048	-0.020
C3	1.0867	0.4039	0.5961	1	0.118	0.097	0.097	0.013	0.020	-0.020
H1	0.815	0.354	0.646	1	/	/	/	/	/	/
H2	1.160	0.417	0.617	1	/	/	/	/	/	/

Table 21. Atomic coordinates, occupancies and anisotropic ADP values for the pure ZIF-8@OxdB1 biohybrid. Space group:  $I\overline{4}3m$ . Cell parameters: a = 16.88(2) Å.

U22 U12 U23 X Occ U11 U33 U13 Zn 1.00 0.50 0.75 0.079 0.079 0.0800.0000.000 0.0000.082 0.13 0.015 0.050 N 0.9695 0.41350.6822 1 0.20 0.015C1 1.0131 0.3743 0.6257 0.027 -0.05 0.038 -0.038 1 0.1110.111 C20.901 0.36730.6883 1 0.21 0.079 0.069 -0.035 0.023 -0.03 C3 1.0770.40390.5961 0.11 0.18 0.180.02 0.09 -0.09 H1 0.815 0.342 0.658 1 / / H2 1.143 0.418 0.614 1

Table 22. Atomic coordinates, occupancies and anisotropic ADP values for the pure MOF-74.

*Space group:*  $R\bar{3}$ . *Cell parameters:* a = 25.406(4) Å, c = 6.748(1) Å.

		<i>spuce</i> 8. 01					\ / /	1110	/	T.102
	X	У	Z	Occ	U11	U22	U33	U12	U13	U23
Zn	0.61863	0.64614	0.8618	1	0.0453	0.0405	0.0157	-0.0019	0.0024	0.0182
C1	0.4440	0.4546	0.4235	1	0.044	0.044	0.009	0.003	0.005	0.004
C2	0.5778	0.5940	0.2367	1	0.040	0.030	0.007	0.005	0.003	-0.002

C3	0.4853	0.5011	0.3074	1	0.035	0.041	0.014	0.002	0.002	0.004
C4	0.5401	0.5460	0.3764	1	0.052	0.040	0.006	-0.001	-0.001	0.003
01	0.3915	0.4124	0.3435	1	0.037	0.041	0.012	0.002	0.000	0.011
O2	0.5610	0.5933	0.0662	1	0.048	0.048	0.014	0.005	0.000	0.011
O3	0.6270	0.6347	0.2984	1	0.049	0.060	0.020	0.008	-0.010	-0.002
H1	0.815	0.354	0.646	1	/	/	/	/	/	/

Table 23. Atomic coordinates, occupancies and anisotropic ADP values for the MOF-74@OxdB1 biohybrid. Space group:  $R\overline{3}$ . Cell parameters: a = 25.605(5) Å, c = 6.753(2) Å.

	X	у	Z	Осс	U11	U22	U33	U12	U13	U23
Zn	0.68719	0.63938	0.5288	1	/	/	/	/	/	/
C1	0.4216	0.4059	0.7608	1	/	/	/	/	/	/
C2	0.5157	0.4993	0.6935	1	/	/	/	/	/	/
C3	0.5558	0.5456	0.5759	1	/	/	/	/	/	/
C4	0.4608	0.4540	0.6230	1	/	/	/	/	/	/
O1	0.6082	0.5866	0.6562	1	/	/	/	/	/	/
O2	0.4392	0.4071	0.9349	1	/	/	/	/	/	/
О3	0.3709	0.3652	0.7030	1	/	/	/	/	/	/
H1	0.5328	0.5009	0.844	1	/	/	/	/	/	/

Atomic coordinates for the final UA-4 structure discussed in chapter 4.3.

Table 24. Atomic coordinates and occupancies for the final UA-4 structure. Space group: P6. PXRD optimized cell parameters: a = 39.75 Å, c = 16.122 Å.

	1 Mil Opillium	ca cen parameters. a	37.73 11, 0	10.122 11.
	X	у	Z	Occ
Zr1	0.6407	0.3316	0.4171	1
Zr2	0.6655	0.3810	0.4629	1
Zr3	0.6091	0.3043	0.2278	1
Zr4	0.6092	0.2915	0.3610	1
Zr5	0.6430	0.3407	0.3209	1
Zr6	0.3652	0.6248	1.2198	1
H1	0.4172	0.4825	0.7770	1
H2	0.4042	0.4082	0.9812	1
Н3	0.3864	0.5124	0.8491	1
H4	0.3731	0.4380	1.0687	1
H5	0.4693	0.4497	0.9700	1
Н6	0.4364	0.3656	0.7611	1
H7	0.5027	0.4196	1.0480	1
H8	0.4695	0.3357	0.8387	1
H9	0.4733	0.3365	1.1129	1
H10	0.5184	0.3080	1.1551	1
H11	0.3045	0.4725	0.9478	1
H12	0.2888	0.5122	1.0640	1
H13	0.5021	0.4379	0.7542	1
H14	0.4024	0.3804	0.5846	1
H15	0.5354	0.4107	0.6653	1

H16	0.4356	0.3531	0.4961	1
H17	0.4643	0.4943	0.6331	1
H18	0.3541	0.3997	0.7164	1
H19	0.4308	0.5253	0.5600	1
H20	0.3209	0.4306	0.6428	1
H21	0.3506	0.4791	0.4182	1
H22	0.3145	0.5179	0.3838	1
H23	0.4661	0.3393	0.4112	1
H24	0.5146	0.3189	0.3452	1
S1	0.5431	0.3555	0.9507	1
S2	0.3803	0.5227	1.0975	1
S3	0.3406	0.5242	0.6067	1
S4	0.5471	0.3680	0.5464	1
O1	0.3338	0.5769	1.1820	1
O2	0.3616	0.5541	1.2710	1
O3	0.5814	0.3037	0.9679	1
O4	0.5990	0.3258	1.1046	1
O5	0.3089	0.5804	0.4718	1
O6	0.2792	0.5528	0.5975	1
O7	0.6159	0.3668	0.4448	1
O8	0.5766	0.3036	0.4288	1
C1	0.4312	0.4267	0.8135	1
C2	0.4125	0.4436	0.8664	1
C3	0.4074	0.4726	0.8299	1
C4	0.4003	0.4314	0.9518	1
C5	0.3904	0.4892	0.8785	1
C6	0.3830	0.4478	1.0004	1
C7	0.3781	0.4769	0.9637	1
C8	0.4510	0.4094	0.8612	1
C9	0.4694	0.4243	0.9409	1
C10	0.4511	0.3777	0.8249	1
C11	0.4880	0.4077	0.9842	1
C12	0.4695	0.3611	0.8680	1
C13	0.4879	0.3760	0.9474	1
C14	0.5074	0.3577	0.9908	1
C15	0.4973	0.3391	1.0713	1
C16	0.5210	0.3241	1.0935	1
C17	0.5482	0.3316	1.0288	1
C18	0.3605	0.4949	1.0153	1
C19	0.3243	0.4905	1.0011	1
C20	0.3463	0.5310	1.1206	1
C21	0.3161	0.5113	1.0622	1
C22	0.3467	0.5556	1.1929	1
C23	0.5772	0.3195	1.0313	1
C24	0.4309	0.4275	0.7246	1
C25	0.4504	0.4107	0.6740	1

C26       0.4873       0.4190       0.6967       1         C27       0.4321       0.3873       0.6025       1         C28       0.5058       0.4040       0.6473       1	
C28 0.5058 0.4040 0.6473 1	
0.000	
C29 0.4504 0.3720 0.5534 1	
C30 0.4874 0.3805 0.5756 1	
C31 0.4111 0.4454 0.6792 1	
C32 0.4324 0.4802 0.6355 1	
C33 0.3713 0.4277 0.6818 1	
C34 0.4139 0.4975 0.5948 1	
C35 0.3528 0.4448 0.6409 1	
C36 0.3740 0.4797 0.5977 1	
C37 0.3543 0.4982 0.5560 1	
C38 0.3442 0.4954 0.4680 1	
C39 0.3216 0.5336 0.5247 1	
C40 0.3253 0.5159 0.4498 1	
C41 0.5068 0.3648 0.5220 1	
C42 0.4936 0.3455 0.4428 1	
C43 0.5191 0.3347 0.4082 1	
C44 0.5508 0.3462 0.4623 1	
C45 0.3030 0.5571 0.5291 1	
C46 0.5833 0.3398 0.4449 1	